# Preparation, Characterization, and Applications of Several Optically-Switchable Azo-Polymers

Thomas A. Singleton

A thesis submitted to McGill University in partial fulfilment
of the requirements for the degree of Doctor of Philosophy

Department of Chemistry,
McGill University, Montreal,
Quebec, Canada

October 2014

# Table of Contents

# Table of Figures

# List of Abbreviations

| | |
|---|---|
| $\lambda_{max}$ | Wavelength of maximum absorbance |
| AA | Acrylic acid |
| CAN | Acetonitrile |
| AIBN | Azoisobutyronitrile |
| APTMS | (3-aminopropyl)trimethoxysilane |
| Boc | *tert*-butyl carbonate |
| cAB | *cis*-azobenzene |
| CCD | Charge-coupled device |
| DAC | Diamond Anvil Cell |
| DC | Direct current |
| DCM | Dichloromethane |
| DMF | N,N-Dimethylformamide |
| DMSO | Dimethylsulfoxide |
| DR1 | Disperse Red 1 |
| ESI | Electrospray ionization |
| EtOAc | Ethyl acetate |
| GPC | Gel permeation chromatography |
| HCl | Hydrochloric acid |
| HPLC | High-performance liquid chromatography |
| HMBC | Heteronuclear multiple-bond quantum coherence |
| HRMS | High resolution mass spectrometry |
| HSQC | Heteronuclear single quantum coherence |
| IOF | Inverse opal film |
| MeOH | Methanol |
| NIR | Near infrared |
| NMR | Nuclear magnetic resonance |
| NT | Neurotransmitter |
| OD | Optical density |

| | |
|---|---|
| PAA | poly(acrylic acid) |
| PAH | poly(allylamine hydrochloride) |
| PDADMAC | Poly(diallyldimethylammonium chloride) |
| PDI | Polydispersity index |
| PDR1A | poly(Disperse Red 1 acrylate) |
| p(DR1A-*co*-AA) | poly(Disperse Red 1 acrylate-*co*-acrylic acid) |
| PEM | Polyelectrolyte multilayer |
| Piranha Solution | 3:1 conc. sulfuric acid/30% hydrogen peroxide solution |
| PMMA | poly(methyl methacrylate) |
| PTFE | Poly(tetrafluoroethylene) |
| tAB | *trans*-azobenzene |
| TEOS | Tetraethoxysilane (tetraethyl orthosilicate) |
| THF | Tetrahydrofuran |
| TLC | Thin-layer chromatography |
| UV | Ultraviolet |
| UV-vis | Ultraviolet-visible spectroscopy |
| Nd:YAG | Neodymium/yttrium aluminum garnet |

# Abstract

This thesis explores a variety of applications for photoactive materials based on the azobenzene chromophore. Chapter 1, the introduction, provides background and context for the research chapters. The second chapter expands on the experimental methods described in the research chapters, providing additional details not covered in the chapters themselves.

Chapter 3 explores the fundamental limits of the characteristic *trans-cis* isomerization of these molecules under extremely high pressure. Pressure has been implicated in several well-studied applications of azobenzene-functionalized polymers: namely the formation of surface relief gratings as a result of surface mass transport, azo-functionalized liquid crystal systems for photomechanics, and the use of azobenzene chromophores as 'molecular muscles' for molecular machines.

Chapter 4 describes our efforts to create a photo-induced change in the wettability of a photonic nanostructure. Azobenzene-functionalized polymers have been demonstrated to undergo a light-induced change in surface energy, and this research applied that effect to inverse-opal photonic crystals. The result was a photonic crystal that could be used for liquid identification, based on the disappearance of structural colour upon wetting. The change in wettability could be tightly controlled by the amount of light exposure, which could distinguish between liquid mixtures in increments as small as 2.5 vol %. The resulting structures hold applications in microfluidics as remote, light-activated liquid gates, or as sensitive anti-tampering and encryption devices.

The final two research chapters, 5 and 6, describe the development of an all-optical detection system for neural impulses. Chapter 5 outlines the synthesis and characterization of several candidate boronic acid-functionalized azobenzene derivatives, which undergo a change in visible absorbance spectrum upon exposure to the neurotransmitter dopamine. The indicator molecules were assessed based on the degree of change in their visible absorption spectrum, as well as the concentration of analyte required to induce the change.

The candidate indicator molecules were incorporated into polyelectrolyte multilayers in Chapter 6, allowing them to be applied as coatings to fibre optics to act as implantable detectors

for neural activity. The polyelectrolyte multilayers act as a support matrix for the detector molecules, while simultaneously enhancing the biocompatibility of the substrate. The indicator molecules were incorporated into the multilayers through covalent attachment, or electrostatic attraction. The coated fibre optic detectors were assessed for their colourimetric response to pH-balanced solution-phase neurotransmitters, as a model for a biological system.

# Résumé

Cette thèse explore une variété d'application de matériaux photo-actifs basés sur le chromophore azobenzène. Le premier chapitre, l'introduction, présente le contexte et l'information nécessaire à la compréhension des chapitres de recherche. Le second chapitre développe les méthodes expérimentales décrites dans les sections de recherche, en fournissant des détails additionnels qui ne sont pas abordés dans lesdits chapitres.

Le troisième chapitre explore les limites fondamentales, sous pression extrême, de l'isomérisation *trans-cis,* caractéristique de ces molécules. La pression a déjà été mise en cause dans plusieurs applications bien étudiés des polymères fonctionnalisés d'azobenzène: notamment pour la formation de « surface relief grating » résultant du transport de masse en surface, de cristaux liquide fonctionnalisés azo pour des systèmes photomécaniques et dans l'utilisation de chromophore d'azobenzène comme « muscle moléculaire » pour machines moléculaires.

Le quatrième chapitre décrit nos efforts pour contrôler des changements photo-induits du mouillage d'une nanostructure photonique. Il a été démontré que l'énergie de surface des polymères fonctionnalisés d'azobenzène, lorsque irradiés par la lumière, manifeste des changements. Cette recherche a appliqué cet effet à des cristaux photonique opale-inversé. Ceci résulte en un cristal photonique pouvant être utilise pour l'identification de liquide, basée sur la disparition de la couleur structurelle lors de mouillage. Les changements en mouillage peuvent être minutieusement contrôlés par la quantité d'exposition lumineuse, ce qui permet de distinguer certain mélanges de liquides par changement de composition aussi petit que 2,5% du volume. La structure résultante peut être utilisée en « micro-fluidique » en tant que grille liquide activé à distance par lumière, ou en tant que composante sensible au sabotage et à l'encryptage.

Les deux derniers chapitres de recherche, cinq et six, décrivent le développement d'un système entièrement optique pour la détection d'impulsions neuronales. Le chapitre cinq décrit la synthèse et la caractérisation de plusieurs dérivés d'azobenzène fonctionnalisés avec la fonction acide boronique qui subissent un changement dans leurs spectres d'absorption visible lorsqu'exposé au neurotransmetteur dopamine. Ces molécules sondes ont été évalué par l'ampleur

du changement de leur spectre d'absorption visible ainsi que par la concentration d'analyte requise pour induire ce changement.

Le chapitre six explique comment les sondes moléculaires ont été incorporées dans des multicouches poly-électrolytique, permettant ainsi de les appliquer comme enduit sur fibre optique pour agir comme détecteur implantable pour l'activité neuronale. Les multicouches poly-électrolytique agissent comme matrice de support pour les molécules de détection en plus d'augmenter la biocompatibilité du substrat. Les molécules sondes ont été incorporés dans les multicouches par liaison covalente ou par attraction électrostatique. Les détecteurs enduits sur les fibres optiques ont été évalué par leur réponse colorimétrique à des solutions à pH balancé de neurotransmetteur, servant de modèle pour un système biologique.

# Acknowledgements

Firstly, I wish to thank the wonderful people I have had the privilege and pleasure of sharing a laboratory with over the years: Alex, Janet, Oleksandr, Chris, Yingshan, Mikel, Frédéric, Mila, Peter, Zahid, and Lucie. Their support and friendship have made my time as a graduate student both fulfilling and enjoyable. Special thanks to Alex, Oleksandr, and Chris for their help editing this thesis, and Fred and Guillaume for translating. In addition, I have had the pleasure of working with several excellent undergraduate students: Guillaume, James, Alexander, Kaien, and Taylor. As well, visitors to the lab including Jaana, Raquel, and Mark have all enriched my education greatly. Of course, I must offer my thanks to my supervisor, Dr. Chris Barrett, for his support and mentorship over the past five years. Thank you for the support and encouragement to pursue my research goals.

My gratitude to the members of Zamboni Chemical Solutions: Bob, John, Michel, and Helmi, who have all provided incredible advice. As well, I wish to thank Dr. Sleiman's research group, especially Tom Edwardson, for their invaluable assistance with HPLC separations. Special thanks to Dr. Butler for the enjoyable collaboration that led to Chapter 3.

Many people in the department have contributed greatly to my success over the past five years. Thank you to the many people I have worked with as a teaching assistant: Sam, Jean-Marc, Mitch, and Grace. Thanks also to the office staff, especially Chantal, Claude, and Sandra, as well as the technical staff members: JP, Rick, Weihua, Fred, Alex, and Nadim.

In addition to the many people whom I spent my work days with, I must thank my wonderful friends whose companionship kept me sane during the degree. Thank you for listening to my complaints about my failures, and celebrating my successes. Alex, Bryan, Patricia, Krause, Adam, Andrew, and everyone else I enjoyed having a beer with from time to time. I must also thank my parents, who have shown nothing but support and encouragement during my entire education. Thank you for listening, and making the numerous trips to Montreal to visit.

Lastly, I must thank Katie for her patience and support over the past five years. I couldn't have done it without you, and I wouldn't have wanted to.

# Preface and Contribution of Authors

### Chapter 1: Introduction

Written entirely by Thomas A. Singleton, with help from Prof. Barrett in minor final editing.

### Chapter 2: Experimental Methods

Written entirely by Thomas A. Singleton, with help from Prof. Barrett in minor final editing.

### Chapter 3: Azobenzene Photoisomerization Under High External Pressures: Testing the Strength of a Light-Activated Molecular Muscle

Reprinted (adapted) with permission from: T. A. Singleton, K. S. Ramsay, M. M. Barsan, I. S. Butler, and C. J. Barrett, *J. Phys. Chem. B*, 2012, **116**, 9860–9865. Copyright 2012 American Chemical Society.

Experimental work was performed by Thomas A. Singleton and undergraduate summer student K. S. Ramsay. The article was written entirely by Thomas A. Singleton: K. S. Ramsay contributed to the section on crystalline azobenzene isomerization, and Profs. Barrett and Butler helped in final editing and manuscript preparation. Dr. Barsan was the instrument technician.

### Chapter 4: Photo-Tuning of Highly Selective Wetting in Inverse Opals

Adapted from: T. A. Singleton, I. B. Burgess, B. A. Nerger, A. Goulet-Hanssens, N. Koay, C. J. Barrett, and J. Aizenberg, *Soft Matter*, 2014, **10**, 1325–1328 with permission from The Royal Society of Chemistry.

The article was written by Thomas A. Singleton: Drs. Goulet-Hanssens and Burgess, and Profs. Barrett and Aizenberg assisted with final editing and manuscript preparation. B. A. Nerger and N. Koay, undergraduate student interns at Harvard University and the Wyss Institute working with Dr. Burgess and Prof. Aizenberg, assisted with inverse opal film preparation.

**Chapter 5: Azobenzene Boronic Acids for Colourimetric Dopamine Detection**

T. A. Singleton, T. Aubry-Komin, and C.J. Barrett. *Prepared manuscript*.

All experimental work and writing was completed by Thomas. A. Singleton. Analysis of analyte response was performed by Thomas A. Singleton, with assistance from undergraduate summer student T. Aubry-Komin. Prof. Barrett advised on the project and manuscript preparation.

**Chapter 6: Polymer Coatings for Neurotransmitter Detection**

T. A. Singleton and C.J. Barrett. *Prepared manuscript*.

All experimental work was performed by Thomas A. Singleton. The manuscript was written by Thomas A. Singleton, with advice and minor editing from Prof. Barrett.

# Chapter 1: Introduction

## 1.1 Azobenzene

Azobenzene is composed of two benzene rings joined by an N=N bond. The conjugated structure yields a chromophore with a high extinction coefficient which can be tuned, via substitution on the rings, to absorb light with energy ranging from the near-UV[1] to the red.[2] Derivatives of the parent compound are ubiquitous in industry and everyday life: they make up more than 70% of commercial dyes, owing to their durability towards irradiation, as well as their highly variable colour.[3,4] What makes azobenzene different from other chromophores, and as a result so well studied,[5–8] is its ability to undergo reversible isomerization about the N=N bond from the *trans* to the *cis* isomer, as discussed in detail in Section 1.1.2. The *trans*-isomer is the more stable under normal circumstances, however the *cis* isomer can be 'locked' sterically by substitution in special cases.[9] The isomerization from *trans* to *cis* proceeds photochemically, via absorption of a single photon, while the reverse process can proceed either photochemically or thermally.

### 1.1.1 Absorption Spectra and Isomerization Kinetics

Azobenzenes have classically been organized into three broad classes as defined by Rau (see Reference 10): the *azobenzene*-type, with the longest half-lives of the *cis*-isomer (hours–days) and most blue-shifted absorption spectra (UV–blue); the *aminoazobenzenes*, with an electron-donating substituent, slightly red-shifted absorption (blue–blue-green), and shorter half-life (minutes–hours); and the *pseudostilbenes*, with alternate electron-donating and electron-withdrawing groups on opposite ends of the molecule, the most red-shifted absorption spectra (green), and shortest half-lives (minutes–seconds). In addition, the absorption spectra of the azobenzene-class tend to exhibit well-separated $n\rightarrow\pi^*$ and $\pi\rightarrow\pi^*$ transitions, while those of the pseudo-stilbene class exhibit significant overlap. There are, inevitably, many exceptions to these general rules,[11] however these guiding principles are still useful when designing new chromophores. Examples of derivatives with exceedingly long[12] or very short[13] half-lives exist, as do derivatives with extremely red-shifted absorption spectra,[2] or the spectral properties that resemble the separated absorption features of azobenzene-types, but with the red-shifted $\lambda_{max}$

characteristic of the pseudo-stilbenes.[14] These exceptions enrich the overall chemistry of the field, and demonstrate the versatility and control possible using the azobenzene chromophore.

The quantum yields of azobenzene isomerization are generally quite high[15–19] and few side reactions are observed. This stands in contrast to the geometrical analogue stilbene, where the N=N moiety is instead replaced by CH=CH. Stilbene undergoes a photo-induced cyclisation to dihydrophenanthrene, which gradually (via oxidation) changes to phenanthrene, which is stable and has no photo-activity. Azobenzene derivatives are not prone to this reaction, and instead can undergo many cycles of isomerization under ambient light conditions without significant degradation.[20]

### 1.1.2 Azobenzene Isomerization

Although initial interest in azobenzene derivatives was for use as dyes due to their vibrant colours, Hartley[1] noted an interesting effect over 80 years after the first reports of the synthesis of azobenzene.[21,22] While attempting to determine the solubility of azobenzene, he noted that exposure to light appeared to influence both the solubility and the molar absorption coefficient of the chromophore. The compound formed on irradiation was significantly more polar, which affected the solubility, and that the molar absorptivity in the visible range increased over the initial sample. He also showed that this new compound could be converted back to the original form by irradiation with blue light or by heating. He posited that this new form was *cis*-azobenzene, and was also able to measure the dipole moment of the new compound at 3 Debye,[23] which was later confirmed by X-ray crystallography.[24] Both the geometry and the ability of azobenzene derivatives to isomerize appears to be quite general (see Figure 1.1).[15]

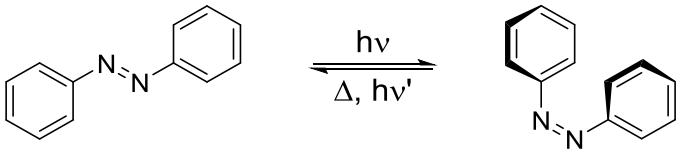


Figure 1.1 The two isomers of the azobenzene chromophore. *trans*-Azobenzene is roughly planar and has no net dipole moment: *cis*-azobenzene is more globular with the two benzene rings laying out-of-plane,[25] and has a dipole moment of 3 Debye.

### 1.1.3 Azobenzene Absorption and Excited State

Two distinct absorptions arise from the two highest-occupied molecular orbitals: either directly from the π orbital over the N=N bond, or from the nonbonding n orbitals on the two nitrogen atoms (HOMO–1 and HOMO, respectively). Regardless of the initial orbital, an electron is excited to the π* orbital (LUMO), forming the first excited state $S_1$.[26]

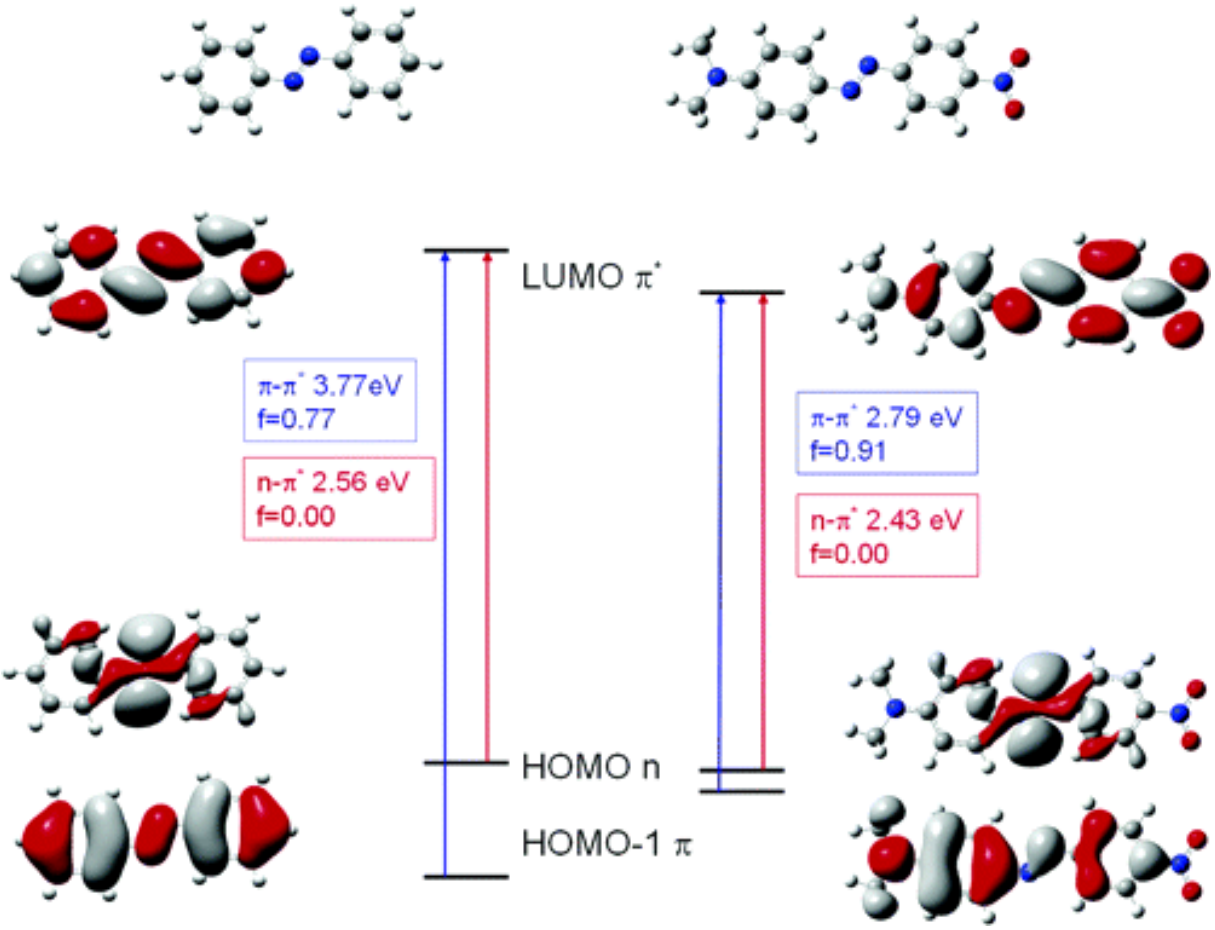


Figure 1.2 Molecular orbital diagrams and oscillator strengths (transition probabilities) of the possible electronic transitions in azobenzene (left) and 4-(*N,N*-dimethylamino)-4′-nitroazobenzene (right). Reprinted (adapted) with permission from Reference 26, Copyright 2006 American Chemical Society.

In the parent azobenzene molecule, the n→π* transition is symmetry forbidden: this restriction is removed for most derivatives (since most are not centrosymmetric), however overlap between the orbitals remains poor and the extinction coefficient tends to be much lower for this

transition (see transition probabilities in Figure 1.2). This transition can gain intensity via coupling with an appropriate vibrational motion, which can serve to temporarily reduce the symmetry of the molecule, thereby giving some overlap to otherwise orthogonal orbitals. No such symmetry restriction exists for the $\pi \rightarrow \pi^*$ transition, however, giving rise to the large extinction coefficients characteristic of the majority of azobenzene derivatives (*ca.* $10^3 - 10^5$ $M^{-1} \cdot cm^{-1}$).

#### 1.1.3.1 Isomerization Mechanism

Although the azobenzene chromophore's *trans*-*cis* isomerization has been known for over 70 years, there is still considerable debate over the mechanism by which one isomer becomes the other. There are two possible mechanisms by which isomerization can occur: rotation and inversion. Azobenzene derivatives can isomerize through either of these pathways, as the lone pairs on the two nitrogen atoms allow inversion. This is not the case for the close structural analogue stilbene, where the two hydrogen atoms on the C=C bond preclude inversion, leaving stilbene with only one possible isomerization pathway.

The actual mechanism of isomerization is still the subject of rigorous debate in the scientific community, and appears to be dependent on the type of azobenzene as well as its environment. Interpretation of the isomerization based on the classical valence bond theory suggest that the $\pi \rightarrow \pi^*$ excitation favours rotation (as in stilbene), due to the weakening of the $\pi$ N=N bond while simultaneously populating the antibonding $\pi^*$ orbital.[27] Alternatively, the $n \rightarrow \pi^*$ transition draws electron density from the nonbonding nitrogen orbital and populates the $\pi^*$ orbital, allowing for inversion about the nitrogen atom. This mechanism has been corroborated experimentally with sterically hindered derivatives, where isomerization is still observed even when the rotation mechanism is impossible.[28] Computations and ultrafast measurements, indicate solvent polarity, viscosity, and the steric and electronic effects of substituents play a large role in determining the mechanism of isomerization.[29–46]

The two isomerization mechanisms also have very different free volume requirements, due to the different paths the displacing group takes through space. For the parent azobenzene chromophore, the volume varies from 120 – 250 $Å^3$ for inversion vs. rotation, respectively.[47] The volume increases substantially as the pendant groups increase in size, which has important

implications for the isomerization kinetics in strained environments such as the crystalline phase,[48] and under high external pressure as discussed in Chapter 3.

### 1.1.4 Azobenzene Synthesis

The popularity of azobenzene as a photoswitch in diverse applications, as discussed in Section 1.1.5 below, means that there are no shortage of synthetic methods available to create new chromophores,[49] with synthetic methodologies still being developed.[50] Perhaps the most common, though certainly not the first method,[22] is the diazonium coupling reaction, colloquially referred to as the *azo coupling* reaction. This reaction was the most frequently used in this work, due to its simplicity and reliability. The general scheme (Figure 1.3) is simple, and the reaction tolerates a wide variety of functional groups.

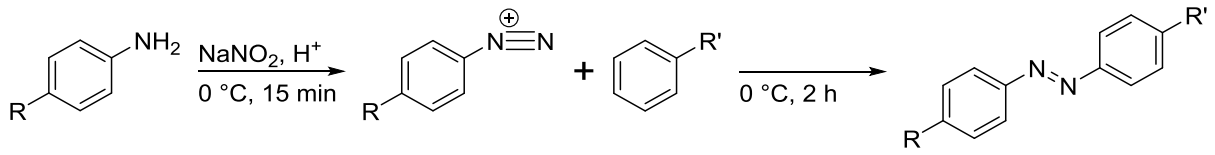


Figure 1.3 Diazonium coupling scheme. The diazonium cation is formed by reaction of an aniline with nitrous acid, followed by the addition of an electron-rich aromatic substrate (R′=$NH_2$, OH, etc.) which attacks the electron poor diazonium resulting in formation of a stable azo bond.

Perhaps the main drawback of this method is the requirement that at least one side of the desired chromophore must be relatively electron-rich, which limits the utility of the reaction. Additionally, due to the *para*/*ortho*-directing nature of electron-donating groups in phenyl rings, a variable amount of the *ortho*-derivative is also formed. This can be minimized by sterically blocking the *ortho*-position, which again places additional restrictions on the nature of the substrate. Alternative synthetic methods for substrates with no electron-donating groups are often based on direct oxidation of aromatic amines, with the corresponding low yields and high levels of impurities typical of such oxidations. Direct oxidative coupling of two aromatic amines with solid potassium permanganate/copper sulfate is a popular example of this method, due to the ease of preparation and (comparatively) clean product, however the strong nature of potassium permanganate as an oxidant precludes many sensitive functional groups.[49]

One of the greatest weaknesses of oxidative azo coupling reactions for the formation of asymmetrical products is the statistical nature of product formation, namely AA, AB, and BB. Several asymmetric methods that involve oxidation of one half of the molecule have also been proposed to solve this problem, however they also often result in the formation of unwanted byproducts.[51] Alternatively, partial oxidation of an aromatic amine to the nitroso intermediate (Figure 1.4), followed by an acid-catalyzed condensation reaction with a second aromatic amine, can yield the corresponding azo derivative. Oxone (potassium monopersulfate), a cheap and mild oxidation reagent, can give excellent yields of the nitroso compound, though the stability of the nitroso compound is highly variable depending on the substitution of the ring.[52]

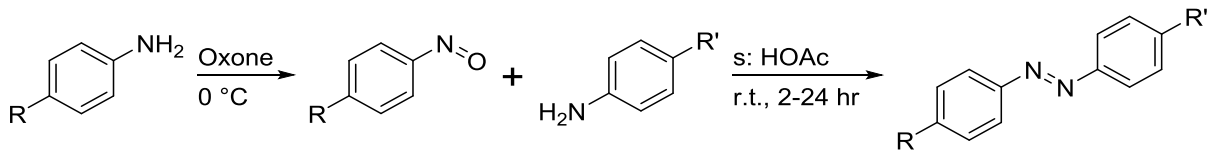


Figure 1.4 Azo formation via nitroso intermediate, made via oxidation with Oxone.

Purification is also frequently an issue, as azo compounds almost universally elute as broad bands when purification is attempted via column chromatography and HPLC, a phenomenon which is almost certainly aggravated by photoisomerization from ambient light during the separation. Recrystallization, or the use of repeated chromatographic separations, are often the best option for purification, both of which have the unfortunate side effect of reduced yield. Perhaps the only positive feature of azo purification is the easily-identified product band during chromatography, owing to the bright, vivid colour of the product.

### 1.1.5 Azobenzene Applications

Derivatives of azobenzene have found many uses in the chemical literature, including as photoswitches to control protein conformation,[53] to modulate neural activity (see Section 1.6),[54,55] to driving molecular machines[56] and altering the wettability of complex materials (see Chapter 4).[57] Some of these applications are outlined in the following sections, with a focus on those relevant to Chapters 3 – 6.

#### 1.1.5.1 Photo-Orientation

One of the best-investigated optical properties of azobenzene derivatives is photo-orientation: the process by which azobenzene chromophores can be "poled" by exposure to polarized light or electric fields. The review by Natansohn and Rochon covers the mechanisms and applications of this effect.[58] First reported in viscous solution in 1957,[59] and "solid solution" in 1984 using methyl orange doped in poly(vinyl alcohol),[60] the effect exploits the dipole moment of the azo chromophore. Exposure to polarized light induces isomerization in the chromophores, and the resulting random motion reorients the chromophores. Photon absorption is favoured along the axis of the molecular dipole: as the chromophores randomly reorient, they statistically become trapped perpendicular to the polarization of the light, where their absorbance is smallest. This results in anisotropy in the sample, and any light passing through the medium becomes sympathetically polarized. Polarization-based diffraction patterns are the basis of holography, and as a result a considerable amount of research into exploiting this effect followed in the field of data storage.[61] Additionally, because the material is not chemically changed by the data inscription, the patterns are erasable by light, allowing data to be stored and erased at will.[62–74]

The choice of matrix material suspending the azobenzene chromophores is also very important, as the chromophores need the freedom to reorient themselves. It was found that the formation of azobenzene microcrystals quenched the effect, as isomerization and orientation are hindered. Interestingly, if the chromophores are doped in a strongly organized material, such as a liquid crystal, or if the chromophores are attached directly to the polymer, a larger effect is noted: the photoisomerization of the chromophores can actually orient the nanoscale domains of the material itself. Matrix orientation results in a material with much higher anisotropy, since the matrix also contributes to the resulting optical effects. These effects are heavily affected by both the temperature at which the pattern is inscribed (relating to the glass transition temperature of the polymer matrix), and the external pressure applied to the sample. Both temperature and pressure affect the effective viscosity, or resistance of the material to flow against an applied force, and the amount of free volume available in the film. The effect of external pressure on photo-orientation of azobenzene chromophores has been explored in the past by Sekkat *et al.*: our investigation of these effects on the rate of thermal *cis-trans* isomerization is described in Chapter 3.

### 1.1.5.2 Surface Mass Transport and Surface Relief Gratings

Perhaps the largest-scale effect of azobenzene isomerization is *surface mass transport*, where azobenzene isomerization induces large-scale movement in a polymer thin film. Discovered in 1995, this effect can perhaps be viewed as an extension of the birefringence and domain reorientation described in the previous section.[75] Irradiation with an arbitrary pattern of light, such as an interference pattern between two laser sources, results in an impression of the pattern in the thin film (a *surface relief grating*: SRG). These patterns can be arbitrarily large in area, and the features demonstrated were on the order of 0.2 μm in height and microns wide, and can be repeatedly erased and re-written, with no lasting damage to the sample (i.e., the writing is not due to ablation).

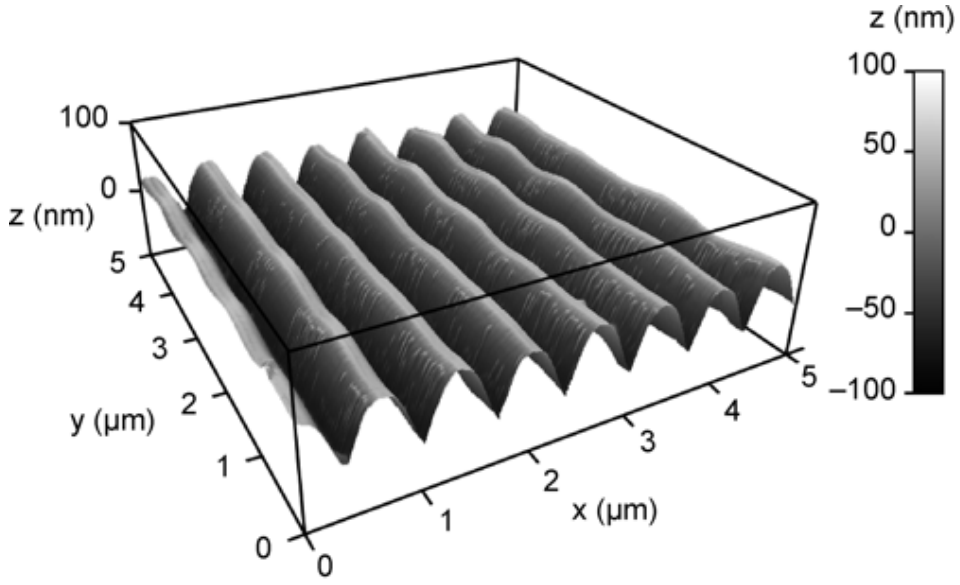


Figure 1.5 Atomic-force micrograph of an SRG inscribed in poly(Disperse Red 1 acrylate). Reproduced (adapted) with permission from Reference 76, Copyright 2006 American Chemical Society.

The mechanism proposed for this movement is based on local areas of high pressure, where the irradiation occurs: as isomerization occurs in areas where the light impinges on the sample, the higher free volume requirement of the transition state species[77] compared with either of the *trans* or *cis* isomers creates regions of higher pressure, causing the azo-doped polymer to migrate away from the light.[78]

#### 1.1.5.3 Artificial Muscles

A visually striking effect demonstrated by azobenzene materials is the massive macroscale deformations exhibited by some azo-doped liquid crystalline systems, developed by Ikeda and coworkers. In one of the seminal reports, irradiation of a small square of LC film with polarized light resulted in deformation towards the source of the light.[79] The azobenzene derivatives contained in LC domains aligned along the same axis as the irradiation light underwent isomerization, resulting in contraction of the domains and deformation of the film. The same effect could be induced in any polarization direction. The deformation could be modulated by alternating exposure with near-UV (360 nm, to induce deformation) and visible (>540 nm, to return the film to the resting state). To demonstrate the versatility of this motion, the same effect was demonstrated using sunlight and a pair of filters.[80]

A third report harnessed this deformation to perform simple mechanical action: a loop of azo-LC, by simultaneous irradiation in specific areas with *trans-cis* and *cis-trans* isomerizing wavelengths, was shown to be able to drive a simple set of pulleys.[81] In these cases, the photomechanical effect manifests not as a result of the volume increase due to isomerization, but by contraction of the LC chains into which the azo moieties are incorporated, as the end-to-end distance in isomerization decreases.[82–85]

The implication of pressure in the formation of SRGs, as well as the actuation of these molecular muscles makes the effect of external pressure on the formation of these features, as well as the underlying isomerization driving it, interesting. This is discussed in greater deal in Chapter 3.

## 1.2 High Pressure Experiments

While it is common practise to vary the temperature when conducting a chemical experiment, the effect of pressure is much less frequently investigated. This is mostly due to the relative ease with which one can increase the temperature of a reaction, whereas increases in pressure generally require specialized equipment and very different protocols. A variety of effects have been noted in high-pressure studies, such as change in molecular vibrational energy, phase transitions, changes in molecular symmetry (including changes in spin state), shifts in fluorescence intensity and peak position, as well as differences in reaction kinetics.[86] Many different techniques

are used to investigate these interesting phenomena,[87] some of which are discussed in the following sections. The discussion of high-pressure experiments in this section are framed in the context of Chapter 3, where the isomerization behaviour of an azo-functionalized polymer (poly(Disperse Red 1 acrylate)) was investigated under high external pressure.

### 1.2.1 The Diamond Anvil Cell

One important tool to study the effects of extreme pressures on chemical systems is the Diamond Anvil Cell (DAC). The DAC was developed at the National Bureau of Standards (now NIST) by Charles Weir as a method of attaining extremely high pressures without large, complicated pieces of machinery.[88] The basic principle is quite simple: the sample, which is generally submillimetre in size, is held between the culets of two diamond anvils by a gasket (typically stainless steel). The diamond anvils are then forced together by a pressure plate attached to a cantilever system connected to a knob attached to a spring, which can be turned to increase the force applied by the lever system. Different versions of the cell have since been developed for different instrument geometries and orientations, but the basic principles of DAC construction remain the same, as depicted in Figure 1.6 below.

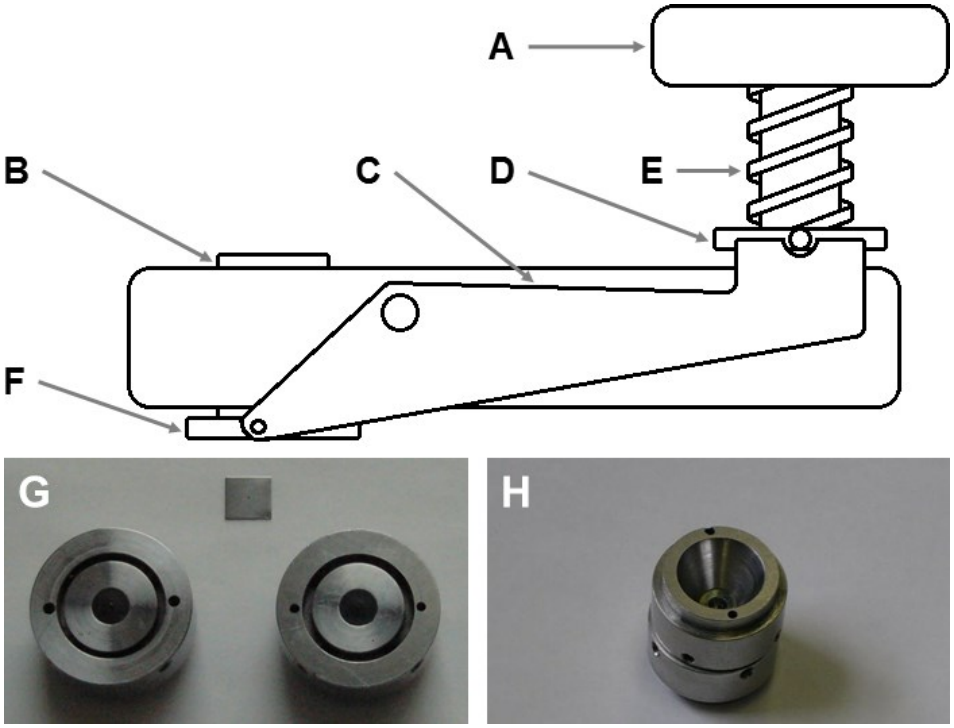


Figure 1.6 The basic diamond anvil cell. A) Knob for pressure adjustment B) top diamond anvil C) lever arm D) top pressure plate E) spring F) bottom pressure plate G) diamond anvil faces with steel gasket H) diamond anvils assembled as in the cell.

The whole apparatus is small enough to be handheld, and is therefore easy to fit into various instruments for measurements to be made. Aside from the obvious advantages of having a handheld cell compared with large hydraulic presses that were previously required for pressure studies, perhaps the single largest advantage of the DAC is that the pressure-transmitting part of the cell is diamond, and thus transparent to a very broad spectrum of radiation, which can pass directly to the sample. The DAC lends itself well to a variety of spectroscopic techniques: IR and Raman spectroscopy,[89] X-ray diffraction,[87] and even more exotic techniques like Mössbauer spectroscopy.[90] As well, both low and high temperature experiments can be conducted, with the proper equipment and minor adjustments to the pressure calibration equations.

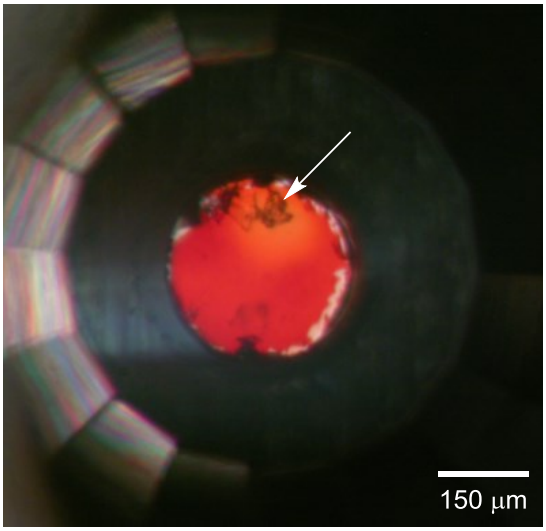


Figure 1.7 Top-down view of a sample inside the DAC. The red sample (PDR1A, as discussed in Chapter 3) is in the centre, surrounded by the stainless steel gasket. The geometric pattern is formed by the facets of the diamond surrounding the flat culet. The white arrow indicates a ruby chip used for pressure calibration (see Section 1.2.2).

### 1.2.2 Pressure Calibration

Although the DAC provides a facile method of applying pressure to samples, it offers no intrinsic method of measuring the pressure inside the cell. Instead, a number of different internal standards are available, depending on the type of measurement and the desired pressure regime. For X-ray type measurements, a sample with a known change in unit cell parameter can be included with the sample, such as solid rare gasses of neon,[86] or a variety of metals.[91] Measurements with an infrared spectrophotometer can be calibrated using the asymmetric stretching bands of the nitrite and nitrate ions, which have a well-characterized change in wavenumber position as a function of pressure.[92]

The most popular method of pressure calibration inside the DAC makes use of the highly pressure-dependent wavelength of the ruby $R_1$ fluorescence line, which corresponds to the $^2E \rightarrow {}^4A_2$ electronic transition.[91] This transition occurs at 694.3 nm at ambient pressure, and can be excited by visible green-blue light. The resulting deep red fluorescence can be analyzed by a fluorimeter (or a Raman spectrometer), and converted into a pressure value using Equation 1.1:

$$P(\text{Mbar}) = \frac{a}{b}\left(\left(\frac{\lambda_0+\Delta\lambda}{\lambda_0}\right)^b - 1\right) \qquad \text{Equation 1.1}$$

where $a$ and $b$ are empirical parameters ($a$ = 19.04, $b$ = 5), $\lambda_0$ is the fluorescence wavelength at ambient pressure ($\lambda_0$ = 694.3 nm), $\Delta\lambda$ is the change in wavelength at pressure, and P is the pressure expressed in megabars. This relation holds between 1 bar and 1 Mbar (100 kPa to 100 GPa) to within 0.1%.[91] An example of the shift in fluorescence over the pressure range investigated in Chapter 3 is given in Figure 1.8.

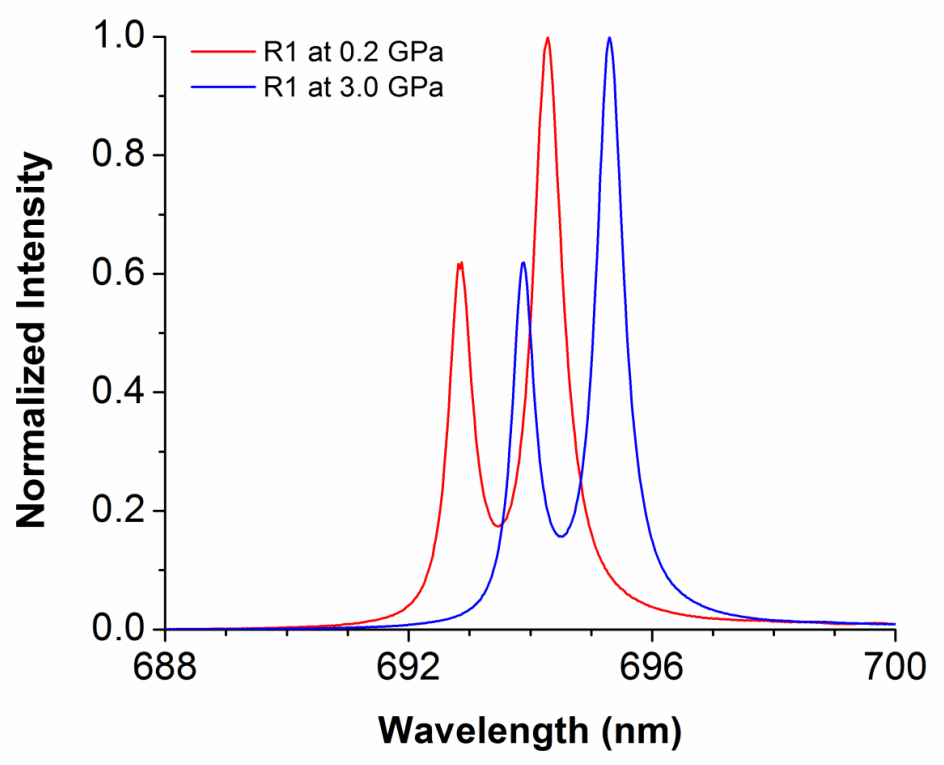


Figure 1.8 Ruby fluorescence inside the DAC at 0.2 GPa (red) and 3.0 GPa (blue). The $\lambda_{max}$ shifts by approximately 1 nm over this range.

### 1.2.3 Molecular Behaviour at High Pressure

#### 1.2.3.1 Molecular Vibration at High Pressure

As pressure increases, molecules and atoms are forced closer and closer together. This increases resistance to movement: molecular vibrations become higher in energy as the local free energy into which they vibrate decreases. A general upward trend in vibrational energy can be

observed as a function of increasing pressure. An exception to this trend is the negative shift in vibrational energy which can arise in scenarios where the bonds involved have antibonding character. An increase in electron density in these regions leads to weakening of the bond, an effect that is especially prevalent in organometallic complexes.[93] Both effects shed light on the nature of the bonds being observed: those with large changes in atomic coordinates during the vibration tend to be affected the most (stretching modes), while relatively subtle movements tend to have relatively stable vibrational energies (wagging, rocking, bending, scissoring, and twisting).

#### 1.2.3.2 Phase Transitions

If the sample is crystalline, it is possible for a material to undergo a phase transition as pressure increases. This often manifests itself as a discontinuity in a plot of vibrational wavenumber vs. pressure, since the chemical environment is no longer changing in direct proportion to the pressure, but abruptly and (depending on the space group) anisotropically.[89] Glass transition, a second-order phenomenon which is analogous to the first-order phase transition (solid-liquid) in crystalline solids, is also strongly influenced by external pressure. The glass transition temperature ($T_g$) typically increases linearly with pressure, though the strength of this dependence is highly influenced by the chemical nature of the system.[94]

#### 1.2.3.3 Relation to Free Volume

Free volume, defined as the space not occupied by atoms or molecules in a given volume of material, allows movement to occur in the condensed phase. In liquids, the 'holes' that make up the free volume are in constant motion, while in glassy or crystalline phases they are effectively fixed.[95] The fractional free volume in the polymer thin film determines the viscosity, which is described as a function of temperature by the Williams-Landel-Ferry equation.[96] In a crystalline close-packed structure (hexagonal or face-centred cubic), the fractional free volume is 0.26: this represents the upper limit of packing efficiency under standard conditions.[97] As pressure is increased, the fractional free volume decreases, increasing $T_g$. Viscosity is resistance to flow, and on a molecular level corresponds to the restriction of translational degrees of freedom by fewer available voids in which to move, as well as increased intermolecular interactions due to the higher density. The pockets of free volume occur as an approximately Gaussian distribution of size pockets, with a slightly higher population of larger pockets.[98]

#### 1.2.3.4 Azobenzene at High Pressure

The parent azobenzene molecule tends to receive little attention in the literature, except in fundamental studies of isomerization behaviour and mechanics, due to the low utility of a molecule with no functional groups. The absorption spectrum of *trans*-azobenzene embedded in various polymer matrices was investigated from ambient pressure to 2.5 GPa in 1966 using a hydraulic press. The group found shifts in the absorption intensity, as well as blueshifting of the positions of the $n \rightarrow \pi^*$ and $\pi \rightarrow \pi^*$ absorptions.[99]

One major high-pressure study of azobenzene that was undertaken by Song et al. investigated the vibrational behaviour of both *trans*-azobenzene and hydrazobenzene (azobenzene, where the N=N moiety is replaced by an NH–NH single bond).[100] Both *trans*-azobenzene and hydrazobenzene were found to undergo phase transitions around 10 GPa, however azobenzene underwent decomposition at 18 GPa, while hydrazobenzene persisted until 28 GPa before decomposition.

Though Chapter 3 investigates a much smaller pressure range, the emphasis is on the isomerization behaviour, instead of the pressure effects on the vibrational motions. The vibrational characteristics of *trans*- and *cis*-azobenzene were studied, as well as their ability to undergo photochemically- or mechanically-induced isomerization under pressure. Interestingly, since the original publication of Chapter 3, where no mechanical isomerization took place (that is, isomerization due to the effect of pressure alone), it has since been demonstrated that a polymer-appended azo derivative can be mechanically isomerized via sonication in solution.[101]

Despite the implication of pressure in the formation of surface relief gratings and in photo-orientation, relatively little research has been done on the direct effect. Knoll, Kleideiter, and Sekkat conducted two studies in this area: the first investigated the effect of pressure on the isomerization of poly(methyl Disperse Red 1 acrylate-*co*-methyl methacrylate),[102] which was later verified by Knoll and Kleideiter;[103] the second investigated the photo-orientation of the same system,[104] at pressures up to 0.2 GPa. They found that as the external pressure increased, the mobility of the chromophores was reduced, optical orientation was suppressed, and they were able to extract the free volume of the transition state present during the *trans*-*cis* isomerization event via Equation 1.2.

$$\ln(k) = \ln(k_0) - \Delta V^{\ddagger}\frac{P}{RT} \qquad \text{Equation 1.2}$$

where $k$ is the kinetic rate at pressure $P$, $k_0$ is the kinetic rate at ambient pressure, $R$ is the universal gas constant, and $T$ is the temperature (in Kelvin) at which the isomerization takes place. The activation volume, $\Delta V^{\ddagger}$, is the volume required for the reaction to proceed, and is equal to the volume of the transition state (taken from Reference 104). Sekkat and his co-authors found that $k$ decreased linearly with applied pressure, a trend which continued in the pressure regime investigated in Chapter 3.

The experiments outlined in Chapter 3 expand upon this research, and demonstrate it is possible to completely suppress the isomerization event at extremely high pressures (2 GPa; 10× the previous studies). This indicates a continuation of the reduction in free volume observed by Sekkat *et al.* during optical orientation experiments (with orientation of the entire chromophore), to the point where there is inadequate space for even the proportionally smaller volume requirement of isomerization. As the polymer film is compressed with increasing pressure, the size of the free volume pockets decreases, which constrains the chromophores and inhibits their ability to undergo *trans* to *cis* isomerization. The distribution in size of the free volume pockets in polymer films gives rise to the anomalously fast relaxation observed in the azo species.[105]

## 1.3 Inverse Opal Film Background

Inverse opals are a type of *photonic crystal*, which possess *structural colour* due to the photonic properties of the material itself, and not due to an intrinsic absorbance of light, like conventional chromophoric materials. Although synthetic photonic crystals have been a subject of increasing study since their invention in 1987,[106] photonic crystals have existed in nature since at least the Cambrian explosion 500 million years ago,[107] and can be observed today in a wide variety of flora and fauna including the iridescent wings of many species of the *morpho* genus of butterfly, the scales of many species of fish, peacock feathers, and various beetle shells (Figure 1.9).[108,109] Structural colour is also found in minerals such as the opal, which are the natural inspiration for the *inverse opal* structures described in Chapter 4 (Figure 1.10).[110,111]

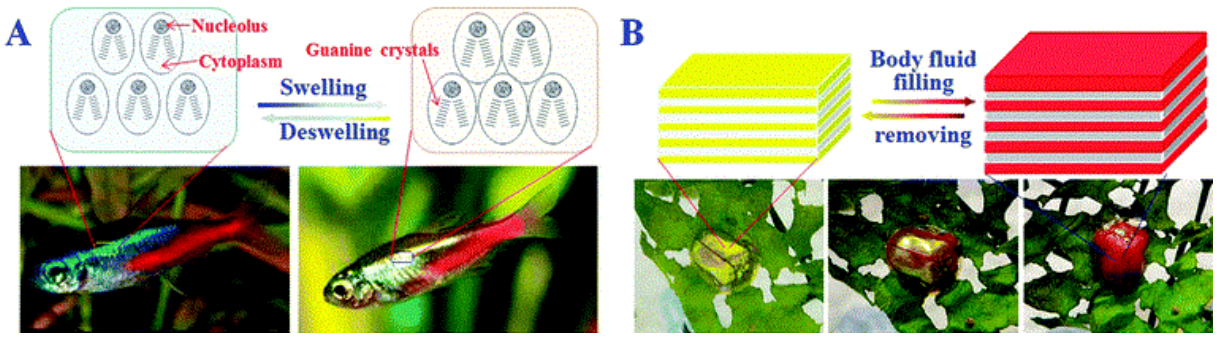


Figure 1.9 Examples of natural photonic crystals in A) *Paracheirodon innesi*, resulting from guanine crystals in special cells and B) the shell of the *Charidotella egregia* beetle. Reproduced (adapted) from Reference 109 with permission of the Royal Society of Chemistry.

Inverse opals take their name from natural opals, which are gemstones made of simple silica that exhibit intense structural colour. Opals are composed of microspheres of pure silica embedded in a partially hydrated silica matrix: the contrast between the indices of refraction of the two subtypes of silica, coupled with the partially oriented microcrystallites, diffracts the light impinging on the material. The size of the microspheres determines which wavelengths of light are diffracted, resulting in different colour opals being generated due to variations in the size of the microspheres.[112]

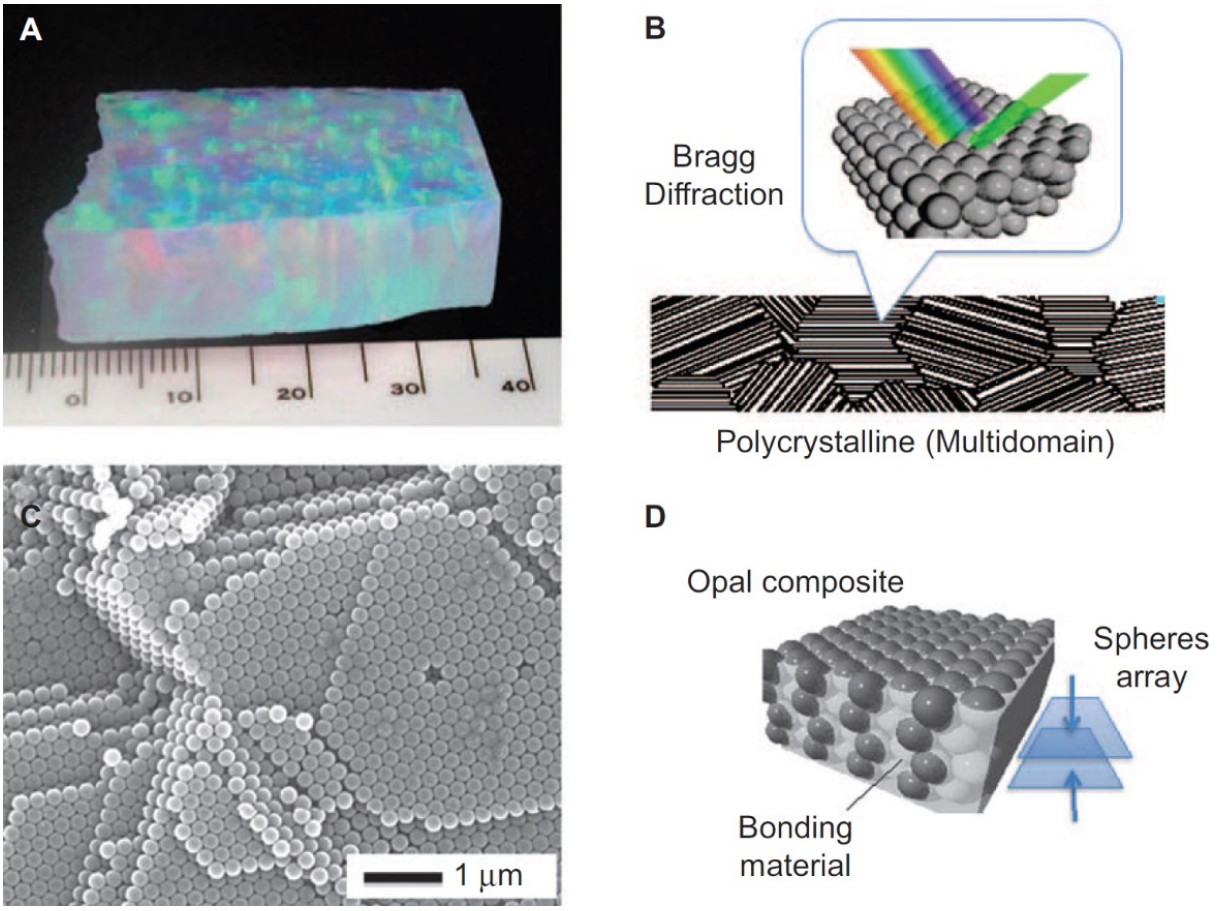


Figure 1.10 A) synthetic opal displaying iridescent structural colour B) Bragg diffraction (described in Section 1.3.1 below) from the domains of ordered silica microspheres giving rise to the opal colouration C) electron micrograph of the ordered silica microspheres D) schematic of the internal structure in natural opal. Reproduced from Reference 111 by permission from the Royal Society of Chemistry.

Inverse opals, as the name suggests, possess the same crystalline order of spherical inclusions in a matrix, however, instead of the silica/hydrated silica found in opals, inverse opals have spherical air holes in a silica (or other sol gel) matrix. The larger difference in index of refraction between air and silica allows for a greater diffraction efficiency, and also allows a great deal of freedom to modify the matrix material as well as alter the chemical functionality of the interior surfaces.

### 1.3.1 Optical Properties

The colour exhibited by inverse opals is a result of light scattering by features (in this case, spherical voids in a silica matrix) on the same length scale as visible light. The spacing of the features is the critical characteristic: the holes must be on the order of the wavelength of light to be diffracted. The diffraction effect observed in inverse opals is a type of Bragg scattering, which was first proposed to describe the patterns given by x-rays being diffracted by crystals. Light is scattered isotropically by the air inclusions in the opal. Because the inclusions are roughly the same size as visible light (*ca.* 300 nm in diameter), photons scattered by adjacent inclusions are offset from one another, depending on the angle of incidence. This relationship between the size of scattering features and the wavelength of radiation can be described by analogy to the Bragg relation:

$$n\lambda = 2d \sin\theta \qquad \text{Equation 1.3}$$

where $\lambda$ is the wavelength of light, $d$ is the distance between scattering centres, $n$ is any integer, and $\theta$ is the angle at which the radiation meets the plane described by the scattering centres. The inverse opal films discussed in Chapter 4 are fabricated using microspheres of approximately 300 nm diameter, giving a material with a peak scattering in the middle of the visible range of light.

More rigorously, the periodic variation in dielectric constant (how strongly an insulating material responds to an applied electric field)[97] replaces the electron density in the Bragg relation, and the difference in index of refraction between the two media describes the strength of the scattering.[112] The periodic variation in dielectric constant creates a photonic band gap in the material, which selects which wavelengths of light are allowed to propagate through the structure and which are reflected back. The Maxwell equations describe the interaction of light (a coupled electric and magnetic field) with dielectrics, give rise to the Bragg-Snell equation:

$$\lambda = 2d\left(n_{eff}{}^2 - \cos^2\theta\right)^{1/2} \qquad \text{Equation 1.4}$$

where $n_{eff}$ is the average index of refraction of the photonic crystal.[109]

### 1.3.2 Material Fabrication

Inverse opal fabrication is based on a templated matrix assembly around polymer microspheres, which self-assemble into a hexagonal closest-packed array. The matrix, typically a sol gel, can then be cast in the interstitial space, and subsequently, the microsphere template removed. A reliable method for forming large-scale photonic crystal coatings in this way has been described by Aizenberg *et. al*.[113] A solution of hydrolyzed silanes is added to an aqueous suspension of PMMA polymer microspheres and a solid substrate is then suspended vertically in the silane/microsphere suspension. As the solvent is slowly evaporated with mild heating, an Inverse Opal Film (IOF) of ordered microspheres embedded in a silica matrix is left behind adhered to the substrate. An electron micrograph of the resulting structure can be seen in Figure 1.11, in Section 1.3.3 below.

### 1.3.3 Wettability and Surface Energy

The *wettability* of a substrate is the degree to which a given liquid interacts with a surface. The degree to which this interaction occurs is determined by the relative magnitude of the adhesive forces (the attraction of the liquid to the solid) and cohesive forces (the attraction of the liquid to itself). The magnitude of the spreading can be determined by placing a small droplet of liquid on a solid surface. The liquid will try to minimize its surface area with the substrate, resulting in a truncated sphere as it rests on the surface. The angle between the solid surface and the droplet edge is related to the surface energies involved, via the Young equation (Equation 1.5). The larger the angle, the higher the cohesive forces relative to the adhesive, and the less wetting the liquid is to the substrate, and accordingly a small angle indicates relatively high adhesive forces.

The Young equation for surface wetting (Equation 1.5 below) shows the relation between the surface energies between three interfaces, in the specific case of a liquid droplet on a flat surface.

$$\gamma_{S-G} = \gamma_{S-L} + \gamma_{L-G} \cos \theta_R \qquad \text{Equation 1.5}$$

If, as is often the case, the liquid is water, a surface that gives a high contact angle can be termed *hydrophobic*, while a low contact angle surface is *hydrophilic*, with a contact angle of 65° being the rough boundary between the two.

These equations describe liquid wetting behaviour on a flat surface, but can be expanded to more complex geometries, such as the interior of an inverse opal photonic crystal, as described in Chapter 4. The ability of a liquid to infiltrate an inverse opal film is governed by two important parameters: the geometric parameters of the IOF itself, specifically the angle of the *necks* between the inverse opal pores; and the intrinsic wettability, represented by the flat contact angle of the liquid on a flat surface. The neck angle, which can be seen in Figure 1.11 below, is defined as:

$$\varphi_0 = \arcsin\left(\frac{r_{neck}}{r_{pore}}\right) \qquad \text{Equation 1.6}$$

where $r_{neck}$ is the radius of the circular neck between pores, $r_{pore}$ is the radius of the pore itself, and $\varphi_0$ is the neck angle. It is entirely a geometric parameter, determined by the size of the polymer spheres used to construct the IOF. The intrinsic wettability is dependent on the surface chemistry, which can be altered by chemical functionalization of the IOF surface.[114]

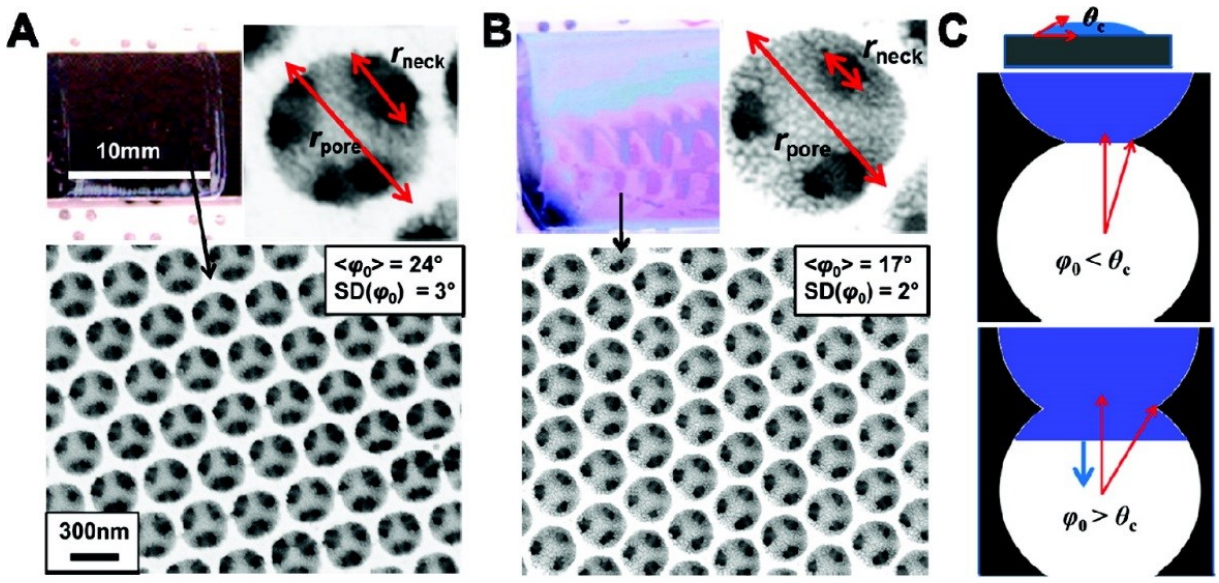


Figure 1.11 An electron micrograph of an inverse opal film, showing the periodic microstructure of air-filled spheres in a silica matrix. The $r_{neck}$ and $r_{pore}$ parameters are shown, as is their relation to $\varphi_0$ and $\theta_c$, the static contact angle of the liquid on a flat surface. The liquid can infiltrate the IOF only when $\varphi_0 > \theta_c$.

### 1.3.4 The Wetting In Colour Kit (WICK) System

A direct application of selective liquid infiltration into inverse opal films has been demonstrated by the Aizenberg research group at Harvard University.[114,115] The highly-specific transition from non-wetting to wetting in IOFs (*ca.* 2°)[114] is exploited by carefully varying the surface chemistry along the length of a coated substrate. Liquids are only able to wet the areas with an appropriate intrinsic contact angle (i.e. when $\varphi_0 > \theta_c$). The areas wet by the liquid lose the contrast in index of refraction necessary for scattering to occur, resulting in a colourless section of film whose edge defines the static contact angle of the liquid. Complex patterns can be inscribed into the film, yielding an easy to read colourimetric dip sensor capable of discerning a wide variety of liquids including alcohols (methanol, ethanol, isopropanol), ethanol/water solutions to high precision, and even different lengths of alkane (and different fuels such as gasoline and diesel), as shown below in Figure 1.12.

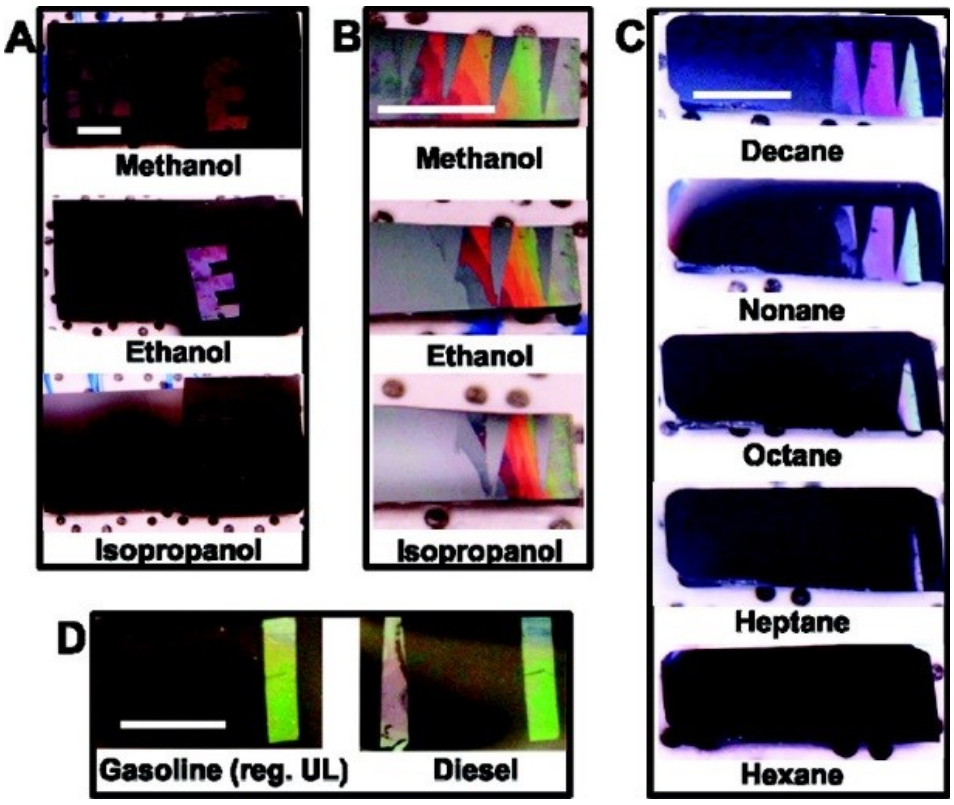


Figure 1.12 Three examples of IOFs inscribed with specific areas of surface energy, allowing differentiation of A) and B) methanol, ethanol, and isopropanol; C) decane, nonane, octane,

heptane, and hexane; and D) gasoline and diesel. Reprinted (adapted) with permission from Reference 114, Copyright 2012 American Chemical Society.

### 1.3.5 Photo-Induced Wettability Changes

Numerous materials are currently known to exhibit photo-induced changes in surface energy, both organic and inorganic in nature. Titania (and to a lesser extent zirconium oxide) is one of the best-studied systems for photomodulated wettability.[116,117] Heavily investigated due to its self-cleaning and semiconductor properties, it undergoes large changes in surface energy under illumination. The contact angle is highly dependent on the surface roughness, typically resulting in optically opaque films due to scattering, and UV light is required for the photomodulation. Additionally, the change in contact angle only persists as long as the light exposure lasts.[116] Organic systems are typically polymeric in nature, which can be applied to substrates as coatings. The photo-sensitivity is added by doping the polymer with photo-active organic molecules, such as those belonging to the azobenzene[118–120] or spiropyran[121] families, which are discussed in greater detail below.

#### 1.3.5.1 Spiropyran

The spiropyrans are another popular class of organic photoswitch, which undergo a reversible bond breaking/formation under irradiation.[122] Because the photoisomer is a zwitterion, a large change in dipole moment accompanies the transformation to the ring-opened merocyanine form (see Figure 1.13).

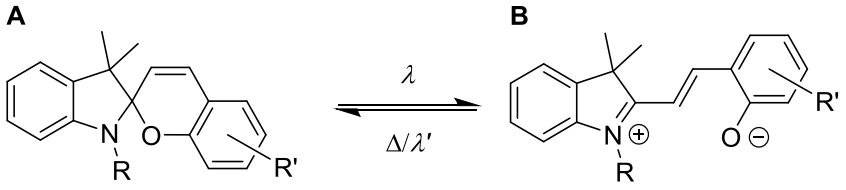


Figure 1.13 A) Spiropyran and B) the merocyanine photoproduct formed upon irradiation with UV light. The C-O bond breaks in concert with the *trans-cis* isomerization of the C=C bond, forming a zwitterion. The reaction is reversible with either heat or absorption of a visible photon.

Spiropyrans have been incorporated into surfaces coatings as a photo-sensitive switch to modulate surface energy, much like the azobenzenes discussed in Section 1.3.5.2 below.[121]

Changes in the contact angle with a magnitude on the order of 11 – 14° were observed upon irradiation, which were reversible over several cycles.

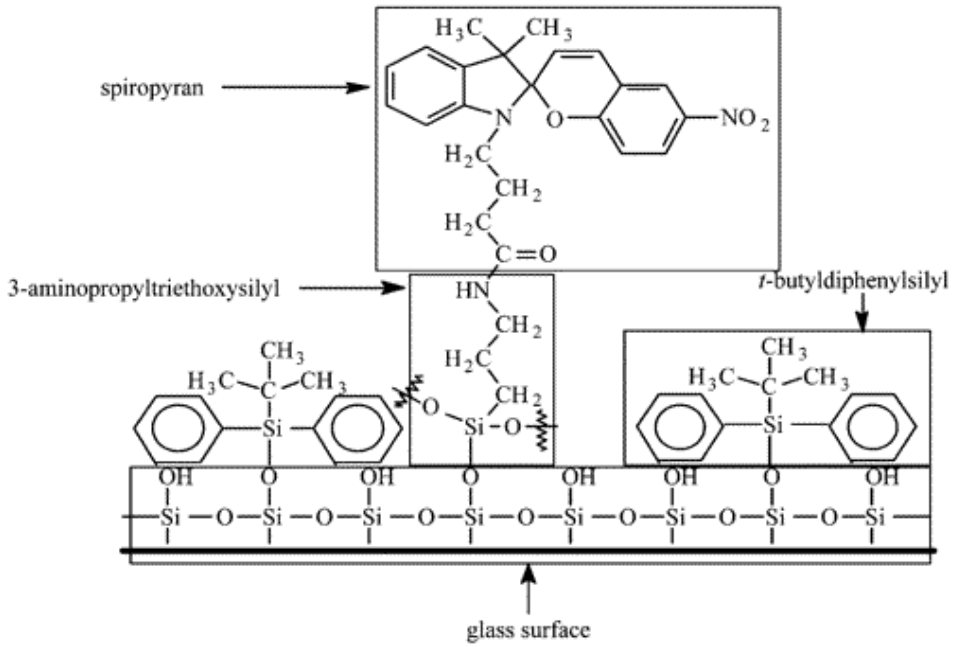


Figure 1.14 Photo-induced surface energy changes using spiropyran on an organic-functionalized silica surface. The conversion from the spiropyran to the merocyanine form results in a more polar surface, and corresponding decrease in water contact angle. Reprinted (adapted) with permission from Reference 121. Copyright 2002 American Chemical Society.

Ultimately, concerns over the stability of the spiropyran photoswitch compared with the azobenzene systems may limit the utility of the spiropyran coatings. The long-lived triplet state during photoisomerization makes the chromophore susceptible to atmospheric oxygen, as well as side reactions with other spiropyran chromophores.[123] Although solid-supported spiropyran derivatives are less susceptible to degradation than in the solution phase, several studies have shown that even ten switching cycles can induce photodegradation of *ca.* 20 mol % of the chromophores.[124] This effect can be reduced by ensuring the chromophores are less densely-packed on the surface, precluding the possibility of chromophore-chromophore interactions.[125]

#### 1.3.5.2 Azobenzene-Containing Materials

Among the numerous systems capable of dynamic surface energy modulation are azo-doped polymer films. Studies have been conducted using monolayers of azobenzene and

azobenzene-functionalized polymers, where the effects are due to the different polarity of the *trans* and *cis* isomers directly, but the changes are typically on the order of only a few degrees.[126,127] Larger changes can be induced with more complex supramolecular systems,[128] but the largest changes are initiated by polymeric systems. Two reports by Ahmad *et al.* using azo-doped polymers investigate the effect of different head groups, as well as the properties of the irradiating light on the resulting change in contact angle.[120,129]

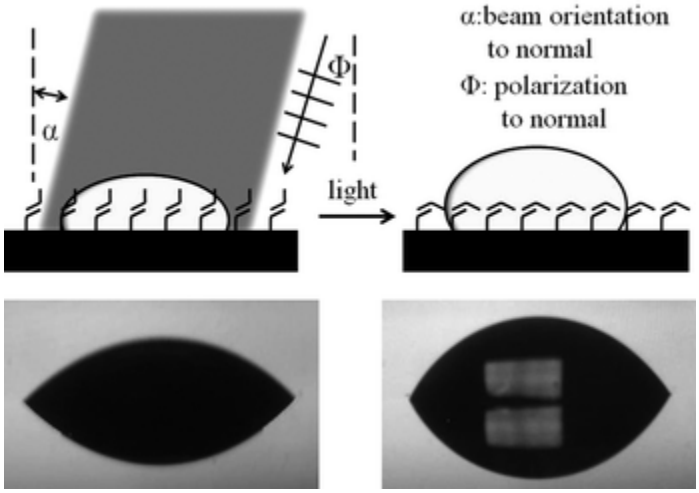


Figure 1.15 Change in contact angle of an azo-coated substrate upon irradiation. The degree of change in contact angle is related both to the polarization state of the irradiating light, as well as the angle it forms with the surface. Reproduced from Reference 129 with permission from the Royal Society of Chemistry.

Although the mechanism of action is yet to be fully elucidated, evidence points to molecular reorientation exposing the azobenzene head groups to the surface as the phenomenon that gives rise to the changes in wettability. The switchable wettability of the poly(Disperse Red 1 acrylate-*co*-acrylic acid) polyelectrolyte system described in Reference 129 forms the basis of the photo-induced wettability changes in inverse opal films described in Chapter 4. In it, the wettability of an inverse opal film coated with the p(DR1A-*co*-AA) polymer was modulated by varying levels of exposure to UV and visible light. The change in wettability was induced not by the reversible molecular orientation described in the previous section, but by photobleaching of the chromophores. This process is irreversible, but the degree of change in contact angle was shown to be dependent on the wavelength of light used (visible or UV), the intensity of the light, and the duration of exposure.

## 1.4 Polyelectrolyte Multilayers

Polyelectrolyte multilayers (PEMs) are thin coatings built from alternating layers of positively and negatively charged polymer chains (polyelectrolytes). The layers are formed by self-assembly, yielding a solvent-stable film with highly tuneable properties. The seminal report by Decher[130] is the first in a huge number of publications exploring the fabrication and application of these versatile, useful and easily assembled films.[131] PEMs appear in Chapters 4 and 6 of this work, both as a photoactive layer for modulating surface energy, and as a biocompatible matrix for azobenzene-based indicators for neurotransmitters.

### 1.4.1 Polyelectrolyte Assembly

The PEM fabrication process is outlined in Figure 1.16. A glass or silicon substrate, cleaned with "acid piranha" solution (a mixture of sulfuric acid and hydrogen peroxide) or exposure to plasma, adopts a slight negative charge, and is placed in a solution of positively-charged polyelectrolyte polymer. The surface charge attracts the positively-charged polymer, which adsorbs irreversibly to the surface through electrostatic interactions. The loops and bends in the adsorbed polymer have no matching counterion and thus generate a net charge reversal on the surface, allowing an oppositely-charged polyelectrolyte to be deposited on top. The entire process can be repeated *ad infinitum*, yielding a film with the desired thickness.[132]

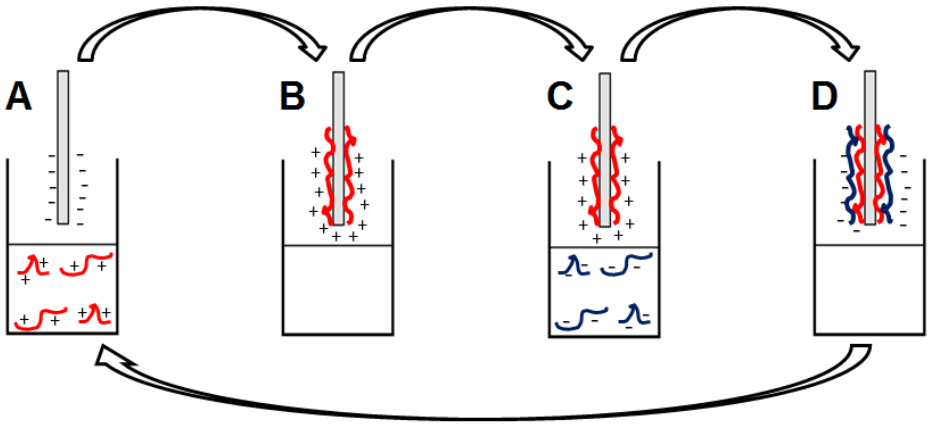


Figure 1.16 Process for fabricating PEMs. A) A clean, negatively-charged substrate is immersed in a cationic polyelectrolyte solution. B) Rinsing with deionized water. C) The cationic substrate is immersed in an anionic polyelectrolyte. D) Rinsing with deionized water.

#### 1.4.1.1 Assembly Conditions

Several factors determine the thickness and modulus of the resulting PEM. The choice of polyelectrolytes is perhaps the most important, as the $pK_a$ of the acid and base groups on the polymer chain determine the degree to which the charge on the polyelectrolytes can be altered.[133] At extremely high or low $pK_a$ values (strong acids such as sulfonate, or strong bases such as quaternary ammonium groups), the polymers will be effectively fully charged regardless of the assembly solution pH. This results in thin, high-modulus films, since the high polyelectrolyte charge maximizes adsorption and leaves relatively few loops and bends in the polymer. Polyelectrolytes with comparatively weak acid and base groups (carboxylic acids, secondary and tertiary amines) allow for much finer control of the properties of the multilayer, since the degree of charge is easily tuned by changing the pH of the assembly solution. Many more bends and loops result, yielding a softer, more water-filled matrix. Additionally, the ionic strength of the assembly solutions has a large effect on the properties of the final film, due to the charge-screening effect of high ionic strength solutions, and acts in the same way as reducing the charge via pH.[134] This can be an effective method of altering the material properties of strongly acidic or basic polyelectrolytes.

#### 1.4.1.2 Thickness Determination

The thickness of PEMs is commonly measured using null ellipsometry. Ellipsometry measures the change in polarization state of light as it is reflected from a thin film. This change is proportional to the phase and amplitude of light when it undergoes reflection by a material, as described by Equation 1.7:[135]

$$\rho = \frac{r_p}{r_s} = \tan(\Psi)\, e^{i\Delta} \qquad \text{Equation 1.7}$$

where $\rho$ is the ratio of the reflected intensity of the *p*- and *s*-polarized components of the light, $\Psi$ is the ratio of the absolute values of the amplitudes of *p*- and *s*-polarized components of the reflected light, and $\Delta$ is the phase change of the light upon reflection. The reflectance ratio is measured by an ellipsometer, which shines polarized laser light at a coated surface. The intensity of *p*- and *s*-polarized light reflected is then measured using a polarizer and photodetector, and modelled to determine the thickness of the film. Analysis requires knowledge of the indices of

refraction of all components in the system, including the air, the film itself, and the underlying substrate. Data analysis is performed via a regression method that yields a thickness with some ambiguity, due to the cyclic nature of the phase parameter. The unambiguous thickness has been verified using neutron reflectometry, allowing ellipsometry to be used directly.[136,137]

### 1.4.2 Applications of Polyelectrolyte Multilayers

PEMs enjoy a wide variety of applications in materials chemistry, biology, and materials science. They represent a facile method of applying thin films of tuneable thickness and functionality onto a variety of substrate materials and geometries. Their applications to the research in this work are summarized below, where PEMs are used as photoactive thin films, and as substrates for small molecules capable of detecting specific biomolecules.

#### 1.4.2.1 Photoactive Multilayers

The first reports of photoactive PEMs surfaced shortly after the initial discovery of PEMs. Polyelectrolytes doped with photoactive groups were used to image the internal structure and amount of chain diffusion between layers, allowing the internal structure of the films to be elucidated.[138,139] Photoactive films have also been used to guide cell growth,[140,141] as films that can be photodecomposed,[142] for photoinitiating the release of chemical cargo,[143] and to modulate the wettability of substrates upon irradiation, as discussed in detail in Section 1.3.5.[120]

#### 1.4.2.2 Biological Applications

The unique material requirements for interfacing with biological systems can make designing biocompatible materials difficult. Biology is not only sensitive to the chemical properties of implants and devices, but to the modulus and surface properties.[144–149] Additionally, the specific material properties vary depending on their location in an organism, with cells tending to prefer conditions similar to those they experience in their native environment. Since implants, such as artificial hips and mechanical hearts, are typically constructed from hard metals and plastics, the ability to "camouflage" these hard surfaces in the body is essential to prevent rejection. PEMs have been demonstrated as effective substrates for neural cells, which are comparatively difficult to culture *ex vivo*.[140,150] The ability to tune these coatings to specific areas of the body is an essential concept in Chapter 6, which details PEMs doped with azo-boronic acids sensitive to

the presence of neurotransmitters. The PEM acts both as a host for the molecular reporters (either covalently or electrostatically bound, as detailed in the following section), as well as a biocompatible coating for the hard optical fibre required to extract the optical signal from the reporters.

#### 1.4.2.3 Small Molecule Uptake

The water-rich, loosely-associated polyelectrolyte matrix provides an ideal platform for small-molecule absorption. The pH-dependent character of polyelectrolyte films also allows for controlled uptake and release, which has been demonstrated in a number of different systems. One such system, investigated by Susan Burke *et al.*, demonstrated the ability of multilayers composed of poly(allylamine hydrochloride) and hyaluronic acid (structures in Figure 1.17) to swell by a factor of two on changing the solution pH from neutral to pH<5.[151] In addition, small charged molecules were shown to be absorbed by the film at extreme pH conditions (either strongly acidic or strongly basic), and held in the film under near-neutral pH conditions.

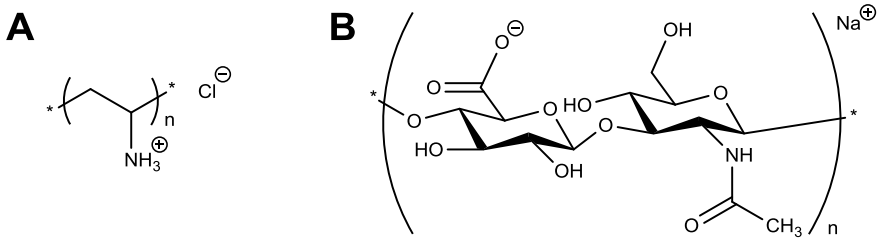


Figure 1.17 Structures of the polyelectrolytes (A) poly(allylamine hydrochloride) and (B) hyaluronic acid sodium salt.

This effect was exploited in the current study to immobilize candidate indicator molecules (especially the charged sulfonate-containing compounds) in the film, yielding a stable detection platform on any desired surface.

## 1.5 Neurophotonics and Optical Neurotransmitter Reporters

Chapters 5 and 6 in this work detail our efforts towards realizing an all-optical method of detecting neurological impulses. The ability to interpret impulses in the brain has far-reaching consequences for numerous fields of study, including fundamental research in trying to understand how the brain communicates with the peripheral nervous system and transmits information

internally, understanding how memories are formed, and how thoughts take shape. There are currently several different methods for monitoring brain activity in use. These can be classified into two broad categories based on the placement of the recording apparatus in relation to the skull: external detection (e.g. functional magnetic resonance imaging, positron emission tomography, and electroencephalography); and internal detection, which currently consists primarily of implanted electrodes as well as recent progress with optical fibres.[152] These techniques are discussed in Section 1.5.2 below.

Electronic probes are historically the most important and currently the most widely-used technique of internal detection, but are severely limited by their fundamentally bio-incompatible composition (typically hard, conductive materials such as metals or semiconductors). Long-term implantation (>hours) results in *gliosis*, or neural scar formation around the implant, which acts as an insulator to neural activity, significantly reducing the utility of the probe.[152] Gliosis is a response to brain injury, further aggravated by the small movements the probe inevitably undergoes as the subject moves. Shielding the probe from the cellular surroundings via biocompatible coatings (such as those discussed in Section 1.4.2.2) is also difficult, as these coatings tend to act as insulators, negating the utility of the probe.

Recently developed optical methods for interfacing with the brain, which lack the above mentioned limitations, have attracted significant attention: some of the most successful of which are described briefly herein. One of the most direct methods is the light-induced stimulation of specific areas of the brain by the photo-induced release of caged neurotransmitters.[55] Another method involves chemical modification of neural receptors: azobenzene derivatives have been grafted onto engineered neurotransmitter receptors adding photo-sensitivity to neurons and allowing for remote optical control of receptor channels.[54,153,154] These molecular methods contrast with the more powerful and permanent technique *optogenetics*, the most rapidly growing method of interfacing with neurological processes.[155,156] Optogenetics permanently alters the neural cells by genetically encoding light sensitivity into specific neural cells, allowing for light-induced activation of targeted neural cells. Although enormously powerful, its use is limited to animal research, as it requires altering the genes of the organism, which is not feasible as a therapeutic technique in humans. This introduction summarizes the current optical techniques in use, and attempts to place the work of Chapters 5 and 6 in the larger context of this body of

research. This work is best described as *neurophotonics*: the application of optical techniques to neuroscience.

### 1.5.1 Neurons and Chemical Signalling

Information is transmitted in the brain via two main pathways: as electrochemical gradients (electrical impulses, colloquially) and as chemical signals. Neural cells are not directly connected to each other, and instead meet at junctions known as *synapses*. A small space, the *synaptic gap*, separates the cells, and signals which are mediated electrochemically inside a cell body stimulate the release of specific molecules at the synaptic gap (see Figure 1.18 below). These molecules, known as *neurotransmitters* (NTs), then carry the signal via diffusion to a receptor site on a target cell.[157] Although a large number of specific compounds — as many as 50 small molecules and up to 100 neuropeptides — have been identified, nine are considered the most important, mediating the majority of neural signals.[157] The type of neurotransmitter used by a cell is highly dependent on the type of neural cell, its location in the body and the type of signal being transmitted.[158] Special receptors on the neighbouring cell are stimulated by the uptake of these compounds, and an electrochemical impulse is then propagated along that cell.

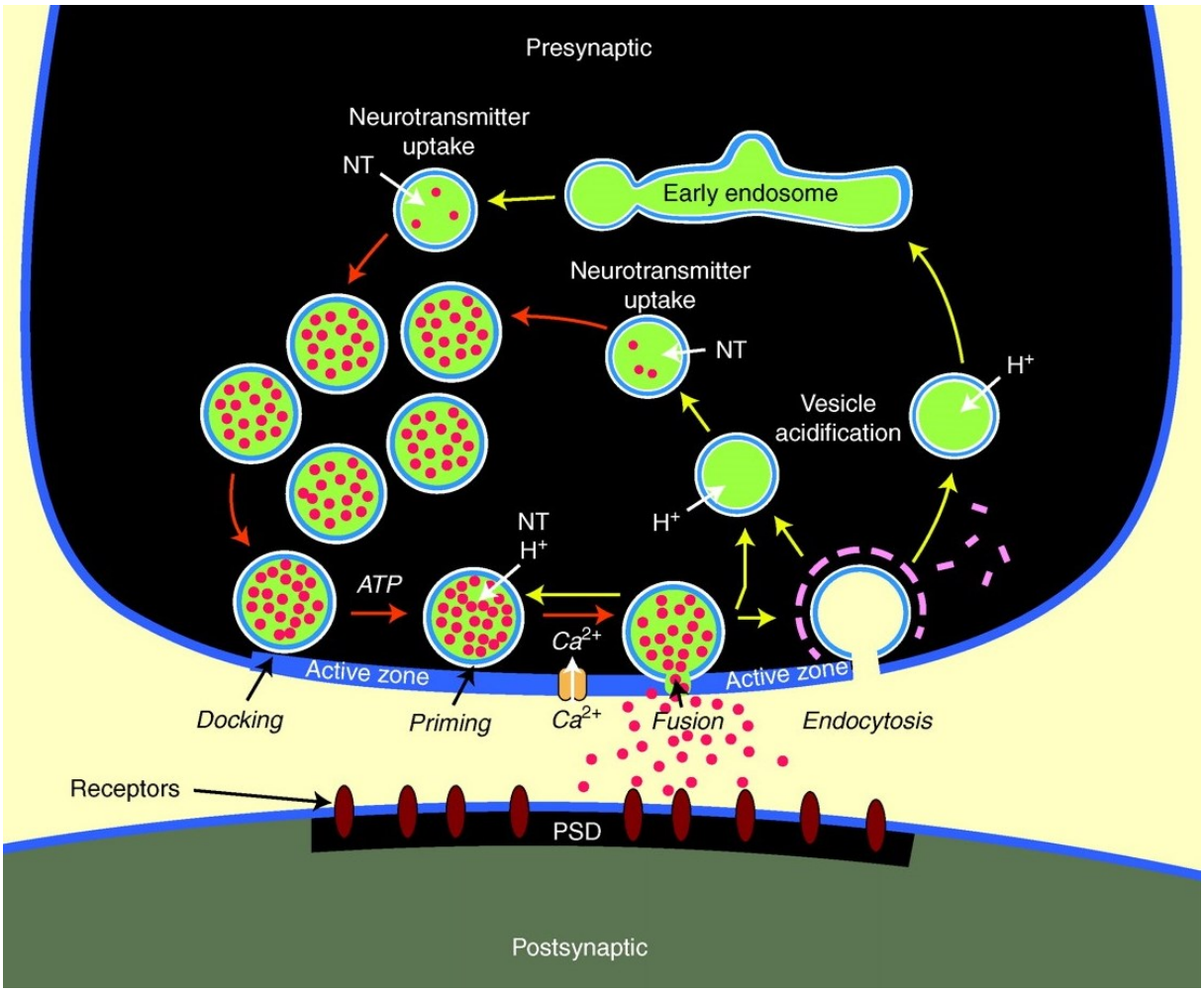


Figure 1.18 The synaptic gap. Top: the signal originates from the presynaptic terminal of the neural cell, filling vesicles with neurotransmitter molecules. The vesicles merge with the cell membrane when the electrochemical signal arrives, releasing neurotransmitters into the synaptic gap where they bind to postsynaptic receptors on the postsynaptic cell. Reprinted with permission from Reference 159. Copyright 2011 Cold Spring Harbor Laboratory Press.

Some of the common NTs, including adrenaline, norepinephrine, and dopamine share a common *catechol* (1,2-dihydroxybenzene) motif (Figure 1.19). As a result of their structural similarity and biological importance, these provide an interesting series for detection studies, which is the subject of study in Chapter 5.

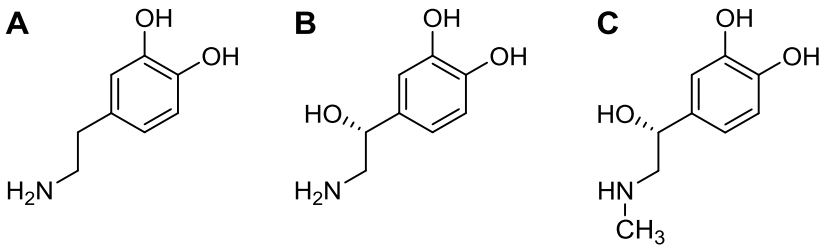


Figure 1.19 Three of the main biogenic aminocatecholates: A) dopamine, B) norepinephrine, and C) epinephrine.[158]

Dopamine occurs naturally at low levels in the body (*ca.* 0.5 – 25 nM in cerebrospinal fluid),[160] but the instantaneous concentration in the synaptic gap can be considerably higher, reaching into the tens of millimolar concentration range in the millisecond timescale of neuronal impulses.[161] The concentration inside the *vesicles*, the tiny containers that hold the NTs prior to release into the synaptic gap, can be even higher, at 100 – 200 mM. NT-molecules are loaded into vesicles via active proton pumping, resulting in a drop in pH upon vesicle release during the transmission of neural impulses.[162] As a result, the pH conditions in the brain vary depending on the location and the level of brain activity, and can be lower by ~0.5 pH units from the baseline physiological pH of 7.4. The pH conditions are important to this study due to the pH-dependent nature of NT-binding by boronic acids, as discussed in Section 1.5.3.1.

### 1.5.2 Intracranial Measurements

Intracranial measurements are, by definition, conducted within the cranial cavity, and therefore the measurement apparatus is typically implanted directly into the brain. These techniques require invasive surgery to implant and remove the probes. However, they provide a significantly higher spatial precision when compared with extracranial measurements (electroencephalograms, functional magnetic resonance imaging), since the probes are placed directly in contact with the region of the brain to be investigated.[163] Most intracranial probes collect electrical signals, either measuring the electrochemical gradients propagating along the axons before terminating at the synaptic gap, or by electrochemically detecting the presence of neurotransmitters based on their oxidation potential.

There are four main types of electrodes for intracranial, intracortical (inside the skull but outside the cell) measurements: metal microelectrodes, glass micropipettes, glass patch clamps (a

variant of micropipettes), and micromachined electrode arrays.[164] Each represents a different stage in design, and have different specialties: microelectrodes and micromachined electrode arrays are useful for looking at relatively large numbers of cells, and represent the highest bandwidth for information transfer, while the glass pipettes and microelectrodes are capable of interacting with specific regions of single cells, allowing very precise but also limited measurements of single-cellular activity. At the interface between extra- and intracranial electrodes are electrode grids, which can be placed on the *dura mater* (the topmost of three membranes between the skull and neural tissue). These provide a greater spatial precision than extracranial electrodes (typically 1 – 10 mm in length per electrode), and can give a generalized map of brain activity. These types of probes do not induce gliosis, since they don't penetrate the *dura mater*, but the larger distance to the brain limits their sensitivity: this is generally useful for diagnosis of which area of the brain is active in an epileptic seizure,[164] but provide significantly less spatial resolution compared to intracranial probes.

The main issue plaguing all neural implants is the mismatch in material properties that leads to gliosis.[165] This limits the utility of implants, since gliosis creates an insulating layer, blocking electrical impulses. Additionally, although many techniques exist for improving the biocompatibility of implants by matching the modulus and water content of the environment, these coatings are typically not conductive, rendering them useless for electrical applications. This is perhaps the greatest advantage of optical probes, which can be made biocompatible by coating with polyelectrolyte multilayers (see Section 1.4.2.2) with little optical interference. Probes with the appropriate biocompatible coating could provide useful information for much longer time periods than their electrical equivalents.

Another downside of electrical techniques is the inherent interference from neighbouring neurons, muscle activity, and instrument noise from the electrical equipment itself, all of which increase the background noise and reduce the sensitivity of the measurement. Optical measurements are not susceptible to the same sources of interference as electrical measurements, and experiments inside the body already have greatly reduced background light levels. Additionally, by carefully choosing the measurement wavelength and with the use of highly-selective filters and chopping, the background noise in a given optical experiment can be reduced even further.

### 1.5.3 Current Methods of Catecholamine Detection

A variety of different methods for detecting dopamine (and the related neurotransmitters epinephrine and norepinephrine, all of which are *catecholamines*) have been described: electrochemical methods are the most popular, due to the maturity of electrical and electrochemical measurements in neuroscience.[164,166–170] However, optical methods, including both fluorescence- and absorption-based measurements are becoming more prevalent in the literature, and are discussed in more detail below. The vast majority of chemical sensors utilise the ability of organic boronic acids to selectively bind 1,2-diols, which are chemically durable and easy to append to the reporter molecule.

#### 1.5.3.1 Boronic Acids for Diol Recognition

At the core of Chapter 5 is the ability of boronic acids to strongly and selectively bind vicinal diols.[171,172] This functionality is present in many biologically-relevant molecules, notably saccharides, for which many indicator molecules incorporating a boronic acid moiety have already been developed (see Sections 1.5.3.2 and 1.5.3.3),[173–175] and the neurotransmitter molecules dopamine, norepinephrine, adrenaline, and L-DOPA, as discussed in Section 1.5.1. The binding is a reversible condensation reaction, evolving two equivalents of water and forming a 1:1 complex. The binding is favoured at high pH conditions and disfavoured at low pH, as shown in Figure 1.20.[176]

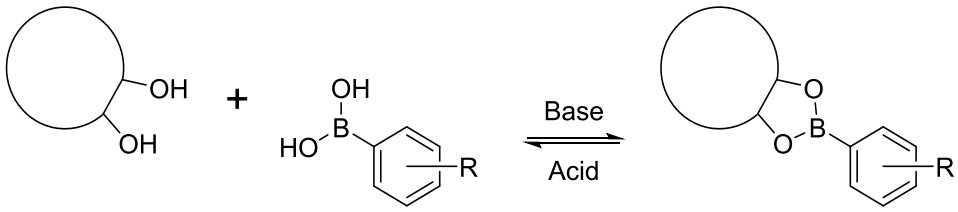


Figure 1.20 Generic scheme for the reversible binding of diols with an arylboronic acid. Generally, the diol can be considered strongly bound above pH = 10, and the dissociation reaction can be promoted at pH < 6, however the nature of the R group strongly affects the equilibrium.[176]

One of the first reports of the geometry of the phenylboronate ion used the reversible binding of diols to help confirm the structure (tetrahedral, with coordination of an $OH^-$ ion giving $B(OH)_4^-$, rather than as a Brønsted acid $BO_2H^-$).[171] Here, it was shown that the binding constant

for catechol, which forms the core of the dopamine molecule, is around $20\times10^3$, while fructose has a binding constant of $4\times10^3$. The significantly stronger binding of catechol suggests that the optical detectors designed to detect saccharides such as glucose and fructose (discussed in Section 1.5.3.3 below) will respond to even lower concentrations of catecholates such as dopamine.

#### 1.5.3.2 Fluorescence Sensors

A wide variety of compounds have been proposed for detecting diols, typically saccharides, via a change in fluorescence response.[175] The first reported fluorescent sensor was boronic acid-appended anthracene, which showed a lowering of fluorescence intensity as a function of analyte concentration.[177] Many other reports followed, with varying levels of selectivity, responsiveness, and stability. Because of the obvious biological relevance of glucose, many of these sensors were tested under biological pH conditions.[178–186] In addition to optimization of excitation wavelength for biological applications, considerable effort has been expended to make molecules which selectively detect one type of saccharide over others. Since the saccharides have more than one pair of diols, small molecules functionalized with two (or sometimes more) boronic acid groups can be geometrically tailored to specifically bind one type of saccharide over others: this includes mono vs. disaccharides,[187] different classes of monosaccharide,[178,179,183,188–190] and even different enantiomers of a single monosaccharide.[191] The detection of dopamine via fluorescence has been reported in several publications, including small molecules,[192–196] functionalized nanoparticles,[197] and biomimetic binding pockets.[198–200] Perhaps the greatest disadvantage of fluorescence-based molecular detectors is that most require excitation in the UV range, which is not ideal for compounds intended to operate inside an organism. UV light is harmful to the surrounding tissue, and will eventually result in photodecomposition of the sensor molecules themselves.

#### 1.5.3.3 Absorbance Sensors

In addition to fluorescence sensors, there also exist sensor molecules based on changes in visible absorbance upon binding to an analyte. This research has primarily been targeted towards glucose reporters for diabetics,[174,201,202] sugar analysis for industrial production,[203] and as dyes for inkjet printing,[204] as well as at least one example reported for reporting dopamine sensing (see Figure 1.21).[192]

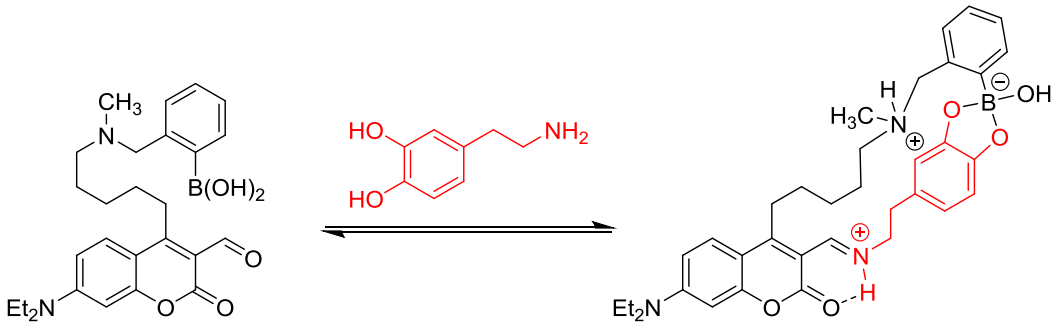


Figure 1.21 An absorption-based chemical indicator for dopamine, based on a boronic acid and aldehyde binding sites. The resulting complex shows a 30 nm shift in $\lambda_{max}$, as well as a twofold fluorescence reduction on binding. Reprinted (adapted) with permission from Reference 192. Copyright 2004 American Chemical Society.

The vast majority of papers published in this field focus on visible detection of glucose and other saccharides, with several patents having been filed for glucose indicators.[203,205–207] Most of these systems are based on boronic acid-functionalized azobenzene derivatives, due to the deep colouration and robust nature of the azobenzene chromophore.[173] The visible response of one of the most successful systems is shown in Figure 1.22,[174] and many similar systems have been reported,[201,208,209] including two polymer-appended sensors in solution.[210,211] Absorption-based indicators are typically active in the visible spectrum, in contrast to the UV light required for most fluorophores. This represents one of the largest advantages of absorbance-based sensing with visible-light chromophores, since visible light poses little risk to biological tissue.

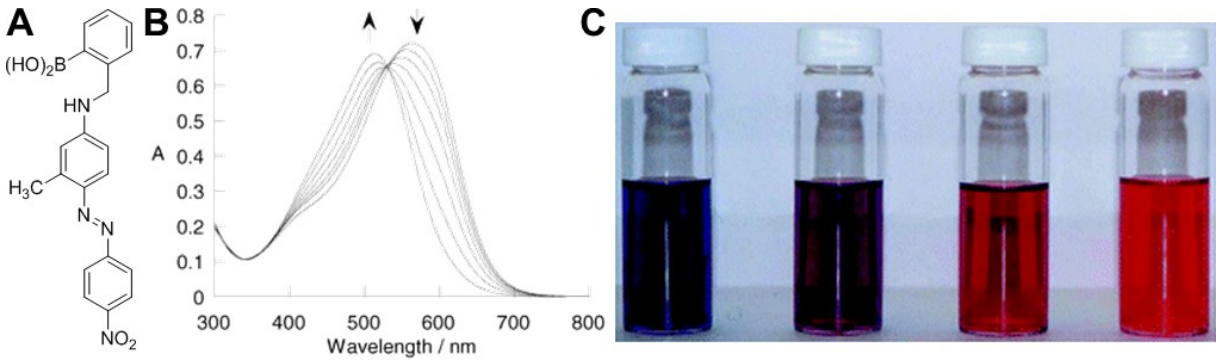


Figure 1.22 A) Molecular structure of the azo-boronic acid B) Spectral change from 0 – 60 mM glucose at pH = 11 C) Visible change of the glucose sensor from 0 – 25 mM at pH = 11. Reproduced from Reference 174 with permission from The Royal Society of Chemistry.

Currently, the majority of the compounds reported operate optimally at considerably higher pH (*ca.* 10 – 11) than our target range, namely biological pH ≈ 7.4, due to the nature of the boronic acid-diol binding event.[174,202] The development of indicator molecules capable of operating at biological pH is the subject of Chapter 5, while Chapter 6 describes the incorporation of successful indicators into a biocompatible material.

## 1.6 Fibre Optic Detection

Chapter 6 of this work describes the design and fabrication of a fibre-optic sensor for optical detection of neurotransmitter molecules, with the ultimate goal of creating a biocompatible sensor which can be implanted *in vivo* for long periods of time. Fibre optics are ubiquitous in modern optics, both in fundamental research and industrial applications. They allow light to be easily guided for significant distances with minimal loss, while preserving the important characteristics of the signal (polarization, time resolution, and phase). The ease of guiding light to a desired area, combined with the wide variety of possible surface chemistries, makes fibres an ideal sensor platform. Unlike the electrical probes discussed in Section 1.5.2, coatings for fibre optic sensors are only limited by their optical properties.

### 1.6.1 Fibre Optic Fundamentals

Fibre optics are a type of waveguide, which exploits the phenomenon of *total internal reflection*, where light travelling through a medium is effectively trapped inside that medium due to a difference in indices of refraction between the fibre and its surroundings. A light ray impinging on the interface between two materials with differing indices of refraction will refract as it passes through the interface, according to Snell's law (Equation 1.8):

$$n_1 \sin\theta_i = n_2 \sin\theta_t \qquad \text{Equation 1.8}$$

where $n_1$ and $n_2$ are the indices of refraction of the two materials, $\theta_i$ is the angle of the incident ray, and $\theta_t$ is the angle of the refracted (transmitted) ray, both with respect to normal. If $n_1 > n_2$, there will be a point at which $\theta_t$ is 90°, implying all the light is reflected at the interface: this is called the critical angle.

Rearranging the equation, and substituting in $\theta_t = 90°$, Snell's Law can be solved for the critical angle:

$$\theta_i = \arcsin\left(\frac{n_2}{n_1}\right) \qquad \text{Equation 1.9}$$

Fibre optics exploit the phenomenon of total internal reflection by having a small width relative to the angle at which light can enter: all the light entering one end of a fibre within the *cone of acceptance* (determined by the critical angle) will undergo total internal reflection each time it meets the fibre/environment interface, and thus no light (in principle) is lost through the length of the fibre.

#### 1.6.1.1 Evanescent Wave Absorption

Although there is no transmitted beam once the condition of total internal reflection is met, and thus formally no light is lost to the exterior of a fibre optic, the electric field does not diminish to zero intensity at the interface. Instead, it penetrates into the second medium (with the lower index of refraction) with an intensity proportional to the refractive indices of the materials. Although no energy is transferred under the simple geometric model of wave propagation, if another medium with a higher index of refraction is brought into intimate contact, some of the light is able to escape the optical fibre and be absorbed. The penetration depth of the evanescent wave, defined as the distance it takes for the field to decay to $^1/_e$, is small: typically within a few wavelengths of the surface, and can be described by Equation 1.10:

$$d_p = \frac{\lambda}{4\pi\left(n_1^2 \sin\theta - n_2^2\right)^{1/2}} \qquad \text{Equation 1.10}$$

where $d_p$ is the penetration depth of the electromagnetic field, $\lambda$ is the wavelength of light in nanometres, $\theta$ is the angle of incidence, and $n_1$ and $n_2$ are the indices of refraction of the fibre and surroundings, respectively.[212] For a typical fibre with an index of refraction of ~1.6, and assuming water is the surrounding medium ($n$ = 1.33), the penetration depth varies from roughly 20 – 50 nanometres over the visible wavelength range (350 – 800 nm). Although these lengths are extremely small, polyelectrolyte multilayer films can be easily fabricated within this thickness regime, ensuring the indicator chromophores fall within the useful range of the evanescent wave.

### 1.6.2 Fibre Optic Sensors

Although fibre optics are still used overwhelmingly for data transfer, they have also become popular platforms for a wide variety of sensing applications over the past forty years. Probes designed to measure strain, temperature, and pressure make up the bulk of sensing applications, however a multitude of different applications in chemistry and biology have also been reported.[213–215] A recent review by Kostovski *et al.* describes the wide variety of ways fibre optics are used as micro- and nanoscale sensor platforms.[216] Fluorescence and Raman spectroscopy are among the most popular sensing methods, and there are many reports describing biological applications.[217] With such a wide variety of measurement types and applications the configuration of active sensor can take many forms, several of which relevant to Chapter 6 are summarized below.

#### 1.6.2.1 U-bend

Perhaps the simplest type of evanescent wave detector is simply a bend in the optical fibre, allowing the fibre to be immersed in a solution of analyte. The bend can be coated with the sensor layer and dipped into a solution containing analyte, with the light travelling from one end of the fibre, past the sensor area, and to a detector attached to the terminal end. This results in minimal loss from light leakage compared with the methods discussed below, since the light still undergoes total internal reflection for the length of the sensor. The u-bend is simply formed by heating the optical fibre past the $T_g$, and bending it into the desired shape. Although simple to construct and easy to handle, this geometry does not scale well to the size required for *in vivo* measurements. Too sharp a turn in the fibre results in light leakage as the total internal reflection condition is no longer met, resulting in too little signal getting returned to the detector.

A fibre-optic pH sensor using a u-bend fibre was reported, using Neutral Red as the active indicator molecule. Neutral Red was added to a solution of poly(allylamine hydrochloride) and layered alternatingly with poly(acrylic acid) to form an indicator-doped polyelectrolyte multilayer on the fibre. The coated u-bend fibre, seen in Figure 1.23 below, acts as an optical pH sensor when immersed in solution.[218]

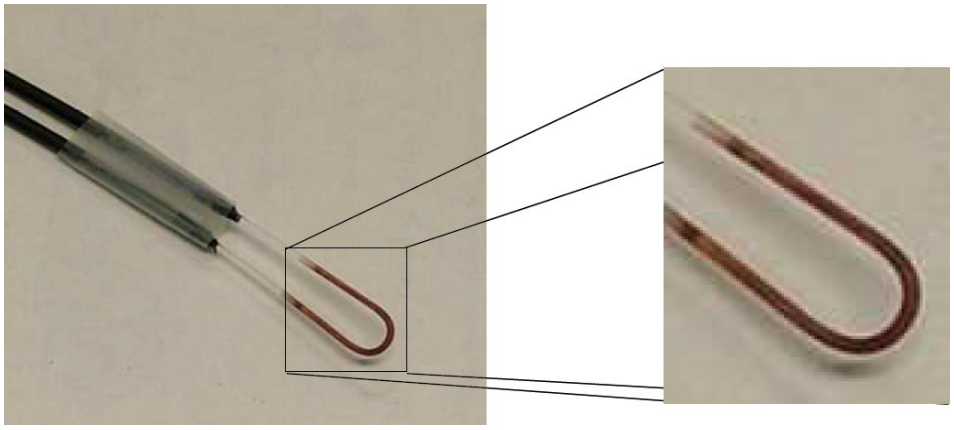

Figure 1.23 A u-bend optical fibre, coated with a polyelectrolyte multilayer composed of poly(allylamine hydrochloride) and poly(acrylic acid), doped with Neutral Red. The core diameter of the fibre is 1 mm, while the coated region is approximately 2 cm in length. 

#### 1.6.2.2 Terminal Reflection

If the fibre is simply cleaved and the resulting end coated in sensor, much of the light is lost through the end into the environment, since the condition for total internal reflection is no longer met. However, as with light propagation through any region with a change in index of refraction, some light will be reflected back down the length of the fibre. The amount of light reflected instead of transmitted is described by the Fresnel equations, proportional to the angle at which the ray meets the end surface and the difference in index of refraction between the fibre and surroundings. An evanescent wave is also formed at the interface, and so the reflected light contains information on the optical absorbance of the tip.

A fibre terminal absorbance measurement was used for a dip-sensor described by Sciacca and Monro (Figure 1.24).[219] In this paper, the authors functionalized a cleaved fibre tip with either gold or silver nanoparticles coated with different antibodies. When the fibre tip was exposed to a solution of protein antigens, the antigens were bound by the antibodies, which shifted the position of the plasmon resonance band.

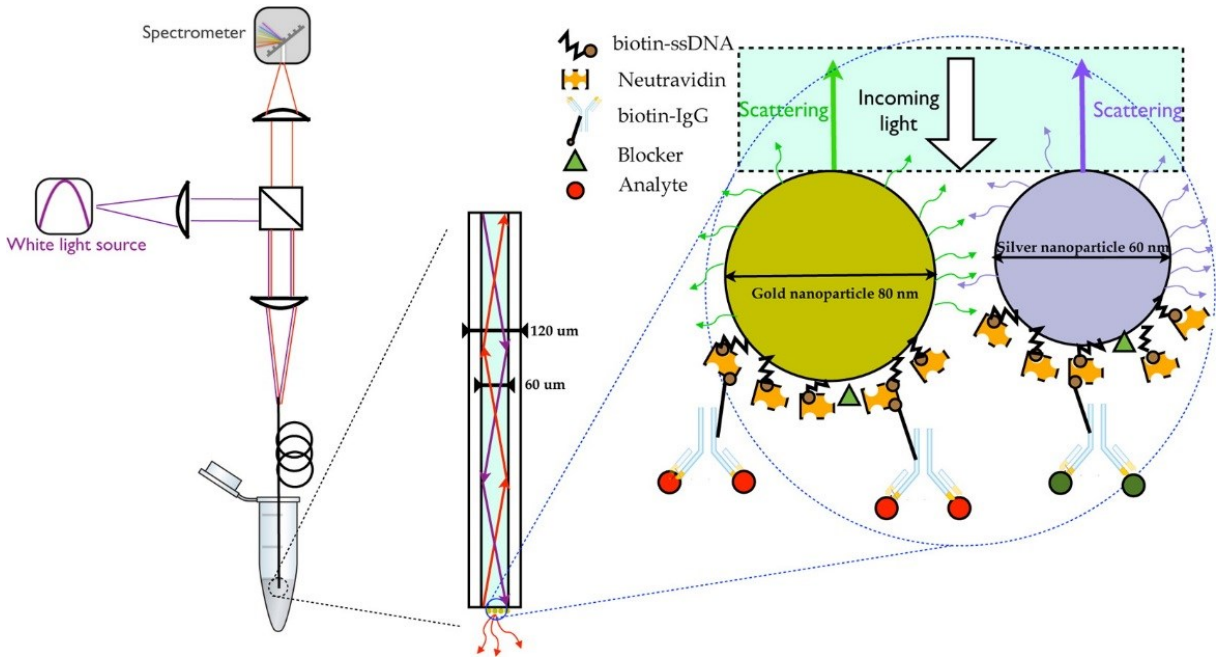


Figure 1.24 Schematic for the dip biosensor based on observing changes in plasmon resonance upon protein binding. Gold or silver nanoparticles functionalized with specific antibodies are coated on the end of a cleaved fibre optic: light sent down the fibre is reflected back and analyzed with a UV-vis spectrometer. Reprinted (adapted) with permission from Reference 219. Copyright 2014 American Chemical Society.

Reflection can be enhanced by capping the fibre with a reflective layer such as a metal: absorption of the evanescent wave occurs on the side of the fibre, rather than the cleaved tip. Coating with metal reflective layers can easily be accomplished by vapour deposition techniques, metal-impregnated epoxy coatings, or with solution based chemical coating techniques like the "silver mirror" generated with the Tollens reagent. An optical pH sensor incorporating a terminal reflective layer is shown in Figure 1.25 below, which exhibits an enhanced amount of signal returned and precludes the need for a complete light circuit as in Figure 1.23 in the previous section. Although this increases the amount of light returned to the detector which improves the signal to noise ratio, the choice of metal layer must be made carefully since many metals are cytotoxic, especially over the long timescales of implant use.[220,221]

The fundamentals of the experiments described above are similar to the fibre-based sensor described in Chapter 6. A broad-spectrum source is coupled to an optical fibre, with the opposite end stripped of cladding and coated with a boronic acid-functionalized azo derivative. The light

is partially reflected from the interface, containing the absorbance spectrum of the tip. As the concentration of the analyte changes, the absorbance spectrum changes as well, giving an optical signal which can be recorded.

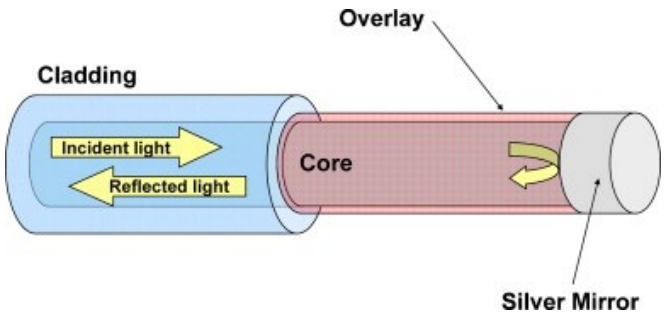


Figure 1.25 An optical pH sensor doped with Neutral Red (overlay), including a mirror layer on the fibre terminus to enhance reflection. Reproduced from Reference 222 with permission from Elsevier, copyright 2008.

#### 1.6.2.3 Tapered Terminal Fibres

Similar to the simple flat fibre end formed by cleaving, tapered fibre tips present several advantages for optical sensors. The smaller working surface allows for greater spatial resolution, and for increased durability of the small features necessary for a cellular probe. Although relatively small-diameter single-mode fibres are commercially available (*ca.* 10 µm core diameter), these fibres are fragile and easily broken during handling. Tapering the terminal end of the fibre allows for the bulk to have the durability of a larger fibre, while leaving a relatively sharp tip for sensing and manipulation. This can be accomplished by pulling, where a heated fibre is placed under tension, and the point where it breaks leaves a sharp point. This technique is well-developed, and can yield very sharp fibre tips as depicted in Figure 1.26.[223,224] An alternative method is to place a polymer-clad silica fibre in a container containing a solution of hydrofluoric acid. The silica core is etched away preferentially at the core/cladding interface, leaving a sharp tip in a very reproducible manner.[223]

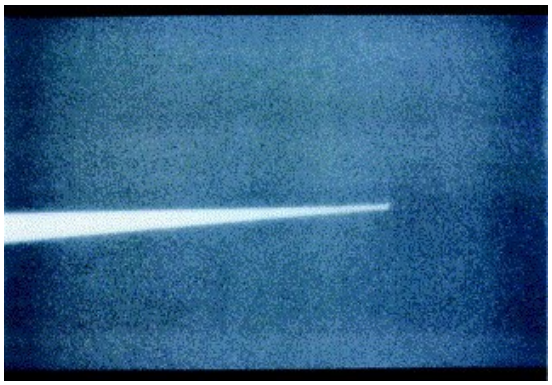

Figure 1.26 A scanning electron micrograph of a pulled fibre tip. The tip diameter is approximately 50 nm. Reproduced from Reference 223 with permission from Elsevier, copyright 2000.

The techniques developed for tapering glass to a sharp point are the fundamental tool behind the patch clamp technique used in electrophysiology, where a hollow glass micropipette can hold a single cell in place, allowing sensitive electrical measurements to be performed on a small area of the cell membrane.[152,225] Sensitive evanescent wave absorption measurements have been demonstrated on regions of tapered fibre, suggesting that this technique could be easily adapted to the type of measurements performed in Chapter 6.[226,227]

#### 1.6.2.4 Fibre Bragg Gratings

An alternative to reflection at the terminus of a coated optical fibre is to inscribe a fibre Bragg grating into the surface coating. A Bragg grating is a type of wavelength-specific reflector, constructed by inscribing periodic changes in index of refraction in the fibre. The spacing of the features, like the spacing in a conventional dielectric mirror, determines the wavelengths of light to be reflected or transmitted, with very high precision. The variation in index of refraction can be directly written into the fibre itself using UV light or dopants, but it has also been demonstrated with azo-doped coatings in the same manner as inscribing surface relief gratings.[228,229] The reflection coefficient can be extremely high, and since the wavelength specificity originates from the spacing of the variations in the index of refraction in the film, not the absorbance band of the azo film itself, it allows the coating to serve the dual purpose of sensor layer and reflector.

#### 1.6.2.5 Whispering Gallery/Microsphere Termination

Whispering gallery modes, first discovered as an acoustic wave phenomenon by Lord Rayleigh and later expanded into electromagnetic theory,[230] are a popular tool in optical sensing due to their ability to drastically increase the signal to noise ratio. Typically constructed using glass or polymer microspheres connected to an optical fibre, whispering galleries effectively trap light 'injected' from a fibre into the microsphere (via the evanescent wave), where it circulates for a large number of cycles via total internal reflection before escaping back into the fibre. The time spent trapped in the microsphere allows the light to undergo many evanescent wave absorption events, greatly increasing the signal to noise ratio. Microspheres coated with a sensor layer and arrayed along an optical fibre could potentially act as a single sensor with multiple inputs.

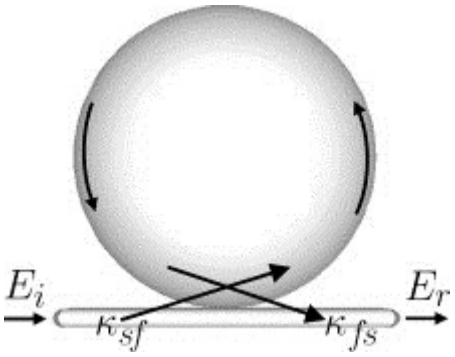


Figure 1.27 A schematic of a microsphere coupled with an optical fibre. Light propagating along the fibre couples with the microsphere via the evanescent wave, circulates repeatedly via total internal reflection undergoing evanescent wave absorption by a coating doped with biosensors, then couples back into the fibre and travels to the detector. Reproduced from Reference 231 with permission from Elsevier, copyright 2007.

In addition to the enhancement of optical signal offered by the use of whispering gallery microspheres, neural cells have been shown to preferentially adhere to curved surfaces.[232] This suggests that neurites may actively seek out optically sensitive areas on a fibre optic decorated with microspheres, which might help to solve the issue of probe migration over long implant periods. Additionally, *ex vivo* neural cell growth studies could be extremely simple to interface fibre probes with, since an array of whispering gallery spheres could be constructed on a surface, with cell growth tending to concentrate on the sensitive areas.

This thesis describes the development and characterization of new azo materials for a wide variety of applications, three of which were investigated in detail and are presented in Chapters 4 – 6 below.

## 1.7 References


1. G. S. Hartley, *Nature*, 1937, **140**, 281.

2. S. Samanta, A. A. Beharry, O. Sadovski, T. M. McCormick, A. Babalhavaeji, V. Tropepe, and G. A. Woolley, *J. Am. Chem. Soc.*, 2013, **135**, 9777–9784.

3. H. Zollinger, *Azo and Diazo Chemistry*, Interscience, New York, 1961.

4. H. Zollinger, *Colour Chemistry, Synthesis, Properties, and Applications of Organic Dyes*, VCH, Weinheim, 1987.

5. A. A. Beharry and G. A. Woolley, *Chem. Soc. Rev.*, 2011, **40**, 4422–4437.

6. H. M. D. Bandara and S. C. Burdette, *Chem. Soc. Rev.*, 2012, **41**, 1809–1825.

7. J. Griffiths, *Chem. Soc. Rev.*, 1972, **1**, 481–493.

8. M. Natali and S. Giordani, *Chem. Soc. Rev.*, 2012, **41**, 4010–4029.

9. N. J. Bunce, G. Ferguson, C. L. Forber, and G. J. Stachnyk, *J. Org. Chem.*, 1987, **52**, 394–398.

10. H. Rau, in *Photochemistry and Photophysics*, eds. J. F. Rabek and G. W. Scott, CRC Press, Boca Raton, Florida, 2nd edn., 1989, pp. 119–141.

11. D. Bléger, J. Schwarz, A. M. Brouwer, and S. Hecht, *J. Am. Chem. Soc.*, 2012, **134**, 20597–20600.

12. O. S. Bushuyev, A. Tomberg, T. Friščić, and C. J. Barrett, *J. Am. Chem. Soc.*, 2013, **135**, 12556–12559.

13. J. Garcia-Amorós, M. Díaz-Lobo, S. Nonell, and D. Velasco, *Angew. Chem. Int. Ed. Engl.*, 2012, **51**, 12820–12823.

14. A. A. Beharry, O. Sadovski, and G. A. Woolley, *J. Am. Chem. Soc.*, 2011, **133**, 19684–19687.

15. P. P. Birnbaum and D. W. G. Style, *Trans. Faraday Soc.*, 1954, **50**, 1192–1196.

16. H. Rau, in *Photochemistry and Photophysics*, eds. J. F. Rabek and G. W. Scott, CRC Press, Boca Raton, Florida, 2nd edn., 1989, pp. 119–141.

17. P. Bortolus and S. Monti, *J. Phys. Chem.*, 1979, **83**, 648–652.

18. H. Stegemeyer, *J. Phys. Chem.*, 1962, **66**, 2555–2560.

19. D. Gegiou, K. A. Muszkat, and E. Fischer, *J. Am. Chem. Soc.*, 1968, **90**, 12–18.

20. N. C. Holme, P. S. Ramanujam, and S. Hvilsted, *Opt. Lett.*, 1996, **21**, 902–904.

21. E. Mitscherlich, *Ann. der Pharm.*, 1834, **12**, 311–314.

22. A. Noble, *Justus Liebigs Ann. Chem.*, 1856, **98**, 253–256.

23. G. S. Hartley and R. J. W. Le Fèvre, *J. Chem. Soc.*, 1939, 531–535.

24. J. M. Robertson, *J. Chem. Soc.*, 1939, 232.

25. A. Mostad and C. Rømming, *Acta Chem. Scand.*, 1971, **25**, 3561–3568.

26. M. Poprawa-Smoluch, J. Baggerman, H. Zhang, H. P. A. Maas, L. De Cola, and A. M. Brouwer, *J. Phys. Chem. A*, 2006, **110**, 11926–11937.

27. H. Rau, *J. Photochem.*, 1984, **26**, 221–225.

28. H. Rau and E. Lueddecke, *J. Am. Chem. Soc.*, 1982, **104**, 1616–1620.

29. C. Ciminelli, G. Granucci, and M. Persico, *Chemistry*, 2004, **10**, 2327–2341.

30. D. P. Hoffman and R. a Mathies, *Phys. Chem. Chem. Phys.*, 2012, **14**, 6298–6306.

31. C. Nonnenberg, H. Gaub, and I. Frank, *ChemPhysChem*, 2006, **7**, 1455–1461.

32. M. Han and T. Honda, *Sci. China Chem.*, 2011, **54**, 1955–1961.

33. D.-M. Shin and D. G. Whitten, *J. Am. Chem. Soc.*, 1988, **110**, 5206–5208.

34. R. Cimiraglia and H.-J. Hofmann, *Chem. Phys. Lett.*, 1994, **217**, 430–435.

35. H. K. Cammenga, V. N. Emel'yanenko, and S. P. Verevkin, *Ind. Eng. Chem. Res.*, 2009, **48**, 10120–10128.

36. H. M. D. Bandara, T. R. Friss, M. M. Enriquez, W. Isley, C. Incarvito, H. A. Frank, J. Gascon, and S. C. Burdette, *J. Org. Chem.*, 2010, **75**, 4817–4827.

37. T. Ikegami, N. Kurita, H. Sekino, and Y. Ishikawa, *J. Phys. Chem. A*, 2003, **107**, 4555–4562.

38. T. Fujino, S. Y. Arzhantsev, and T. Tahara, *J. Phys. Chem. A*, 2001, **105**, 8123–8129.

39. T. Fujino, S. Y. Arzhantsev, and T. Tahara, *Bull. Chem. Soc. Jpn.*, 2002, **75**, 1031–1040.

40. B. Schmidt, C. Sobotta, S. Malkmus, S. Laimgruber, M. Braun, W. Zinth, and P. Gilch, *J. Phys. Chem. A*, 2004, **108**, 4399–4404.

41. H. Satzger, C. Root, and M. Braun, *J. Phys. Chem. A*, 2004, **108**, 6265–6271.

42. G. Granucci and M. Persico, *Theor. Chem. Acc.*, 2006, **117**, 1131–1143.

43. E. Wei-Guang Diau, *J. Phys. Chem. A*, 2004, **108**, 950–956.

44. L. Wang and X. Wang, *J. Mol. Struct.*, 2007, **847**, 1–9.

45. S. Kawauchi, T. Imase, Y. Tamura, and J. Watanabe, *Mol. Cryst. Liq. Cryst. Sci. Technol. Sect. A. Mol. Cryst. Liq. Cryst.*, 2000, **345**, 69–74.

46. E. R. Talaty and J. C. Fargo, *Chem. Commun.*, 1967, 65–66.

47. T. Naito, K. Horie, and I. Mita, *Macromolecules*, 1991, **24**, 2907–2911.

48. O. S. Bushuyev, T. A. Singleton, and C. J. Barrett, *Adv. Mater.*, 2013, **25**, 1796–1800.

49. E. Merino, *Chem. Soc. Rev.*, 2011, **40**, 3835–3853.

50. X. Liu, H.-Q. Li, S. Ye, Y.-M. Liu, H.-Y. He, and Y. Cao, *Angew. Chem. Int. Ed. Engl.*, 2014, **53**, 7624–7628.

51. Y. Takeda, S. Okumura, and S. Minakata, *Angew. Chem. Int. Ed. Engl.*, 2012, **51**, 7804–7808.

52. B. Priewisch and K. Rück-Braun, *J. Org. Chem.*, 2005, **70**, 2350–2352.

53. G. A. Woolley, *Acc. Chem. Res.*, 2005, **38**, 486–493.

54. A. Polosukhina, J. Litt, I. Tochitsky, J. Nemargut, Y. Sychev, I. De Kouchkovsky, T. Huang, K. Borges, D. Trauner, R. N. Van Gelder, and R. H. Kramer, *Neuron*, 2012, **75**, 271–282.

55. R. H. Kramer, J. J. Chambers, and D. Trauner, *Nat. Chem. Biol.*, 2005, **1**, 360–365.

56. T. Hugel, N. B. Holland, A. Cattani, L. Moroder, M. Seitz, and H. E. Gaub, *Science*, 2002, **296**, 1103–1106.

57. T. A. Singleton, I. B. Burgess, B. A. Nerger, A. Goulet-Hanssens, N. Koay, C. J. Barrett, and J. Aizenberg, *Soft Matter*, 2014, **10**, 1325–1328.

58. A. Natansohn and P. Rochon, *Chem. Rev.*, 2002, **102**, 4139–4175.

59. A. Teitel, *Naturwissenschaften*, 1957, **44**, 370–371.

60. T. Todorov, L. Nikolova, and N. Tomova, *Appl. Opt.*, 1984, **23**, 4309–4312.

61. S. Hvilsted, C. Sánchez, and R. Alcalá, *J. Mater. Chem.*, 2009, **19**, 6641–6648.

62. A. Natansohn, P. Rochon, J. Gosselin, and S. Xie, *Macromolecules*, 1992, **25**, 2268–2273.

63. A. Natansohn, S. Xie, and P. Rochon, *Macromolecules*, 1992, **25**, 5531–5532.

64. P. Rochon, D. Bissonnette, A. Natansohn, and S. Xie, *Appl. Opt.*, 1993, **32**, 7277–7280.

65. A. Natansohn, P. Rochon, M. Pezolet, P. Audet, D. Brown, and S. To, *Macromolecules*, 1994, **27**, 2580–2585.

66. D. Brown, A. Natansohn, and P. Rochon, *Macromolecules*, 1995, **28**, 6116–6123.

67. A. Natansohn, P. Rochon, M.-S. Ho, and C. Barrett, *Macromolecules*, 1995, **28**, 4179–4183.

68. M. S. Ho, A. Natansohn, and P. Rochon, *Macromolecules*, 1995, **28**, 6124–6127.

69. M.-S. Ho, A. Natansohn, C. Barrett, and P. Rochon, *Can. J. Chem.*, 1995, **73**, 1773–1778.

70. M. Ho, A. Natansohn, and P. Rochon, *Macromolecules*, 1996, **29**, 44–49.

71. X. Meng, A. Natansohn, C. Barrett, and P. Rochon, *Macromolecules*, 1996, **29**, 946–952.

72. X. Meng, A. Natansohn, and P. Rochon, *J. Polym. Sci. Part B Polym. Phys.*, 1996, **34**, 1461–1466.

73. X. Meng, A. Natansohn, and P. Rochon, *Supramol. Sci.*, 1996, **3**, 207–213.

74. X. Meng, A. Natansohn, and P. Rochon, *Polymer*, 1997, **38**, 2677–2682.

75. P. Rochon, E. Batalla, and A. Natansohn, *Appl. Phys. Lett.*, 1995, **66**, 136–138.

76. K. G. Yager and C. J. Barrett, *Macromolecules*, 2006, **39**, 9320–9326.

77. C. J. Barrett, A. L. Natansohn, and P. L. Rochon, *J. Phys. Chem.*, 1996, **100**, 8836–8842.

78. C. J. Barrett, P. L. Rochon, and A. L. Natansohn, *J. Chem. Phys.*, 1998, **109**, 1505–1516.

79. Y. Yu, M. Nakano, and T. Ikeda, *Nature*, 2003, **425**, 145.

80. R. Yin, W. Xu, M. Kondo, C.-C. Yen, J. Mamiya, T. Ikeda, and Y. Yu, *J. Mater. Chem.*, 2009, **19**, 3141–3143.

81. C. J. Barrett, J. Mamiya, K. G. Yager, and T. Ikeda, *Soft Matter*, 2007, **3**, 1249–1261.

82. H. Finkelmann, E. Nishikawa, G. Pereira, and M. Warner, *Phys. Rev. Lett.*, 2001, **87**, 015501.

83. V. Teboul and J. B. Accary, *Phys. Rev. E*, 2014, **89**, 012303.

84. M.-H. Li, P. Keller, B. Li, X. Wang, and M. Brunet, *Adv. Mater.*, 2003, **15**, 569–572.

85. T. Ikeda, M. Nakano, Y. Yu, O. Tsutsumi, and A. Kanazawa, *Adv. Mater.*, 2003, **15**, 201–205.

86. J. R. Ferraro, *Vibrational Spectroscopy at High External Pressures: The Diamond Anvil Cell*, Academic Press, Inc., Orlando, 1984.

87. A. Jayaraman, *Rev. Sci. Instrum.*, 1986, **57**, 1013–1031.

88. S. Block and G. Piermarini, *Phys. Today*, 1976, **29**, 44–55.

89. J. R. Ferraro, in *Handbook of Vibrational Spectroscopy*, Academic Press, Inc., New York, N.Y., 2002.

90. F. E. Huggins, H. K. Mao, and D. Virgo, *Carnegie Inst. Washingt. Yearb.*, 1975, **74**, 405–410.

91. H. K. Mao, P. M. Bell, J. W. Shaner, and D. J. Steinberg, *J. Appl. Phys.*, 1978, **49**, 3276–3283.

92. D. D. Klug, *Rev. Sci. Instrum.*, 1983, **54**, 1205–1208.

93. W. F. Sherman, *J. Phys. C Solid State Phys.*, 2000, **13**, 4601–4613.

94. T. Atake and C. A. Angell, *J. Phys. Chem.*, 1979, **83**, 3218–3223.

95. P. M. Budd, N. B. McKeown, and D. Fritsch, *J. Mater. Chem.*, 2005, **15**, 1977–1986.

96. M. L. Williams, R. F. Landel, and J. D. Ferry, *J. Am. Chem. Soc.*, 1955, **77**, 3701–3707.

97. P. Atkins and J. de Paula, *Physical Chemistry*, Oxford University Press, New York, N.Y., 8th edn., 2006.

98. Q. Deng and Y. C. Jean, *Macromolecules*, 1993, **26**, 30–34.

99. A. H. Kadhim and H. W. Offen, *J. Am. Chem. Soc.*, 1967, **89**, 1805–1809.

100. Z. Dong, N. M. Seemann, N. Lu, and Y. Song, *J. Phys. Chem. B*, 2011, **115**, 14912–14918.

101. S. K. Surampudi, H. R. Patel, G. Nagarjuna, and D. Venkataraman, *Chem. Commun.*, 2013, **49**, 7519–7521.

102. G. Kleideiter, Z. Sekkat, M. Kreiter, M. Dieter Lechner, and W. Knoll, *J. Mol. Struct.*, 2000, **521**, 167–178.

103. A. Baba, G. Kleideiter, T. Jakob, and W. Knoll, *Macromol. Chem. Phys.*, 2004, **205**, 2267–2274.

104. Z. Sekkat, G. Kleideiter, and W. Knoll, *J. Opt. Soc. Am. B*, 2001, **18**, 1854–1857.

105. C. J. Barrett, A. Natansohn, and P. Rochon, *Chem. Mater.*, 1995, **7**, 899–903.

106. E. Yablonovitch, *Phys. Rev. Lett.*, 1987, **58**, 2059–2062.

107. P. Vukusic and J. R. Sambles, *Nature*, 2003, **424**, 852–855.

108. J. Sun, B. Bhushan, and J. Tong, *RSC Adv.*, 2013, **3**, 14862–14889.

109. Y. Zhao, Z. Xie, H. Gu, C. Zhu, and Z. Gu, *Chem. Soc. Rev.*, 2012, **41**, 3297–3317.

110. J. V. Sanders, *Acta Crystallogr. Sect. A*, 1968, **24**, 427–434.

111. H. Fudouzi, in *Responsive Photonic Nanostructures: Smart Nanoscale Optical Materials*, ed. Y. Yadong, RSC Publishing, Cambridge, U.K., 2013, pp. 44–62.

112. J. D. Joannopoulos, S. G. Johnson, J. N. Winn, and R. D. Meade, *Photonic Crystals: Molding the Flow of Light*, Princeton University Press, Princeton, New Jersey, 2nd edn., 2008.

113. B. Hatton, L. Mishchenko, S. Davis, K. H. Sandhage, and J. Aizenberg, *Proc. Natl. Acad. Sci.*, 2010, **107**, 10354–10359.

114. I. B. Burgess, N. Koay, K. P. Raymond, M. Kolle, M. Lončar, and J. Aizenberg, *ACS Nano*, 2012, **6**, 1427–1437.

115. A. Stein, B. E. Wilson, and S. G. Rudisill, *Chem. Soc. Rev.*, 2013, **42**, 2763–2803.

116. B. Xin and J. Hao, *Chem. Soc. Rev.*, 2010, **39**, 769–782.

117. R. Wang, K. Hashimoto, A. Fujishima, M. Chikuni, E. Kojima, A. Kitamura, M. Shimohigoshi, and T. Watanabe, *Nature*, 1997, **388**, 431–432.

118. K. Ichimura, S.-K. Oh, and M. Nakagawa, *Science*, 2000, **288**, 1624–1626.

119. S.-K. Oh, M. Nakagawa, and K. Ichimura, *J. Mater. Chem.*, 2002, **12**, 2262–2269.

120. N. M. Ahmad, M. Saqib, and C. J. Barrett, *J. Macromol. Sci. Part A*, 2010, **47**, 534–544.

121. R. Rosario, D. Gust, M. Hayes, F. Jahnke, J. Springer, and A. A. Garcia, *Langmuir*, 2002, **18**, 8062–8069.

122. E. Fischer and Y. Hirshberg, *J. Chem. Soc.*, 1952, 4522–4524.

123. J. Maisuradze, *Bull. Georg. Natl. Acad. Sci.*, 2008, **2**, 90–93.

124. R. Klajn, *Chem. Soc. Rev.*, 2014, **43**, 148–184.

125. P. K. Kundu, G. L. Olsen, V. Kiss, and R. Klajn, *Nat. Commun.*, 2014, **5**, 3588.

126. X. Pei, A. Fernandes, B. Mathy, X. Laloyaux, B. Nysten, O. Riant, and A. M. Jonas, *Langmuir*, 2011, **27**, 9403–9412.

127. J. Groten, C. Bunte, and J. Rühe, *Langmuir*, 2012, **28**, 15038–15046.

128. O. Nachtigall, C. Kördel, L. H. Urner, and R. Haag, *Angew. Chemie Int. Ed.*, 2014.

129. N. M. Ahmad, X. Lu, and C. J. Barrett, *J. Mater. Chem.*, 2010, **20**, 244–247.

130. G. Decher, *Science*, 1997, **277**, 1232–1237.

131. J. W. Nicholson, *Chem. Soc. Rev.*, 1994, **23**, 53–58.

132. S. T. Dubas and J. B. Schlenoff, *Macromolecules*, 1999, **32**, 8153–8160.

133. S. E. Burke and C. J. Barrett, *Pure Appl. Chem.*, 2004, **76**, 10–15.

134. K. Ariga, J. P. Hill, and Q. Ji, *Phys. Chem. Chem. Phys.*, 2007, **9**, 2319–2340.

135. H. G. Tompkins and W. A. McGahan, *Spectroscopic Ellipsometry and Reflectometry*, John Wiley & Sons, Inc., New York, N.Y., 1999.

136. K. G. Yager, O. M. Tanchak, C. Godbout, H. Fritzsche, and C. J. Barrett, *Macromolecules*, 2006, **39**, 9311–9319.

137. T. A. Harroun, H. Fritzsche, M. J. Watson, K. G. Yager, O. M. Tanchak, C. J. Barrett, and J. Katsaras, *Rev. Sci. Instrum.*, 2005, **76**, 065101.

138. C. Picart, J. Mutterer, L. Richert, Y. Luo, G. D. Prestwich, P. Schaaf, J.-C. Voegel, and P. Lavalle, *Proc. Natl. Acad. Sci. U. S. A.*, 2002, **99**, 12531–12535.

139. S. Zapotoczny, M. Golonka, and M. Nowakowska, *Macromol. Rapid Commun.*, 2005, **26**, 1049–1054.

140. A. Goulet-Hanssens, K. Lai Wing Sun, T. E. Kennedy, and C. J. Barrett, *Biomacromolecules*, 2012, **13**, 2958–2963.

141. A. Goulet-Hanssens and C. J. Barrett, *J. Polym. Sci. Part A Polym. Chem.*, 2013, **51**, 3058–3070.

142. D. Koylu, M. Thapa, P. Gumbley, and S. W. Thomas, *Adv. Mater.*, 2012, **24**, 1451–1454.

143. J. Borges, L. C. Rodrigues, R. L. Reis, and J. F. Mano, *Adv. Funct. Mater.*, 2014, **24**, 5624–5648.

144. J. Huang, X. Peng, C. Xiong, and J. Fang, *J. Colloid Interface Sci.*, 2011, **355**, 503–508.

145. J. A. Lichter, M. T. Thompson, M. Delgadillo, T. Nishikawa, M. F. Rubner, and K. J. Van Vliet, *Biomacromolecules*, 2008, **9**, 1571–1578.

146. K. Ren, T. Crouzier, C. Roy, and C. Picart, *Adv. Funct. Mater.*, 2008, **18**, 1378–1389.

147. D. E. Discher, P. Janmey, and Y.-L. Wang, *Science*, 2005, **310**, 1139–1143.

148. M. Sailer and C. J. Barrett, *Macromolecules*, 2012, **45**, 5704–5711.

149. T. Yeung, P. C. Georges, L. a Flanagan, B. Marg, M. Ortiz, M. Funaki, N. Zahir, W. Ming, V. Weaver, and P. a Janmey, *Cell Motil. Cytoskeleton*, 2005, **60**, 24–34.

150. I.-C. Lee and Y.-C. Wu, *ACS Appl. Mater. Interfaces*, 2014, **6**, 14439–14450.

151. S. E. Burke and C. J. Barrett, *Macromolecules*, 2004, **37**, 5375–5384.

152. A. P. Alivisatos, A. M. Andrews, E. S. Boyden, M. Chun, G. M. Church, K. Deisseroth, J. P. Donoghue, S. E. Fraser, J. Lippincott-Schwartz, L. L. Looger, S. Masmanidis, P. L. McEuen, A. V Nurmikko, H. Park, D. S. Peterka, C. Reid, M. L. Roukes, A. Scherer, M. Schnitzer, T. J. Sejnowski, K. L. Shepard, D. Tsao, G. Turrigiano, P. S. Weiss, C. Xu, R. Yuste, and X. Zhuang, *ACS Nano*, 2013, **7**, 1850–1866.

153. M. A. Zarbin, C. Montemagno, J. F. Leary, and R. Ritch, *Wiley Interdiscip. Rev. Nanomed. Nanobiotechnol.*, 2012, **4**, 113–137.

154. M. Volgraf, P. Gorostiza, R. Numano, R. H. Kramer, E. Y. Isacoff, and D. Trauner, *Nat. Chem. Biol.*, 2006, **2**, 47–52.

155. K. Deisseroth, *Nat. Methods*, 2011, **8**, 26–29.

156. E. S. Boyden, *F1000 Biol. Rep.*, 2011, **3**.

157. E. R. Kandel, J. H. Schwartz, and T. M. Jessell, Eds., *Principles of Neural Science*, McGraw-Hill, New York, 4th edn., 2000.

158. J. H. Schwartz, in *Encyclopaedia of Life Sciences*, Wiley-Interscience, 2001, pp. 1–9.

159. T. C. Südhof and J. Rizo, *Cold Spring Harb. Perspect. Biol.*, 2011, **3**, 1–14.

160. T. Pradhan, H. S. Jung, J. H. Jang, T. W. Kim, C. Kang, and J. S. Kim, *Chem. Soc. Rev.*, 2014, **43**, 4684–4713.

161. A. Scimemi and M. Beato, *Mol. Neurobiol.*, 2009, **40**, 289–306.

162. M. Chesler, *Physiol. Rev.*, 2003, **83**, 1183–1221.

163. R. Brette, A. Destexhe, T. Stieglitz, K. H. Pettersen, H. Lindén, A. M. Dale, G. T. Einevoll, C. Bédard, J. C. de Munck, C. H. Wolters, M. Clerc, S. P. Ahlfors, M. S. Hämäläinen, R. D. Frostig, C. H. Chen-Bee, S. Chemla, F. Chavane, F. Helmchen, A. Bartels, J. Goense, and N. Logothetis, *Handbook of Neural Activity Measurement*, Cambridge University Press, Cambridge, U.K., 2012.

164. T. Stieglitz, in *Handbook of Neural Activity Measurement*, eds. R. Brette and A. Destexhe, Cambridge University Press, Cambridge, U.K., 2002, pp. 8–43.

165. V. S. Polikov, P. A. Tresco, and W. M. Reichert, *J. Neurosci. Methods*, 2005, **148**, 1–18.

166. S. R. Ali, R. R. Parajuli, Y. Balogun, Y. Ma, and H. He, *Sensors*, 2008, **8**, 8423–8452.

167. F.-L. Chan, W.-Y. Chang, L.-M. Kuo, C.-H. Lin, S.-W. Wang, Y.-S. Yang, and M. S.-C. Lu, *J. Micromechanics Microengineering*, 2008, **18**, 075028.

168. W. Song, Y. Chen, J. Xu, X.-R. Yang, and D.-B. Tian, *J. Solid State Electrochem.*, 2010, **14**, 1909–1914.

169. M.-J. Song, S.-K. Lee, J.-H. Kim, and D.-S. Lim, *Anal. Sci.*, 2012, **28**, 583–587.

170. Y. Wu, L. Cui, Y. Liu, G. Lv, T. Pu, D. Liu, and X. He, *Analyst*, 2013, **138**, 1204–1211.

171. J. P. Lorand and J. O. Edwards, *J. Org. Chem.*, 1959, **24**, 769–774.

172. D. G. Hall, in *Boronic Acids: Preparation and Applications in Organic Synthesis and Medicine*, ed. D. Hall, Wiley-VCH Verlag GmbH & Co. KGaA, Weinheim, 2011.

173. X. Wu, Z. Li, X.-X. Chen, J. S. Fossey, T. D. James, and Y.-B. Jiang, *Chem. Soc. Rev.*, 2013, **42**, 8032–8048.

174. C. J. Ward, P. Patel, and T. D. James, *J. Chem. Soc. Perkin Trans. 1*, 2002, 462–470.

175. H. Cao and M. D. Heagy, *J. Fluoresc.*, 2004, **14**, 569–584.

176. S. Mothana, J.-M. Grassot, and D. G. Hall, *Angew. Chem. Int. Ed. Engl.*, 2010, **49**, 2883–2887.

177. J. Yoon and A. W. Czarnik, *J. Am. Chem. Soc.*, 1992, **114**, 5874–5875.

178. H. Murakami, T. Nagasaki, I. Hamachi, and S. Shinkai, *Tetrahedron Lett.*, 1993, **34**, 6273–6276.

179. M. Takeuchi, T. Mizuno, H. Shinmori, M. Nakashima, and S. Shinkai, *Tetrahedron*, 1996, **52**, 1195–1204.

180. M. J. Deetz and B. D. Smith, *Tetrahedron Lett.*, 1998, **39**, 6841–6844.

181. B. Kukrer and E. U. Akkaya, *Tetrahedron Lett.*, 1999, **40**, 9125–9128.

182. N. DiCesare and J. R. Lakowicz, *Tetrahedron Lett.*, 2001, **42**, 9105–9108.

183. S. Arimori, C. J. Ward, and T. D. James, *Tetrahedron Lett.*, 2002, **43**, 303–305.

184. N. DiCesare and J. R. Lakowicz, *Tetrahedron Lett.*, 2002, **43**, 2615–2618.

185. J. N. Camara, J. T. Suri, F. E. Cappuccio, R. a Wessling, and B. Singaram, *Tetrahedron Lett.*, 2002, **43**, 1139–1141.

186. J. T. Suri, D. B. Cordes, F. E. Cappuccio, R. A. Wessling, and B. Singaram, *Langmuir*, 2003, **19**, 5145–5152.

187. K. R. A. S. Sandanayake, K. Nakashima, and S. Shinkai, *J. Chem. Soc. Chem. Commun.*, 1994, **6**, 1621–1622.

188. T. D. James, H. Shinmori, and S. Shinkai, *Chem. Commun.*, 1997, 71–72.

189. W. Yang, H. He, and D. G. Drueckhammer, *Angew. Chem. Int. Ed. Engl.*, 2001, **40**, 1714–1718.

190. S. Arimori, M. L. Bell, C. S. Oh, and T. D. James, *Org. Lett.*, 2002, **4**, 4249–4251.

191. T. D. James, K. R. A. Samankumara Sandanayake, and S. Shinkai, *Nature*, 1995, **374**, 345–347.

192. K. E. Secor and T. E. Glass, *Org. Lett.*, 2004, **6**, 3727–3730.

193. M.-F. Paugam, L. S. Valencia, B. Boggess, and B. D. Smith, *J. Am. Chem. Soc.*, 1994, **116**, 11203–11204.

194. F. Reviriego, M. I. Rodríguez-Franco, P. Navarro, E. García-España, M. Liu-Gonzalez, B. Verdejo, and A. Domènech, *J. Am. Chem. Soc.*, 2006, **128**, 16458–16459.

195. L. Campayo, J. M. Bueno, P. Navarro, C. Ochoa, J. Jimenez-Barbero, G. Pèpe, and A. Samat, *J. Org. Chem.*, 1997, **62**, 2684–2693.

196. A. Coskun and E. U. Akkaya, *Org. Lett.*, 2004, **6**, 3107–3109.

197. R. Freeman, L. Bahshi, T. Finder, R. Gill, and I. Willner, *Chem. Commun.*, 2009, 764–766.

198. M. Ganguly, C. Mondal, J. Jana, A. Pal, and T. Pal, *Langmuir*, 2014, **30**, 4120–4128.

199. J. Kim, B. Raman, and K. H. Ahn, *J. Org. Chem.*, 2006, **71**, 38–45.

200. S. Kolusheva, O. Molt, M. Herm, T. Schrader, and R. Jelinek, *J. Am. Chem. Soc.*, 2005, **127**, 10000–10001.

201. Y. Egawa, R. Gotoh, S. Niina, and J. Anzai, *Bioorg. Med. Chem. Lett.*, 2007, **17**, 3789–3792.

202. C. J. Ward, P. R. Ashton, T. D. James, and P. Patel, *Chem. Commun.*, 2000, 229–230.

203. P. Patel, C. J. Ward, and T. D. James, Detection of polyhydroxyl compounds. International Patent WO0112727A1 2001.

204. K. Tateishi, S. Hayashi, Y. Nagata, and T. Nakamura, Azo pigment, and pigment dispersion, coloring composition and ink composition for inkjet recording containing the same. International Patent WO2009031687A2 2009.

205. N. E. Pawlowski, D. D. Russell, and K. M. Robotti, Boronic acid dyes. US Patent 5,108,502 1991.

206. K. M. Robotti, Cis-diol detection method and solid supports. European Patent EP0596700A1, 1993.

207. E. Schleicher, Method, reagents and equipment for the simple determination of non-enzymatically glycosylated proteins in body fluids. German Patent DE3720736A1 1989.

208. N. DiCesare and J. R. Lakowicz, *Org. Lett.*, 2001, **3**, 3891–3893.

209. K. R. A. S. Sandanayake and S. Shinkai, *J. Chem. Soc. Chem. Commun.*, 1994, **4**, 1083–1084.

210. Y. Okasaka and H. Kitano, *Colloids Surf. B. Biointerfaces*, 2010, **79**, 434–439.

211. Y. Egawa, R. Gotoh, T. Seki, and J. Anzai, *Mater. Sci. Eng. C*, 2009, **29**, 115–118.

212. G. P. Anderson and C. R. Taitt, in *Optical Biosensors: Today and Tomorrow*, eds. F. S. Ligler and C. R. Taitt, Elsevier B.V., 2nd edn., 2008, pp. 83–138.

213. B. Lee, *Opt. Fiber Technol.*, 2003, **9**, 57–79.

214. S. T. Lee, P. S. Kumar, K. P. Unnikrishnan, V. P. N. Nampoori, C. P. G. Vallabhan, S. Sugunan, and P. Radhakrishnan, *Meas. Sci. Technol.*, 2003, **14**, 858–861.

215. E. E. Carlyon, C. R. Lowe, D. Reid, and I. Bennion, *Biosens. Bioelectron.*, 1992, **7**, 141–146.

216. G. Kostovski, P. R. Stoddart, and A. Mitchell, *Adv. Mater.*, 2014, **26**, 3798–3820.

217. N. Ma, P. C. Ashok, D. J. Stevenson, F. J. Gunn-Moore, and K. Dholakia, *Biomed. Opt. Express*, 2010, **1**, 694–705.

218. F. Surre, W. B. Lyons, T. Sun, K. T. V Grattan, S. O'Keeffe, E. Lewis, C. Elosua, M. Hernaez, and C. Barian, *J. Phys. Conf. Ser.*, 2009, **178**, 012046.

219. B. Sciacca and T. M. Monro, *Langmuir*, 2014, **30**, 946–954.

220. E. Borenfreund and J. A. Puerner, *Toxicology*, 1986, **39**, 121–134.

221. A. Burd, C. H. Kwok, S. C. Hung, H. S. Chan, H. Gu, W. K. Lam, and L. Huang, *Wound Repair Regen.*, 2007, **15**, 94–104.

222. J. Goicoechea, C. R. Zamarreño, I. R. Matías, and F. J. Arregui, *Sensors Actuators B Chem.*, 2008, **132**, 305–311.

223. B. M. Cullum and T. Vo-Dinh, *Trends Biotechnol.*, 2000, **18**, 388–393.

224. Y. LeChasseur, S. Dufour, G. Lavertu, C. Bories, M. Deschênes, R. Vallée, and Y. De Koninck, *Nat. Methods*, 2011, **8**, 319–325.

225. R. Segev, J. Goodhouse, J. Puchalla, and M. J. Berry, *Nat. Neurosci.*, 2004, **7**, 1154–1161.

226. W. M. Henry, *Sensors Actuators B Chem.*, 1994, **22**, 101–107.

227. P. N. Moar, S. T. Huntington, J. Katsifolis, L. W. Cahill, A. Roberts, and K. A. Nugent, *J. Appl. Phys.*, 1999, **85**, 3395–3398.

228. R. Lausten, P. Rochon, M. Ivanov, P. Cheben, S. Janz, P. Desjardins, J. Ripmeester, T. Siebert, and A. Stolow, *Appl. Opt.*, 2005, **44**, 7039–7042.

229. D.-S. Choi, H.-K. Kim, and T.-J. Ahn, *Korean J. Opt. Photonics*, 2011, **22**, 67–71.

230. N. A. Logan, *Proc. IEEE*, 1965, **53**, 773–785.

231. M. J. Humphrey, E. Dale, A. T. Rosenberger, and D. K. Bandy, *Opt. Commun.*, 2007, **271**, 124–131.

232. G. Gopalakrishnan, P. Thostrup, I. Rouiller, A. L. Lucido, W. Belkaïd, D. R. Colman, and R. B. Lennox, *ACS Chem. Neurosci.*, 2010, **1**, 86–94.

# Chapter 2: Experimental Methods

This section outlines the experimental techniques used in each of the four research chapters in this work (with a special emphasis on the two published manuscripts). It provides additional detail not described in the short Experimental sections, especially the optical equipment and high pressure apparatus in Chapter 3, and the synthesis and assembly of the inverse opal films and photoactive polymers discussed in Chapter 4.

## 2.1 Pump-Probe Spectroscopy

### 2.1.1 Pump-Probe Basics

The basic principle behind pump-probe spectroscopy is to both induce and monitor the optical changes in a sample using light. This is accomplished by irradiating the sample with two different beams of light: the first beam, the probe, is used to monitor the optical density of the sample over time. This can either be a single wavelength, typically a laser, or a broadband source (either an ordinary incandescent bulb, or supercontinuum), which can give information over any range of wavelengths desired. The probe beam is typically weak, to minimize the influence of the measurement itself on the sample. The second beam, the pump, is considerably stronger (in Chapter 3, approximately $10^5$ times more intense), and is introduced to induce an optical change in the sample: in this work, the change in absorption during *trans-cis* and *cis-trans* photoisomerization in PDR1A.

The intensity of the probe beam is monitored using a detector: here, the detector is a photodiode, which produces a current proportional to the intensity of the light irradiating it via the photoelectric effect. The probe beam in the experiments described here is continuous (excluding the optical chopper: see Section 2.1.1.1 below), but the technique can also be applied to a pulsed laser system, which forms the basis of the widely-used ultrafast version of the same experiment.

#### 2.1.1.1 Optical Chopping

The pump probe experiments described in this thesis are all *single-beam* experiments: the probe beam has no reference beam to account for variations in the background light levels in the area where the experiment occurs. These variations can be minimized by using an optical chopper,

which is a slotted wheel that rotates in the path of the probe beam. As the vanes of the wheel alternately block and pass the probe light at a fixed frequency, the photodetector feeds the resulting square-wave signal into a lock-in amplifier, where it is combined with the frequency information to remove the ambient light (when the beam is blocked) from the real signal (when the beam is allowed to pass).

### 2.1.2 Pump-Probe Experimental

The pump-probe experiments in Chapter 3 were conducted using a custom-built apparatus, depicted in Figure 2.1. All optics and mountings were furnished by Melles Griot and Edmund Optics. The two laser sources were an $Ar^+$-ion operating at 488 nm (Melles Griot) and a frequency-doubled Nd:YAG operating at 532 nm (Dragon Lasers) for the probe and pump beams, respectively. The detector used was a silicon photodiode, sensitive to 400 – 1050 nm light, operating in current output mode (Edmund Optics).

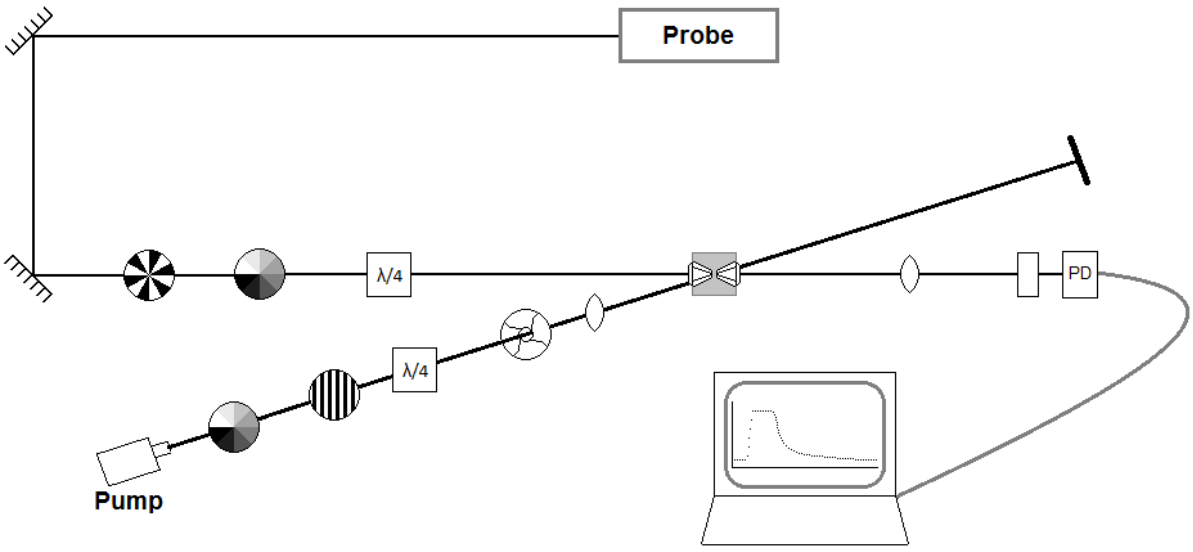


Figure 2.1 Pump-probe setup for measuring thermal azobenzene isomerization rates at high external pressure. The probe beam, at 488 nm, travels through an optical chopper, a variable neutral density filter, and a $\lambda/4$ waveplate before passing through the sample to a photodiode. The pump beam, at 532 nm, also passes through a variable neutral density filter, followed by a linear polarizer, a $\lambda/4$ waveplate, and a shutter before passing through the sample.

The current output from the silicon detector was combined with the chopper signal (Stanford Research Systems) and amplified by a lock-in amplifier (Stanford Research Systems), and the resulting DC signal was processed by a digital-analog converter (National Instruments), and recorded by a custom-programmed LabView routine coded by Dr. Kevin G. Yager.

### 2.1.3 Probe Beam

The PDR1A samples investigated have a visible absorbance maximum around 470 nm (Figure 2.2), which falls near the 488 nm emission of an $Ar^+$-ion laser source. This line was used to monitor the transmittance of the sample.

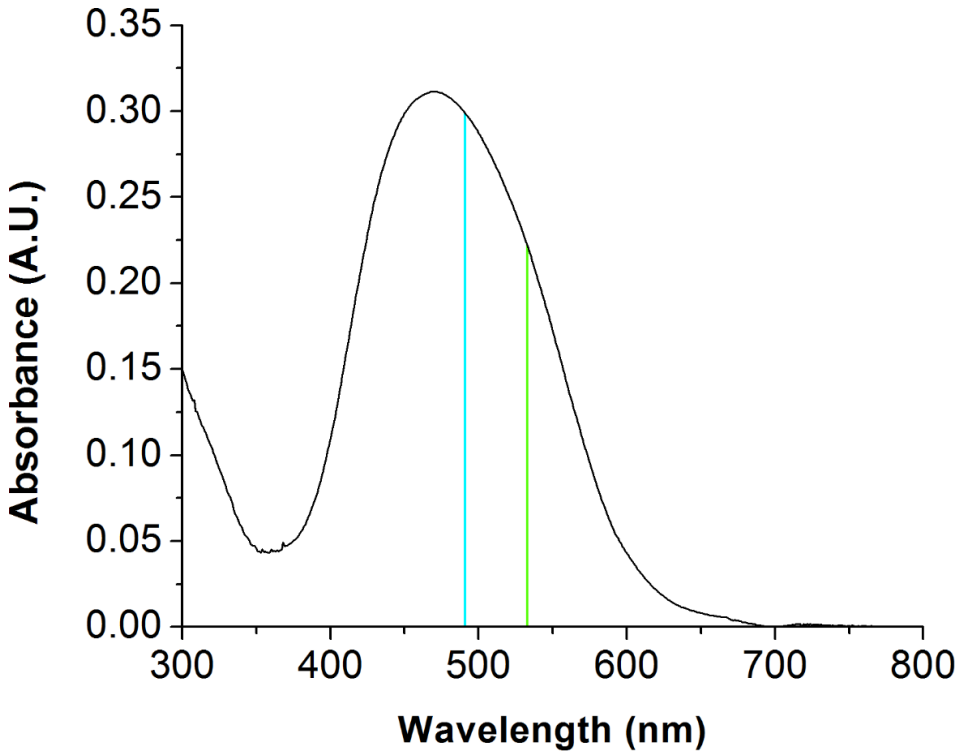


Figure 2.2 The visible absorbance spectrum of PDR1A spin-coated on a glass slide, with a $\lambda_{max}$ at approximately 470 nm. The optical density of this sample is representative of a typical sample used in the diamond anvil cell. The probe line at 488 nm and pump line at 532 nm are superimposed on the spectrum.

The power was typically modulated to between 0.02 – 0.2 $mW \cdot cm^{-2}$ using a variable neutral density filter, which gave a reasonable signal to noise value while minimizing the effect on the sample. The probe beam was initially vertically polarized from the laser source, and was

passed through a $\lambda/4$ waveplate to generate circularly polarized light (to avoid molecular orientation[1,2]). The isotropic nature of circularly polarized light ensures no orientational anisotropy arises in the material while the experiment occurs.

### 2.1.4 Pump Beam

The pump beam was at 532 nm from a frequency-doubled Nd:YAG laser. The beam intensity was modulated with a variable neutral density filter, with a typical intensity of approximately 100 $mW \cdot cm^{-2}$. The intensity of the pump beam was minimized while ensuring a stable photostationary state, to minimize any potential damage to the sample, and was optimized after each pressure adjustment. The pump laser was first passed through a vertical polarizer, followed by a $\lambda/4$ waveplate to generate circularly polarized light, to avoid sample orientation in the same manner as the probe beam.

## 2.2 High-Pressure Measurements

### 2.2.1 The Diamond Anvil Cell

The diamond anvil cell used in this study was furnished by High Pressure Diamond Optics (Tucson, Arizona). The diamonds in the cell were type IIA, which provide the best spectral transmission for Raman spectroscopy due to their low visible absorption and intrinsic fluorescence.[3] The cell used in these experiments was capable of sustaining pressures up to ~4 GPa.

### 2.2.2 Diamond Anvil Cell Sample Preparation

#### 2.2.2.1 Crystalline *trans*- and *cis*-Azobenzene

*trans*-Azobenzene was used as received (Sigma-Aldrich, ≥99% purity by HPLC). *Cis*-azobenzene was generated from the *trans* sample by irradiating a concentrated solution with 365 nm light (Driel 200 W mercury-xenon lamp) for 16 hours at 23 °C. The *cis*-azobenzene was then separated from the *trans* on a silica column with a petroleum ether eluent: the *trans* isomer has a 0 D dipole moment and eluted easily, followed by the pure *cis* fraction eluted with acetone. Most of the solvent was removed under reduced pressure on an ice bath, and the product was isolated as

orange crystals by vacuum filtration and stored at –15 °C in the dark. The purity was verified by thin layer chromatography, which showed no evidence of the *trans*-isomer.

The azobenzene samples were loaded into a 270 μm-thick stainless steel gasket with a 300 μm hole drilled in the centre, mounted on top of the culet of one of the diamond anvils. Ruby chips were added for pressure calibration, and the cell was sealed by placing the other anvil on top. No pressure-transmitting medium was used with the azobenzene samples.

#### 2.2.2.2 Poly(Disperse Red 1 Acrylate) Films

PDR1A films were prepared by drop-casting onto the culet of one diamond anvil. A drop (~1 μL) of PDR1A (Sigma Aldrich) dissolved in THF (HLPC grade, stabilizer free) was dropped onto the culet of one diamond anvil, with the THF being allowed to evaporate between drops. This process was repeated until a uniform film with an optical density (O.D.) of ~1.5 was formed. This O.D. value was found to yield the best signal to noise ratio. The commercial PDR1A used was low molecular weight, with 100% chromophore loading (i.e. a homopolymer of Disperse Red 1 acrylate).

The DAC was assembled with the polymer-coated anvil on the bottom, followed by a 270 μm-thick stainless steel gasket with a 300 μm hole drilled in the centre. At least one ruby chip was added on top of the film, then the remaining void volume was filled with glycerol to act as a pressure-transmitting medium before the cell was sealed with the second diamond anvil.

### 2.2.3 High Pressure Experiments

For both the Raman and the kinetic pump-probe experimental series, the same general procedure was followed. Once the samples were prepared in the DAC, as outlined in Section 2.2.2, the cell was allowed to equilibrate for a minimum of 20 minutes. The pressure was then determined by measuring the ruby fluorescence, described in the next section. Finally, the experiment was performed (either Raman or kinetic pump-probe). The pressure was then incremented, and the process repeated until the desired maximum pressure was reached.

#### 2.2.3.1 Pressure Determination

Fluorescence spectra to determine the pressure inside the DAC via the ruby fluorescence method described in the Introduction were acquired using the Raman spectrometer.[4] The excitation source at 514 nm was focussed on the ruby calibrant with the Raman microscope. The acquisition window was approximately 20 nm, centred at 694 nm to capture the characteristic ruby doublet. The peak value of the $R_1$ band (the more intense of the two) was analyzed and recorded using the provided WiRE software.[5] The $\lambda_{max}$ of $R_1$ was then converted into a pressure value using Equation 1.1, as described in Section 1.2.2 of Chapter 1.

### 2.2.4 Raman Spectroscopy at High Pressure

Raman experiments were conducted using an inVia Renishaw Raman microscope spectrometer equipped with a CCD detector and two laser sources (514 nm visible $Ar^+$-ion and 785 nm NIR diode). Spectra acquired with the 514 nm excitation source used a holographic notch filter to remove the excitation light, and a 2400 line/mm diffraction grating; spectra acquired with the 785 nm excitation source used an edge filter, and a 1200 line/mm diffraction grating. The 514 nm laser was kept between 0.15 – 1.5 mW, while the 785 nm source was varied between 3 – 30 mW to avoid burning damage to the sample. The spectrometer was calibrated prior to each measurement by performing an offset correction referencing to the silicon phonon mode centred at 520 $cm^{-1}$. The DAC was mounted under the Raman microscope using a custom-built mount connected to the microscope's x-y-z translation stage. A long-working-distance 20× objective was used in all cases.

#### 2.2.4.1 Raman Spectroscopy of *cis*-Azobenzene

Because *cis*-azobenzene was found to photoisomerize when exposed to the 514 nm laser source, measurements were made with the 785 nm source when acquiring Raman spectra at different pressures. For the photoisomerization studies, the sample was divided into five sections: a Raman spectrum was acquired with the 785 nm source, followed by irradiation with the isomerizing 514 nm source and a second Raman spectrum acquired, and finally a Raman spectrum was acquired on the same spot with the 785 nm source. A different spot was used at each subsequent pressure, to assess the ability of *cis*-azobenzene to undergo photoisomerization at different external pressures.

### 2.2.5 Pump-Probe Experiments at High Pressure

The pump-probe apparatus described in Section 2.1 yields a signal equal to the amount of light passed by the sample, which is proportional to the optical density of the sample. In solution, azobenzene derivatives undergo first-order relaxation from the *cis*-isomer back to the *trans*, as it is a monomolecular process. This is also true in the solid phase, however the restricted chemical environment of the chromophores results in a variety of rate constants.[6,7] A pseudo-first order rate constant can be extracted by ignoring the first small portion of kinetic data, as demonstrated in Chapter 3.[8] The expression for extracting the first-order rate constant can be derived from the Beer-Lambert relation (Equation 2.1):

$$A = \varepsilon l c = \alpha c \qquad \text{Equation 2.1}$$

where the $\alpha c$ term is a simplified expression combining the path length and molar absorptivity, which are assumed to be constant. The expression for the total absorbance at an arbitrary time ($A_t$) of a sample containing some amount of *trans*- and *cis*-azobenzene chromophores as a simple sum of the individual absorbance values:

$$A_t = A_{cis} + A_{trans} \qquad \text{Equation 2.2}$$

The $A_{cis}$ and $A_{trans}$ variables can be further expanded to give two expressions including the time-dependence of the concentration of the *cis*-isomer:

$$A_{cis} = \alpha_{cis}[cis]_0 e^{-kt} \quad \text{for } cis$$
$$A_{trans} = \alpha_{trans}([trans]_\infty - [cis]_0 e^{-kt}) \quad \text{for } trans \qquad \text{Equation 2.3}$$

where $\alpha_{cis}$ and $\alpha_{trans}$ are the reduced molar absorptivity expressions for the *cis*- and *trans*-isomers, $[trans]_\infty$ is the concentration of *trans*-isomer at infinite time (equal to the total concentration of chromophores in the sample), $[cis]_0$ is the concentration of *cis*-isomer in the photostationary state (the maximum concentration of *cis* possible in the sample), and $e^{-kt}$ is the time-dependent term for a first-order kinetic process. Combining the terms of Equation 2.3 into Equation 2.2 gives:

$$A_t = \alpha_{cis}[cis]_0 e^{-kt} + \alpha_{trans}([trans]_\infty - [cis]_0 e^{-kt}) \qquad \text{Equation 2.4}$$

Expanding terms gives:

$$A_t = (\alpha_{cis} - \alpha_{trans})[cis]_0 e^{-kt} + \alpha_{trans}[trans]_\infty \quad \text{Equation 2.5}$$

Combining terms, recognizing that the $\alpha_{trans}[trans]_\infty$ term is the definition of $A_\infty$:

$$A_t = (\alpha_{cis} - \alpha_{trans})[cis]_0 e^{-kt} + A_\infty \quad \text{Equation 2.6}$$

Finally, rearranging terms and taking the natural logarithm yields:

$$\ln(A_t - A_\infty) = -kt(ln[(\alpha_{cis} - \alpha_{trans})[cis]_0]) \quad \text{Equation 2.7}$$

from which a plot of $\ln[A_\infty - A_0]$ as a function of time gives a linear expression with $-k$ as the slope. Because the experimental setup is single-beam (*i.e.*, it does not have a reference beam), the real optical density of the sample is not known. Instead, only the transmitted intensity, $I$, can be measured, which is related to the optical density (absorbance) by the form of the Beer-Lambert relation given in Equation 2.8:

$$A = -\ln\left(\frac{I}{I_0}\right) \quad \text{Equation 2.8}$$

where $A$ is the absorbance (optical density), proportional to the product of the concentration of the absorber ($c$), the path length ($l$), and the molar absorptivity of the absorber ($\varepsilon$). The optical density is also equal to the negative natural logarithm of the transmitted intensity ($I$), divided by the intensity of the incident beam ($I_0$). Although $I_0$ is not directly measured in this experiment, it is not required to treat the data:

$$A_\infty = -\ln\left(\frac{I_\infty}{I_0}\right) \text{ and } A_t = -\ln\left(\frac{I_t}{I_0}\right) \quad \text{Equation 2.9}$$

Taking the difference between the two expressions:

$$A_\infty - A_t = \left(-\ln\frac{I_\infty}{I_0}\right) - \left(-\ln\frac{I_t}{I_0}\right) \quad \text{Equation 2.10}$$

And rearranging the logarithms:

$$A_\infty - A_t = \big(\ln(I_t) - \ln(I_0)\big) - \big(\ln(I_\infty) - \ln(I_0)\big) \quad \text{Equation 2.11}$$

Combining terms leaves behind the final expression, free of $I_0$:

$$A_\infty - A_t = \ln(I_t) - \ln(I_\infty) \qquad \text{Equation 2.12}$$

showing that the natural logarithm of this expression is the ordinate value in the linear plot of ln[$A_\infty - A_t$] vs. time, which does not depend on the value of $I_0$.

## 2.3 Ultraviolet-Visible Absorption Spectroscopy

### 2.3.1 Instrumentation

Three different configurations of spectrometer were used in this work: an Agilent Cary 100 UV-vis dual-beam spectrophotometer (Chapter 5), a microscope-mounted Ocean Optics USB2000 single beam spectrophotometer set up for reflectance measurements (Chapter 4) and a fibre-coupled Ocean Optics USB2000 single beam spectrophotometer for the analysis of fibre probes (Chapter 6).

#### 2.3.1.1 Solution-Phase Absorbance Measurements

Solution-phase samples were analyzed using the Cary instrument, which yields the most accurate values of absorbance and peak maximum in both the solution phase, as well as thin films coated onto microscope slides. The Cary spectrometer was equipped with a temperature-controlled cuvette stage, which was set to 21.0 °C for all binding constant determinations. Liquid samples were analyzed in Spectrosil quartz cuvettes with 10 mm path length and a spectral range of 170 – 2700 nm (Starna Cells). The instrument was zeroed before each set of runs, and a baseline correction was acquired using the same solvent as the sample solution. Measurements were referenced to the paired cuvette containing the same solvent as the sample.

#### 2.3.1.2 Thin Film Absorbance Measurements

Thin film samples, such as the PDR1A polymer described in Chapter 3, were analyzed on clean glass microscope slides (FisherBrand Economy plain glass) by spin-coating the solution-phase polymer. The coated slides were analyzed using a slide-holder mount in the instrument, and references to a clean slide from the same lot where possible.

#### 2.3.1.3 Fibre Absorbance Measurements

Absorbance measurements made on fibre optics via the evanescent wave are described in more detail in the Experimental section of Chapter 6.

## 2.4 Inverse Opal Films

### 2.4.1 Substrate Preparation

IOFs were prepared on P-type silicon [100] wafers (University Wafer), cut into 1 cm-wide strips. Immediately prior to use, substrates were cleaned by immersion in 3:1 concentrated sulfuric acid/30% hydrogen peroxide, while heating for 30 minutes. The wafers were then rinsed with 18.2 MΩ·cm water and dried under a stream of air.

### 2.4.2 Inverse Opal Film Synthesis

Large-area crack-free inverse opal films were fabricated using the technique first reported in Reference 9, and used extensively by the Aizenberg group as reported in References 10 – 13. A suspension of monodisperse poly(methylmethacrylate) microspheres in a solution of silica precursor was slowly evaporated onto an immersed substrate. A thin film of silica with ordered PMMA microspheres was left behind, and the film was then calcined to remove the polymer sphere template.

#### 2.4.2.1 Monodisperse PMMA Microspheres

PMMA microspheres were synthesized by surfactant-free emulsion polymerization, as described in References 9 and 14. 90 mL deionized water and 0.2 g ammonium persulfate were added to a 500 mL round bottom flask equipped with a reflux condenser and stir bar. The flask was heated to 80 °C in an oil bath, and the solution was stirred at 400 rpm for a minimum of one hour. Separately, 10.5 mL methyl methacrylate, 0.0948 mL ethylene glycol dimethacrylate, and 0.0473 mL 1-decanethiol were combined in a vial and sonicated for 5 minutes. The monomer mixture was then injected into the round bottom flask as rapidly as possible, while minimizing the disturbance to the solution. The combined monomer and initiator solution was then allowed to stir at 80 °C for 5 – 6 hours, until the suspension became opaque and white.

The crude colloidal suspension was allowed to cool, then poured into a dialysis bag and dialyzed in a 2 L beaker filled with deionized water while slowly stirring. The dialysis was allowed to run for 7 days, with the water being changed every 24 hours. The monodispersity of the microspheres was then verified by allowing a droplet of suspended spheres to dry on a glass slide. The presence of iridescence in the resulting film indicates a high degree of monodispersity, owing to the high sensitivity of the optical phenomenon to the regularity of the crystal elements. The spheres used in this study had a diameter of 300 nm, with a 3% standard deviation.

#### 2.4.2.2 Opal Film Synthesis

Opaline films were fabricated by combining the PMMA microsphere suspension with a pre-hydrolyzed silane solution, followed by evaporation onto a silicon wafer. The silane solution was prepared by mixing 5.0 mL of 0.01 M HCl, and 9.5 mL ethanol in a 25 mL vial, along with a magnetic stir bar. To this solution was added 5.0 g tetraethoxysilane. The resulting solution was stirred for 1 hour at 300 rpm to allow the silane to hydrolyze.

The colloidal suspension was sonicated to ensure good dispersion. Approximately 0.2 mL of the colloidal suspension was mixed with 20 mL deionized water in a 25 mL vial, followed by 0.95 mL of the TEOS solution from the previous section. A piece of pre-cleaned silicon wafer (Section 2.4.1) was suspended vertically in the solution, and the vial was placed in a 65 °C oven on a vibration-free table. The solution was allowed to evaporate completely, leaving behind opaline films.

#### 2.4.2.3 Inverse Opal Film Synthesis

The silicon wafers coated with the opaline films were placed, polished side up, in a muffle furnace. The temperature was increased from ambient temperature to 500 °C over five hours, held at that temperature for 2 hours, and then allowed to cool back to room temperature over one hour. This process oxidized the polymer microspheres, leaving behind a network of interconnected holes surrounded by a silica matrix.

### 2.4.3 Multilayering on Inverse Opal Films

The multilayering procedure here differ only from the general procedure described in Section 2.6 below in the amount of time the substrates were immersed in the polyelectrolyte

solutions. The immersion time was increased to compensate for the slower diffusion of polyelectrolytes into the complex architecture of the IOFs. IOFs were cleaned by immersing samples in 'acid piranha' (3:1 concentrated sulfuric acid: 30% hydrogen peroxide solution) and heating for 30 minutes. The samples were then rinsed well with water and allowed to dry in air. IOFs were surface-functionalized prior to multilayering with an amine-terminated silane, to give the surface a positive charge. Cleaned IOFs were immersed in a 2% w/v solution of (3-aminopropyl)trimethoxysilane (APTMS: Figure 2.1 A) in acetone for 30 minutes, then rinsed thoroughly with water and allowed to dry.

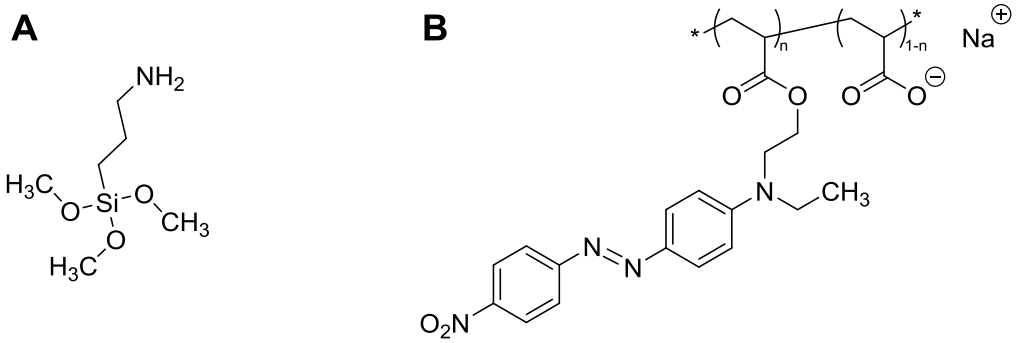


Figure 2.3 A) (3-aminopropyl)trimethoxysilane, used to impart a positive charge on the silica surface of the IOFs. B) poly(Disperse Red 1 acrylate–*co*–acrylic acid).

The surface-functionalized IOFs were then immersed in a saturated solution of poly(Disperse Red 1 acrylate–*co*–acrylic acid), Figure 2.3 B, in a 1:1 mixture of DMF/water. The DMF was necessary to ensure solubility of the polymer, as well as completely wet the internal structure of the IOF. The IOFs were allowed to sit in the polymer solution for 8 hours, which gave a stable final colour to the structure, and ensured a thermodynamically stable polymer layer was deposited. The IOFs were then rinsed twice for one hour in fresh 1:1 DMF/water solution to ensure any excess polymer was removed.

## 2.5 Synthesis

### 2.5.1 General Considerations

Specific synthetic procedures for individual compounds are given in the Supplementary Information of their corresponding chapter. Except where noted, water used was always 18.2

MΩ·cm, from a Millipore Milli-Q Academic water filtration unit. Solvents were used as received, and supplied by either Caledon or Fisher Scientific.

### 2.5.2 Purification

Indicator molecules were typically purified by HPLC due to the highly polar boronic acid and amine functional groups. As a result, yields reported in Chapters 5 and 6 are the crude yield, prior to HPLC purification.

#### 2.5.2.1 Flash Chromatography

Flash chromatography was performed automatically using a Teledyne Isco CombiFlash Companion $R_f$, with dual detection at 254 and 280 nm. Typically, samples were loaded by evaporating a solution of crude product onto Celite 545 (Fisher Scientific) under reduced pressure, and placed above the column using a solid-loading attachment; where noted, the sample was injected directly onto the column as a solution in toluene. Columns were pre-packed SiliaSep™ silica columns, 40 – 63 μm particle size with 60 Å pores (SiliCycle). The mobile phase was either a gradient of EtOAc in hexanes (Fisher Scientific, ACS grade), or MeOH in DCM (Fisher Scientific, ACS grade) for more polar compounds.

#### 2.5.2.2 High Performance Liquid Chromatography

High performance liquid chromatography (HPLC) was found to be the most effective method of purification for the highly polar azobenzene derivatives with both amine and boronic acid moieties. Separations were performed using an Agilent 1260 Infinity system, running OpenLab CDS ChemStation Edition control software. Fractions were detected using a diode array detector, acquiring at 300 and 550 nm (±2 nm), referenced to the absorption at 800 nm (±25 nm).

All separations were performed using a YMC AQ12S05 C18 250×10 mm semi-preparative column, with 5 μm beads and 120 Å pore diameters. Typically, separations were run over 50 minutes, with a 32 minute gradient of ACN in 18.2 MΩ·cm water plus purge cycle. The specific gradient conditions were optimized for each compound, and can be found in the Experimental section in Chapter 4. Samples were dissolved in HPLC-grade MeOH (Fisher Scientific) and filtered through a 0.22 μm PTFE syringe filter (Wyvern Scientific) prior to injection.

### 2.5.3 Characterization Methods

#### 2.5.3.1 Mass Spectrometry

High-resolution mass spectra were acquired on a Bruker Maxis Impact Quadrupole-Time of Flight mass spectrometer, with a source voltage of 4.5 kV. The boronic acid derivatives described in Chapter 5 were typically observed as the dimethyl ester of the parent, plus a sodium ion.

#### 2.5.3.2 Nuclear Magnetic Resonance Spectroscopy

$^{1}$H NMR spectra were acquired using either 500 or 400 MHz Bruker instrument, or a 400 MHz Varian spectrometer. $^{13}$C spectra were acquired with a Varian 75 MHz instrument. The $^{13}$C signal from the carbon atom directly attached to boron atoms was often absent, as has been noted in the literature, likely due to quadrupolar relaxation.[15,16]

Proton-detected heteronuclear single quantum coherence (HSQC) and heteronuclear multiple quantum coherence (HMQC) pulse sequences were used to acquire carbon chemical shift data for the boronic acid compounds, where the amount of sample available was insufficient for a direct $^{13}$C measurement. The HSQC pulse sequence detects $^{13}$C signals directly connected to $^{1}$H atoms, while the HMBC sequence yields $^{13}$C signals from atoms up to 3 bonds away from a $^{1}$H atom: the combination of the two techniques yields a complete set of $^{13}$C data for these compounds.

#### 2.5.3.3 Gel Permeation Chromatography

Gel permeation chromatography was used to determine the molecular weight range of synthesized polymers. Measurements were performed using an Agilent GPC 50 instrument (Agilent/PolymerLab), equipped with two analytical columns (mix beds, PolyAnalytik) and guard column. Calibration was performed with polystyrene standards from PolyAnalytik. Runs were performed at 30 °C, with 1 mL·min$^{-1}$ flow of HPLC-grade THF.

### 2.5.4 Polymerization Reactions

The acrylate polymers used in Chapters 4 (poly(Disperse Red 1 acrylate-*co*-acrylic acid)) and 6 (boronic acid-functionalized azobenzene acrylate/acrylic acid copolymers) were synthesized

via free-radical polymerization, thermally initiated with azobisisobutyronitrile (see Figure 2.4 below).

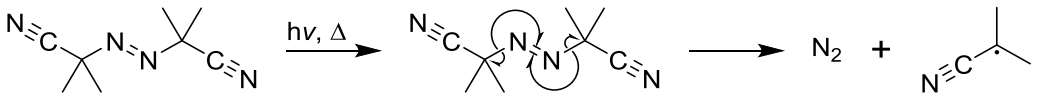


Figure 2.4 Azoisobutyronitrile (AIBN) radical generation for free-radical polymerization. AIBN (left) undergoes homolytic cleavage either thermally or photochemically according to the mechanism in the centre, yielding one equivalent of nitrogen gas and two equivalents of 2-cyanoprop-2-yl radical.

AIBN undergoes homolytic cleavage to form two 2-cyanoprop-2-yl radicals, which has an approximately 10-hour half-life at 60 °C.[17] The radicals go on to attack the acrylate monomers according to the scheme in Figure 2.5. The radical attacks the double bond on an acrylate group (R = OH, azo), forming a new C-C bond and migrating the radical to the acrylate group. The new acrylate radical attacks another acrylate group, and the reaction propagates until termination by another 2-cyanoprop-2-yl radical, a second growing polymer chain radical, or other contaminant present in the polymerization flask.

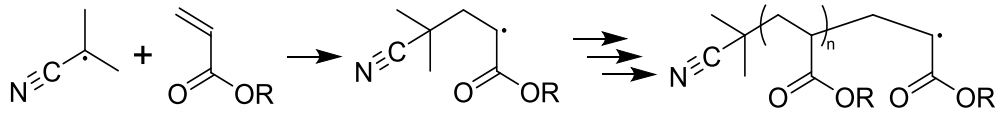


Figure 2.5 Polymerization initiation by the 2-cyanoprop-2-yl radical. After an initial attack of the radical on an acrylate group (initiation), the acrylate radical then attacks other acrylates in the propagation phase. Propagation continues until termination, which can be another 2-cyanoprop-2-yl radical, or a contaminant such as oxygen.

Thermally-initiated free-radical polymerization is a facile method of generating polymers, and works well for acrylate derivatives. Molecular weights of the resulting polymers tend to be relatively low, and the polydispersity indices (PDIs) are often high. Although these factors are important for typical polymers due to their effect on the material properties of bulk samples, the same is not true for polymers used to construct polyelectrolyte multilayers. Above a relatively small polymer weight, stable polyelectrolyte adsorption is achieved, and the material properties

(modulus, charge, water content) are determined primarily by the assembly conditions (pH, ionic strength, polymer $pK_a$) rather than the molecular weight or PDI.[18–20]

Polymer purification was accomplished in the current work by precipitation, since column chromatography was not possible. The polymer was dissolved in a minimum of favourable solvent, then precipitated by slow addition of the polymer solution to a rapidly stirring beaker containing excess (*ca.* 200× v/v) of an unfavourable solvent for the polymer. The relatively higher solubility of the monomer in the second solvent results in the removal of residual monomer and oligomers from the polymer, and the pure solid was then recovered by vacuum filtration.

## 2.6 Polyelectrolyte Multilayers

Polyelectrolyte multilayers were assembled on various substrates in Chapters 4 and 6. Substrates were cleaned by immersion in 'acid piranha' solution (3:1 concentrated sulfuric acid/30% hydrogen peroxide) for 30 minutes, followed by rinsing with water prior to polyelectrolyte assembly. The negatively-charged substrate generated by the piranha cleaning was then immersed in a $10^{-2}$ M solution of cationic polyelectrolyte (concentration calculated by monomer), typically with $10^{-2}$ M sodium chloride to keep the ionic strength approximately equal between solutions (ionic strength varies slightly due to the pH adjustment). Substrates were immersed in the polyelectrolyte solution for 10 minutes, followed by three washes in pH-adjusted water to remove excess polymer. The sequence was then repeated in the anionic solution. Section 1.4.1 in Chapter 1 outlines the theory of polyelectrolyte multilayer assembly.

### 2.6.1 Multilayer Thickness Measurements

Null ellipsometry was used to measure the thickness of the polyelectrolyte multilayers, where possible. Ellipsometry is not an accurate method of measurement on substrates with complex geometries such as the IOFs discussed in Chapter 4 and the fibre optic probes in Chapter 6 instead, films were fabricated on clean P-type silicon [100] wafers (University Wafer) in parallel with the other substrates. Silicon wafers are suitably flat to allow for ellipsometric measurements to be useful, and the films deposited on the silicon substrates serve as a good analogue to the other surfaces.

#### 2.6.1.1 Null Ellipsometry

Thickness measurements by null-ellipsometry were performed using a Gaertner Scientific L2W16D.830 single-wavelength ellipsometer. Measurements were made on single crystal silicon substrates to ensure adequate substrate flatness. The similar surface chemistry of silicon and glass (silica) substrates allows thickness on glass substrates to be considered the same as those measured on silicon.

#### 2.6.1.2 Thickness of PDR1A on IOFs

The PDR1A-*co*-AA layers applied to the IOFs were only a single layer, and proved too thin to measure directly with ellipsometry. Instead, a series of bilayers (PDR1A-*co*-AA/PDADMAC) were fabricated, and the thickness was measured every 5 bilayers. This gives an approximately linear plot of film thickness as a function of the number of bilayers (Figure 2.6), with a slope of 2.6 nm·bilayer$^{-1}$. The single layers used in the bleaching experiments were thus determined to be on the order of 1 nm thick.

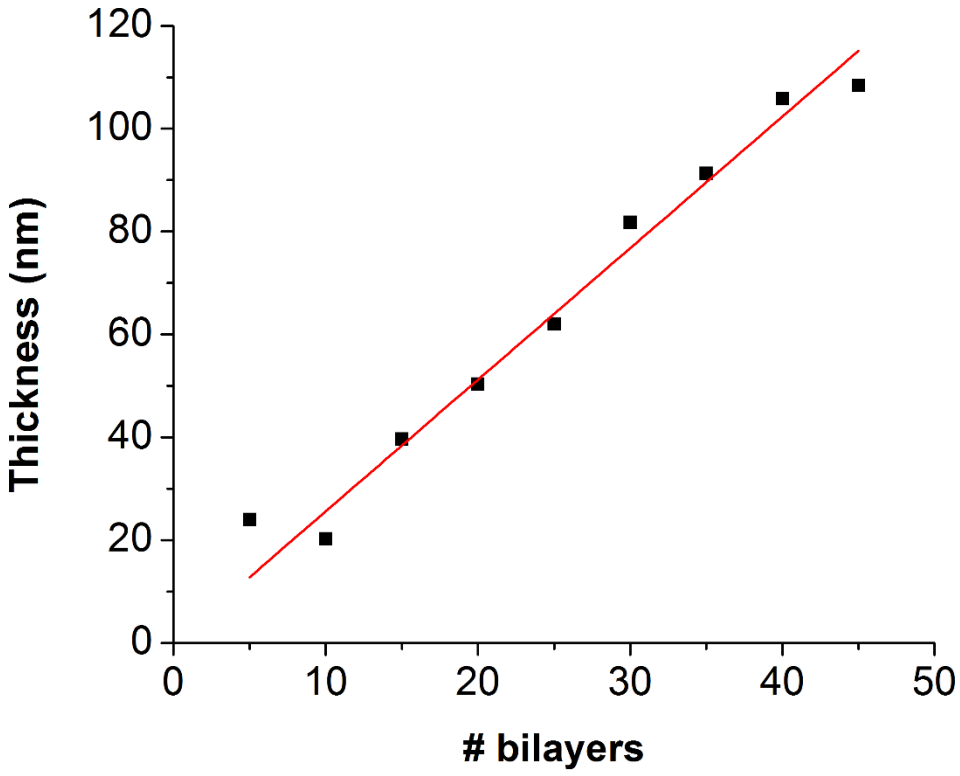


Figure 2.6 Plot of film thickness as a function of the number of bilayers deposited.

## 2.7 References


1. C. J. Barrett, A. Natansohn, and P. Rochon, *Macromolecules*, 1994, **27**, 4781–4786.

2. R. Hagen and T. Bieringer, *Adv. Mater.*, 2001, **13**, 1805–1810.

3. J. R. Ferraro, *Vibrational Spectroscopy at High External Pressures: The Diamond Anvil Cell*, Academic Press, Inc., Orlando, 1984.

4. H. K. Mao, P. M. Bell, J. W. Shaner, and D. J. Steinberg, *J. Appl. Phys.*, 1978, **49**, 3276–3283.

5. *WiRE*, version 2.0 service pack 6; Renishaw plc: Wotton-under-Edge, Gloucestershire, U.K., 2002.

6. T. Naito, K. Horie, and I. Mita, *Macromolecules*, 1991, **24**, 2907–2911.

7. C. J. Barrett, A. Natansohn, and P. Rochon, *Chem. Mater.*, 1995, **7**, 899–903.

8. T. A. Singleton, K. S. Ramsay, M. M. Barsan, I. S. Butler, and C. J. Barrett, *J. Phys. Chem. B*, 2012, **116**, 9860–9865.

9. B. Hatton, L. Mishchenko, S. Davis, K. H. Sandhage, and J. Aizenberg, *Proc. Natl. Acad. Sci.*, 2010, **107**, 10354–10359.

10. I. B. Burgess, N. Koay, K. P. Raymond, M. Kolle, M. Lončar, and J. Aizenberg, *ACS Nano*, 2012, **6**, 1427–1437.

11. K. P. Raymond, I. B. Burgess, M. H. Kinney, M. Lončar, and J. Aizenberg, *Lab Chip*, 2012, **12**, 3666–3669.

12. X. Yao, Y. Hu, A. Grinthal, T.-S. Wong, L. Mahadevan, and J. Aizenberg, *Nat. Mater.*, 2013, **12**, 1–6.

13. I. B. Burgess, M. Lončar, and J. Aizenberg, *J. Mater. Chem. C*, 2013, **1**, 6075–6086.

14. I. B. Burgess, Ph.D. Thesis, Harvard University, 2012.

15. C. J. Ward, P. Patel, and T. D. James, *J. Chem. Soc. Perkin Trans. 1*, 2002, 462–470.

16. Y. Egawa, R. Gotoh, S. Niina, and J. Anzai, *Bioorg. Med. Chem. Lett.*, 2007, **17**, 3789–3792.

17. J. Brandrup, E. H. Immergut, and E. A. Grulke, Eds., *Polymer Handbook*, John Wiley & Sons, Inc., New York, 4$^{th}$ edn., 1999.

18. R. N. Smith, M. McCormick, C. J. Barrett, L. Reven, and H. W. Spiess, *Macromolecules*, 2004, **37**, 4830–4838.

19. M. McCormick, R. N. Smith, R. Graf, C. J. Barrett, L. Reven, and H. W. Spiess, *Macromolecules*, 2003, **36**, 3616–3625.

20. R. N. Smith, L. Reven, and C. J. Barrett, *Macromolecules*, 2003, **36**, 1876–1881.

21. N. M. Ahmad, M. Saqib, and C. J. Barrett, *J. Macromol. Sci. Part A*, 2010, **47**, 106–118.

22. S. E. Burke and C. J. Barrett, *Macromolecules*, 2004, **37**, 5375–5384.

23. B. Sciacca and T. M. Monro, *Langmuir*, 2014, **30**, 946–954.

## Rationale for: Azobenzene Photoisomerization Under High External Pressures: Testing the Strength of a Light-Activated Molecular Muscle

The *trans-cis* isomerization of azobenzene derivatives has been extensively investigated and exploited in the scientific literature, as outlined in the Introduction section. The ability to measure and quantify the extent of this process, as well as the rate at which it occurs, is interesting from a fundamental perspective, and essential if the molecules are to be used as a photoswitch. Chapter 3 of this work, which was published in the Journal of Physical Chemistry B under the title "Azobenzene Photoisomerization under High External Pressures: Testing the Strength of a Light-Activated Molecular Muscle," investigates the effect of external pressure on the isomerization behaviour of a polymeric azobenzene derivative.

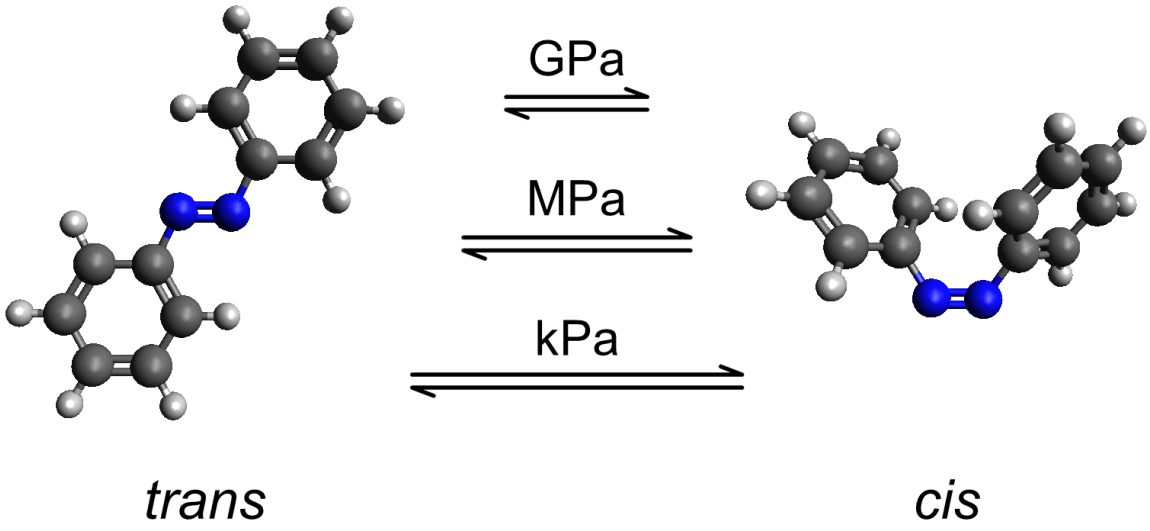

# Chapter 3: Azobenzene Photoisomerization Under High External Pressures: Testing the Strength of a Light-Activated Molecular Muscle

## 3.1 Abstract

The photo-induced isomerization and thermal back relaxation of an azobenzene-functionalized polymer poly(Disperse Red 1 acrylate) were investigated at increasing external pressures up to 1.5 GPa inside a diamond-anvil spectroscopic cell. The thermal *cis*-*trans* isomerization was monitored by laser pump-probe spectroscopy, which demonstrated an increase in the half-life of the isomerization process with increasing pressure. Additionally, the *cis* content of the photostationary state gradually decreased as a function of pressure, with complete arrest of the *trans*-*cis* photoisomerization above 1.5 GPa. The fact that the photoswitching behaviour however could still be observed beyond 1 GPa is remarkable, and is effectively a measure of the strength of the azobenzene chromophore as an artificial muscle. The changes in the Raman shifts of both *trans*- and *cis*-azobenzene were also investigated from ambient pressure up to 4 GPa and no discontinuities were observed in the pressure *vs*. wavenumber plots indicating no change in phase. The *cis*-*trans* photoisomerization of azobenzene was shown however to still be inducible at all the pressures investigated, confirming the suitability of these molecules for high efficiency light actuation.

## 3.2 Introduction

At the heart of all members of the large family of azo-aromatic chromophores is the parent azobenzene molecule, which consists of two benzene rings joined by an N=N double bond. These molecules are ubiquitous in everyday life, forming the core of more than 70% of commercial dyes owing to their vibrant, chemically tuneable colours, and extreme durability even upon continuous irradiation.[1,2] Most recently, azo compounds have also been the subject of numerous photo-switching studies by the chemistry, physics, and engineering communities because of their wide-ranging photochemical and photophysical properties. Upon irradiation with a suitable wavelength of light (in the UV or visible), a change from the stable *trans*-isomer to the metastable *cis*-isomer

is induced, a process which can be reversed either photochemically or thermally. This reversible geometric effect was first noted in 1937 by Hartley, when he observed that the solubility of azobenzene changed upon irradiation.[3] Except for some special cases where isomerization is extremely sterically hindered,[4,5] essentially all azobenzene derivatives are capable of undergoing this reversible *cis*-*trans* photoisomerization (Figure 3.1 A).

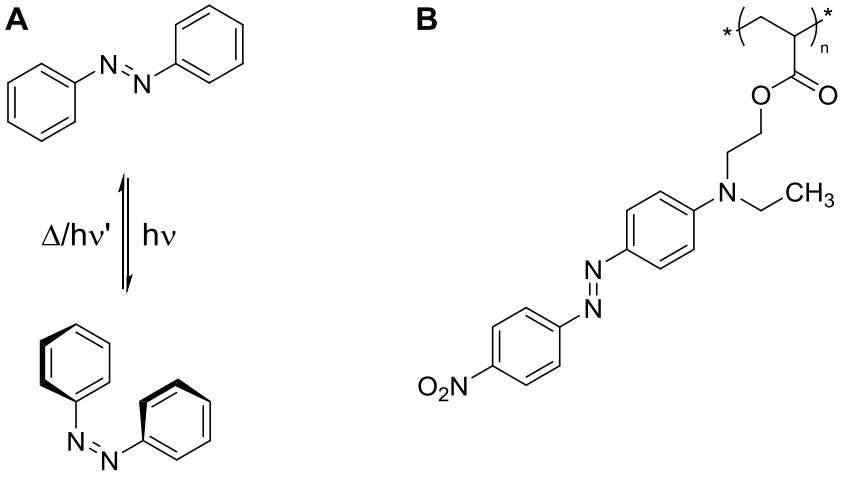


Figure 3.1 The two azobenzene chromophores investigated in this study: A) *trans*-(*Z*)-azobenzene, on the top left, adopts a planar geometry, while the benzene rings on *cis*-(*E*)-azobenzene are skewed out of plane[6] B) PDR1A, on the right, consists of the Disperse Red 1 chromophore bound to a polymeric acrylate backbone.

Although influenced somewhat by the electronic and steric effects of particular derivatives, the same basic geometry is present in most azo-containing molecules.[7] Of most recent interest, in addition to the microscopic change in molecular structure, isomerization has now been developed to induce large-scale secondary effects in polymers and materials containing azo-chromophores. These effects vary in sizescale and magnitude, ranging from the molecular lengthscale as light power for molecular machines,[8–10] through to macroscopic formation of micron sized surface patterns upon irradiation,[11,12] and even deformation of coated substrates to transfer mechanical work as layers of 'artificial muscles' actuating over many centimetres.[13,14] Despite these many recent applications however, there remains great uncertainty over the basic mechanism of photo-mechanics, and even the isomerization itself, and the limits of how much light energy can be harvested and transduced. Until there is a far more complete set of basic physical measurements into the effect, materials cannot be optimized for any of these applications.

In this pressure study, we examined both the simple parent molecule azobenzene, and one of the most successful photo-switch derivatives, poly(Disperse Red 1 acrylate) (PDR1A; structure depicted in Figure 3.1 B), based on the Disperse Red 1 azo dye. The simple parent azobenzene molecule receives less attention in recent material applications, but is well suited for fundamental studies into its isomerization mechanism and due to its structural simplicity is valuable as a starting point for new spectroscopic techniques. Azobenzene also exhibits a very slow thermal *cis*-*trans* reconversion rate relative to most functionalized derivatives, allowing the most facile investigation of the *cis* form by Raman spectroscopy under pressure at ambient temperature conditions, since these experiments require samples to be stable for hours. PDR1A is a more recent azo derivative polymer material that was developed in the 1990s and widely applied to optic, photonic, and holographic applications owing to its fast switching, photo-refractivity, photo-reorientation and stability as a data-storage medium. It was developed to optimize optical properties and speed and efficiency of photo-switching, necessary for the transmission-based kinetics measurements reported here: thermal reconversion rates are on the order of seconds. This allows for a substantial amount of kinetic data to be acquired in a relatively short timeframe without requiring the use of ultrafast laser equipment. The absorption spectrum of PDR1A is also amenable to pump-probe kinetic measurements at convenient and non-interfering wavelengths in the visible—the peak absorbance is a broad feature at approximately 480 nm in the solid phase—making the choice of pump and probe wavelengths straightforward and not requiring the added complication of UV light sources.

Mass surface migration of azo thin films upon irradiation with isomerizing wavelengths of light is another fascinating and curious effect unique to azo-functionalized materials.[15–19] Pressure has been implicated as the leading mechanism by which repeated isomerization could induce macroscopic movement of the material, yet more fundamental studies are needed.[20,21] The free volume requirement for isomerization to proceed is larger than the volume of either the *trans* or *cis*-azo chromophore,[22–24] and thus isomerization occurring in free volume pockets in the host material smaller than this isomerization requirement can generate a local pressure. A chromophore birefringence study of the effect of pressure up to 0.2 GPa on information storage ability in an azo-doped polymer was reported by Sekkat *et al.*, which noted a retardation in the rate of orientation at these moderate pressures: another study by this group also suggested the onset of isomerization hindrance in this modest pressure regime.[25,26] We report here the results of a full high-pressure

visible and Raman spectroscopic study of the basic process (up to 4GPa) of the thermal and photo-induced *cis-trans* isomerization of the azobenzene molecule**,** as well as an examination of the kinetics of the *cis-trans* thermal isomerization of PDR1A under pressure.

## 3.3 Experimental Section

### 3.3.1 Raman Measurements

Raman spectra were obtained using an inVia Renishaw spectrometer equipped with a CCD detector and two laser sources (514 nm visible $Ar^+$ ion and 785 nm NIR diode). Measurements made using the 514 nm laser (Spectra-Physics) involved a 2400 line/mm diffraction grating and a holographic notch filter, while for the 785 nm laser (Renishaw), a 1200 line/mm diffraction grating and an edge filter were employed. In order to achieve the best possible resolution while avoiding damage to the sample, the power of the 514 and 785 nm lasers was varied in the ranges of 0.15–1.5 and 3–30 mW, respectively. The Raman spectrometer was calibrated prior to each set of measurements by exciting a silicon sample placed under the microscope and performing an automatic offset correction. The proprietary Renishaw WiRE 2.0 software was used for the data acquisition and subsequent treatment.[27] All measurements were performed at room temperature and the experimental data are considered to be accurate to within ±1 $cm^{-1}$.

### 3.3.2 High Pressure Apparatus

The high-pressure measurements were carried-out in a diamond-anvil cell (DAC), furnished by High Pressure Diamond Optics, Tucson, AZ and fitted with type-IIA diamonds. Samples were introduced, together with several ruby chips, into the 300-μm circular hole of a stainless-steel gasket (7 mm x 7 mm x 270 μm) and squeezed between the parallel faces of the DAC. The change in fluorescence wavelength of the $R_1$ line ($^2E \rightarrow {}^4A_2$) of ruby was used to determine the applied pressure.[28] The DAC was mounted on the XYZ manual stage of a Leica microscope and the laser beam was focused onto the sample through a long-working-distance 20× objective. No pressure-transmitting medium was used for solid azobenzene samples; glycerol was used for the kinetic measurements of the PDR1A isomerization. After each increase in pressure, the sample was allowed to equilibrate for a minimum of 20 min prior to data collection.

### 3.3.3 Kinetic Measurements

The thermal *cis*-*trans* isomerization of PDR1A films was measured at various pressures between ambient and 4 GPa using the diamond-anvil cell. A thin film of the polymeric chromophore was deposited on one face of the diamond anvil cell by placing a drop of concentrated solution of PDR1A in THF (Fisher Scientific, HPLC grade) on the face of one diamond anvil, and allowing the solvent to evaporate. Owing to the thermally sensitive nature of the apparatus, the films were not annealed, so some residual solvent likely remained in the film thus lowering the bulk modulus. The optical density of the films investigated varied between approximately 1.3 and 1.5 at 488 nm. The films were inspected for optical clarity and then the DAC was assembled as described in the previous section. Pump-probe *trans*-*cis* flash photolysis kinetic measurements at various pressures were acquired using the optical apparatus shown in Figure 3.2. *Trans*-*cis* photochemical isomerization was induced in the film by irradiation with a 100 $mW \cdot cm^{-2}$ circularly-polarized, unfocussed beam from a frequency-doubled Nd:YAG laser operating at 532 nm. Circular polarization was used to avoid orientation of the azobenzene chromophores, which could result in anisotropic absorbance readings.[25] Typically, a pump cycle of between 0.5 and 1 s was used to induce isomerization and ensure saturation of *cis* isomer in the photostationary state; this period of irradiation at 100 $mW \cdot cm^{-2}$ was low enough to avoid heating the sample, so the kinetic measurements can be considered acquired at room temperature.[29] A 488 nm probe beam from an argon ion laser was chopped mechanically at 1410 Hz and attenuated to <1 μW, and then passed through the sample to a photodiode detector, where the intensity was recorded as a function of time. The intensity of the probe beam is proportional to the *cis*-content of the film, and can be converted to an approximate fraction of the film isomerized to the *cis* isomer using the molar absorptivity values for *cis* and *trans*-PDR1A from Reference 30.

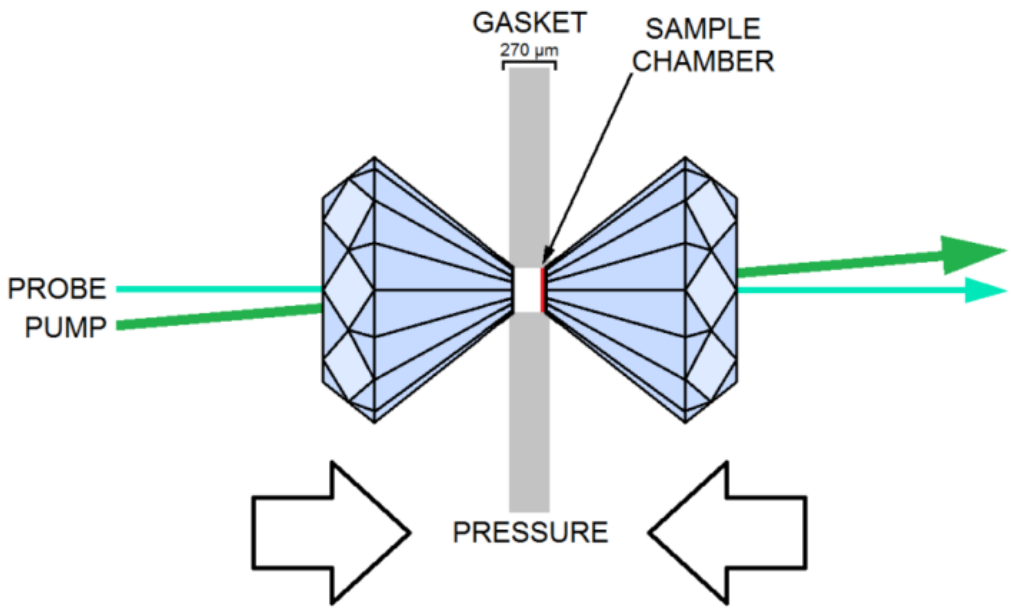


Figure 3.2 Pump-probe beam geometry through the diamond anvil cell. A film of PDR1A approximately 1 µm thick is held in a 270 µm-thick gasket between the two diamond faces. The void volume of the gasket (300 µm diameter) is filled with glycerol to act as a pressure-transmitting medium.

### 3.3.4 Sample Preparation

*trans*-Azobenzene (tAB) was purchased from Sigma-Aldrich (≥99% purity by HPLC) and was used without further purification. *cis*-Azobenzene (cAB) was prepared by adaptations of the method used by Cook and the observations of Frankel and Wolovsky.[31,32] A concentrated solution of tAB in light petroleum ether was irradiated at 365 nm with a Driel 200 W mercury-xenon UV lamp for 16 h at 23 °C in order to generate cAB. The cAB was then separated from the tAB on a 20 cm silica column by eluting the mixture with light petroleum ether. The cAB was visible as a dark orange band that was retained in the top 5 cm of the column, while the tAB was eluted by the petroleum ether. After all visible remnants of the tAB had been removed the cAB was eluted with acetone and collected. The cAB was then dried by rotary evaporation in an ice bath (to prevent thermal conversion to tAB) followed by vacuum filtration at room temperature in a dark environment. The cAB was stored in the dark at –15 °C. Before the Raman spectra were collected, the purity was checked by thin layer chromatography (TLC) and there was no evidence of tAB.[33]

The effect of external pressure on the kinetics of the thermal *cis-trans* isomerization was investigated using a low-molecular weight polymer of Disperse Red 1 acrylate, purchased from Sigma Aldrich ($T_g$ 79 °C) and used without further purification.

## 3.4 Results and Discussion

### 3.4.1 poly(Disperse Red 1 acrylate)

A typical pump-probe curve for PDR1A is presented in Figure 3.3. The ordinate value is the *cis* composition of the sample expressed in mole percent, calculated from the optical density of the sample using absorptivity values derived from Reference 30. The absorptivity value employed here, for a poly(methyl methacrylate) (PMMA) film doped with non-polymeric Disperse Red 1 (DR1), should have similar enough optical properties to the PDR1A samples investigated to approximate the composition of the sample as a function of time. For an arbitrary film an all-*trans* DR1-PMMA sample will have an optical density of 0.65, while the same film with all chromophores in the *cis* form will have an optical density of 0.35. The absorbance of the sample at any time for any composition can be written as:

$$A_t = A_{cis} + A_{trans} \qquad \text{Equation 3.1}$$

and, expressing each absorbance as a product of the absorptivity and mole fraction:

$$A_t = \alpha_{cis} f_{cis} + \alpha_{trans} f_{trans} \qquad \text{Equation 3.2}$$

This expression can now be converted to an expression containing only the fraction of the sample in the *cis*-state, using the relation:

$$f_{trans} + f_{cis} = 1 \qquad \text{Equation 3.3}$$

Inputting all the known values gives an expression for the *cis* fraction, normalized to $A_{trans} = 1$:

$$f_{cis} = \frac{1 - A_t}{0.46} \qquad \text{Equation 3.4}$$

This value is then multiplied by 100% to yield the percentage of the sample in the *cis* form.

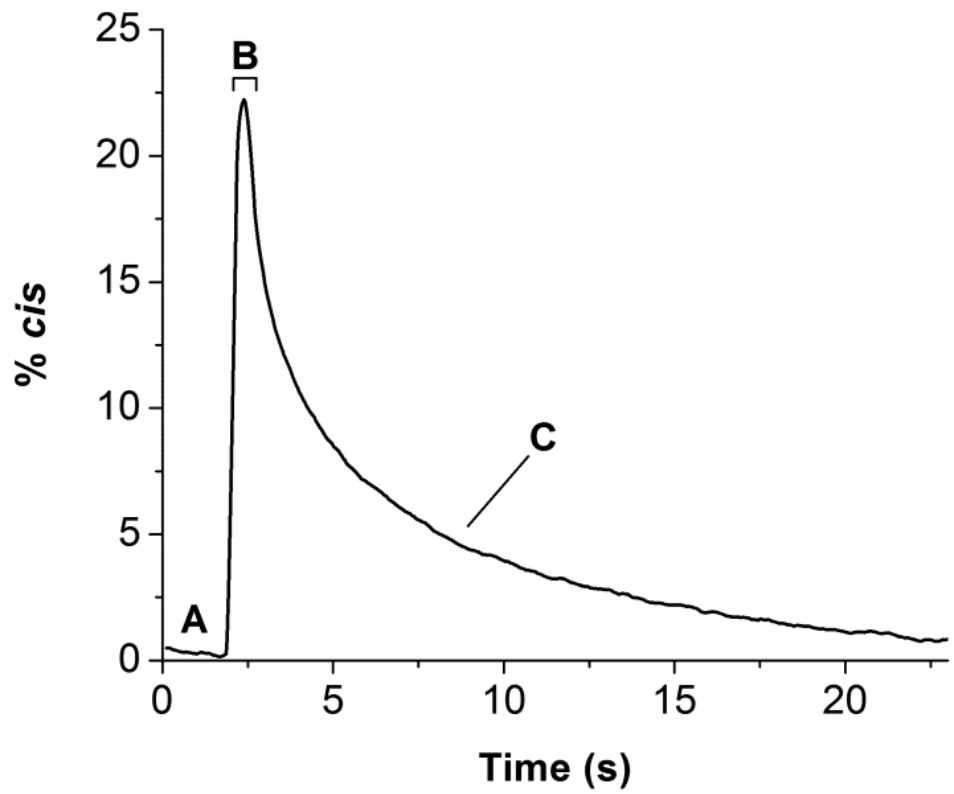


Figure 3.3 Typical pump-probe curve of PDR1A in the diamond anvil cell. The plot can be broken into three sections: A) the initial all-*trans* state with pump light off, followed by B) pump light on where the sample quickly reaches its photostationary state, and finally C) thermal relaxation of the *cis*-PDR1A chromophores after the pump light is turned off.

The pump power necessary to achieve the highest possible *cis* conversion was determined by varying the pump power at ambient pressure until no further decrease in absorption intensity was observed; this situation was also verified periodically at elevated pressures to ensure this value did not change. The effective pump power required was determined by the photochemical quantum yields of the *cis* and *trans* isomers of the azobenzene chromophore, and these values could be determined by the method developed by Sekkat *et al*.[30] A pump intensity of 100 $mW \cdot cm^{-2}$ was found to be adequate to achieve this level of conversion, which is typical for azobenzene samples in the literature. This power has also been shown to be low enough to not cause permanent burn damage to the sample.[34]

The average of several of these curves at a given pressure were plotted as $\ln[A_\infty - A_t]$ versus time, where $A_\infty$ represents the all-*trans* absorptivity at "infinite time," yielding an approximately

linear plot with a slope of $-k$. The data from the first few seconds after the pump beam was shut off were omitted from the analysis, as deviation from linear kinetics was observed in these samples. When this brief anomalous region is omitted, rate analysis is cleanly first-order, as per usual data treatment in the solid state.[22,35]

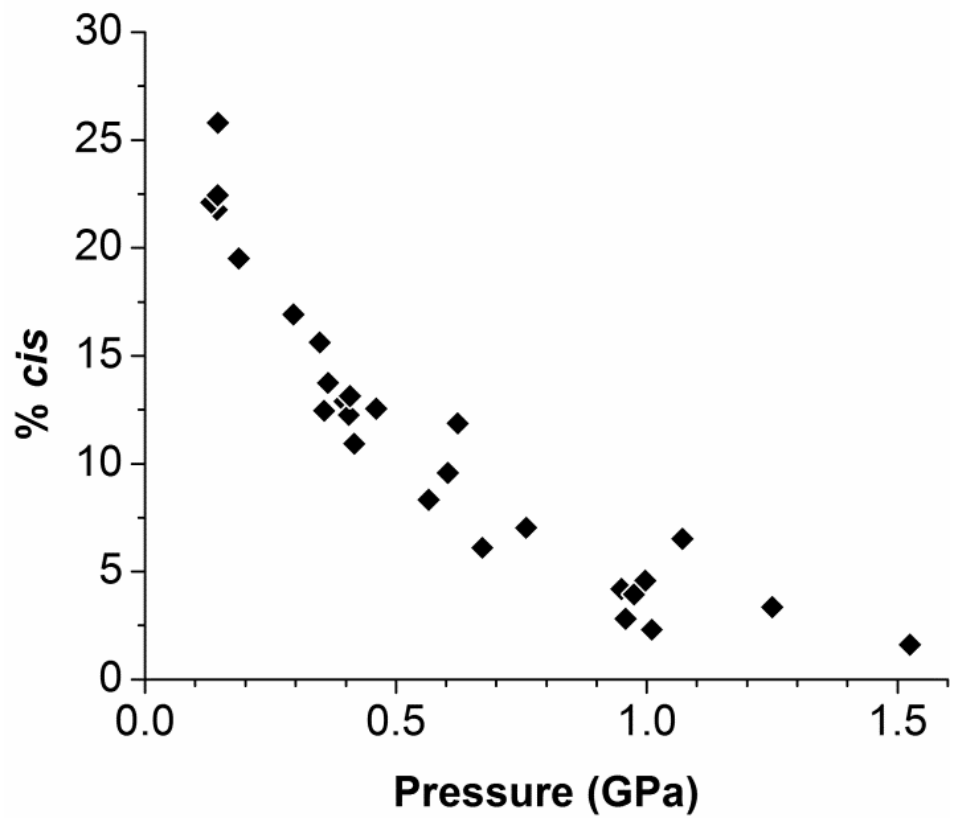


Figure 3.4 Plot of the fraction of *cis* in the photostationary state upon being irradiated by 532 nm light under high external pressure.

Figure 3.4 illustrates the decrease in the *cis* chromophore population in the photostationary state as the external pressure on the sample was increased. In the previous study by Sekkat *et al.* discussed previously,[25] it was found that the free volume of azo-functionalized polymer films exposed to high external pressure decreases, thereby affecting the rate of photo-orientation of the chromophores when exposed to polarized light. These authors found that the extent of chromophores able to reorient within the polymer decreased linearly with applied pressure from ambient up to 0.15 GPa, along with an associated pressure dependence of the thermal *cis-trans* isomerization rate. That observation appears consistent with our measurements, which cover a pressure range an order of magnitude greater than the data in Reference 25. It was suggested that

their results are consistent with a model of motion retarded by molecular friction—the matrix surrounding the chromophores hinders the motion of the chromophore while it sweeps out a relatively large volume during isomerization. Interestingly, the molecular orientation effect investigated in Reference 25 is quenched at 0.15 GPa. It seems clear that reorientation of the entire chromophore to align the dipole with polarized light, along with the covalently attached polymer backbone, has a much higher free volume requirement than does simple *trans-cis* isomerization without orientation. This lends further credence to decreased free volume in the film resulting in increased molecular friction.

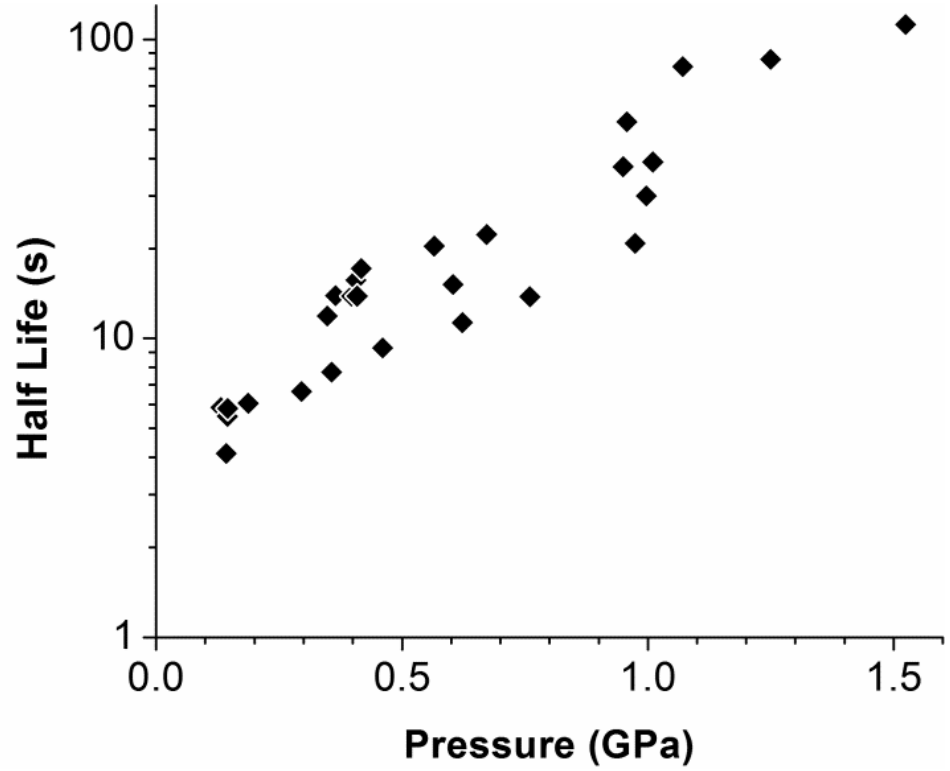


Figure 3.5 Plot of first-order half-life of the thermal *cis-trans* isomerization in PDR1A as a function of external pressure.

The rate of isomerization of PDR1A showed an increase in half-life by an order of magnitude over the range of pressures investigated, before the photochemical process that generates the *cis* isomer is ultimately shut down. First-order kinetic processes are not dependent on the initial concentration of reactants, and it has been shown repeatedly in the literature that repeated pump cycles on typical chromophores have no effect on the kinetics of the process.[34] This indicates that the retardation of the isomerization is purely an effect of the external pressure.

As with the fraction of the sample able to undergo isomerization, discussed above, the decrease in film free volume and corresponding increase in molecular friction appear to hinder the thermal *cis*-*trans* isomerization event, resulting in the observed increase in thermal half-life.

### 3.4.2 *trans*-Azobenzene

It is well known that applying an external pressure to a crystal leads to a compression of the unit cell, an amplification of interatomic and intermolecular interactions, and an increase of the energy of the vibrational modes.[36,37] Solid tAB, at atmospheric pressure, takes up 0.4% less volume than does cAB due to differences in the crystal packing order of the molecule.[7] In solution, calculations have shown that the free volume required for isomerization is 0.12 $nm^3$ for inversion or 0.25 $nm^3$ for rotation,[22] but, to our knowledge, no consideration of the volume for solid isomerization has been undertaken. Given the previously mentioned volume considerations and the energy gap between the two isomers (49.1 $kJ \cdot mol^{-1}$),[38] it would not be expected that mechanical pressure could force isomerization from tAB to cAB, because although the molecular volumes of the *trans* and *cis* isomers are similar, the volume of the transition state required to convert between them is significantly larger.[20]

Successive measurements were made at increasing pressures up to 4 GPa using a 514 nm probe laser. Plots of wavenumber *versus* pressure were linear suggesting that no phase transition occurred up to 4 GPa (Figure 3.6).

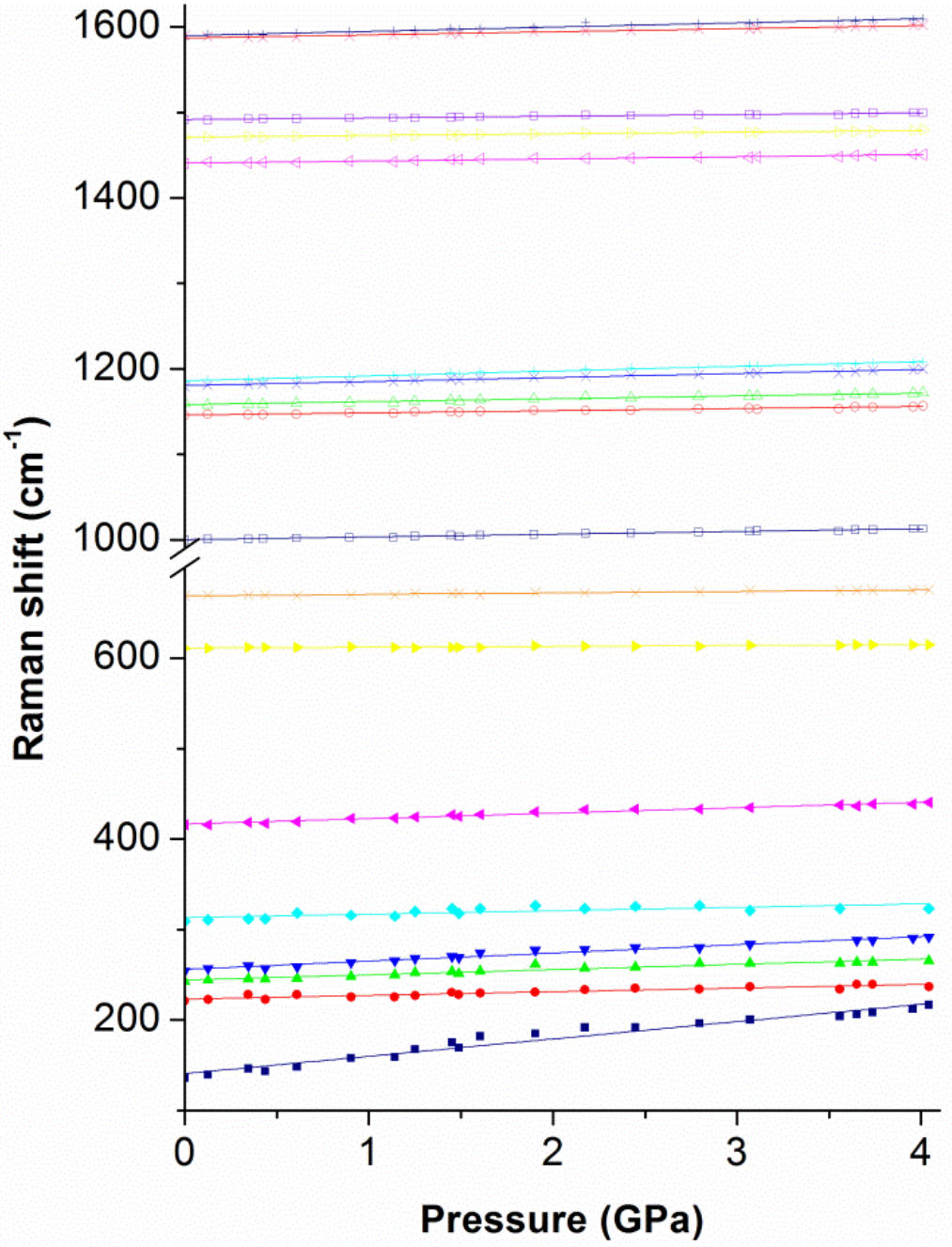


Figure 3.6 Pressure dependences of the principal Raman wavenumbers of tAB.

The associated d$\nu$/d$P$ values for tAB vibration are listed in Table 3.1. No peaks were formed that would correspond to cAB (as determined by comparison with spectral acquisitions for cAB at atmospheric and high pressure with a 785 nm laser), so it was determined that tAB was not being isomerized to cAB by the applied pressure. The peak that was initially present at 1588.9 $cm^{-1}$ split into two peaks. It was observed that several new peaks between 1400 and 1700 $cm^{-1}$

started to appear at a pressure of ~0.6 GPa, and they were persistent until a pressure of ~3GPa. However, it is felt that these few spectral changes cannot be attributed to an actual phase transition, and some related high-pressure work on azobenzene and hydrazobenzene that has recently been reported by Song's group supports this contention.[39] In their study, the two compounds were also compressed in a DAC at room temperature, but up to much higher pressures of 28 GPa, followed by subsequent decompression. *trans*-Azobenzene did undergo a phase transition but at about 10 GPa, and further compression to 18 GPa resulted in an irreversible breakdown of the molecular structure. Some band positions and d$\nu$/d$P$ values were also reported and a few of these data are compared in Table 3.1 (in parentheses).

Table 3.1 Pressure dependences of tAB Raman peaks.

| **Wavenumber ($cm^{-1}$)** | | **d$\nu$/d$P$ ($cm^{-1}$/GPa)** | |
|---|---|---|---|
| 136 | (135) | 19.1 | (9.8) |
| 221 | | 4.4 | |
| 243 | (243) | 5.8 | (5.6) |
| 254 | | 9.0 | |
| 415 | | 5.9 | |
| 613 | (605) | 0.8 | (0.8) |
| 668 | | 1.4 | |
| 1000 | (998) | 3.2 | (2.8) |
| 1145 | (1142) | 2.4 | (3.7) |
| 1158 | (1156) | 3.5 | (4.9) |
| 1180 | (1182) | 4.6 | (4.5) |
| 1185 | | 5.5 | |
| 1440 | | 2.2 | |
| 1471 | | 1.8 | |
| 1491 | (1483) | 1.8 | (2.2) |
| 1586 | | 3.6 | |
| 1590 | (1590) | 4.5 | (3.1) |

The proposed vibrational assignments based upon their *ab initio* calculations are also reported in their paper. The pressure dependences are for the most part in reasonable agreement with one another.

### 3.4.3 *cis*-Azobenzene

The Raman spectrum of a sample of cAB collected using the 514 nm laser shows only the features characteristic of tAB, indicating that cAB converts to tAB on exposure to light of this wavelength. However, when the 785 nm laser was used the Raman spectra of the two isomers were distinct.

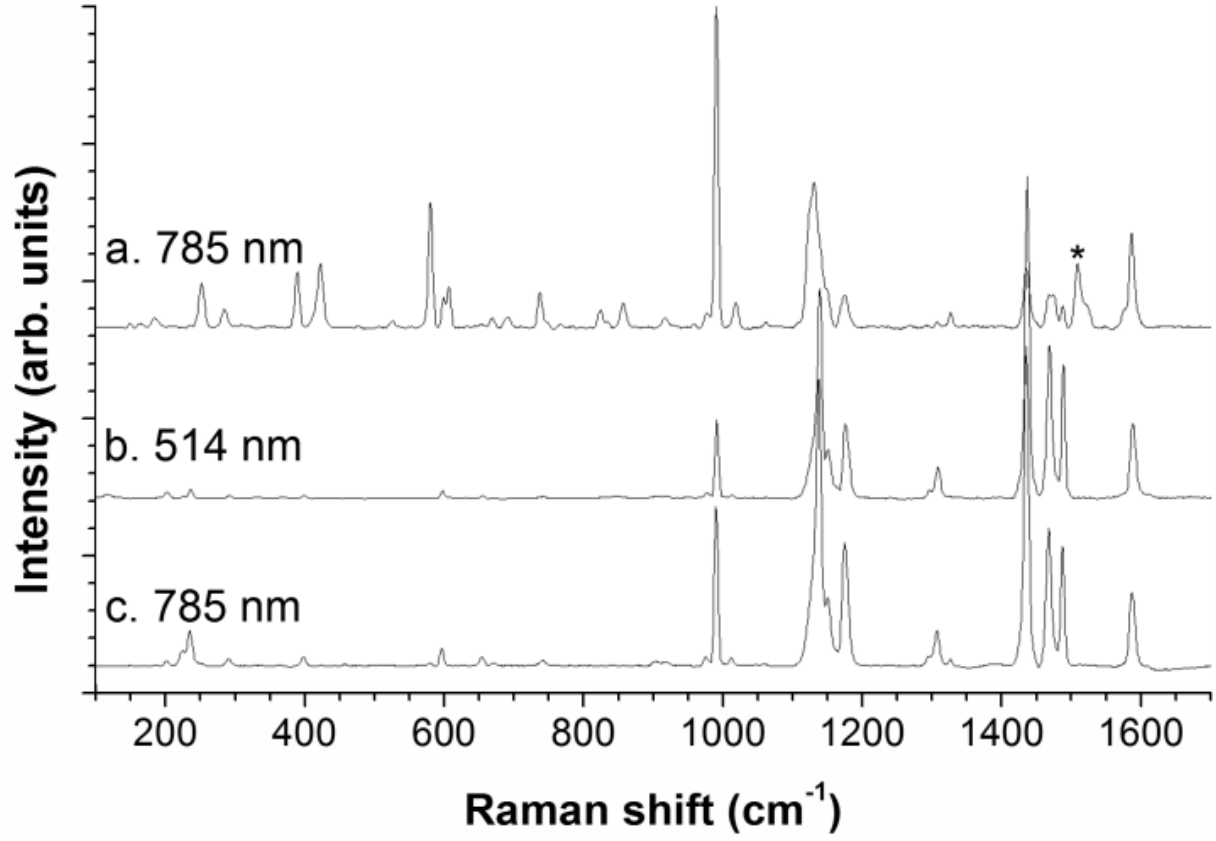


Figure 3.7 Raman spectra of a sample of cAB measured in the same spot with the following sequence of excitation: A) 785 nm; B) 514 nm and C) 785 nm.

Figure 3.7 shows the Raman spectra of a sample of cAB measured in the same spot using the following sequence of excitations lines: 785, 514 and 785 nm. The peak at 1511cm$^{-1}$, assigned to N=N stretching vibration of cAB is only present in the first Raman spectrum measured with the 785 nm laser.[40] After the sample was exposed to the 514 nm laser, which produced a tAB

spectrum, the 785 nm laser also produced a spectrum corresponding to that of tAB. This result was clearly due to photoisomerization occurring when the sample was exposed to the 514 nm excitation. Furthermore, it was found that the area of the cAB isomerized by the 514 nm laser was limited to that part of the sample where the beam had been focussed, while the scattered light did not affect the cAB in the area adjacent to the laser beam.

Up to a pressure of ~3.2 GPa, the Raman spectra from a sample of cAB, collected with the 514 nm laser, still showed features only characteristic to tAB leading to the conclusion that mechanical pressure cannot lock the *cis*-form into a stable enough configuration so that photoisomerization is prevented. Spectra collected from region #5 of a cAB sample with a 785 nm laser—both at high pressure and after the pressure was released—still produced the *cis* spectra and therefore showed that mechanical pressure (up to 3.2 GPa) cannot force isomerization of cAB to tAB. This result shows that photoisomerization can occur not just in solids but even in solids under high pressures.[41,42] Furthermore, the spectra of the azobenzene at atmospheric pressure after being photoisomerized at high pressure is that of pure tAB suggesting that the isomerization occurs just as cleanly (without side reactions) and reversibly as it does in solution at atmospheric pressure.

## 3.5 Conclusions

The *trans*-*cis* photoisomerization and *cis*-*trans* thermal isomerization of poly(Disperse Red 1 acrylate) was investigated over a large range of external pressures. It was found that the fraction of the film that could be photoisomerized to the metastable *cis* form decreased from over 25% at ambient pressure to less than a detectable amount above 1.5 GPa. This indicates a reduction in free volume in the film, which reduces the number of chromophores able to undergo photoisomerization from the *trans* to the *cis* isomer. In addition, the half-life of the thermal *cis*-*trans* reverse reaction increased by an order of magnitude, showing high pressure diminished significantly the rate of isomerization as well as the extent of the isomerization. The effect of high pressure on the Raman spectrum of tAB has been investigated at room temperature with the aid of a DAC up to 4 GPa. All the Raman modes of tAB were shifted linearly towards higher wavenumbers with increasing pressure, indicating no phase transition occurred in this pressure range. In addition, it was found that external pressure up to 4.1 GPa cannot force the isomerization of tAB to cAB. Up to 3.2 GPa, cAB is photoisomerized to tAB, when irradiated with 514 nm light, as shown by the disappearance of the N=N stretching mode at 1511 $cm^{-1}$.

Taken together these studies demonstrate the robustness and effectiveness of the azo chromophores under extreme pressures over many isomerization cycles. The fact that reversible photo-switching could be induced in PDR1A even at more than 1 GPa (albeit somewhat diminished compared to atmospheric pressure) also demonstrates convincingly that the azo molecules have the capacity to be employed as quite powerful molecular muscles. This is also a clear demonstration of harvesting photons of sunlight wavelength and intensity to perform a considerable amount of mechanical work, thus these azo materials can be regarded as promising for solar light transducing materials, directly from light energy to mechanical work, robustly, reversibly, and efficiently.

## 3.6 Acknowledgements

The authors are grateful for funding to NSERC Canada, the Canadian Foundation for Innovation (CFI) infrastructure and equipment grants, and to Professor Mark Andrews for helpful discussions.

## 3.7 References

1. H. Zollinger, *Azo and Diazo Chemistry*, Interscience, New York, 1961.

2. H. Zollinger, *Colour Chemistry, Synthesis, Properties, and Applications of Organic Dyes*, VCH, Weinheim, 1987.

3. G. S. Hartley, *Nature*, 1937, **140**, 281.

4. C. Nonnenberg, H. Gaub, and I. Frank, *ChemPhysChem*, 2006, **7**, 1455–1461.

5. N. J. Bunce, G. Ferguson, C. L. Forber, and G. J. Stachnyk, *J. Org. Chem.*, 1987, **52**, 394–398.

6. G. C. Hampson and J. M. Robertson, *J. Chem. Soc.*, 1941, 409–413.

7. A. Mostad and C. Rømming, *Acta Chem. Scand.*, 1971, **25**, 3561–3568.

8. A. Coskun, M. Banaszak, R. D. Astumian, J. F. Stoddart, and B. Grzybowski, *Chem. Soc. Rev.*, 2011, **41**, 19–30.

9. M. Blanco-Lomas, S. Samanta, P. J. Campos, G. A. Woolley, and D. Sampedro, *J. Am. Chem. Soc.*, 2012, **134**, 6960–6963.

10. D. Bléger, T. Liebig, R. Thiermann, M. Maskos, J. P. Rabe, and S. Hecht, *Angew. Chemie Int. Ed.*, 2011, **50**, 12559–12563.

11. K. G. Yager and C. J. Barrett, *Macromolecules*, 2006, **39**, 9320–9326.

12. X. Wang, J. Yin, and X. Wang, *Langmuir*, 2011, **27**, 12666–12676.

13. M. Yamada, M. Kondo, J. Mamiya, Y. Yu, M. Kinoshita, C. J. Barrett, and T. Ikeda, *Angew. Chemie Int. Ed.*, 2008, **47**, 4986–4988.

14. Y. Yu, M. Nakano, and T. Ikeda, *Nature*, 2003, **425**, 145.

15. J. Vapaavuori, A. Priimagi, and M. Kaivola, *J. Mater. Chem.*, 2010, **20**, 5260–5264.

16. X. Jia, D. Chao, E. B. Berda, S. Pei, H. Liu, T. Zheng, and C. Wang, *J. Mater. Chem.*, 2011, **21**, 18317–18324.

17. L. M. Goldenberg, L. Kulikovsky, Y. Gritsai, O. Kulikovska, J. Tomczyk, and J. Stumpe, *J. Mater. Chem.*, 2010, **20**, 9161–9171.

18. K. G. Yager and C. J. Barrett, *J. Chem. Phys.*, 2007, **126**, 094901–094908.

19. K. G. Yager, O. M. Tanchak, C. Godbout, H. Fritzsche, and C. J. Barrett, *Macromolecules*, 2006, **39**, 9311–9319.

20. C. J. Barrett, A. L. Natansohn, and P. L. Rochon, *J. Phys. Chem.*, 1996, **100**, 8836–8842.

21. P.-O. Åstrand, P. S. Ramanujam, S. Hvilsted, K. L. Bak, and S. P. A. Sauer, *J. Am. Chem. Soc.*, 2000, **122**, 3482–3487.

22. T. Naito, K. Horie, and I. Mita, *Macromolecules*, 1991, **24**, 2907–2911.

23. C. S. Paik and H. Morawetz, *Macromolecules*, 1972, **5**, 171–177.

24. T. Naito, K. Horie, and I. Mita, *Polymer*, 1993, **34**, 4140–4145.

25. Z. Sekkat, G. Kleideiter, and W. Knoll, *J. Opt. Soc. Am. B*, 2001, **18**, 1854–1857.

26. G. Kleideiter, Z. Sekkat, M. Kreiter, M. Dieter Lechner, and W. Knoll, *J. Mol. Struct.*, 2000, **521**, 167–178.

27. *WiRE*, version 2.0 service pack 6; Renishaw plc: Wotton-under-Edge, Gloucestershire, U.K., 2002.

28. H. K. Mao, P. M. Bell, J. W. Shaner, and D. J. Steinberg, *J. Appl. Phys.*, 1978, **49**, 3276–3283.

29. K. G. Yager and C. J. Barrett, *J. Chem. Phys.*, 2004, **120**, 1089–1096.

30. R. Loucif-Saibi, K. Nakatani, J. A. Delaire, M. Dumont, and Z. Sekkat, *Chem. Mater.*, 1993, **5**, 229–236.

31. A. H. Cook, *J. Chem. Soc.*, 1938, 876–881.

32. S. Mizushima, I. Nakagawa, J. V. Quagliano, E. Fischer, M. Frankel, and R. Wolovsky, *J. Chem. Phys.*, 1955, **23**, 1367–1368.

33. J. F. Janssen, *J. Chem. Educ.*, 1969, **46**, 117–118.

34. N. C. Holme, P. S. Ramanujam, and S. Hvilsted, *Opt. Lett.*, 1996, **21**, 902–904.

35. C. J. Barrett, A. Natansohn, and P. Rochon, *Chem. Mater.*, 1995, **7**, 899–903.

36. J. R. Ferraro, in *Handbook of Vibrational Spectroscopy*, Academic Press, Inc., New York, N.Y., 2002.

37. J. R. Ferraro, *Vibrational Spectroscopy at High External Pressures: The Diamond Anvil Cell*, Academic Press, Inc., Orlando, 1984.

38. A. R. Dias, M. E. Minas da Piedade, J. A. Martinho Simões, J. A. Simoni, C. Teixeira, H. P. Diogo, Y. Meng-Yan, and G. Pilcher, *J. Chem. Thermodyn.*, 1992, **24**, 439–447.

39. Z. Dong, N. M. Seemann, N. Lu, and Y. Song, *J. Phys. Chem. B*, 2011, **115**, 14912–14918.

40. C. M. Stuart, R. R. Frontiera, and R. A. Mathies, *J. Phys. Chem. A*, 2007, **111**, 12072–12080.

41. F. Terao, M. Morimoto, and M. Irie, *Angew. Chemie Int. Ed.*, 2012, **51**, 901–904.

42. S. Kobatake, S. Takami, H. Muto, T. Ishikawa, and M. Irie, *Nature*, 2007, **446**, 778–781.

# Rationale for: Photo-tuning of Highly Selective Wetting in Inverse Opals

The work described in the following chapter is the result of a successful collaboration with Prof. Joanna Aizenberg and Dr. Ian Burgess at the Wyss Institute at Harvard University, combining their expertise in photonic crystal sensors and our group's photoactive polymers. Azobenzene-functionalized polymers have been demonstrated to undergo a light-induced change in surface energy, and this research applied that effect to inverse opal photonic crystals. The result was a photonic crystal that could be used for liquid identification, based on the disappearance of structural colour upon wetting. The change in wettability could be tightly controlled by the amount of light exposure, which could distinguish between liquid mixtures in as small as 2.5% increments. The resulting structures may have applications in microfluidics as remote, light-activated liquid gates, or as sensitive anti-tampering and encryption devices.

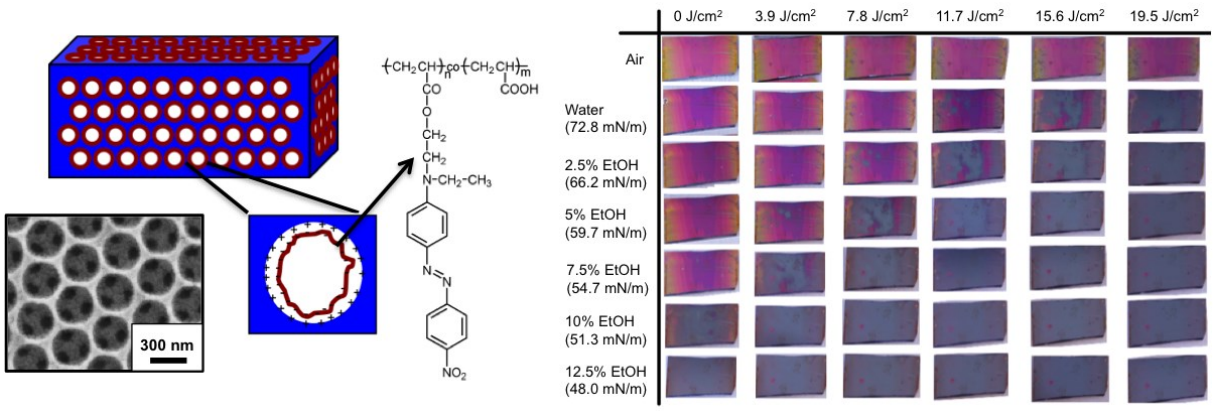

# Chapter 4: Photo-Tuning of Highly Selective Wetting in Inverse Opals

## 4.1 Abstract

Crack-free inverse opals exhibit a sharply defined threshold wettability for infiltration that has enabled their use as colourimetric indicators for liquid identification. Here we demonstrate direct and continuous photo-tuning of this wetting threshold in inverse opals whose surfaces are functionalized with a polymer doped with azobenzene chromophores.

## 4.2 Introduction

Adaptive materials, those whose microscopic or macroscopic properties can adapt to environmental stimuli, are integral components of many classes of emerging technologies, including sensors and indicators,[1,2] drug-delivery systems,[3] submillimetre-scale motors,[4] self-healing materials,[5] building materials,[6] and clothing[7] that adjust their characteristics to ambient conditions (*e.g.* weather). Materials with stimuli-responsive surface energy and/or fluidic properties have potential for widespread use in micro- and nano-scale devices.[8,9] At these scales, well below the capillary length of most liquids, surface forces are large compared to many other interactions (*e.g.* gravity) and surface effects contribute centrally to device performance.[10] Therefore, the ability to dynamically control surface interactions is integral to many micro- and nano-scale device functions in settings ranging from microfluidics to microscale robots and motors.[11,12] Driven by this motivation, numerous classes of materials have been developed whose surface energy is responsive to a variety of different physical and chemical stimuli.[11]

Using light as a stimulus is particularly useful in a number of settings. For devices that interface with biological materials, light places fewer limitations on the target system compared to most other chemical and physical stimuli (*e.g.* pH, electric fields) because it is minimally invasive and universally abundant.[13] The abundance of light is also advantageous for other applications such as microscale locomotion.[14] Numerous materials are currently known to exhibit photo-induced changes in surface energy, including titania[11] and surfaces coated with a variety of photo-active organic molecules or polymers, such as those belonging to the azobenzene[15–17] or

spiropyran[18] families. While there has been tremendous progress in the development of photo-responsive surfaces, device architectures that effectively translate photo-induced changes in surface energy into macroscopic, visible functions are less developed. A significant challenge faced in this aspect of design is that photo-induced changes in surface energy are generally small, with intrinsic contact angles for water typically changing by less than 30°.[17,19] Application of these materials can be greatly expanded by identifying architectures whereby significant changes in function result from very small changes in surface energy.

Crack-free inverse-opal films (IOFs)[20] have recently emerged as an example of such an architecture, where fluid infiltration is remarkably sensitive to surface energy.[21–23] Owing to the highly symmetric pore structure, the transition from complete non-wetting to complete wetting occurs over a decrease in intrinsic contact angle of only ~3°.[23] Infiltration of the pores is also associated with a dramatic change in the films' colour, due to refractive index matching between the liquid and the silica IOF matrix. This highly selective wetting, coupled with macroscopic colour changes, has been previously exploited for the production of colourimetric indicators for liquids.[22,23] In this paper, we develop photo-responsive IOFs, in which large visible changes in wetting behaviour and colour are triggered by small optically induced changes in their surface energy. By functionalizing the air-solid interface with a co-polymer of a hydrophilic electrolyte monomer (acrylic acid) and a hydrophobic chromophore (Disperse Red 1 acrylate), we created IOFs whose wetting threshold could be continuously tuned via ultraviolet (UV) or visible light exposure, all while maintaining a high wetting selectivity comparable with literature.[23] Photodegradation of the azobenzene chromophores was responsible for the observed irreversible wetting changes. Thus, these films are capable of sensitively and indelibly recording light exposure history, which can be read out directly through the films' colour upon immersion in simple liquids.

## 4.3 Results and Discussion

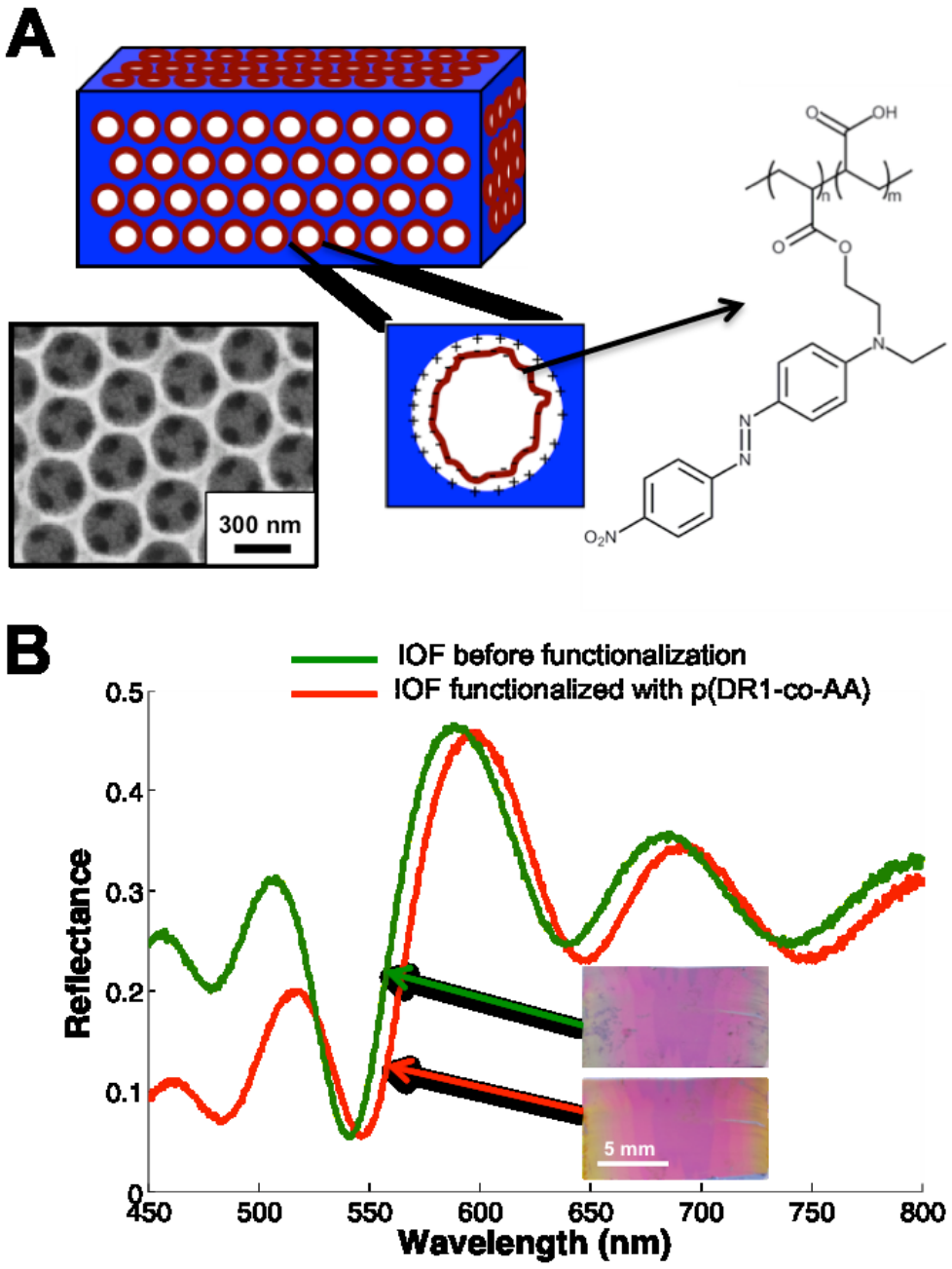


Figure 4.1 A) Schematic depicting the surface functionalization for the inverse-opal film (IOF) pores (scanning electron micrograph is shown at the bottom). The pores were first functionalized with (3-aminopropyl)trimethoxysilane (APTMS) to give them a positive charge in aqueous environments. A layer of the negatively charged polyelectrolyte poly(Disperse Red 1 acrylate-*co*-

acrylic acid) was then adsorbed to the pore surfaces. B) Normal-incidence reflectance spectra for an IOF region with a thickness of 9 close-packed layers before (green) and after (red) functionalization with p(DR1A-*co*-AA), showing suppression of the reflectance by the chromophore in the blue-green region. The inset shows the visual appearance of these films with and without the p(DR1A-*co*-AA) surface coating.

The pore surfaces of IOFs were functionalized with photoactive surface groups using a layer-by-layer polyelectrolyte deposition.[24] IOFs were first functionalized with (3-aminopropyl)trimethoxysilane to give them a positive charge in aqueous media. We then deposited a layer of the negatively charged photoactive polyelectrolyte, poly(Disperse Red 1 acrylate-*co*-acrylic acid) (p(DR1A-*co*-AA); 20 mol% Disperse Red 1 acrylate, shown in Figure 4.1 A: synthesis described in Reference 25). The functionalized IOF displays an enhanced red colour due to light absorption by the chromophore in the blue-green region of the visible spectrum (Figure 4.1 B). The functionalization preserved the highly selective wetting threshold, characteristic of our IOFs. When immersed in mixtures of water and ethanol with increasing ethanol concentration, IOFs functionalized with p(DR1A-*co*-AA) transitioned from non-wetting to wetting behaviour across a concentration change as small as 2.5% (v/v), as shown in the left column of Figure 4.2 A (before light exposure). Some variability in the location of this threshold was observed from one sample to the next, with the onset of wetting occurring between 10% and 20% ethanol (by vol.), likely owing to small batch-to-batch variations in the pore geometry[23] and the degree of polyelectrolyte coverage.

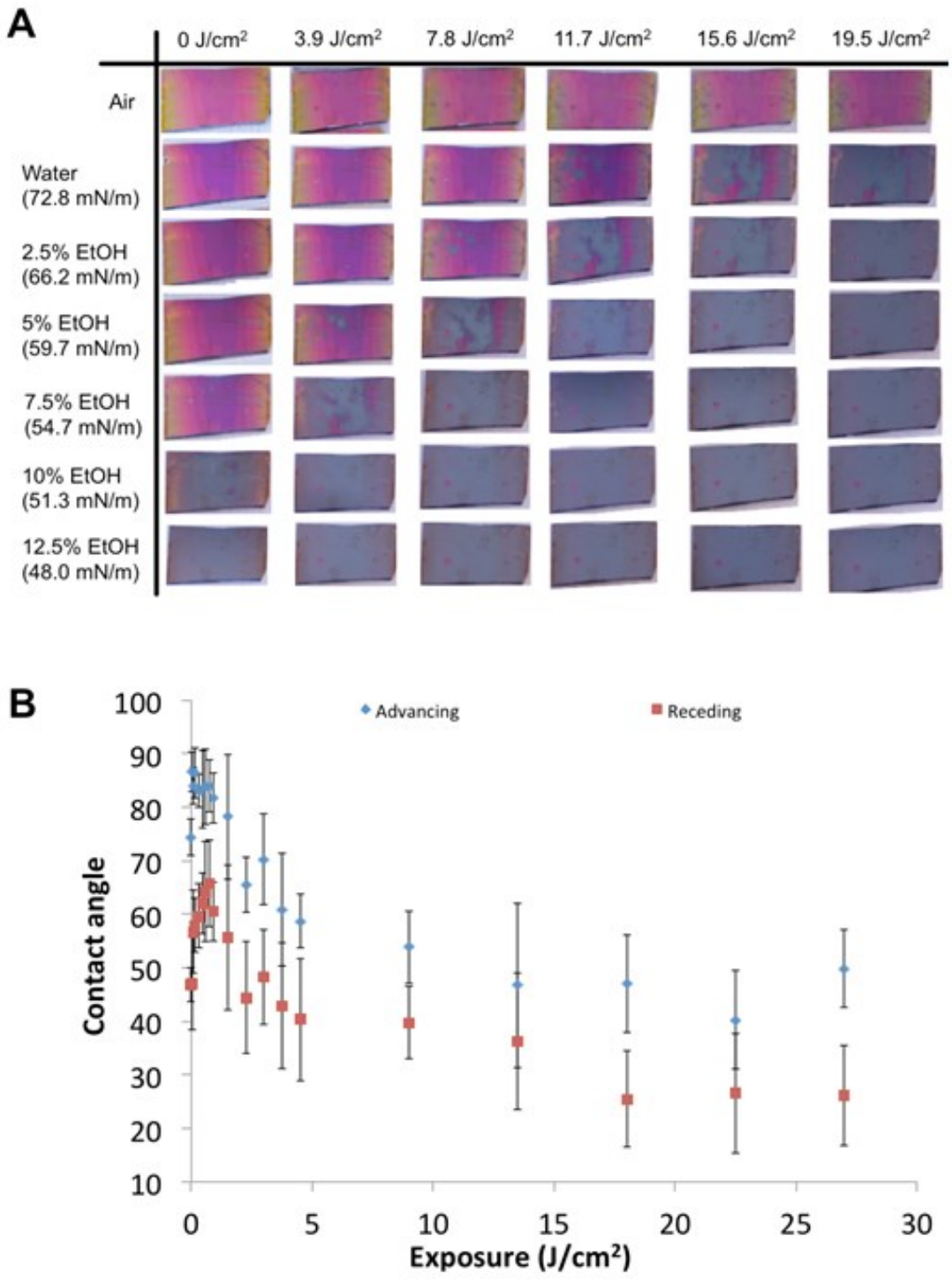


Figure 4.2 A) Wetting response of a p(DR1A-*co*-AA)-functionalized IOF as a function of UV light exposure. For each liquid, surface tensions from Reference 26 are indicated. B) Advancing and receding contact angles (°) of p(DR1A-*co*-AA)-functionalized flat glass slides as a function of UV exposure.

IOFs functionalized with p(DR1A-*co*-AA) displayed increased hydrophilicity after exposure to UV light (Dymax® Bluewave 200, 280–450 nm). As shown in Figure 4.2 A, the wetting threshold tuned continuously toward lower ethanol concentrations with increasing UV exposure, while the selectivity of wetting was preserved. Changes in wetting behaviour also occurred uniformly across the exposed regions. After sufficient exposure, all samples underwent wetting by water (see Figure 4.2 A, far right column). We characterized the magnitude of the photo-induced changes in surface energy by recording the contact angles displayed by water on flat glass slides that were functionalized and exposed to UV in the same manner as p(DR1A-*co*-AA)-functionalized IOFs. Figure 4.2 B shows the evolution of the advancing and receding contact angles as a function of the UV exposure dose. Advancing contact angles decreased steadily with exposure before stabilizing at ~20 J/cm$^2$, exhibiting a total decrease of 28 ± 10°. As also noted in previous studies of wetting in IOFs[21–23], their highly re-entrant geometry causes the onset of imbibition in these structures to occur at intrinsic contact angles well below 90°. It is also worth noting that p(DR1A-*co*-AA)-functionalized surfaces displayed considerable contact angle hysteresis (20–30°) at all doses.

In contrast to other reports of photo-actuated surface energy in azobenzene-containing materials, wetting changes in these IOFs were irreversible. We found that the changes in IOF wetting behaviour correlated with photobleaching (photodegradation) of the DR1A chromophore, rather than the reversible *cis-trans* isomerization or chromophore alignment effects previously reported.[27] Figure 4.3 A shows a p(DR1A-*co*-AA)-functionalized IOF in air (top) and submerged in water (bottom) after a large UV exposure dose (>100 J·cm$^{-2}$) was applied to the left portion of the film, qualitatively illustrating the correlation between photobleaching and wetting. The region where water infiltration is occurring (marked by disappearance of colour in the lower image) matches the region where photobleaching has occurred (marked by the change in colour).

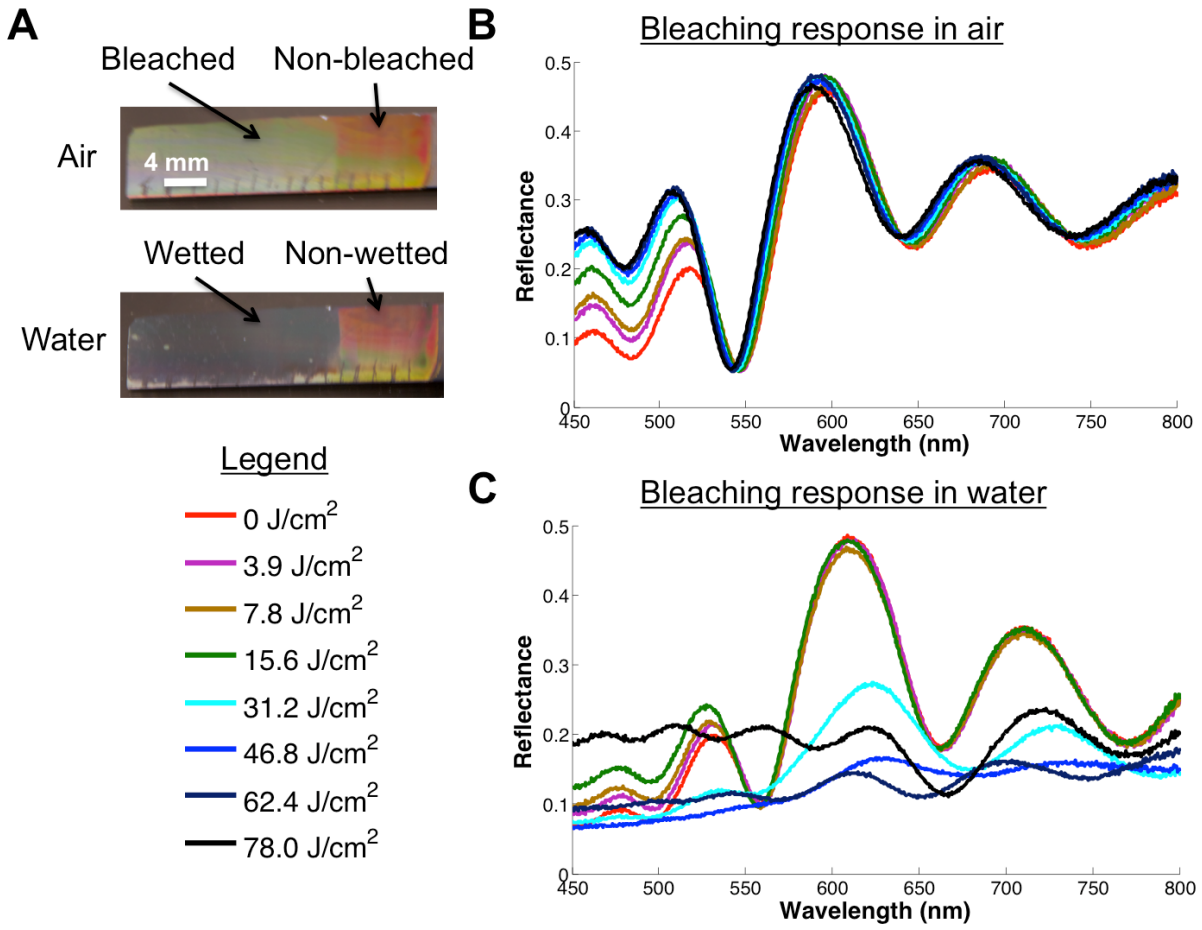


Figure 4.3 A) Images of a p(DR1A-co-AA)-functionalized IOF in air (top) and in water (bottom) where photobleaching via UV exposure has been applied selectively to the left portion. Comparison of the two images shows that wetting occurs in regions where the chromophore has been photobleached (evidenced by colour contrast in the air image). B,C) Evolution of the normal incidence reflectance spectra of an IOF region (9 layers thick) in air (B) and submerged in water (C) as a function of UV exposure dose, showing the correlation between photobleaching and the onset of wetting.

Although the exact mechanism of degradation is poorly understood, it likely involves the scission of the N=N bond, destroying the conjugated electronic structure of the molecule and the strong colouration.[27–29] The correlation between colour changes and changes in wetting behaviour are quantified in Figure 4.3 B, C for a fixed location in the top left-hand corner of the sample shown in Figure 4.2 A (IOF thickness of 9 close-packed layers). Figure 4.3 B shows the evolution of the normal-incidence reflection spectrum in air as a function of UV exposure dose and Figure

4.3 C shows the spectrum of the same region when the film is submerged in water. Before exposure, reflection is suppressed in the blue-green region by the chromophore absorption (see Figure 4.1 B). This suppression is most evident for the reflection maximum near 510 nm (to the left of the main reflection peak), whose peak height is reduced to 60% of its original value after functionalization (Figure 4.1 B). The recovery of this peak with UV exposure can be used as a measure of the degree of photobleaching. Comparing the range of exposure over which this peak recovers in Figure 4.3 B with the range over which wetting changes are observed in Figure 4.2 A, it is apparent that wetting changes strongly correlate with the degree of photobleaching. At the onset of partial wetting of water in Figure 4.3 C (cyan curve, 31.2 $J \cdot cm^{-2}$), the peak at 510 nm (Figure 4.3 B) has recovered to 98% of its value before p(DR1A-*co*-AA) functionalization. By the time complete wetting of water is observed in Figure 4.3 C (black curve, 78 $J \cdot cm^{-2}$), this peak has completely recovered.

A similar effect to bulk UV irradiation was also achieved using visible light, however significantly higher illumination doses were required (see Section 4.6, Supporting Information). Although the azobenzene chromophore is generally quite durable with respect to photo-induced damage under normal circumstances,[30] prolonged exposure to high power densities can have the same photobleaching effect as UV light. Despite higher powers required, using visible light instead of UV light to tune the IOF wetting state may prove useful in applications where UV light would be harmful to other components of a device (*e.g.* dynamically tuneable microfluidics). Furthermore, visible-light-induced wettability changes enabled us to induce fluid infiltration *in situ* by irradiating samples while submerged in water (see Section 4.7, Figure 4.7).

This technique provides a convenient approach to directly tune the wetting threshold of specific IOF regions to a particular liquid. Thus, a fabrication method using a single functionalization tuned by patterned UV exposure dosages is enabled for colourimetric indicators that mutually distinguish between a large number of liquids.[22,23] Alternatively, as opposed to identifying unknown liquids using wetting patterns in regions with known light exposures, wetting a film with known liquids could be used to colourimetrically identify the amount of prior light exposure in a way that requires no instrumentation. In this mode of operation, such a film could be deposited (*e.g.* on a sticker) onto an outdoor surface or appliance and used as a low-cost monitor of its age (if stored outside). The same principle of operation could be used to design anti-tamper films that indicate if a sealed package has been opened. It is worth noting that the photostability

of the azo-chromophore results in a dynamic range of UV-dose sensitivity that is relatively high (corresponding to ~20 minutes–2 hours of direct sunlight exposure).[31] While this may be ideal for longer term exposure monitoring (*e.g.* age reporting), practical tamper-indicating devices would likely require increased light sensitivity by at least one or two orders of magnitude.

## 4.4 Conclusions

We have shown that the sharply defined wetting threshold in crack-free inverse opal films functionalized with p(DR1A-*co*-AA) can be directly and continuously tuned with light exposure. Exposure of films to UV or visible light increased hydrophilicity, allowing liquids of increasing surface tension to penetrate the pores. These wettability changes, caused by photobleaching of the chromophore, were irreversible, indelibly recording light exposure history in a way that is both highly sensitive and easy to identify. These qualities make this type of material potentially useful as a tamper-indicating seal or a low cost monitor of material aging.

## 4.5 Acknowledgements

This work was supported by the Air Force Office of Scientific Research under Award FA9550-09-1-0669-DOD35CAP (Harvard), the Natural Sciences and Engineering Research Council of Canada and Canadian Foundation for Innovation (McGill). AGH would like to acknowledge FQRNT for a B2 doctoral scholarship.

## 4.6 Supplementary Information

### 4.6.1 Fabrication of Defect-Free Inverse Opals

Large-area crack-free inverse opal films (IOFs) were fabricated as described in References 20 and 32. Briefly, monodisperse aqueous suspensions of polymethylmethacrylate (PMMA) microspheres (d~300 nm, ~3% standard deviation) were synthesized by surfactant-free emulsion polymerization.[20,32,33] Suspensions were cleaned using dialysis. Glass slides or Si strips, cleaned in acid piranha solution (3:1 concentrated sulfuric acid/30% hydrogen peroxide), were suspended in 20 mL vials containing 20 mL of deionized water, 0.1–0.5 mL of the colloidal suspension and 0.095–1.5 mL of a pre-hydrolyzed solution of tetraethyl orthosilicate (TEOS, Sigma-Aldrich) prepared as described in Reference 20. The solution was left to evaporate in an oven held at 65

°C for 1-2 days, depositing a close-packed film of the PMMA spheres with $SiO_2$ from condensed TEOS filling the interstitial sites. After deposition, films were fired at 500 °C for 5 h to remove the polymer template and the resulting IOFs were cleaned in acid-piranha solution-for 4 h.

### 4.6.2 Functionalization of Inverse Opals with Chromophore-Containing Polyelectrolyte Layers

Cleaned IOFs were immersed in a 2% w/v solution of (3-aminopropyl)trimethoxysilane (APTMS) in acetone for 30 minutes, followed by flushing with an excess of DI water before drying. The functionalized IOFs were then rinsed with DI water, followed by curing/drying in a 110 °C oven for 30 minutes. This protocol imparts a positive charge throughout the IOF when immersed in water, via protonation of the amine. The IOF was then immersed in a saturated ($\sim 10^{-2}$ M) solution of poly(Disperse Red 1 acrylate-*co*-acrylic acid) (p(DR1A-*co*-AA); 20 mol% Disperse Red 1 acrylate, determined by $^1$H NMR, see Figure 4.4)[17] dissolved in a 1:1 mixture of dimethylformamide (DMF) and water. This solvent blend serves the dual purpose of ensuring adequate polymer solubility, as well as completely wetting the IOF and allowing uniform polymer deposition. The IOF was immersed in the polymer solution for at least 8 hours to allow complete coating of the complex inverse-opal geometry, followed by two iterations of immersion for 1 hour in fresh DMF/water (1:1) mixtures to allow diffusion of unbound polymer from the structure.

### 4.6.3 Light Irradiation, Optical and Wetting Characterization

After functionalization, before and between uses, samples were stored at room temperature and away from ambient light in sealed drawers. Wetting response was characterized visually initially and after light exposure by imaging with a digital camera (Canon Rebel EOS) in air and immersed in water-ethanol mixtures ranging in 2.5% increments of ethanol concentration from 0% ethanol to 25% ethanol (v/v). Samples were introduced to the liquids in the same order (starting with pure water and increasing ethanol concentration) and were dried under an air gun between successive immersions. All images were taken at a similar angle under ambient lighting conditions.

UV irradiation was performed by placing the sample directly at the end of a gooseneck fibre (1 cm diameter) connected to a UV lamp (Dymax®, 280–450 nm). A shutter attached to a timer was used to control exposure time. Lamp power was measured by placing a handheld power

meter (Newport Co.) at the location of the sample. Visible irradiation was performed by placing the sample in front of the collimated output of a frequency-doubled Nd:YAG laser (Coherent, 532 nm, 73 mW). Microscope images and reflection spectra were recorded on a stereomicroscope (Leica) coupled to a fibre-based USB spectrometer (Ocean Optics).

### 4.6.4 Characterization of Flat Surfaces

Flat glass microscope slides (Fisher) were cleaned and functionalized with APTMS and then p(DR1A-*co*-AA) in the same manner as the IOFs. Water contact angles (advancing and receding) were measured on a goniometer (KSV) initially and following each flood exposure under the UV lamp. After each set of contact angle measurements and before the next UV exposure, samples were flushed with water to homogenize any possible water uptake in the film.

## 4.7 Supplementary Figures

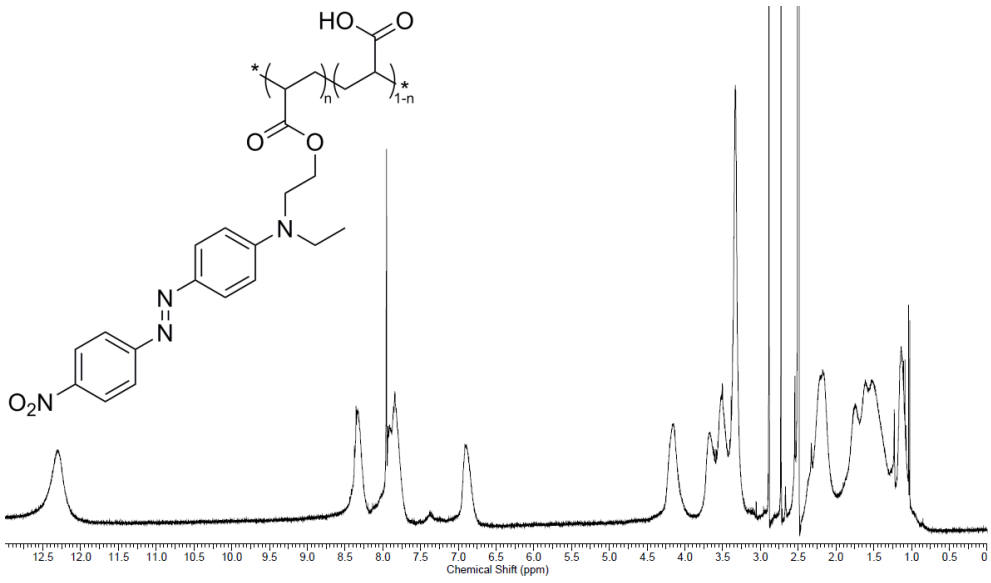


Figure 4.4 $^{1}$H NMR spectrum of poly(Disperse Red 1 acrylate-*co*-acrylic acid) in DMSO-$d_6$. Broad features from 1.5–2.2 ppm correspond to the acrylate backbone; peaks at 1.14 and 3.5–4.2 ppm represent the alkyl groups bound to the amine in the DR1 chromophore. The aromatic features fall in the region of 6.9–8.4 ppm, and the broad feature at 12.3 ppm corresponds to the acrylic acid protons. Sharp features correspond to solvent impurities trapped in the polymer matrix: 1.02 and 1.04 (diisopropyl ether), 2.50 (residual DMSO), 2.73, 2.89, 7.95 (N,N-dimethylformamide), and 3.33 (water).

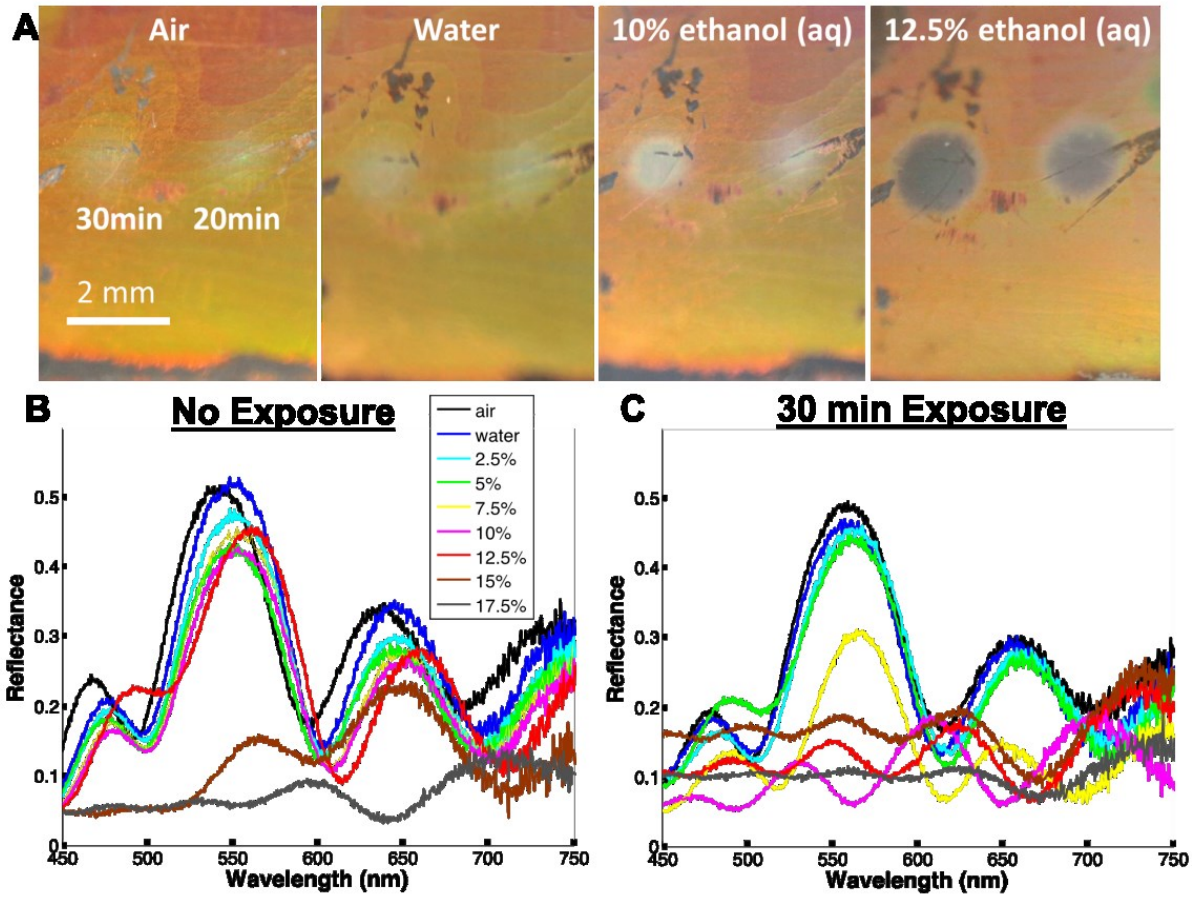


Figure 4.5 A) Photographs of a P(DR1A-*co*-AA)-functionalized IOF after exposure of two regions for 20 min and 30 min to a collimated laser spot (532 nm, 73 mW, ~1 mm in diameter), showing colour change due to photobleaching in air and increased wettability in water-ethanol mixtures. B,C) Reflectance spectra in water and various ethanol-water mixtures (ethanol concentration, v/v, listed in the legend) of two regions of the IOF, one taken in an unexposed region (B) and the other taken at the centre of the spot having had 30 min of laser exposure (C). Both regions have the same thickness (12 layers).

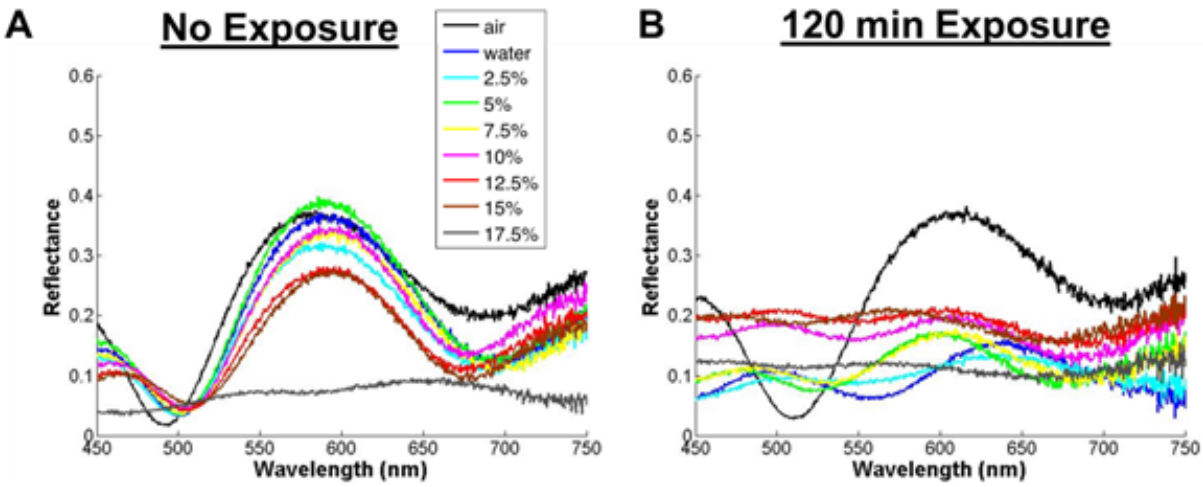


Figure 4.6 Reflectance spectra of a p(DR1A-*co*-AA)-functionalized IOF (7 layers) in water and various ethanol-water mixtures (ethanol concentration, v/v, indicated in legend) in an unexposed spot (A) and at the centre of the laser spot (73 mW, ~1 mm in diameter, collimated) after irradiation for 120 min (B). These spectra show that after sufficient exposure, wetting in water can be achieved, just as was observed for UV-induced photobleaching.

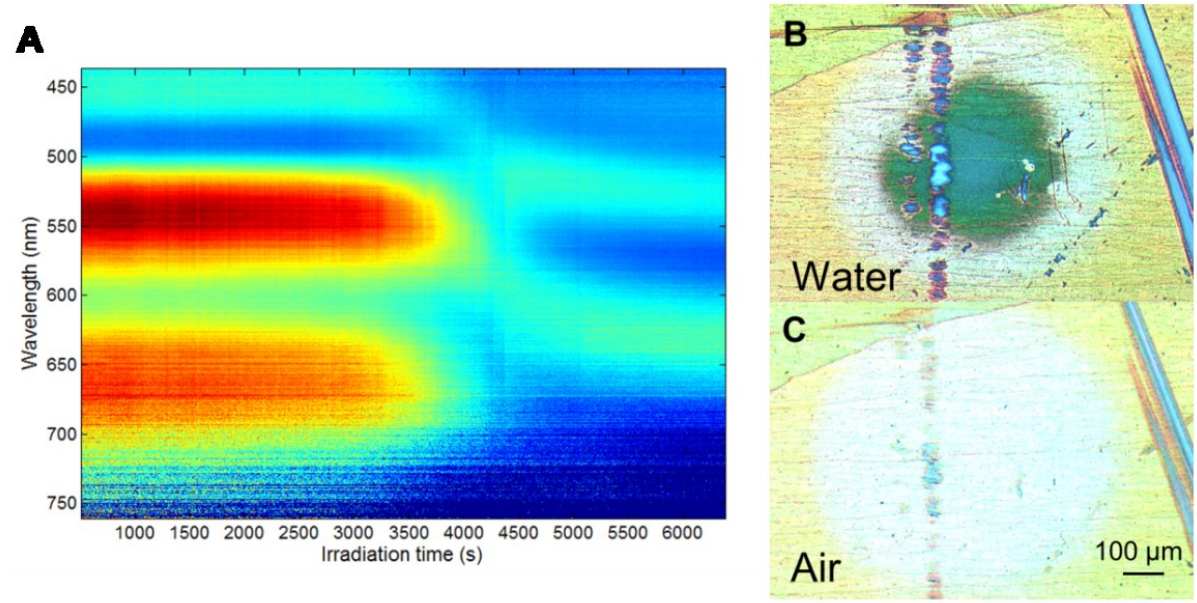


Figure 4.7 *In situ* photo-induced wetting through exposure of a p(DR1A-*co*-AA)-functionalized IOF to visible light while submerged in water. The IOF, submerged in water, was placed under illumination from a 75 W Xenon lamp (LEP Ltd.) under a microscope objective (1000x magnification) and the reflection spectrum was continuously monitored to track changes in wetting

behaviour. A) Temporal evolution of the reflection spectrum showing the onset of wetting (~4000 s). B,C) Images of the IOF taken afterwards while still in water (B) and then after drying (C), showing the spatial correlation between the photobleached region (indicated by the bright spot in C) and the wetted region (dark spot in B).

## 4.8 References


1. I. B. Burgess, M. Lončar, and J. Aizenberg, *J. Mater. Chem. C*, 2013, **1**, 6075–6086.

2. Y. Zhao, X. Zhao, and Z. Gu, *Adv. Funct. Mater.*, 2010, **20**, 2970–2988.

3. O. C. Farokhzad and R. Langer, *ACS Nano*, 2009, **3**, 16–20.

4. J. Wang and K. M. Manesh, *Small*, 2010, **6**, 338–345.

5. R. P. Wool, *Soft Matter*, 2008, **4**, 400–418.

6. R. J. Mortimer, *Chem. Soc. Rev.*, 1997, **26**, 147–156.

7. M. Kolle, A. Lethbridge, M. Kreysing, J. J. Baumberg, J. Aizenberg, and P. Vukusic, *Adv. Mater.*, 2013, **25**, 2239–2245.

8. A. C. Fahrenbach, S. C. Warren, J. T. Incorvati, A.-J. Avestro, J. C. Barnes, J. F. Stoddart, and B. A. Grzybowski, *Adv. Mater.*, 2013, **25**, 331–348.

9. A. Coskun, M. Banaszak, R. D. Astumian, J. F. Stoddart, and B. Grzybowski, *Chem. Soc. Rev.*, 2011, **41**, 19–30.

10. P.-G. de Gennes, F. Brochard-Wyart, and Q. Quere, *Capillarity and Wetting Phenomena: Drops, Bubbles, Pearls, Waves*, Springer, New York, 2004.

11. B. Xin and J. Hao, *Chem. Soc. Rev.*, 2010, **39**, 769–782.

12. X. Yao, Y. Song, and L. Jiang, *Adv. Mater.*, 2011, **23**, 719–734.

13. A. Goulet-Hanssens and C. J. Barrett, *J. Polym. Sci. Part A Polym. Chem.*, 2013, **51**, 3058–3070.

14. M. Yamada, M. Kondo, J. Mamiya, Y. Yu, M. Kinoshita, C. J. Barrett, and T. Ikeda, *Angew. Chemie Int. Ed.*, 2008, **47**, 4986–4988.

15. K. Ichimura, S.-K. Oh, and M. Nakagawa, *Science*, 2000, **288**, 1624–1626.

16. S.-K. Oh, M. Nakagawa, and K. Ichimura, *J. Mater. Chem.*, 2002, **12**, 2262–2269.

17. N. M. Ahmad, M. Saqib, and C. J. Barrett, *J. Macromol. Sci. Part A*, 2010, **47**, 534–544.

18. R. Rosario, D. Gust, M. Hayes, F. Jahnke, J. Springer, and A. A. Garcia, *Langmuir*, 2002, **18**, 8062–8069.

19. N. M. Ahmad, X. Lu, and C. J. Barrett, *J. Mater. Chem.*, 2010, **20**, 244–247.

20. B. Hatton, L. Mishchenko, S. Davis, K. H. Sandhage, and J. Aizenberg, *Proc. Natl. Acad. Sci.*, 2010, **107**, 10354–10359.

21. I. B. Burgess, L. Mishchenko, B. D. Hatton, M. Kolle, M. Lončar, and J. Aizenberg, *J. Am. Chem. Soc.*, 2011, **133**, 12430–12432.

22. K. P. Raymond, I. B. Burgess, M. H. Kinney, M. Lončar, and J. Aizenberg, *Lab Chip*, 2012, **12**, 3666–3669.

23. I. B. Burgess, N. Koay, K. P. Raymond, M. Kolle, M. Lončar, and J. Aizenberg, *ACS Nano*, 2012, **6**, 1427–1437.

24. S. J. Yeo, H. Kang, Y. H. Kim, S. Han, and P. J. Yoo, *ACS Appl. Mater. Interfaces*, 2012, **4**, 2107–2115.

25. N. M. Ahmad, M. Saqib, and C. J. Barrett, *J. Macromol. Sci. Part A*, 2010, **47**, 106–118.

26. G. Vazquez, E. Alvarez, and J. M. Navaza, *J. Chem. Eng. Data*, 1995, **40**, 611–614.

27. S. Bian, J. M. Williams, D. Y. Kim, L. Li, S. Balasubramanian, J. Kumar, and S. Tripathy, *J. Appl. Phys.*, 1999, **86**, 4498–4508.

28. A. Galvan-Gonzalez, M. Canva, G. I. Stegeman, R. Twieg, T. C. Kowalczyk, and H. S. Lackritz, *Opt. Lett.*, 1999, **24**, 1741–1743.

29. A. Galvan-Gonzalez, M. Canva, G. I. Stegeman, L. Sukhomlinova, R. J. Twieg, K. P. Chan, T. C. Kowalczyk, and H. S. Lackritz, *J. Opt. Soc. Am. B*, 2000, **17**, 1992–2000.

30. N. C. Holme, P. S. Ramanujam, and S. Hvilsted, *Opt. Lett.*, 1996, **21**, 902–904.

31. http://rredc.nrel.gov/solar/spectra/am1.5/, Reference Solar Spectral Irradiance: Air Mass 1.5. Retrieved 30 September, 2013.

32. I. B. Burgess, Ph.D. Thesis, Harvard University, 2012.

33. J. W. Goodwin, J. Hearn, C. C. Ho, and R. H. Ottewill, *Colloid Polym. Sci.*, 1974, **252**, 464–471.

# Rationale for: Boronic Acid Azobenzene Derivatives for Colourimetric Dopamine Detection

The detection of various biological analytes is critical to life and the ability to artificially mimic this detection *in vivo* is an important area of research. Current methods for detection of neural activity *in vivo* are typically electrical in nature, requiring hard, conductive electrodes that are difficult to make biocompatible for use as long-term probes. We propose building an all-optical probe capable of remaining embedded *in vivo* for long periods of time, shrouded in a biocompatible coating doped with photoresponsive dyes which change their optical properties when exposed to biologically-relevant analytes. This chapter outlines our efforts to synthesize and assess the sensitivity of several candidate dyes, which respond to the neurotransmitter dopamine by altering their visible absorbance.

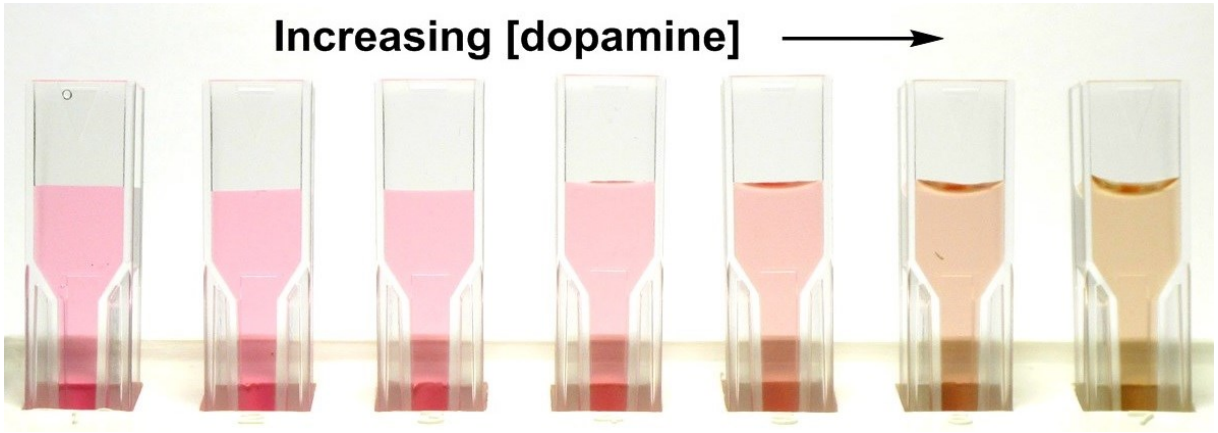


*Strong colour change visible in original thesis submission file format. May not fully reproduce clearly in PDF versions or print.

# Chapter 5: Azobenzene Boronic Acids for Colourimetric Dopamine Detection

## 5.1 Abstract

We present the synthesis and characterization of several boronic acid-functionalized azobenzene derivatives, and demonstrate their utility as colourimetric reporters for the neurotransmitter dopamine. The ability of boronic acids to bind specifically to the vicinal diol-moiety has been demonstrated extensively in the literature as a popular protecting group in organic synthesis. When attached to a chromophore or fluorophore, this binding can turn the photoactive base into a visible reporter for vicinal diols, such as those found on monosaccharides. The degree of change in absorbance spectrum, as well as the concentration range required to induce the change were investigated. From this data, the best candidates for incorporation into a neural probe were identified.

## 5.2 Introduction

Dopamine is one of a small number of core neurotransmitters used to mediate the travel of information in the brain. In addition to its role as an important neurotransmitter, the anomalous depletion of dopamine in neural tissue is closely associated with the onset of Parkinson's disease, and facile, early detection could help mitigate the effects of this crippling disorder.

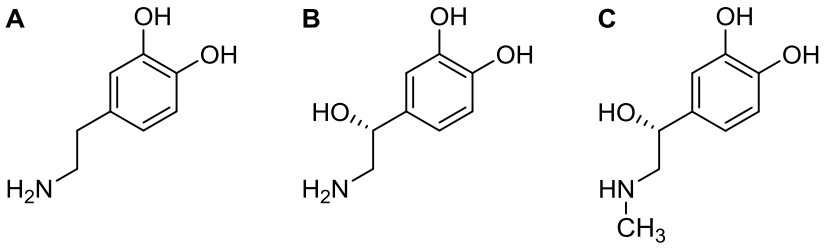


Figure 5.1 The three main aminocatecholate neurotransmitters: A) dopamine mediates signals within the brain, while B) norepinephrine and C) epinephrine are primarily used to convey signals from the sympathetic nervous system to various organs.

Current methods for localized detection of brain activity depend on the implantation of hard, conductive probes into the brain itself. While a great deal of progress has been made in improving the longevity of the probes, the fundamental problem of gliosis (scar formation) around the probe remains, limiting the useful life of the probe.[1,2] Research by our group and others has identified a wide variety of surface coatings which soften this interface, encouraging neural cell growth,[3,4] however, these coatings are typically not suitable for application to electrodes due to their electrically insulating nature. Optical probes do not suffer from the same limitations, and as such the work presented here seeks to develop a material with a colourimetric response to neural impulses which could ultimately form the working chromophore of an all-optical neural interface. Additionally, because the active chromophores in this work are all azobenzene derivatives with absorbance in the visible range, no biologically harmful UV light is required, as in many fluorophore-based systems.

Boronic acids have long been known for their ability to react with vicinal diols to form cyclic boronate esters,[5,6] which are widely used in the field of self-assembly,[7] as well as many popular cross-coupling reactions in modern organic synthesis.[8,9] More recently, boronic acid-appended fluorophores and chromophores have been demonstrated as effective reporters for saccharides and other biomolecules.[10,11] While much of the research has focussed on alkyl diols (especially saccharides),[12,13] the stronger interaction between arylboronic acids and catecholates (1,2-dihydroxybenzene) suggests their potential as reporters for dopamine may be even greater. With this in mind, a set of nine boronic acid-functionalized azobenzene derivatives was prepared (see Figure 5.2 below), and their spectral response to different concentrations of dopamine, glucose, and fructose was assessed.

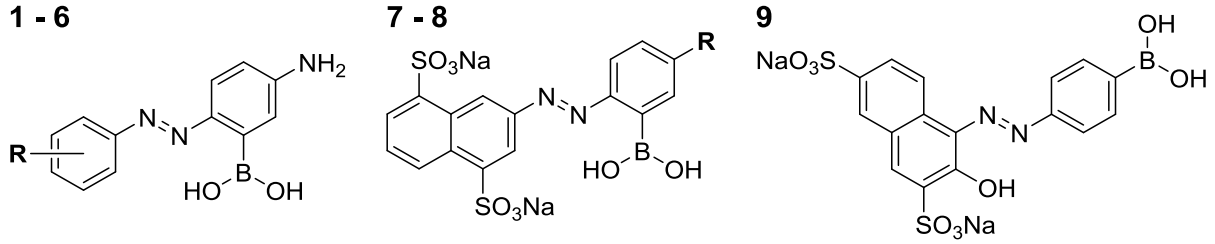


Figure 5.2 The 9 boronic acid-functionalized azobenzene derivatives described in this study. For Compounds 1 – 6, R = H, *p*-$CH_3$, *m*-$CH_3$, *p*-$NO_2$, *p*-$SO_3Na$, and *p*-$NHCOCH_3$, respectively. For Compounds 7 – 8, R = $NH_2$ and $N(CH_3)_2$, respectively.

Due to the nature of neural impulses, quantification of neurotransmitter concentration *in vivo* is not necessary: neural signals are quantized, so measuring neural activity is a matter of detecting spikes in NT concentration, not the absolute concentration. This greatly reduces the problem of NT detection to development of indicators specific to NTs, instead of sensors which have a specific concentration response.

## 5.3 Experimental Section

### 5.3.1 General Aspects

All commercial materials (solvents and reagents) were used as received unless otherwise noted. $^{1}$H, HSQC, and HMBC NMR spectra were acquired with either a Bruker 500 or 400 MHz spectrometer; $^{13}$C spectra were acquired with either a Varian 75 MHz or a Bruker 125 MHz spectrometer. Chemical shifts are reported in ppm on the δ-scale, referenced to the solvent residual signal. High-resolution mass spectrometry was performed using a Bruker Maxis Impact quadrupole-time of flight mass spectrometer with a source voltage of 4.5 kV.

### 5.3.2 Purification Techniques

Normal phase chromatographic separations were performed using an Isco Combiflash Rf 200 system, with pre-packed silica gel columns furnished by Silicycle. Reverse-phase HPLC separations were performed using an Agilent 1260 Infinity system running OpenLab CDS ChemStation Edition control software, equipped with a YMC AQ12S05 C18, 250×10 mm semi-preparative column with 5 μm beads, and 120 Å pore size. The mobile phase was 18.2 MΩ·cm water and HPLC-grade ACN (Fisher).

### 5.3.3 Synthesis of Azo-Boronic Acids

All candidate azo-boronic acids were synthesized via the well-known diazonium coupling reaction.[14] Briefly, aromatic amines were dissolved in acidic solution and cooled to 0 °C. A pre-cooled solution of sodium nitrite was then added, and the solution was stirred on ice to facilitate the formation of the diazonium salt. A pre-cooled solution of the boronic acid-functionalized aniline was then added dropwise, and the resulting mixture was neutralized. The solution was stirred on ice before being allowed to come to room temperature. The azo was then typically collected as a precipitate, and purified by HPLC where necessary.

**Synthesis of (*E*)-(5-amino-2-(phenyldiazenyl)phenyl)boronic acid (Compound 1)**

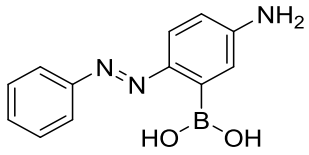


A solution of 0.18 mL of aniline (2.0 mmol, Fisher) dissolved in 3 mL of water, 2 mL of acetone, and 0.52 mL concentrated HCl was cooled, with stirring, in a 25 mL round bottom flask on an ice bath. The solution was stirred until the temperature was <5 °C, then a pre-cooled solution of 0.14 g sodium nitrite (2.0 mmol, Sigma Aldrich) dissolved in 1 mL water was added dropwise. The solution was stirred for 15 minutes to facilitate the formation of the diazonium salt, then a pre-cooled solution of 0.27 g 3-aminophenylboronic acid (2.0 mmol, Boron Molecular) dissolved in 2 mL of water and 2 mL of MeOH was added dropwise. The solution was neutralized with 1.1 mL of 2 M sodium hydroxide, and allowed to stir at 0 °C for 2 hours. The solution was filtered, yielding a dark red solid. The crude product was dissolved in EtOAc, washed once with water and once with brine, then dried with sodium sulfate (Fisher). The solvent was then removed under reduced pressure.

The crude solid was dissolved in HPLC-grade MeOH (5 mg·mL$^{-1}$, Fisher) and purified by HPLC using a gradient of 5:95 ACN/water increasing to 60:40 over 32 minutes. The product was collected between 27.40 and 28.55 minutes elution time. The solid product was isolated as a bright red solid by removing the solvent under reduced pressure.

$^{1}$H NMR (500 MHz, methanol-$d_4$) δ ppm 6.66 (dd, 1 H), 6.76 (d, 1 H), 7.41 (m, 1 H), 7.49 (dd, 2 H), 7.76 (d, 1 H), 8.04 – 8.10 (m, 2 H).

$^{13}$C NMR (125 MHz, methanol-$d_4$, HSQC/HMBC) δ ppm 114.4, 117.3, 121.5, 129.9, 130.2, 133.0, 146.2, 149.3, 158.3.

HR-MS (ESI, 4.5 kV): *m/z* Calculated for $C_{12}H_{12}BN_3NaO_2$ [**M** + Na]$^+$: 264.0915; found: 264.0908.

**Synthesis of (*E*)-(5-amino-2-(*p*-tolyldiazenyl)phenyl)boronic acid (Compound 2)**

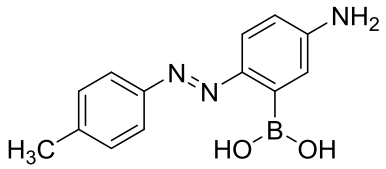


Adapted from the procedure described in Reference 12: 10 mL 1 M HCl and 0.27 g *p*-toluidine (2.0 mmol, Sigma Aldrich) were added to a 25 mL round-bottom flask containing a magnetic stir bar. The solution was cooled on an ice bath to <5 °C, and a pre-cooled solution of 0.18 g sodium nitrite (2.0 mmol, Sigma Aldrich) in 5 mL water was added dropwise. The solution was stirred on ice for 15 minutes, after which a pre-cooled solution of 0.47 g 3-aminobenzeneboronic acid hemisulfate (2.0 mmol, Sigma Aldrich) in 1 mL sodium hydroxide was added dropwise. The solution was neutralized with cold 1 M sodium hydroxide solution, and allowed to stir at 0 °C for 2 hours. The dark red precipitate was filtered and washed with water, then extracted 3 times with EtOAc and rinsed with brine, yielding a red-black solid.

The crude solid was dissolved in HPLC-grade MeOH (5 $mg \cdot mL^{-1}$, Fisher) using a gradient of 5:95 ACN/water increasing to 75:25 over 32 minutes. The product was collected between 27.2 and 28.8 minutes elution time, and isolated as a bright orange solid by removing the solvent under reduced pressure.

$^{1}H$ NMR (500 MHz, methanol-$d_4$) δ ppm 2.41 (s, 3 H), 6.65 (dd, 1 H), 6.74 (d, 1 H), 7.31 (m, 2 H), 7.73 (d, 1 H), 7.97 (m, 2 H).

$^{13}C$ NMR (125 MHz, methanol-$d_4$; HSQC/HMBC) δ ppm 21.0, 114.2, 117.1, 121.4, 130.6, 132.3, 141.0, 143.6, 145.1, 149.0, 157.5.

HR-MS (ESI, 4.5 kV): *m/z* Calculated for $C_{15}H_{18}BN_3NaO_2$ [**M** + $2CH_3OH$ – $2H_2O$ + Na]$^{+}$: 306.1384; found: 306.1393.

**Synthesis of (*E*)-(5-amino-2-(*m*-tolyldiazenyl)phenyl)boronic acid (Compound 3)**

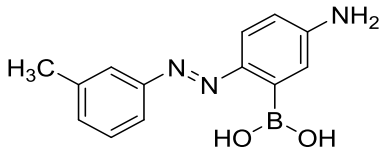


10 mL 1 M HCl and 0.276 mL *m*-toluidine (2.0 mmol, Sigma Aldrich) were added to a 25 mL round-bottom flask containing a magnetic stir bar. The solution was cooled on an ice bath to <5 °C, and a pre-cooled solution of 0.18 g sodium nitrite (2.0 mmol, Sigma Aldrich) in 5 mL water was added dropwise. The solution was stirred on ice for 15 minutes, after which a pre-cooled solution of 0.47 g 3-aminobenzeneboronic acid hemisulfate (2.0 mmol, Sigma Aldrich) in 1 mL sodium hydroxide was added dropwise. The solution was neutralized with cold 1 M sodium hydroxide solution, and allowed to stir at 0 °C for 2 hours. The dark red precipitate was filtered and washed with water, then extracted 3× with EtOAc and rinsed with brine, yielding a dark red solid.

The crude solid was dissolved in HPLC-grade MeOH (5 mg·mL$^{-1}$, Fisher) using a gradient of 5:95 ACN/water increasing to 75:25 over 32 minutes. The product was collected between 27.2 and 28.4 minutes elution time, and isolated as a red solid by removing the solvent under reduced pressure.

$^{1}$H NMR (500 MHz, methanol-$d_4$) δ ppm 2.42 (s, 3 H), 6.66 (dd, 1 H), 6.75 (d, 1 H), 7.24 (d, 1 H), 7.37 (t, 1 H), 7.75 (d, 1 H), 7.87 (d, 1 H), 7.91 (s, 1 H).

$^{13}$C NMR (125 MHz, methanol-$d_4$; HSQC/HMBC) 21.2, 114.3, 117.2, 118.7, 121.7, 130.0, 130.9, 132.8, 140.8.

HR-MS (ESI, 4.5 kV): *m/z* Calculated for $C_{15}H_{18}BN_3NaO_2$ [**M** + $2CH_3OH$ – $2H_2O$ + Na]$^+$: 306.1384; found: 306.1386.

**Synthesis of (*E*)-(5-amino-2-((4-nitrophenyl)diazenyl)phenyl)boronic acid (Compound 4)**

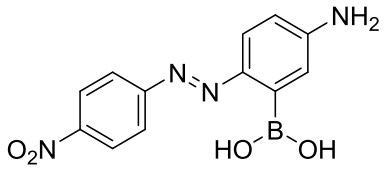


0.55 g 4-nitroaniline (4.0 mmol, Sigma Aldrich) was dissolved in 5 mL water, 8 mL acetone, and 1.04 mL concentrated HCl in a 50 mL round bottom flask equipped with a magnetic stir bar. The flask was cooled in a bath of ice water, and a pre-cooled solution of 0.28 g sodium nitrite (4.0 mmol, Sigma Aldrich) dissolved in 2 mL water was added dropwise. The solution was stirred for 20 minutes on ice, then a pre-cooled solution of 0.74 g 3-aminophenylboronic acid hemisulfate (4.0 mmol, Sigma Aldrich) dissolved in 3 mL 20 wt % sodium hydroxide and 5 mL water was slowly added. The pH was measured to be pH ≈ 7 after the addition. After 2 hours of stirring at 0 °C, the solution was allowed to warm to room temperature, and the solid product was recovered by vacuum filtration. The product was rinsed with water on the Büchner funnel, then allowed to dry in air. The crude product was isolated as a brown solid in an 84.2% yield.

The crude solid was dissolved in HPLC-grade MeOH (5 $mg \cdot mL^{-1}$, Fisher) and purified by HPLC using a gradient of 15:85 ACN/water increasing to 40:60 over 37 minutes. The product was collected between 35.6 and 37.4 minutes elution time. The solvent was removed under reduced pressure, yielding a purple-red solid.

$^{1}$H NMR (500 MHz, methanol-$d_4$) δ ppm 6.73 (dd, 1 H), 6.82 (d, 1 H), 7.83 (d, 1 H), 8.09 – 8.18 (m, 2 H), 8.29 – 8.35 (m, 2 H).

$^{13}$C NMR (125 MHz, methanol-$d_4$, HSQC/HMBC) δ ppm 116.0, 118.3, 120.7, 125.6, 135.7, 146.9, 149.9, 150.0, 160.8.

HR-MS (ESI, 4.5 kV): *m/z* Calculated for $C_{12}H_{11}BN_4NaO_4$ [**M** + Na]$^+$: 309.0766; found: 309.0768.

**Synthesis of sodium (*E*)-4-((4-amino-2-boronophenyl)diazenyl)benzenesulfonate (Compound 5)**

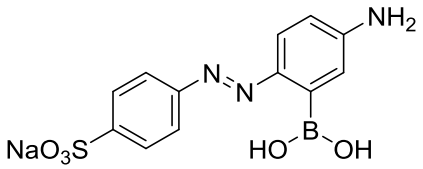


To a 50 mL round bottom flask was added 25 mL water 2 mL acetone, and 0.52 mL concentrated HCl. 0.43 g sodium 4-aminobenzenesulfonate hydrate (2.0 mmol, Sigma Aldrich) was dissolved in the flask, and the solution was cooled to 0 °C on an ice bath with stirring. A pre-cooled solution of 0.14 g sodium nitrite (2.0 mmol, Sigma Aldrich) dissolved in 2 mL of water was added dropwise, and the resulting solution was stirred at 0 °C for 15 minutes to facilitate formation of the diazonium salt. A pre-cooled solution of 0.27 g 3-aminophenylboronic acid (2.0 mmol, Boron Molecular) dissolved in 5 mL of water and 5 mL of MeOH was added dropwise: the resulting solution was then neutralized with 2.5 M sodium hydroxide. The solution was stirred on ice for 2 hours, then allowed to come to room temperature. The solution was washed twice with EtOAc, then the solvent of the aqueous fraction was removed under reduced pressure to yield a dark red solid in 130% yield (contaminated with water).

The crude solid was dissolved in water (5 $mg \cdot mL^{-1}$) and purified by HPLC using a gradient of 2:98 ACN/water increasing to 20:80 over 32 minutes. The product was collected between 13.0 and 13.9 minutes elution time. The solvent was removed under reduced pressure, yielding a dark red solid.

$^{1}$H NMR (500 MHz, methanol-$d_4$) δ ppm 6.68 (dd, 1 H), 6.76 (d, 1 H), 7.79 (d, 1 H), 7.90 – 7.94 (m, 2 H), 8.06 – 8.11 (m, 2 H).

$^{13}$C NMR (125 MHz, methanol-$d_4$, HSQC/HMBC) δ ppm 114.8, 117.5, 121.0, 127.9, 134.0, 146.0, 147.0, 149.4, 158.8.

HR-MS (ESI, 4.5 kV): *m/z* Calculated for $C_{12}H_{11}BN_3Na_2O_5S$ [**M** + Na]$^{+}$: 366.0302; found: 366.0305.

**Synthesis of (*E*)-(2-((4-acetamidophenyl)diazenyl)-5-aminophenyl)boronic acid (Compound 6)**

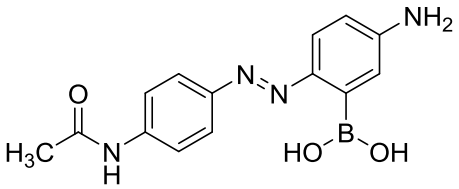


To a 25 mL round bottom flask equipped with a magnetic stir bar was added 4 mL acetone, 1 mL water, 0.52 mL concentrated HCl, and 0.30 g 4-acetamidoaniline (2.0 mmol). The solution was cooled to 0 °C, then a pre-cooled solution of 1 mL 2 M aqueous sodium nitrite (2.0 mmol, Sigma Aldrich) was added dropwise. The solution was allowed to stir for 15 minutes on ice to facilitate the formation of the diazonium salt, then a pre-cooled solution of 0.27 g 3-aminophenylboronic acid (2.0 mmol, Boron Molecular) dissolved in 2 mL of water and 2 mL of acetone was added dropwise. The solution was neutralized with cold 2 M sodium hydroxide, then allowed to stir two hours on ice before warming to room temperature. The aqueous solution was extracted with three portions of EtOAc, and the combined organic fractions were combined and washed with brine and dried with sodium sulfate. The EtOAc was then removed under reduced pressure giving 0.24 g of crude dark red solid in a 39.8% yield.

The crude solid was dissolved in HPLC-grade ACN (5 $mg \cdot mL^{-1}$) and purified by HPLC using a gradient of 5:95 ACN/water increasing to 55:45 over 32 minutes. The product was collected between 23.7 and 24.9 minutes elution time. The product was isolated as a red solid by removing the solvent under reduced pressure.

$^{1}H$ NMR (400 MHz, methanol-$d_4$) δ ppm 2.16 (s, 3 H), 4.58 (s, 1 H), 6.65 (dd, 1 H), 6.74 (d, 1 H), 7.71 (d, 1 H), 7.71 (d, 2 H), 8.04 (d, 2 H).

$^{13}C$ NMR (100 MHz, methanol-$d_4$, from HSQC/HMBC) δ ppm 23.5, 114.3, 117.2, 121.0, 122.2, 132.1, 141.5, 142.1, 149.3, 157.7, 171.6.

HR-MS (ESI, 4.5 kV): *m/z* Calculated for $C_{16}H_{19}BN_4NaO_3$ [**M** + $2CH_3OH$ – $2H_2O$ + Na]$^+$: 349.1442; found: 349.1442.

**Synthesis of sodium (*E*)-3-((4-amino-2-boronophenyl)diazenyl)naphthalene-1,5-disulfonate (Compound 7)**

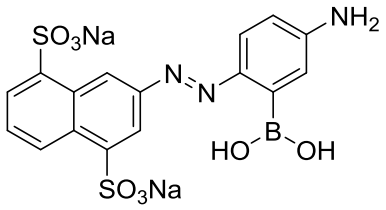


Adapted from Reference 12. 0.87 g sodium 3-amino-1,5-naphthalenedisulfonate (2.5 mmol, Sigma Aldrich) was dissolved in 20 mL 1 M HCl in a 100 mL round bottom flask. The solution was cooled to 0 °C, and then a pre-cooled solution of 0.18 g sodium nitrite (2.6 mmol, Sigma Aldrich) dissolved in 10 mL of water was added dropwise. The solution was allowed to stir for 15 minutes at 0 °C, then a solution of pre-cooled 0.34 g 3-aminophenylboronic acid (2.5 mmol, Boron Molecular) dissolved in 10 mL 1 M sodium hydroxide was added dropwise. The mixture was neutralized with 1 M sodium hydroxide, and stirred for 2 hours at 0 °C followed by 2 hours at room temperature. The reaction mixture was filtered, yielding a yellow powder in 15.1% yield. The product was pure by $^{1}$H NMR, and used without further purification.

$^{1}$H NMR (500 MHz, methanol-$d_4$) δ ppm 7.27 (br. s., 1 H), 7.36 (dd, 1 H), 7.73 (dd, 1 H), 8.16 (d, 1 H), 8.32 (dd, 1 H), 8.76 (d, 1 H), 9.07 (d, 1 H), 9.78 (d, 1 H).

$^{13}$C NMR (125 MHz, methanol-$d_4$) δ ppm 117.2, 122.8, 124.8, 127.5, 127.9, 129.3, 131.0, 131.7, 139.9, 143.4, 144.5, 154.2.

HR-MS (ESI, 4.5 kV): *m/z* Calculated for $C_{18}H_{16}BN_3Na_3O_8S_2$ [**M** + $2CH_3OH$ – $2H_2O$ + Na]$^{+}$: 546.0159; found: 546.0163.

**Synthesis of sodium (*E*)-3-((2-borono-4-(dimethylamino)phenyl)diazenyl) naphthalene-1,5-disulfonate (Compound 8)**

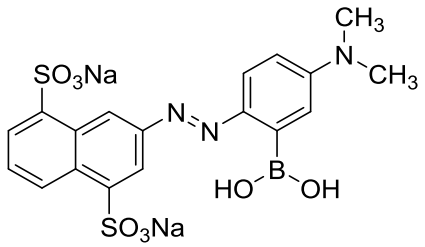


Adapted from the synthesis of Compound 7 above. 0.87 g sodium 3-amino-1,5-naphthalenedisulfonate (2.5 mmol, Sigma Aldrich) was dissolved in 20 mL 1 M HCl in a 100 mL round bottom flask. The solution was cooled to 0 °C, and then a pre-cooled solution of 0.18 g sodium nitrite (2.6 mmol, Sigma Aldrich) dissolved in 10 mL of water was added dropwise. The solution was allowed to stir for 15 minutes at 0 °C, then a solution of pre-cooled 0.34 g 3-(dimethylamino)phenylboronic acid (2.5 mmol, Sigma Aldrich) dissolved in 10 mL 1 M sodium hydroxide was added dropwise. The mixture was neutralized with 1 M sodium hydroxide, and stirred for 2 hours at 0 °C followed by 2 hours at room temperature. The reaction mixture was filtered, yielding a dark red powder in 77.3% crude yield.

The crude solid was dissolved in HPLC grade MeOH (5 $mg \cdot mL^{-1}$) and purified by HPLC using a gradient of 2:98 ACN/water increasing to 40:60 over 32 minutes. The product was collected between 15.5 and 17.8 minutes elution time. The solvent was removed under reduced pressure, yielding a deep purple solid.

$^{1}$H NMR (500 MHz, methanol-$d_4$) δ ppm 3.3 (br. s, 6 H), 7.1 (br. s., 1 H), 7.1 (br. s., 1 H), 7.7 (t, 1 H), 8.0 (br. s., 1 H), 8.3 (d, 1 H), 8.8 (br. s., 1 H), 9.0 (d, 1 H), 9.6 (br. s., 1 H).

$^{13}$C NMR (125 MHz, methanol-$d_4$, from HSQC only) δ ppm 43.6, 117.0, 118.1, 119.6, 127.0, 127.5, 130.5, 130.6.

HR-MS (ESI, 4.5 kV): *m/z* Calculated for $C_{18}H_{16}BN_3Na_3O_8S_2$ [**M** + $2CH_3OH$ – $2H_2O$ + Na]$^{+}$: 574.0472; found: 574.0484.

**Synthesis of sodium (*E*)-4-((4-boronophenyl)diazenyl)-3-hydroxynaphthalene-2,7-disulfonate (Compound 9)**

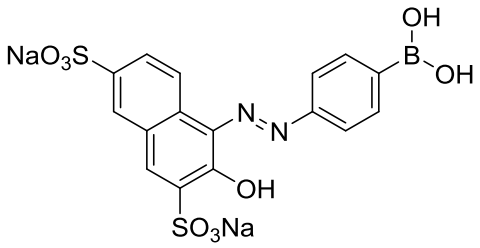


Reproduced from Reference 13. To a 25 mL round bottom flask equipped with a magnetic stir bar was added: 0.20 g of 4-aminophenylboronic acid pinacol ester (0.91 mmol, Sigma Aldrich), 2 mL of water, and 0.3 mL of concentrated HCl. The flask was cooled below 5 °C with an ice bath, then a cold solution of 0.066 g sodium nitrite in 2 mL of water was slowly dropped in. The resulting solution was stirred for 15 minutes at 0 °C, then a cold solution of 0.34 g sodium 3-hydroxynaphthalene-2,7-disulfonic acid disodium salt (0.98 mmol, Sigma Aldrich) dissolved in 2 mL of water was added dropwise. The solution was stirred for 15 minutes at 0 °C, then allowed to warm to room temperature. The solution was basified to pH=6.0 with 20% w/v sodium hydroxide, and the resulting red precipitate was vacuum filtered and rinsed with 5 mL cold water. The solid was then rinsed with acetone until the filtrate ran clear. Yield: 42% red powder, pure by $^{1}$H NMR and was used without further purification. As in the original reference, the pinacol group is removed during the synthesis.

$^{1}$H NMR (500 MHz, DMSO-$d_6$) δ ppm 7.79 (d, 2 H), 7.82 (d, 1 H), 7.95 (d, 2 H), 7.96 (s, 1 H), 8.17 (s, 2 H), 8.28 (s, 1 H), 8.42 (d, 1 H).

$^{13}$C NMR (75 MHz, DMSO-$d_6$) δ ppm 116.6, 120.8, 125.1, 125.4, 126.3, 126.9, 127.3, 129.5, 133.0, 135.5, 138. 6, 140.7, 143.9, 146.2, 172.0.

HR-MS (ESI, 4.5 kV): *m/z* Calculated for $C_{18}H_{15}BN_2Na_3O_9S_2$ [**M** + $2CH_3OH$ – $2H_2O$ + Na]$^{+}$: 547.0000; found: 546.9995.

### 5.3.4 Titration of Candidate Indicator Molecules

Candidate indicator molecules were dissolved in 0.1 M phosphate buffer adjusted to pH = 7.4, to give a final indicator concentration of 10 μM. This concentration was found to give useful absorbance values for all indicators investigated (*ca.* 0.1 – 0.5). Samples were then titrated with glucose, fructose, and dopamine, from 0 – 100 mM, with a visible absorbance spectrum acquired at each step. The process was repeated from 0 – 10 mM depending on the response. UV-vis spectra were acquired with a Cary 100 dual-beam spectrophotometer equipped with a temperature controller set to 21.0 °C.

### 5.3.5 Spectral Response

The spectral response was assessed by tracking the change in absorbance at the $\lambda_{max}$ as a function of titrant concentration. Plots were constructed showing the change as a function of analyte, as well as the percentage change in absorbance from no analyte to saturation.

## 5.4 Results and Discussion

Importantly, it should be noted that the optical responses presented here occur at a pH of 7.4, and as such is a good comparison for the pH conditions the indicator molecules would encounter *in vivo*. The binding of diols by boronic acids is highly pH-dependent, and many of the best indicators reported in the literature exhibit an optimal response at substantially more basic conditions than would be found in a biological setting.[15,16]

### 5.4.1 Spectral Changes

All of the boronic acid-functionalized azobenzene derivatives exhibited spectral changes when exposed to dopamine. Compounds 1 – 8 exhibited large shifts in absorption above 50 mM dopamine, however little change was observed in the lower concentration regions (1 – 25 mM) of the titrations. Compound 9 gave the best response at low concentrations (1 – 5 mM), with a correspondingly higher sensitivity to glucose and fructose as noted in Reference 13. Figure 5.3 shows the visible response of Compound 7 to dopamine (0 – 100 mM), and the comparative appearance of the same compound in 100 mM glucose, fructose, and dopamine (see Figure 5.4), where the compound shows no response to the two saccharides.

Figure 5.3 Visible change in the appearance of Compound 7 (10 μM in pH = 7.4 buffer) on titration with dopamine (0 – 100 mM). From left to right, dopamine concentration is: 0, 1, 5, 10, 25, 50, and 100 mM.

Figure 5.4 Visible change in the appearance of Compound 7 upon exposure to dopamine, glucose, and fructose. The solutions contain 10 μM indicator in pH = 7.4 buffer, and (from left to right) dopamine, glucose, and fructose at 100 mM.

Figures 5.5 – 5.13 show the response of Compounds 1 – 9 to dopamine over a range of concentrations. Compounds 1 – 8 were titrated from 0 – 100 mM, while Compound 9 was found to undergo saturation at much lower concentration and the figure depicts titration from 0 – 10 mM. Note that in all cases, the large absorbance below 320 nm is due to the dopamine itself.

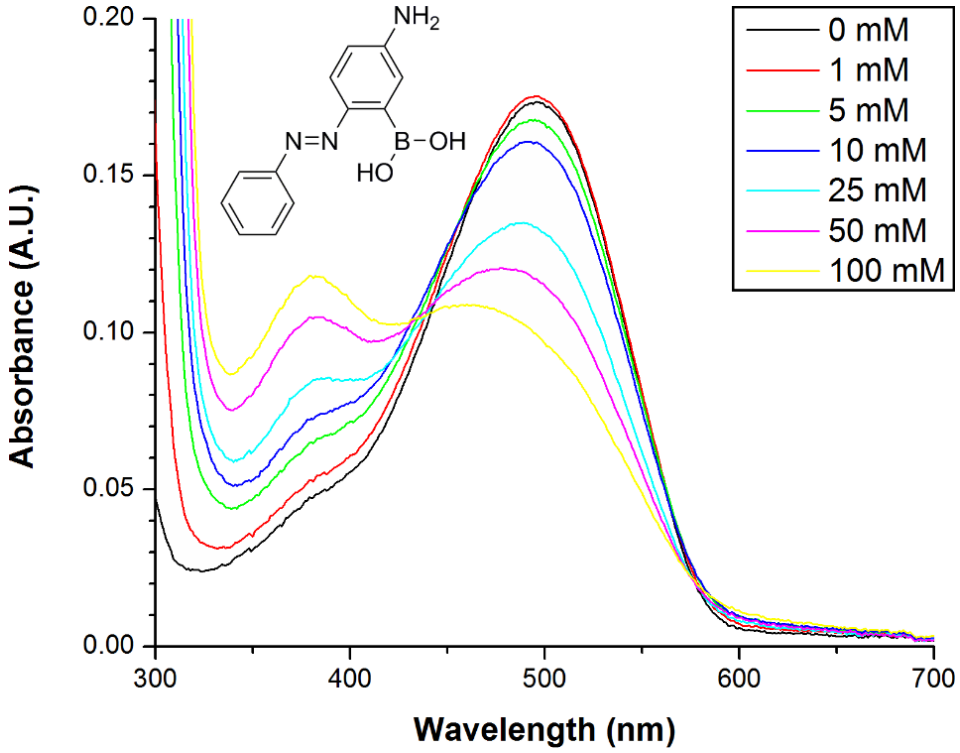


Figure 5.5 Spectral changes in Compound 1 upon titration with dopamine (0 – 100 mM).

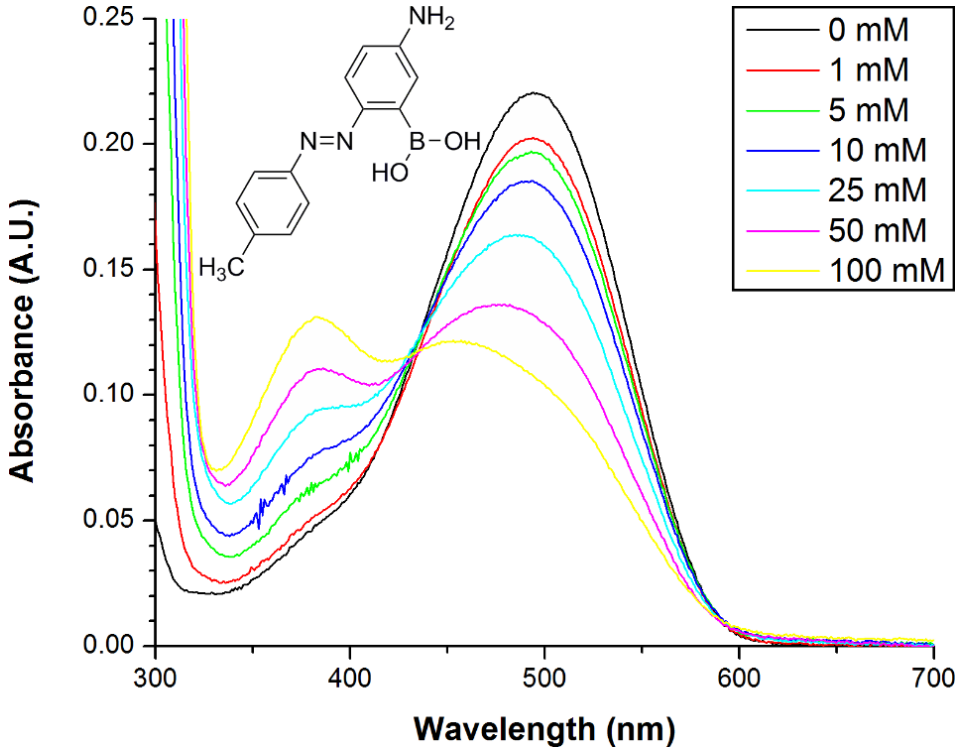


Figure 5.6 Spectral changes in Compound 2 upon titration with dopamine (0 – 100 mM).

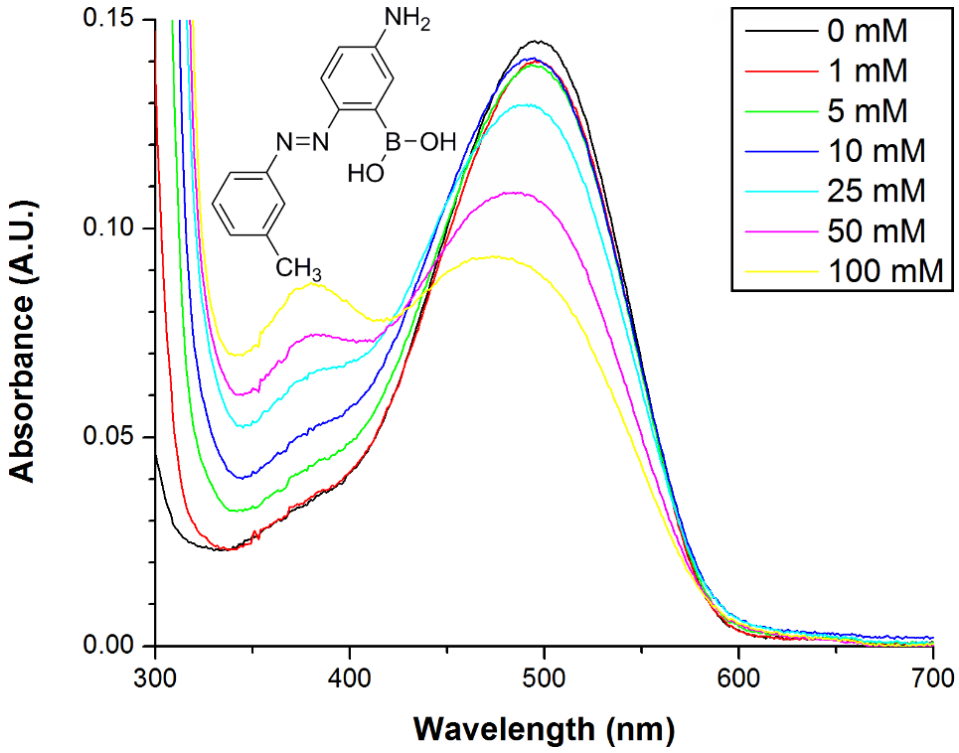


Figure 5.7 Spectral changes in Compound 3 upon titration with dopamine (0 – 100 mM).

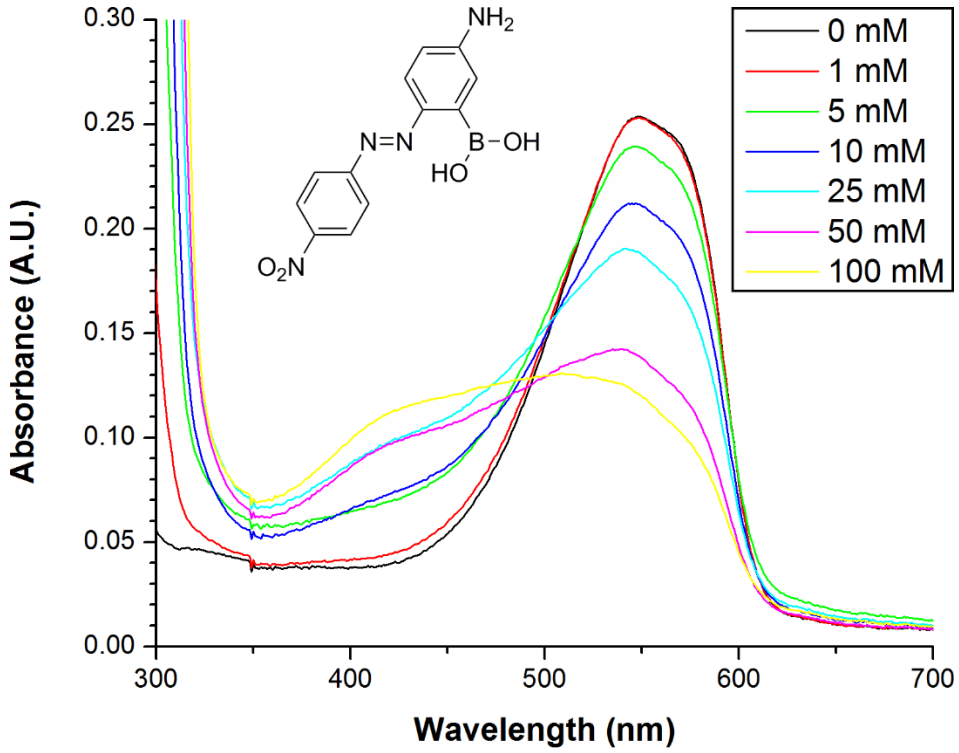


Figure 5.8 Spectral changes in Compound 4 upon titration with dopamine (0 – 100 mM).

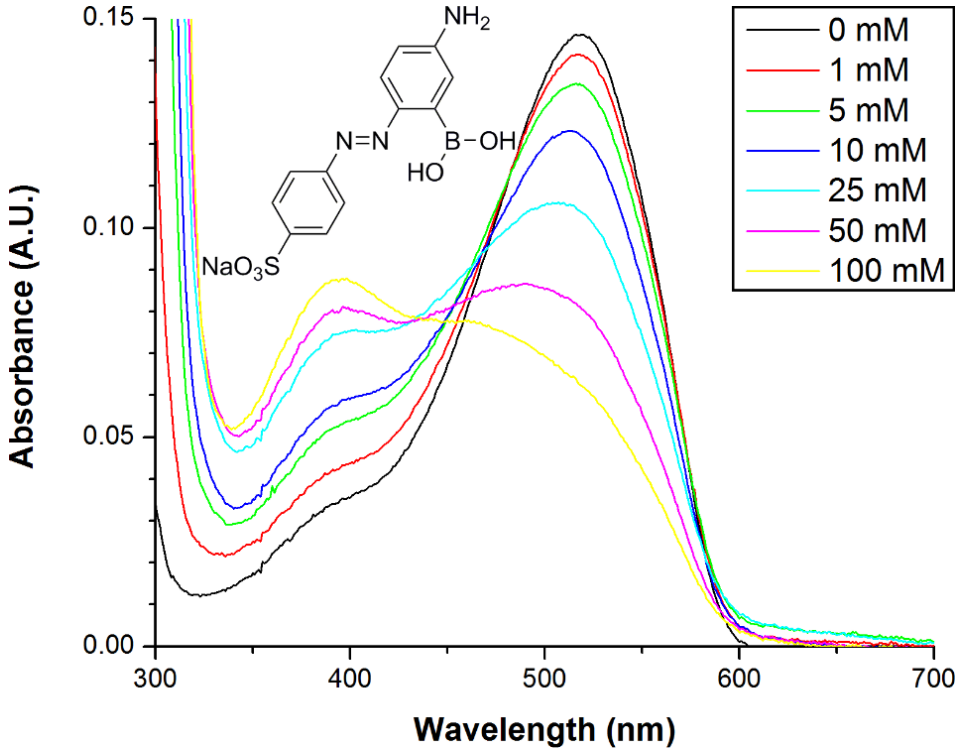


Figure 5.9 Spectral changes in Compound 5 upon titration with dopamine (0 – 100 mM).

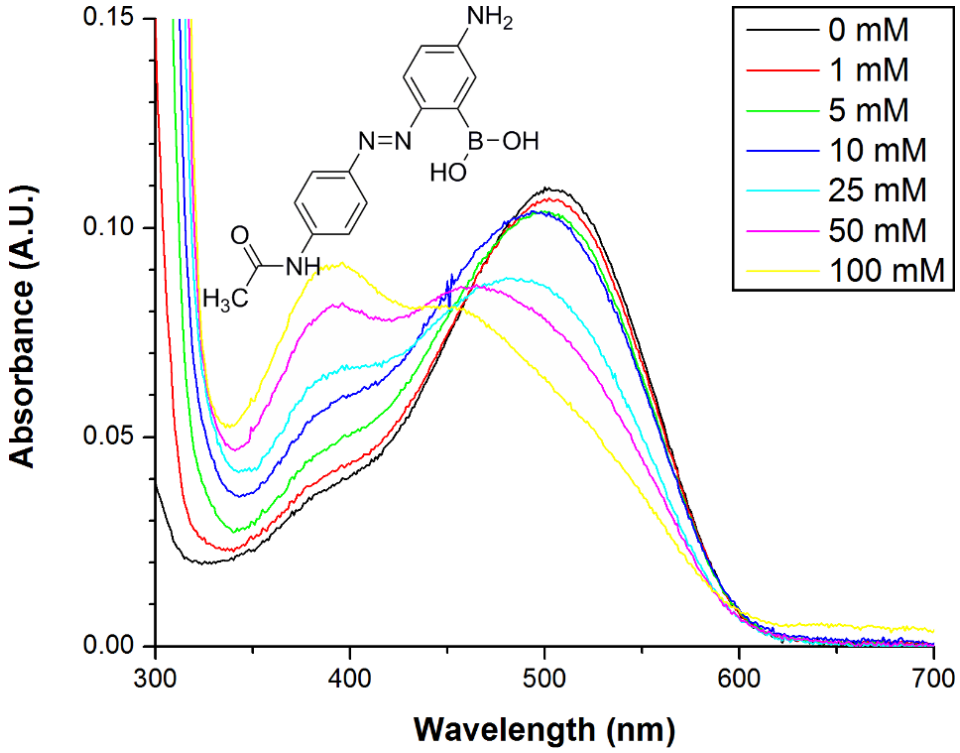


Figure 5.10 Spectral changes in Compound 6 upon titration with dopamine (0 – 100 mM).

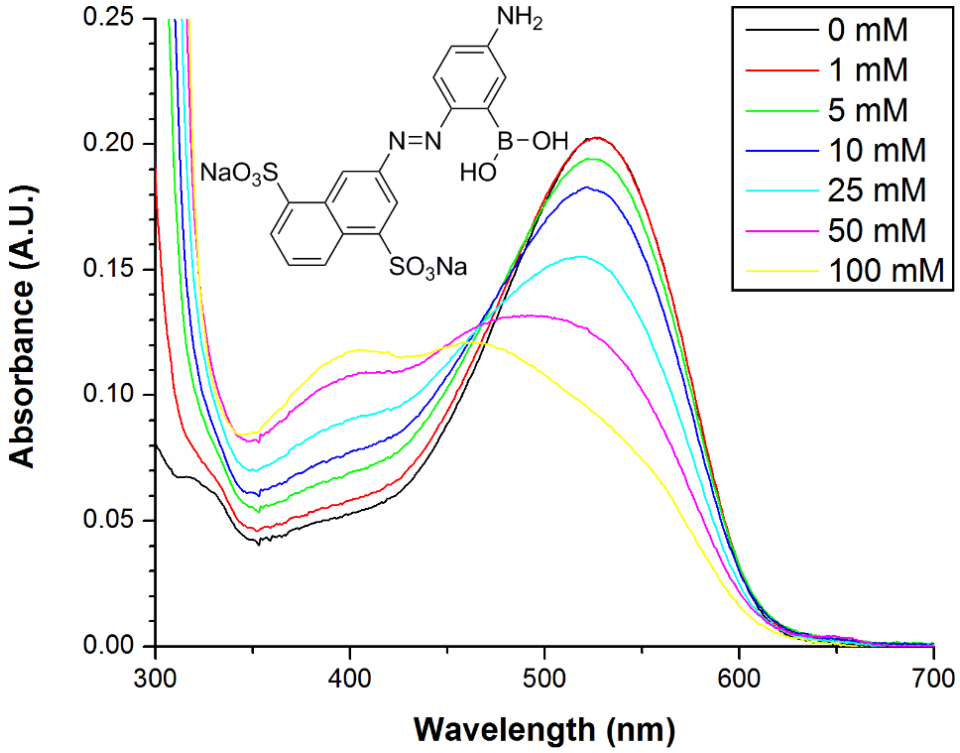


Figure 5.11 Spectral changes in Compound 7 upon titration with dopamine (0 – 100 mM).

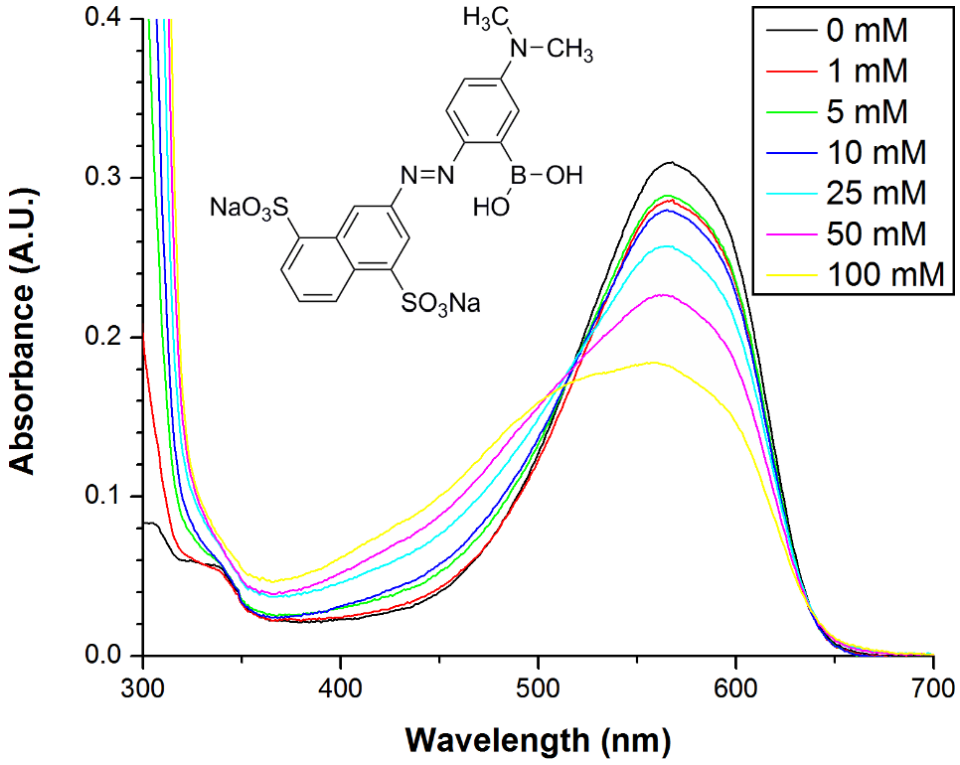


Figure 5.12 Spectral changes in Compound 8 upon titration with dopamine (0 – 100 mM).

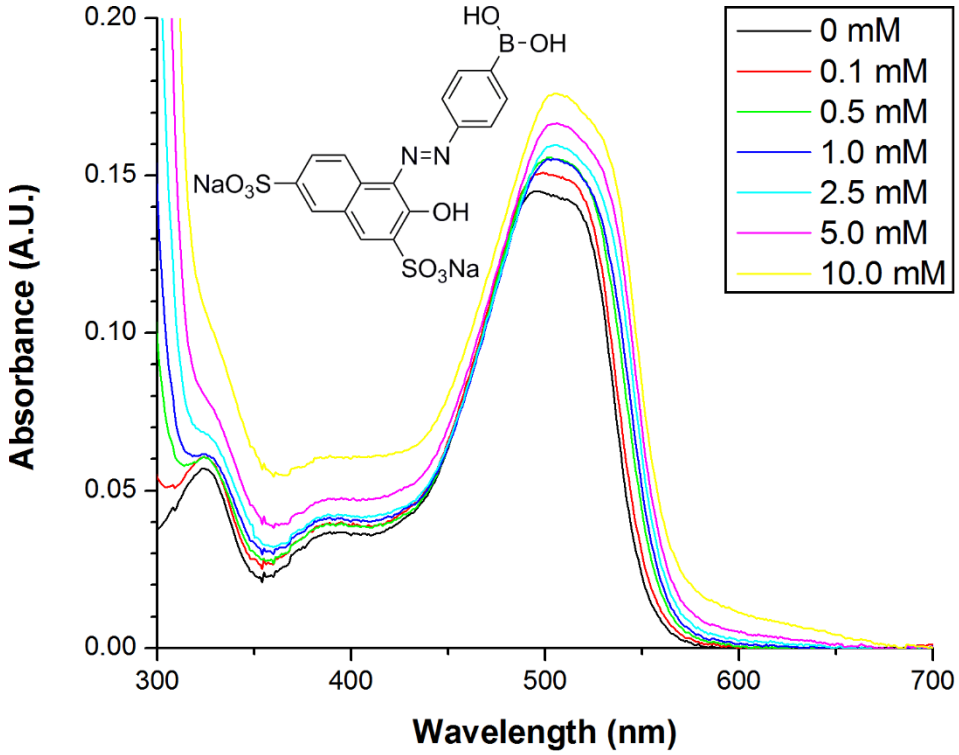


Figure 5.13 Spectral changes in Compound 9 upon titration with dopamine (0 – 10 mM). Although the degree of spectral shift is smaller in this compound, the concentration range is 10× lower than that of Compounds 1 – 8.

The data from the dopamine response curves is summarized in Figure 5.14. The curves for Compounds 1 – 8 all exhibit a similar decrease in absorbance, where Compound 9 exhibits an increase at the $\lambda_{max}$, and develops a redshifted shoulder.

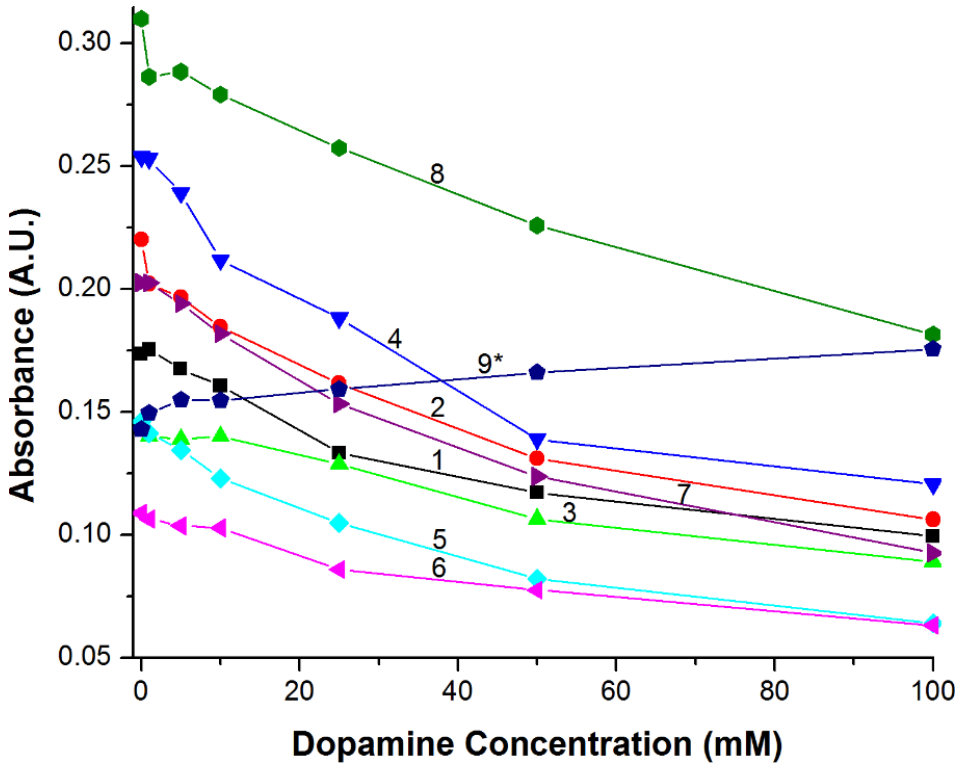


Figure 5.14 Change in visible absorbance of candidate indicator molecules upon titration with dopamine. The indicator molecules are in solution at 10 μM, and were titrated from 0 – 100 mM dopamine, except for Compound 9 which was titrated from 0 – 10 mM dopamine.

Compounds 1 – 6, which are all based on the same core molecule, show very similar responses, with a blueshifted absorbance appearing around 400 nm and a corresponding reduction in absorbance at the $\lambda_{max}$ centred at 525 nm (±25 nm). The feature centred at 400 nm corresponds to the dopamine-boronic acid complex, redshifted from the absorbance of pure dopamine between 200 – 300 nm. However, the degree of change in the $\lambda_{max}$ varies by about 10%, from 40 – 50% depending on the compound (see Figure 5.15 in Section 5.4.2 below). Compounds 7 and 8 vary over the same range, although Compound 8 is by far the most redshifted with a $\lambda_{max}$ at 568 nm, corresponding to its deep purple appearance in solution. Compound 9 only exhibits a 23% change in absorbance at the $\lambda_{max}$, but responds to dopamine concentrations an order of magnitude lower than the other compounds (*ca.* 10 mM).

Only Compound 2 exhibits a clear isosbestic point on titration with dopamine. This is likely due to the broad 350 – 650 nm feature present in the absorbance spectrum of pure dopamine, as shown in Figure 5.37.

### 5.4.2 Dopamine Spectral Response

The utility of the compounds described in this study as visible reporters for dopamine is a combination of the amount of dopamine required to induce binding, and the degree of spectral change upon complexation. Compounds 1 – 8 exhibit suitable levels of spectral change, as shown in Figure 5.15 below, however the concentration range over which they respond is significantly higher than dopamine concentrations *in vivo* (*ca.* 50 mM compared to *ca.* 5 mM in the brain).

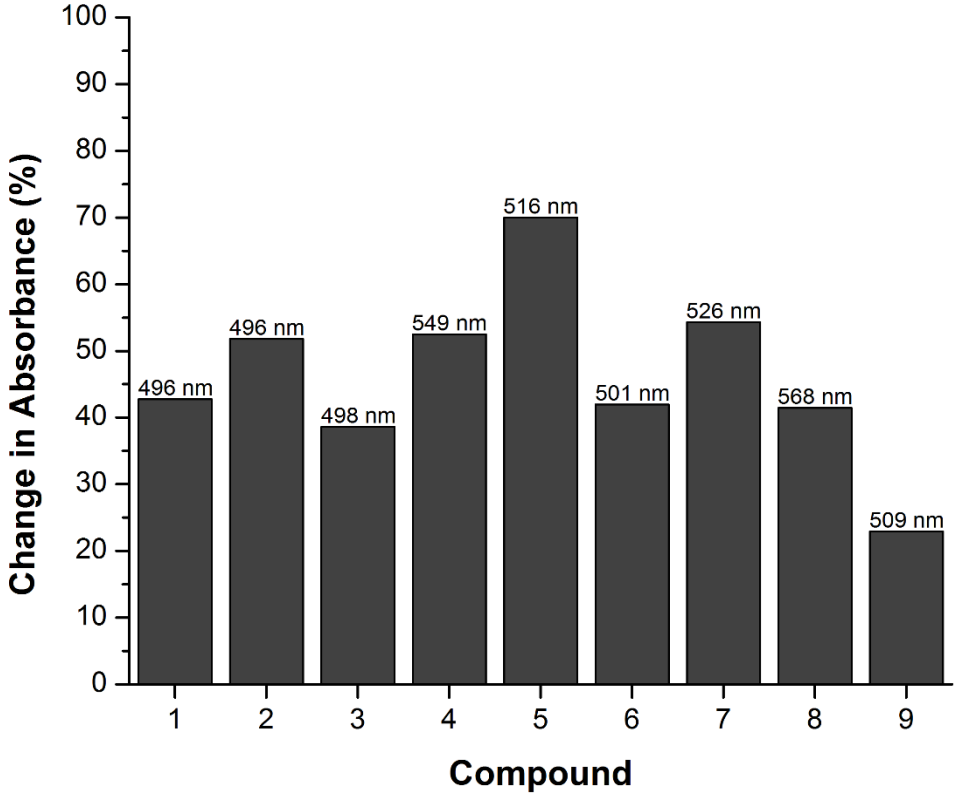


Figure 5.15 Percent change in absorbance at the $\lambda_{max}$ during titration with dopamine, at 10 µM indicator concentration. For Compounds 1 – 8, the maximum dopamine concentration was 100 mM; Compound 9 was titrated to 10 mM.

Compound 9 has a more subtle visible shift, changing from a red-orange colour to pink upon complexation, with a significant amount of overlap between the spectra of the bound and unbound indicator that obscures the change. Figure 5.16 shows the response of Compound 9 over a much lower concentration range (0 – 400 µM), where the visible response is still clearly visible, albeit relatively small at the $\lambda_{max}$.

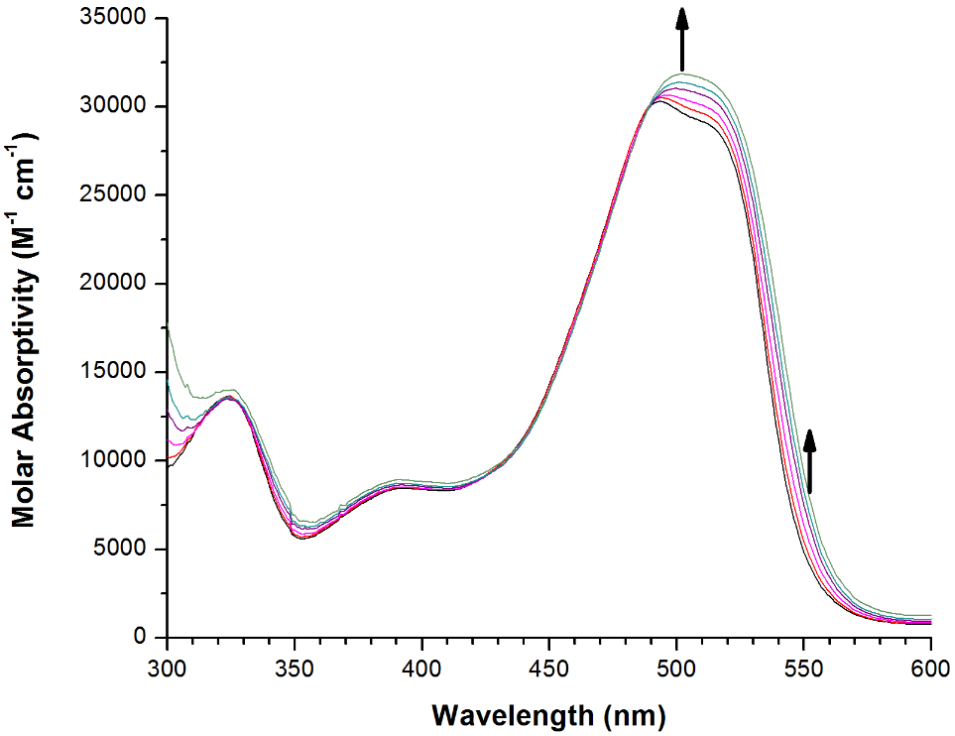


Figure 5.16 Absorbance spectra of Compound 9 upon titration with 0 – 20 equivalents of dopamine (indicator concentration: 20 μM). Note the increase in molar absorptivity near the $\lambda_{max}$ at 502 nm, and the development of a shoulder at 552 nm.

Although the change in absorbance at the $\lambda_{max}$ is small (~50% less) compared to Compounds 1 – 8, it is accompanied by the development of a significant shoulder at 552 nm where there is little absorbance from the unbound indicator (see Figure 5.17 below). Additionally, the compound responds to concentrations of dopamine more than an order of magnitude lower than those with the boronic acid moiety *ortho* to the azo bond, potentially rendering it the most useful compound as an indicator for dopamine.

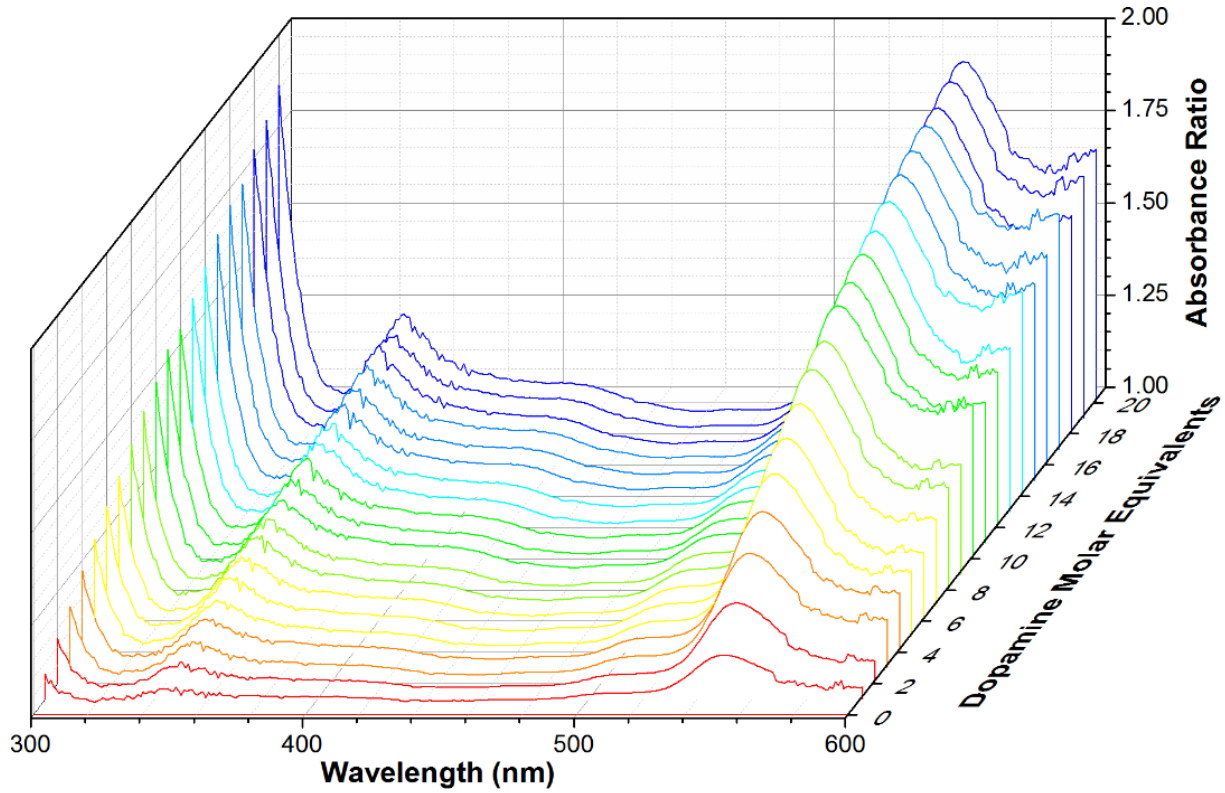


Figure 5.17 Ratio of absorbance spectra of Compound 9 with 0 – 20 equivalents of dopamine (indicator concentration = 20 μM). Note the large feature at 552 nm corresponding to the shoulder in Figure 5.16.

### 5.4.3 Sensitivity to Glucose and Fructose

With the exception of Compound 9, which exhibits a response to dopamine at much lower concentrations, none of the investigated compounds show an appreciable response to either glucose or fructose. This is consistent with the concentration responses for Compounds 1 – 8 vs 9, and is expected based on the previously reported binding constants of phenylboronic acid with saccharides (*ca.* $4\times10^3$) compared with the stronger binding of phenylboronic acid and catechol ($20\times10^3$).[17] Absorbance spectra for titrations with glucose and fructose are shown in the Supplementary Information (Section 5.7).

The lower affinity of the indicator molecules for saccharides compared with the catecholates is critical to their effective operation *in vivo*, where relatively high concentrations (*ca.* 5 mmol)[18] of saccharides can be found. No substantial response to saccharides is observed except for Compound 9, where 5 mM of saccharide produces a non-saturating response. As a result,

spikes in dopamine concentration, like those observed in neural impulses, would still be visible above the baseline change due to the presence of saccharide.

### 5.4.4 Indicator Stability

Several of the compounds exhibited limited stability in solution, undergoing decomposition (typically a large change in colour, often accompanied by the formation of precipitate) after only a few days. Compounds 4 and 5 (with *p*-$NO_2$ and *p*-$SO_3Na$ substituents, respectively) were stable for much longer in dilute solution, with their original colour persisting for weeks. Compound 9 appears to be stable in pH = 7.4 buffer indefinitely (see Figure 5.18), suggesting the higher reactivity may be due to the electronic donation of the azo-bond *ortho* into the boronic acid, which activates the B-N bond.[19,20]

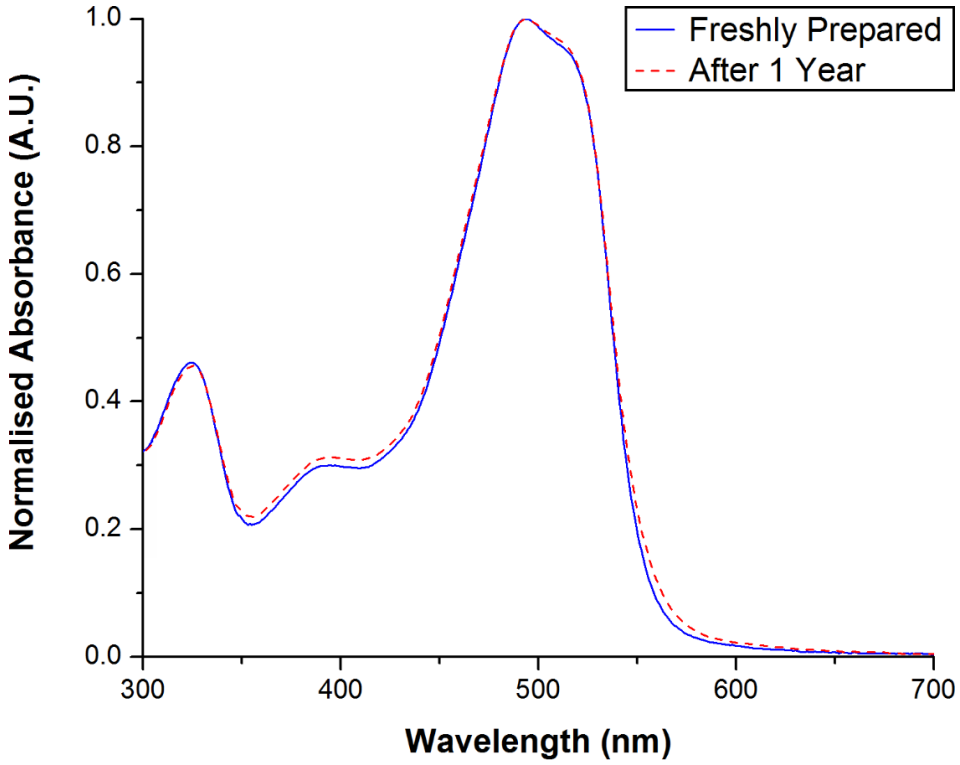


Figure 5.18 UV-vis traces of Compound 9 in pH = 7.4 buffer. The solid blue curve is a freshly prepared solution, while the dashed red line is the same compound after 1 year in solution.

The persistent strong colouration of all the decomposed indicators suggests the preservation of the azo moiety: analysis of the precipitate from a solution of Compound 2 show a single major product, with a similar ring substitution pattern. The high resolution mass spectrum

shows the decomposition product contains no boron, which is further corroborated by the behaviour of Compounds 7 and 8. Both decompose to a species with approximately the same deep red-orange colour after approximately one week in pH = 7.4 buffer, and exhibit no shift in absorbance when exposed to dopamine.

## 5.5 Conclusions

We have synthesized several boronic acid-functionalized azobenzene derivatives that act as colourimetric indicators for the neurotransmitter dopamine. The majority of the candidate indicators show an optical response in the 10 – 100 mM range, with one responding to dopamine concentrations more than an order of magnitude lower. Since biological dopamine concentrations are on the order of 0.1 – 5 mM, a combination of indicators could be used to determine dopamine concentration over a much larger range (0.1 – 100 mM). The candidate indicator compounds were also screened for their response to glucose and fructose, both of which are present in biological systems in up to millimolar concentrations. None of the compounds responded to glucose, and only one exhibited a reduced response to fructose, suggesting that biogenic saccharides do not interfere with the indicator's ability to report the presence and of dopamine. Although the stability of the indicators in biological pH conditions was variable, at least one compound was found to be stable indefinitely under the same conditions. The kinetics of the binding event were not explicitly investigated in this study: however, the colour change was qualitatively nearly instantaneous upon addition of the dopamine to the indicator solution. This represents an area of future study, since the timescale of neuronal impulses is on the order of milliseconds.

It should also be noted that one of the most important characteristics of this method of dopamine detection is that, unlike the vast majority of fluorescent NT and saccharide reporters, all indicators discussed here respond exclusively to visible light, with no need for harsh UV excitation. This is one of the greatest benefits of azo absorption-based compounds, and will greatly improve the biocompatibility of any device built with these systems as the active reporters.

## 5.6 References

1. P. Fattahi, G. Yang, G. Kim, and M. R. Abidian, *Adv. Mater.*, 2014, **26**, 1846–1885.

2. V. S. Polikov, P. A. Tresco, and W. M. Reichert, *J. Neurosci. Methods*, 2005, **148**, 1–18.

3. A. Goulet-Hanssens, K. Lai Wing Sun, T. E. Kennedy, and C. J. Barrett, *Biomacromolecules*, 2012, **13**, 2958–2963.

4. M. Sailer and C. J. Barrett, *Macromolecules*, 2012, **45**, 5704–5711.

5. J. M. Sugihara and C. M. Bowman, *J. Am. Chem. Soc.*, 1958, **80**, 2443–2446.

6. H. G. Kuivila, A. H. Keough, and E. J. Soboczenski, *J. Org. Chem.*, 1954, **19**, 780–783.

7. R. Nishiyabu, Y. Kubo, T. D. James, and J. S. Fossey, *Chem. Commun.*, 2011, **47**, 1124–1150.

8. A. J. J. Lennox and G. C. Lloyd-Jones, *Chem. Soc. Rev.*, 2014, **43**, 412–443.

9. A. Suzuki, *J. Organomet. Chem.*, 1999, **576**, 147–168.

10. X. Wu, Z. Li, X.-X. Chen, J. S. Fossey, T. D. James, and Y.-B. Jiang, *Chem. Soc. Rev.*, 2013, **42**, 8032–8048.

11. K. E. Secor and T. E. Glass, *Org. Lett.*, 2004, **6**, 3727–3730.

12. Y. Egawa, R. Gotoh, S. Niina, and J. Anzai, *Bioorg. Med. Chem. Lett.*, 2007, **17**, 3789–3792.

13. N. DiCesare and J. R. Lakowicz, *Org. Lett.*, 2001, **3**, 3891–3893.

14. E. Merino, *Chem. Soc. Rev.*, 2011, **40**, 3835–3853.

15. K. R. A. S. Sandanayake and S. Shinkai, *J. Chem. Soc. Chem. Commun.*, 1994, **4**, 1083–1084.

16. C. J. Ward, P. R. Ashton, T. D. James, and P. Patel, *Chem. Commun.*, 2000, 229–230.

17. J. P. Lorand and J. O. Edwards, *J. Org. Chem.*, 1959, **24**, 769–774.

18. M. M. Engelgau, K. M. Narayan, and W. H. Herman, *Diabetes Care*, 2000, **23**, 1563–1580.

19. N. Kano, J. Yoshino, and T. Kawashima, *Org. Lett.*, 2005, **7**, 3909–3911.

20. D. G. Hall, in *Boronic Acids: Preparation and Applications in Organic Synthesis and Medicine*, ed. D. Hall, Wiley-VCH Verlag GmbH & Co. KGaA, Weinheim, 2011.

## 5.7 Supplementary Information

### 5.7.1 Glucose Spectral Response

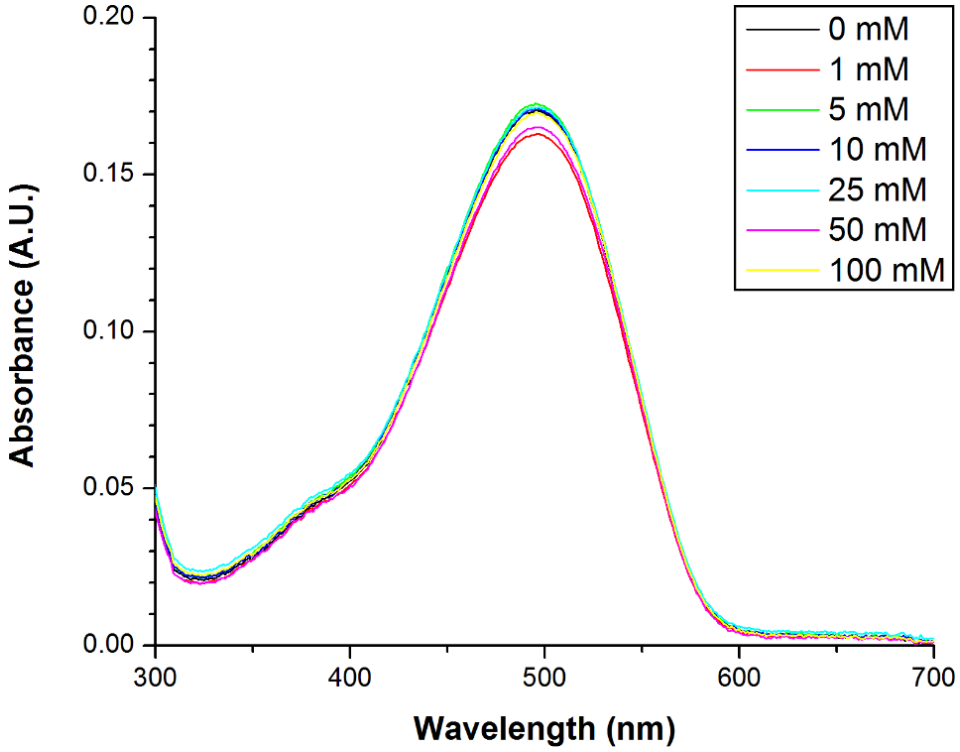


Figure 5.19 Spectral changes in Compound 1 upon titration with glucose (0 – 100 mM).

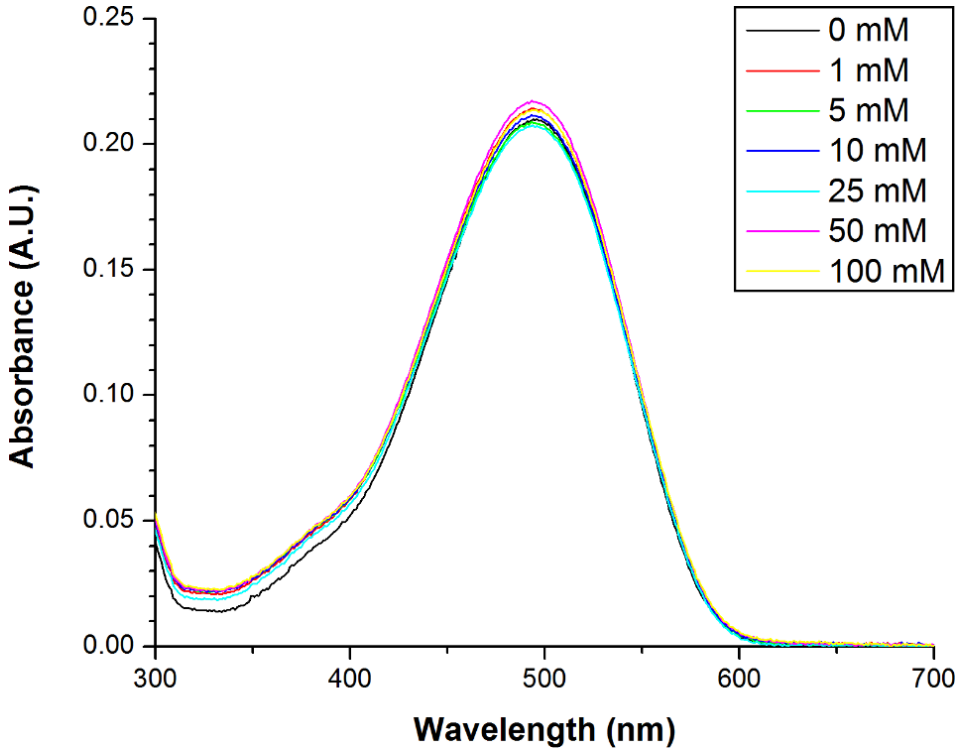


Figure 5.20 Spectral changes in Compound 2 upon titration with glucose (0 – 100 mM).

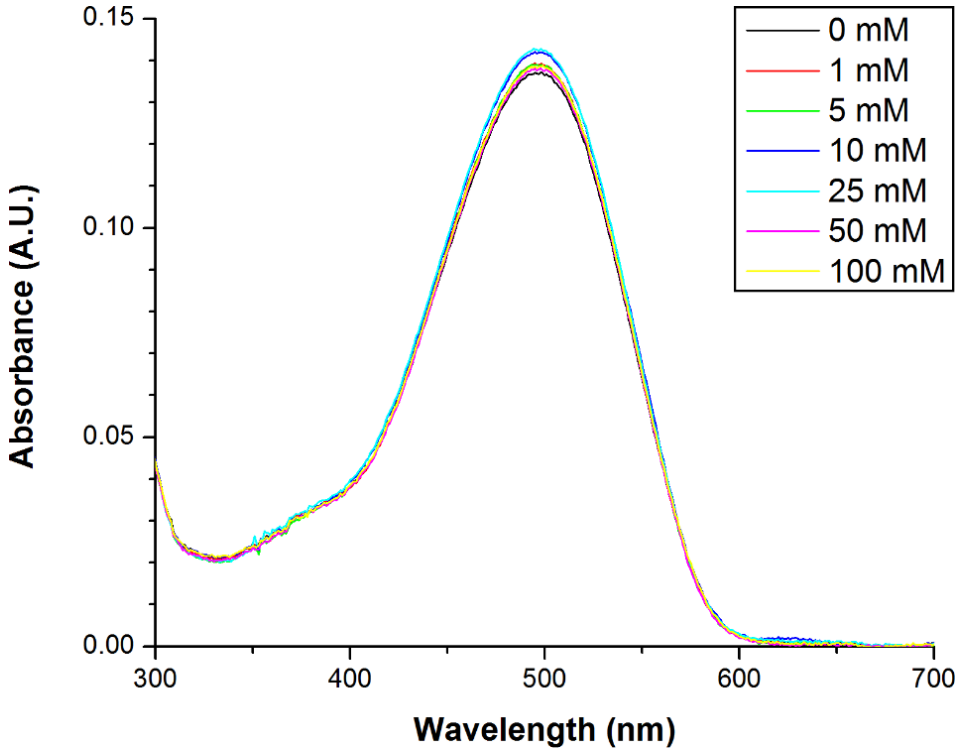


Figure 5.21 Spectral changes in Compound 3 upon titration with glucose (0 – 100 mM).

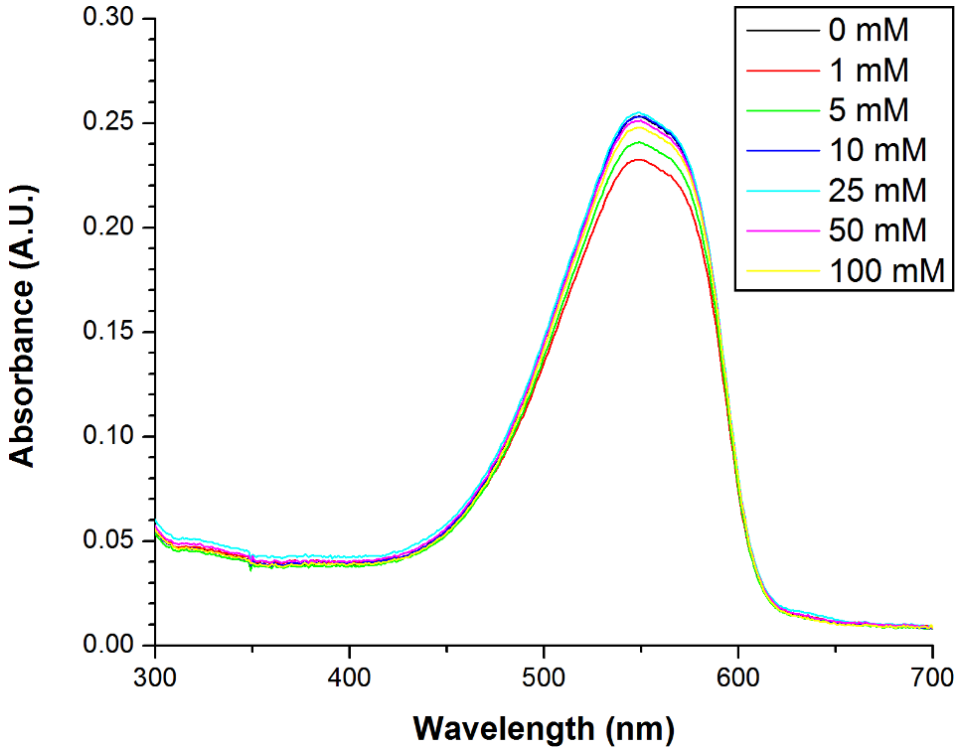


Figure 5.22 Spectral changes in Compound 4 upon titration with glucose (0 – 100 mM).

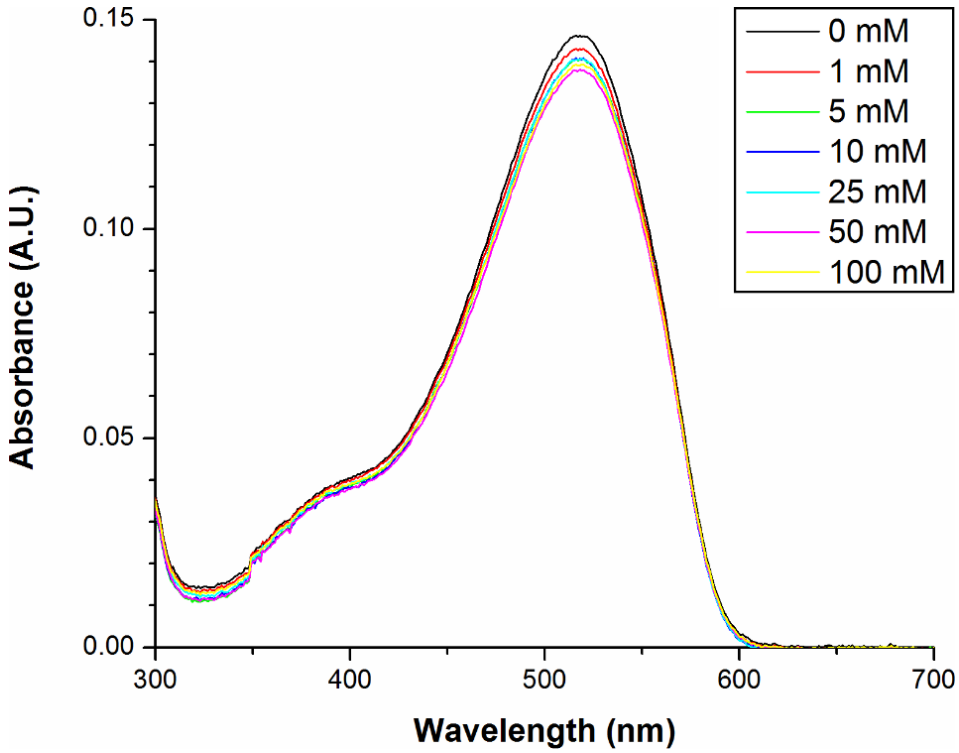


Figure 5.23 Spectral changes in Compound 5 upon titration with glucose (0 – 100 mM).

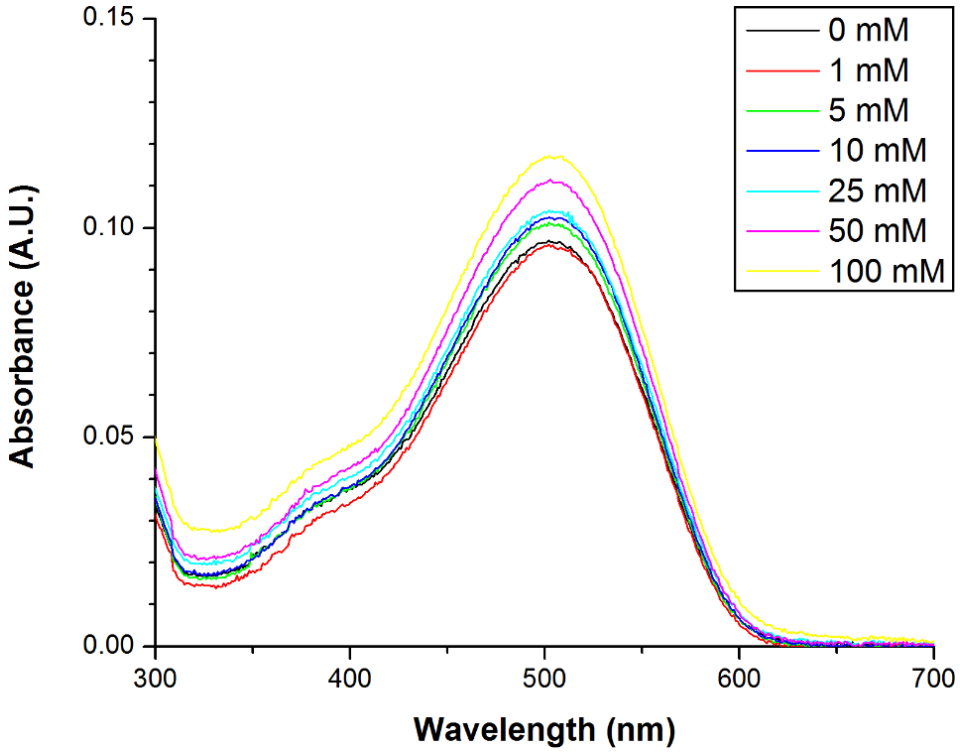


Figure 5.24 Spectral changes in Compound 6 upon titration with glucose (0 – 100 mM).

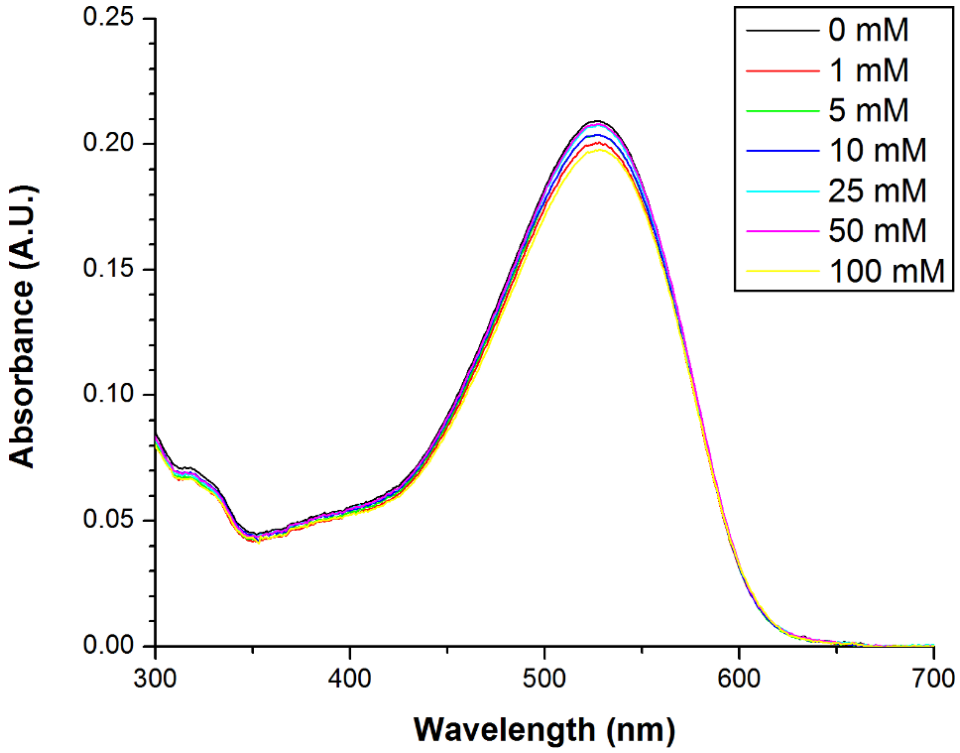


Figure 5.25 Spectral changes in Compound 7 upon titration with glucose (0 – 100 mM).

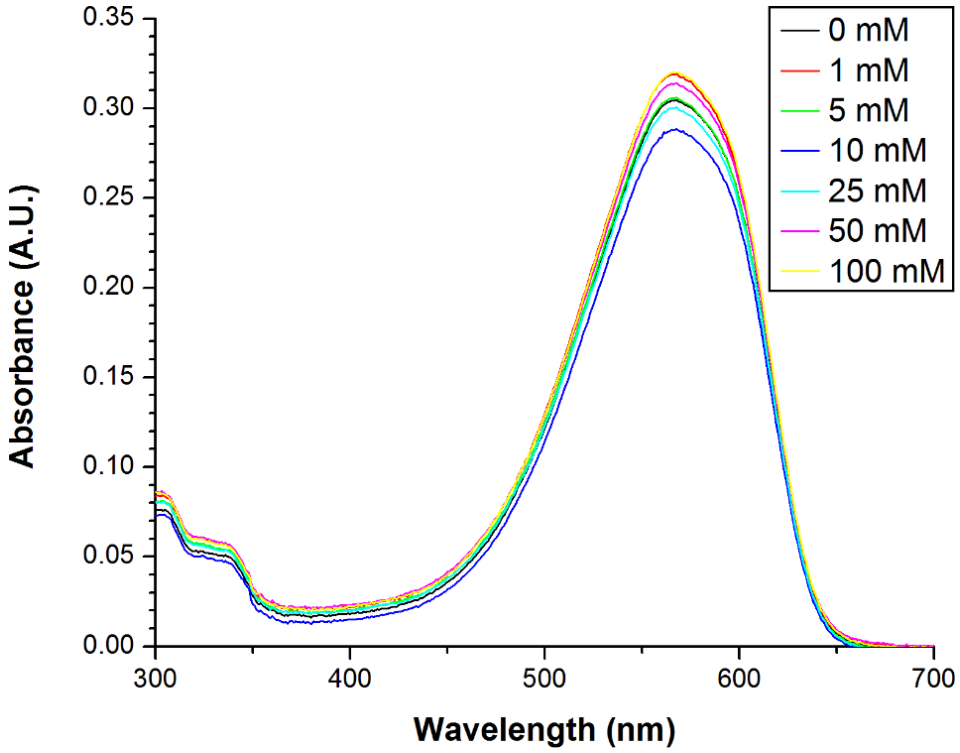


Figure 5.26 Spectral changes in Compound 8 upon titration with glucose (0 – 100 mM).

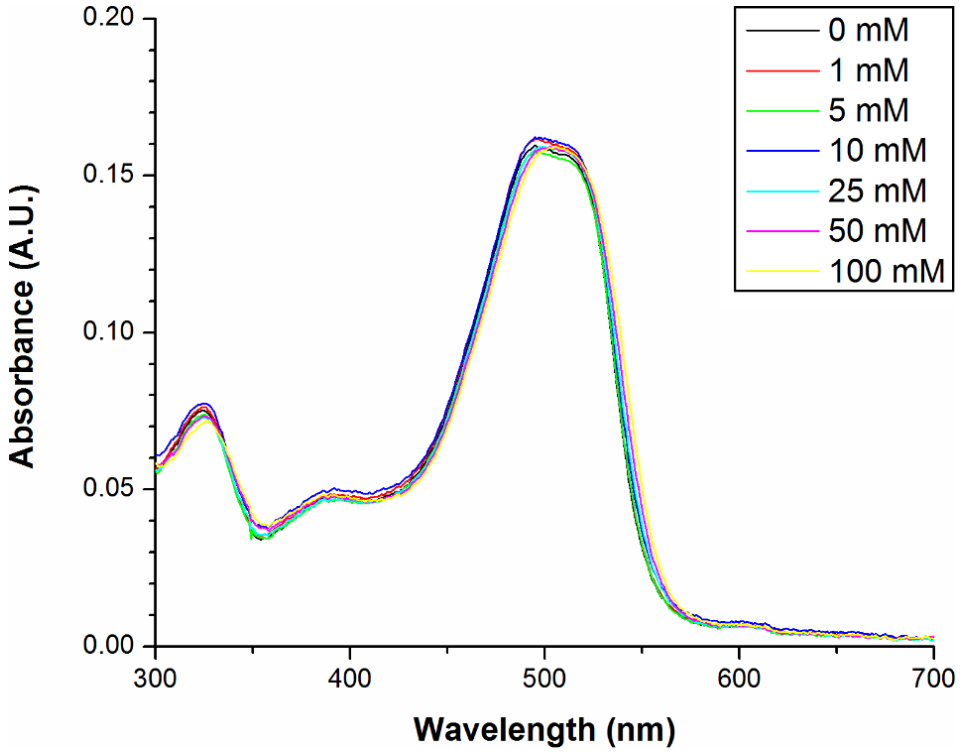


Figure 5.27 Spectral changes in Compound 9 upon titration with glucose (0 – 100 mM).

### 5.7.2 Fructose Spectral Response

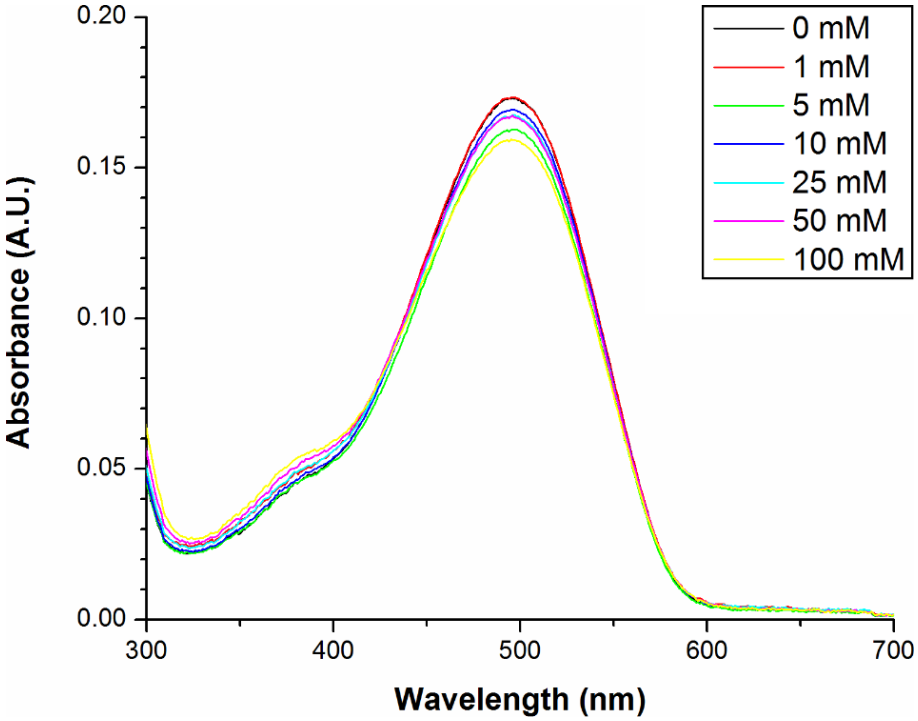


Figure 5.28 Spectral changes in Compound 1 upon titration with fructose (0 – 100 mM).

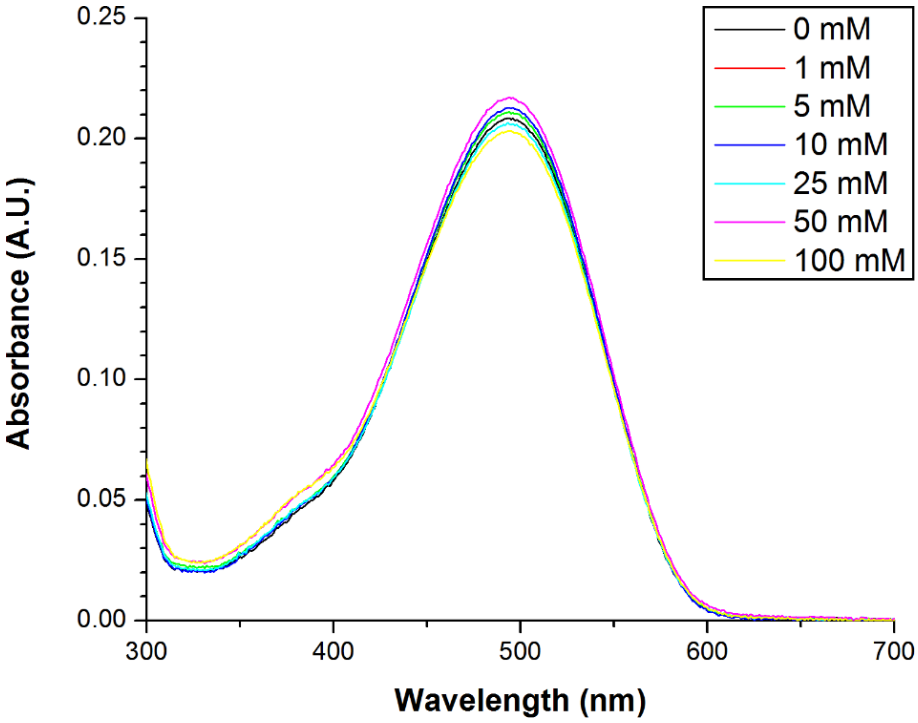


Figure 5.29 Spectral changes in Compound 2 upon titration with fructose (0 – 100 mM).

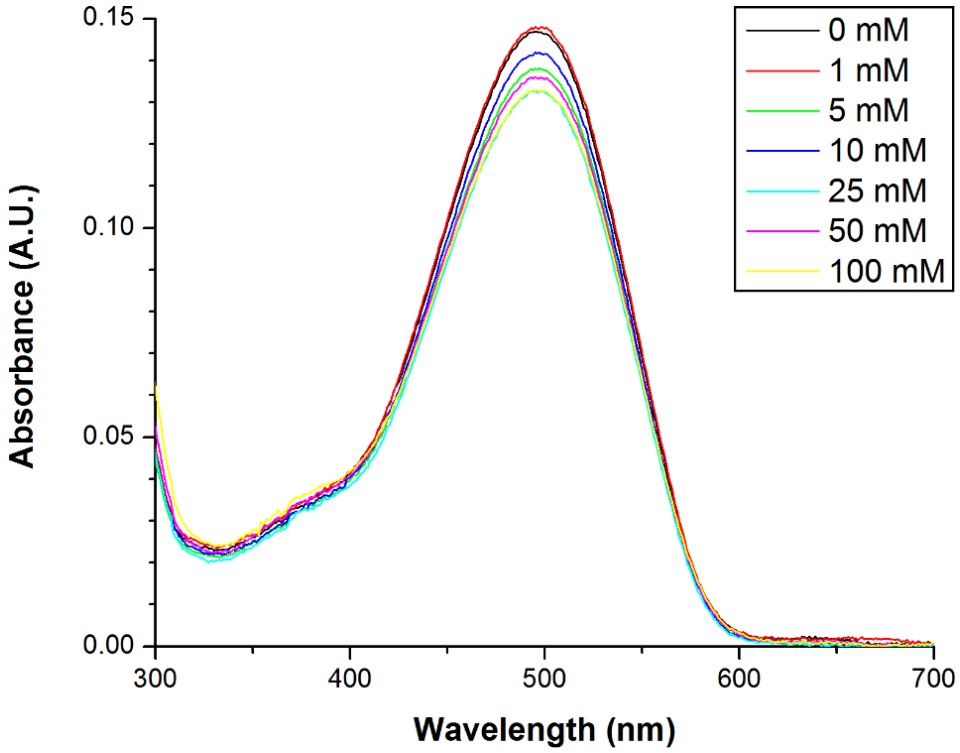


Figure 5.30 Spectral changes in Compound 3 upon titration with fructose (0 – 100 mM).

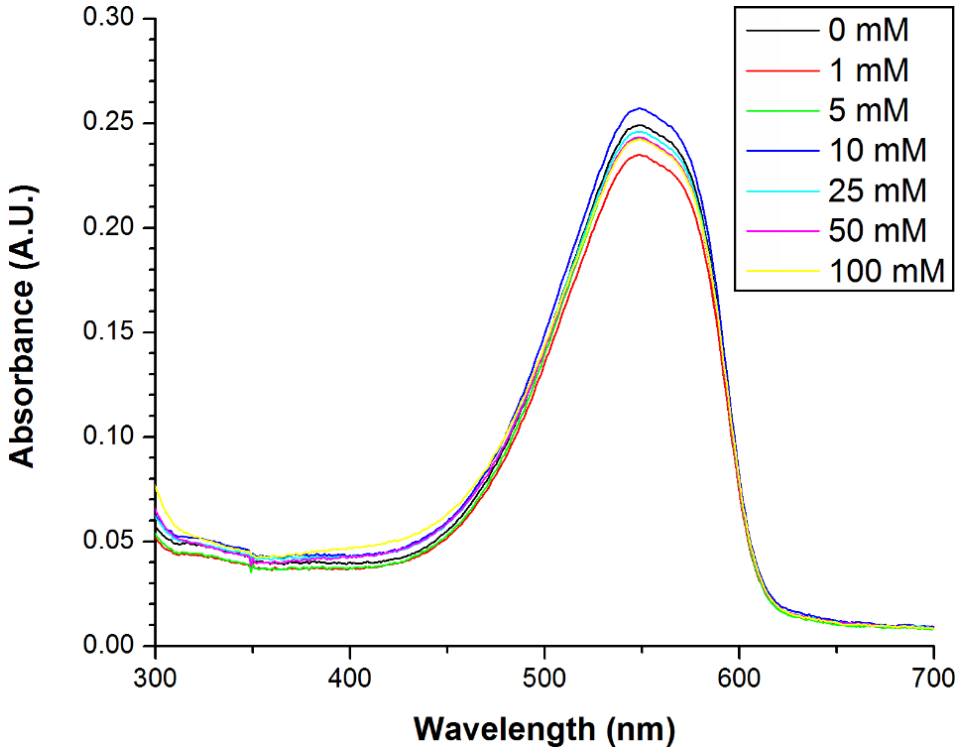


Figure 5.31 Spectral changes in Compound 4 upon titration with fructose (0 – 100 mM).

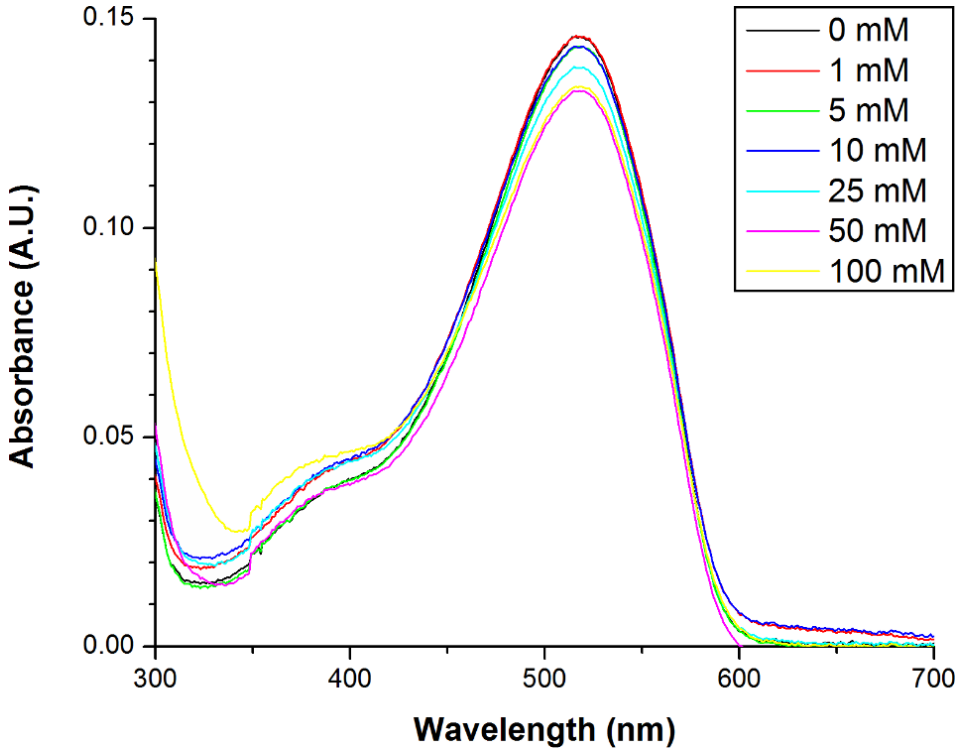


Figure 5.32 Spectral changes in Compound 5 upon titration with fructose (0 – 100 mM).

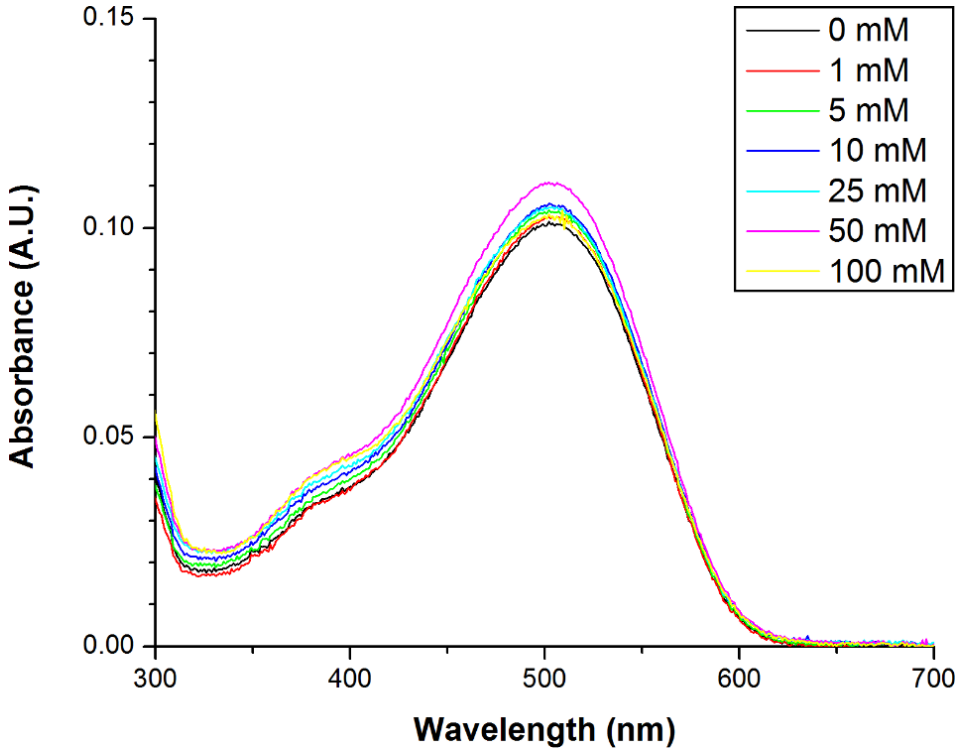


Figure 5.33 Spectral changes in Compound 6 upon titration with fructose (0 – 100 mM).

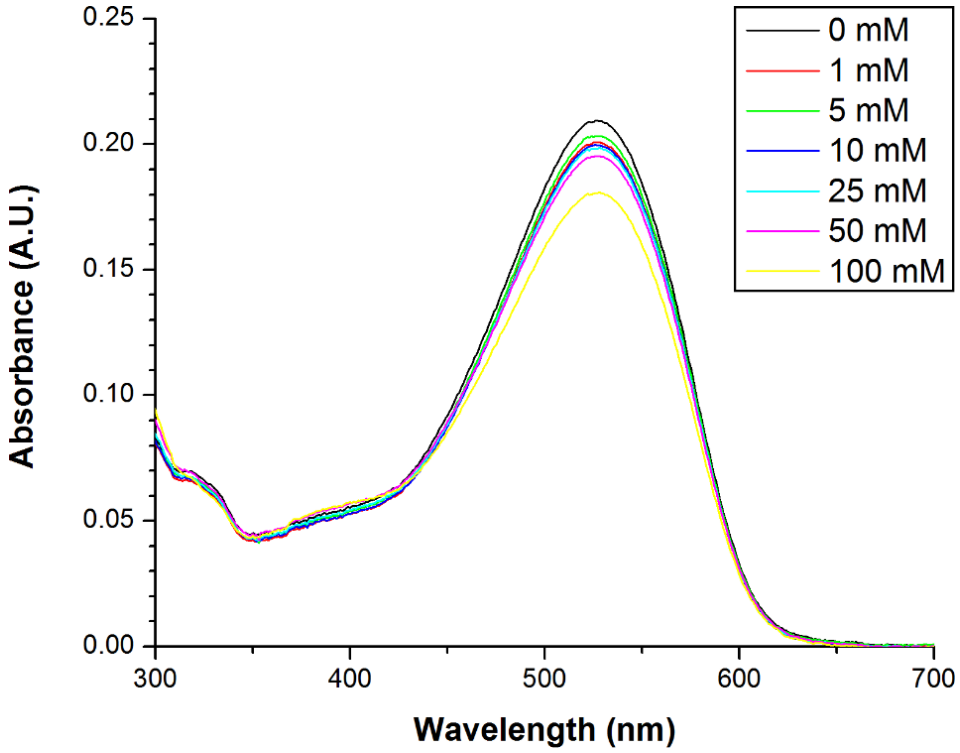


Figure 5.34 Spectral changes in Compound 7 upon titration with fructose (0 – 100 mM).

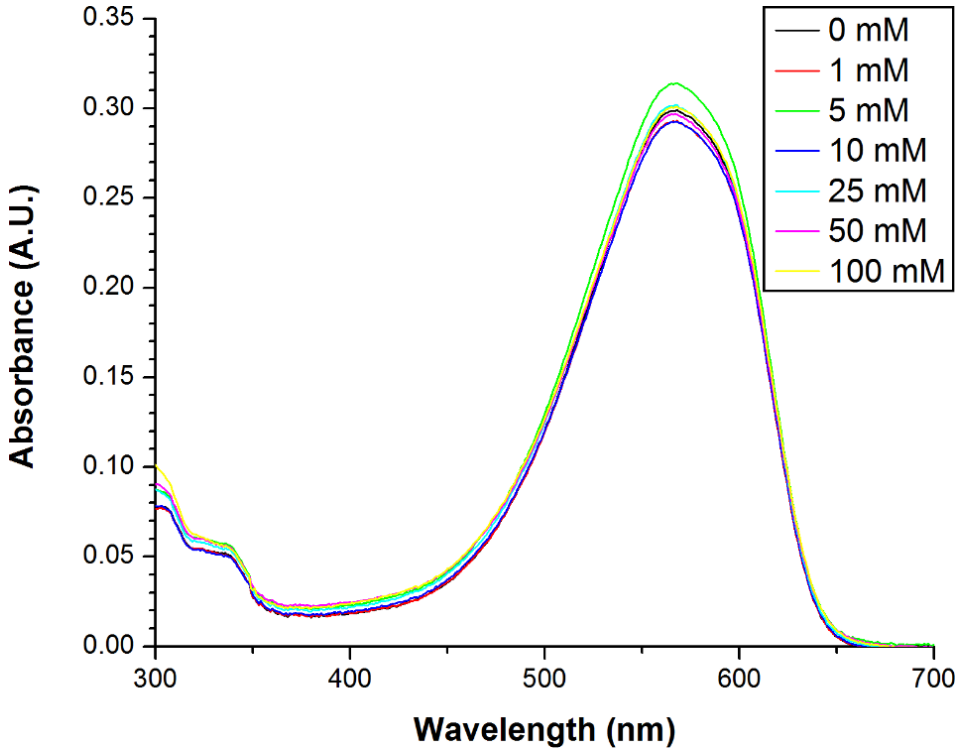


Figure 5.35 Spectral changes in Compound 8 upon titration with fructose (0 – 100 mM).

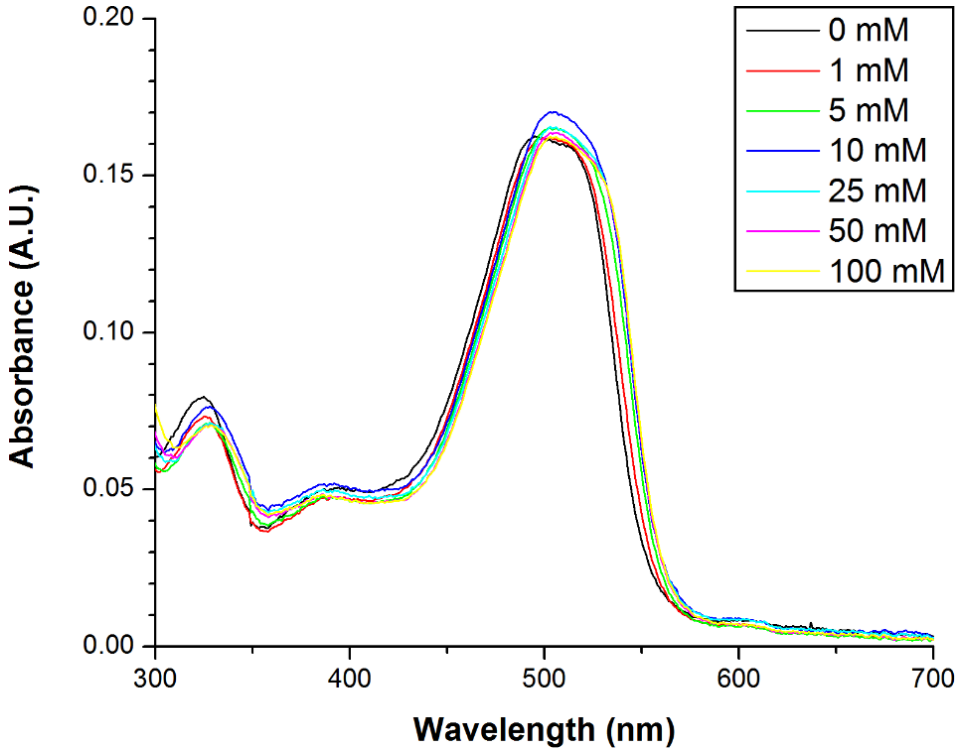


Figure 5.36 Spectral changes in Compound 9 upon titration with fructose (0 – 100 mM).

### 5.7.3 Analyte Spectral Response

Blank titrations were performed with each of the three analytes (dopamine, glucose, and fructose) to ensure the effect of the unbound analyte on the indicator response spectra was minimal. This is true for glucose and fructose, which exhibit effectively no absorbance features above 300 nm, and minimal for dopamine, which has a broad feature at ~475 nm, which only represents an absorbance of ~0.1 A.U. at 100 mM.

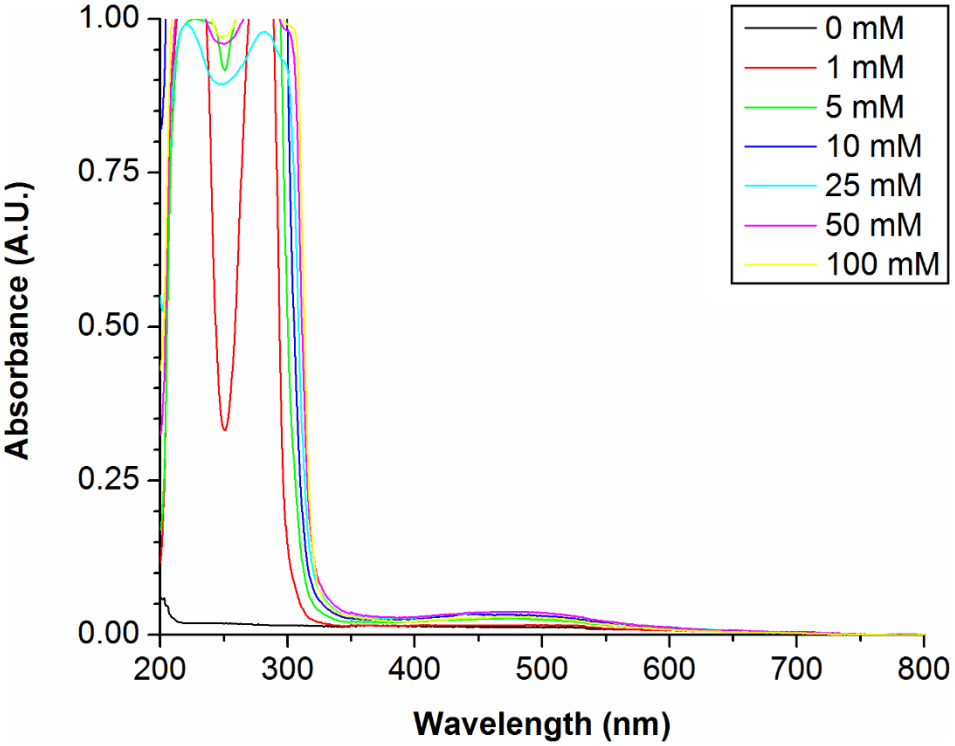


Figure 5.37 Blank titration of dopamine in pH = 7.4 buffer (0 – 100 mM).

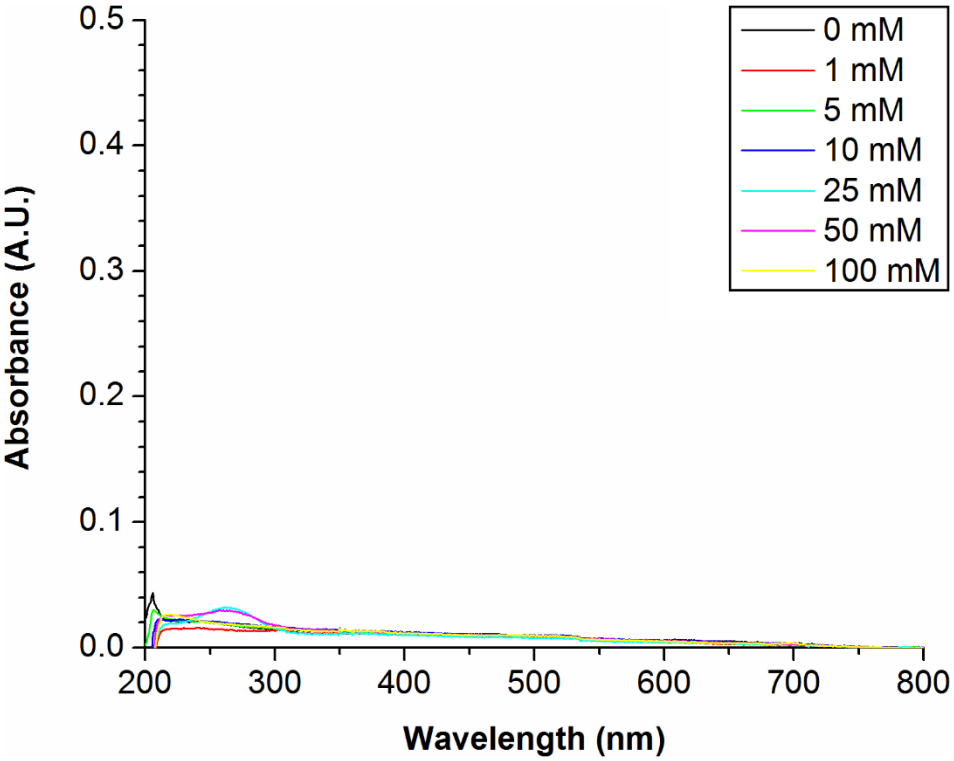


Figure 5.38 Blank titration of glucose in pH = 7.4 buffer (0 – 100 mM).

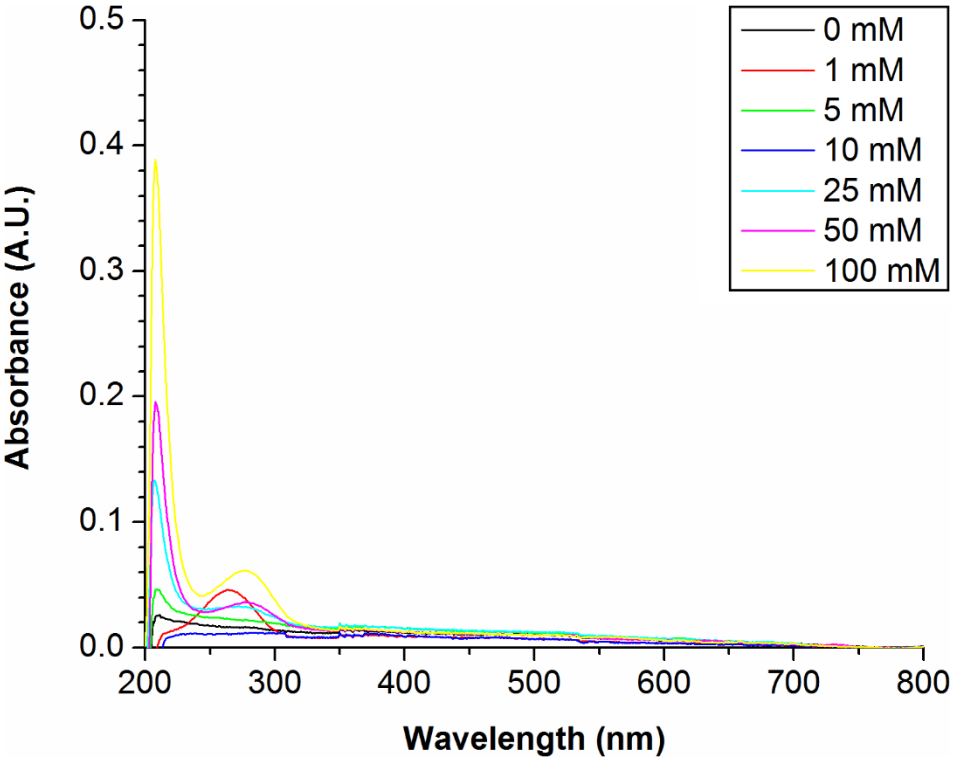


Figure 5.39 Blank titration of glucose in pH = 7.4 buffer (0 – 100 mM).

## Rationale for: Polymer Coatings for Neurotransmitter Detection

The limits of current technology for measuring brain activity demands new techniques capable of operating *in vivo* for much longer periods of time. The inherent bio-incompatibility of hard electrical probes with soft brain tissue results in rejection of implants over relatively short time periods. These probes cannot easily be coated to enhance their biocompatibility, due to the resulting reduction in sensitivity caused by masking the electrode. Optical probes do not suffer from these limitations; the only requirement for surface coatings is that they be transparent to the optical signal. In this chapter, we present a novel approach for detecting neuronal impulses, based on colourimetry. Several boronic acid-functionalized azo compounds from Chapter 5, screened for their spectral response to dopamine, are chemically or physically appended to polyelectrolyte multilayers which act as a convenient platform for the indicator, and additionally act as biocompatible coatings for the probe material. The probe itself is a cleaved fibre optic (glass or plastic), which provides a conduit for the optical measurements to be made.

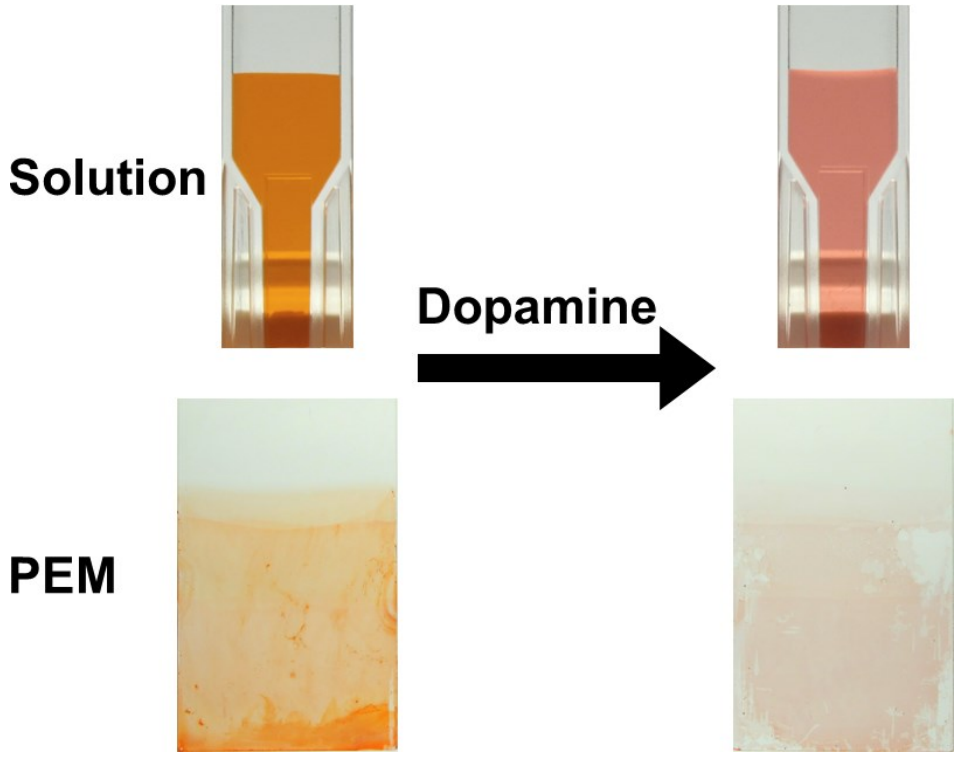


*Strong colour change visible in original thesis submission file format. May not fully reproduce clearly in PDF versions or print.

# Chapter 6: Polymer Coatings for Neurotransmitter Detection

## 6.1 Abstract

Boronic acids are well known for their ability to strongly and selectively bind with vicinal diols. When attached to a chromophore or fluorophore, this binding can turn the photoactive base into a visible reporter for vicinal diols, such as those found on monosaccharides, or on the catecholamine class of neurotransmitters. This detection scheme was demonstrated in the previous chapter for the neurotransmitter dopamine with both indicator and analyte in solution. In this chapter, we present progress towards the development of an all-optical, biocompatible implant capable of detecting neural activity in the form of dopamine release. Five indicator systems, three of which are based on polyelectrolyte multilayer films doped with indicators from Chapter 5, as well as two polyelectrolytes with covalently-bound indicators, have been prepared. Their optical response to dopamine in solution was measured on flat substrates, and some preliminary progress towards adapting the system to the surface of an optical fibre probe is presented to demonstrate future potential.

## 6.2 Introduction

Current methods of locally monitoring neural activity *in vivo* are most often based on the implantation of small, conductive electrical probes into neural tissue to detect electrical impulses. Electrical probes, being almost exclusively made of hard, electrically-conductive materials, suffer the major drawback of rejection by the body after relatively limited periods of time.[1–3] Additionally, even though many technologies exist to enhance the biocompatibility of implants, these techniques tend to fail when applied to electrodes, as they are usually based on polymer coatings which have the unwanted effect of diminishing the electrical sensitivity of the probe. For this reason we propose an all-optical probe, sensitive to the presence of neurotransmitters, which can be made biocompatible without compromising the sensitivity of the measurement.

Dopamine is one of a small number of core neurotransmitters used to mediate neuronal impulses in the brain. Parkinson's disease is characterized by the mass death of dopamine-producing neural cells, resulting in a lack of available dopamine to mediate neural signals and a

corresponding lack of motor function. Dopamine, a catecholamine, is structurally similar to two other important compounds that act both as neurotransmitters and hormones: epinephrine (adrenaline) and norepinephrine (noradrenaline) pictured in Figure 6.1 below. Neuronal impulses occur as spikes of NT release, which simplifies the problem of detection by requiring only the ability to determine changes in concentration of NTs, not absolute concentration.

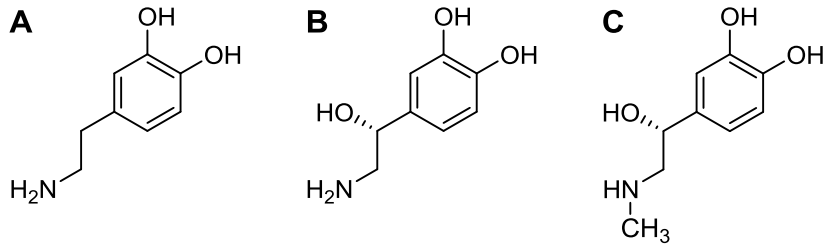


Figure 6.1 The three main aminocatecholate neurotransmitters: A) dopamine mediates signals within the frontal cortex of the brain, while B) norepinephrine and C) epinephrine also act as hormones used to convey signals from the sympathetic nervous system to various organs.

Dopamine occurs naturally at low levels in the body (ca. 0.5 – 25 nM in cerebrospinal fluid),[4] but the instantaneous concentration in the synaptic gap can be considerably higher, reaching into the tens of millimolar concentration range in the millisecond timescale of neuronal impulses.[5] The concentration inside the *vesicles*, the tiny containers that hold the NTs prior to release into the synaptic gap, can be even higher, at 100 – 200 mM. NT-molecules are loaded into vesicles via active proton pumping, resulting in a drop in pH upon vesicle release during the transmission of neural impulses.[6] As a result, the pH conditions in the brain vary depending on the location and the level of brain activity, and can be lower by ~0.5 pH units from the baseline physiological pH of 7.4. The pH conditions are important to this study due to the pH-dependent nature of NT-binding by boronic acids, as discussed in Section 1.5.3.1.

The indicator molecules described in the previous chapter demonstrated the ability of boronic acid-functionalized azo compounds to act as visible reporters for dopamine. Unlike the UV excitation required for many fluorophore-based reporters, the low power visible light required for azobenzene-based chromophores is generally not harmful to biology, which represents a major advantage of our proposed system. To be useful for *in vivo* detection, these indicator molecules must be immobilized on the surface of the probe, which in our proposed system is an optical fibre.

Although optical fibres, which are composed of either glass or polymers, suffer from the same problems of modulus mismatch with biology as electrical probes, fibres can easily be made functionalized with biocompatible films such as polyelectrolyte multilayers, which need only be partially transparent to visible light to allow the probe to operate.

Polyelectrolyte multilayers (PEMs) are formed by the alternating immersion of a substrate into solutions of positive and negative polyelectrolytes (charged polymers).[7] They have been demonstrated in numerous studies to enhance the biocompatibility of hard substrates, due to their high water content, charge, and low, tuneable modulus.[8–10] They can be assembled on effectively any surface which can provide even a modest surface charge,[11] forming thermodynamically and kinetically stable films. Four types of polyelectrolytes are used in this study: hyaluronic acid (HA) and poly(allylamine hydrochloride) (PAH) are used to form a stable matrix to immobilize charged indicator compounds for neurotransmitters, while poly(dimethyldiallylammonium chloride) (PDADMAC) is co-assembled with two indicator-functionalized poly(acrylic acid) (PAA) polymers.

Three of the indicators from the previous chapters were selected to be embedded in a multilayer composed of PAH, a commonly-used weakly cationic polyelectrolyte, and HA, a bio-derived anionic polyelectrolyte. These films were demonstrated in a previous study to undergo large changes in thickness in response to the pH of their environment, and to absorb and immobilize charged small molecules in the biological pH regime.[12] HA-based films have also been demonstrated as good substrates for cell growth *in vitro*,[13,14] and HA itself is found in numerous areas of the body including joints, the vitreous humour, and the brain.[15] The small molecule indicators were chosen based on two main criteria: the first is that the molecule be charged, which is critical both for the uptake and immobilization of the indicator in the multilayer structure. The second criterion is the efficacy of the candidate indicator itself, as determined in Chapter 5 based on the degree of spectral change, and the concentration of dopamine required to induce the change. Three indicators were selected: Compounds 7 – 9 from Chapter 5, shown in Figure 6.2 below:

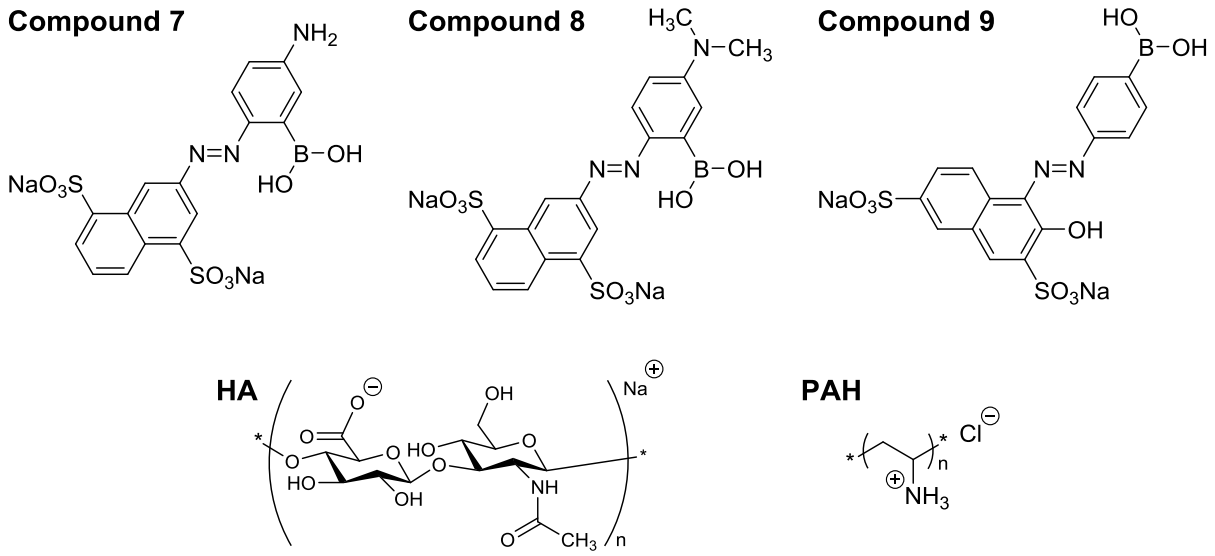


Figure 6.2 The three candidate indicator molecules selected for uptake into the PAH/HA multilayers (Compounds 7 – 9). All three have sulfonate functional groups, which lends an effectively pH-independent negative charge, allowing them to be immobilized in the PEM matrix. The bottom row shows the structure of the polyelectrolytes hyaluronic acid and poly(allylamine hydrochloride), used to fabricate the PEMs for immobilizing the indicator compounds on the fibre surface.

In addition to the three small-molecule indicators immobilized in the polyelectrolyte matrix, two PAA-based polymers covalently functionalized with different indicators were prepared, shown in Figure 6.3. PDADMAC, is a strong, positively-charged polyelectrolyte used to assemble the PEMs in conjunction with Polymers 1A and 1B.

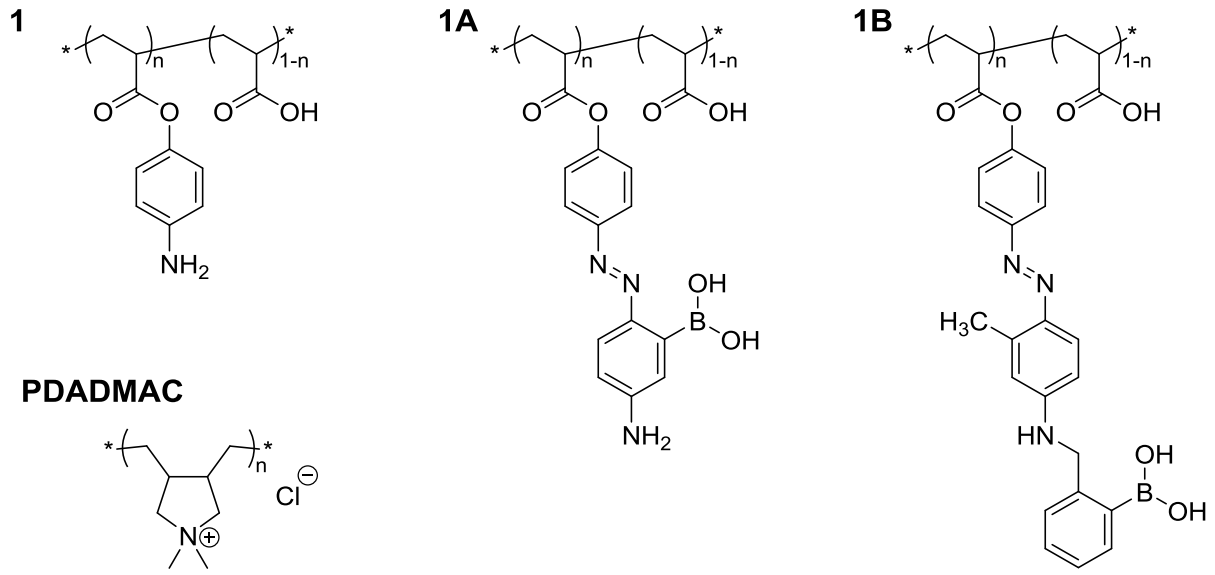


Figure 6.3 The covalently-functionalized polymers used in this study. 1A) and 1B) are poly(acrylates) directly functionalized with azo-boronic acids, based on Polymer 1. PDADMAC is a strongly positively-charged polyelectrolyte used to assemble PEMs with Polymers 1A and 1B.

The indicator-functionalized fibres can be assembled on the surface of an optical fibre with conventional PEM-assembly conditions. The active sensing area of the fibre is stripped of its protective cladding, which acts to optically isolate the fibre from its surroundings. As light propagates through the fibre, some light is able to couple with the chromophores via the evanescent wave, which penetrates a short distance from the fibre surface into the surrounding media where the cladding has been removed (depending on the ratio of indices of refraction of the fibre and surroundings). This coupling allows the absorbance spectrum of the indicators to be measured, including the changes that occur upon dopamine binding. In the first development stages of this work, measurements are made in a large-area linear transmission configuration, with the light travelling from the source, along the length of the fibre and sensor section, to the detector. Ultimately, this configuration could be changed to a small-diameter, coated terminal reflection type single-mode probe (such as the one described in Reference 16), which can more easily be implanted: tip configurations are discussed in more depth in Section 1.6.2 of Chapter 1.

## 6.3 Experimental Section

### 6.3.1 General Considerations

All commercial materials (solvents and reagents) were used as received unless otherwise noted. $^{1}H$, HSQC, and HMBC NMR spectra were acquired with either a Bruker 500 or 400 MHz spectrometer; $^{13}C$ spectra were acquired with a Varian 75 MHz spectrometer. Chemical shifts are reported in ppm on the δ-scale, referenced to the solvent residual signal. High-resolution mass spectrometry was performed using a Bruker Maxis Impact Quadrupole-Time of Flight mass spectrometer with a source voltage of 4.5kV. Gel permeation chromatography was performed with an Agilent GPC 50 equipped with two analytical columns (mixed beds, PolyAnalytik).

### 6.3.2 Synthetic Details

The synthesis of the indicator molecules (Compounds 7 – 9) is described in the previous chapter. Polymer 1 was prepared via free-radical polymerization of acrylic acid and 4-aminophenylacrylate (Compound 3), initiated thermally by asobisisobutyronitrile (AIBN). Polymer 1 was then diazotized, and functionalized with either 3-aminophenylboronic acid or Compound 4 to form Polymers 1A and 1B, respectively.

**Synthesis of *tert*-butyl (4-hydroxyphenyl)carbamate (Compound 1)**

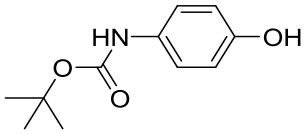


1.09 g *p*-aminophenol (10 mmol, Alfa Aesar) was dissolved in 50 mL THF in a 100 mL round bottom flask. To the stirring solution was added 2.30 mL Boc anhydride (10 mmol, Oakwood). The solution was capped with a vented septum, and set stirring overnight. The reaction progress was followed by TLC (5% MeOH/95% DCM): after 18 hours it was judged complete, and the solvent, Boc anhydride, and *t*-butanol were removed under reduced pressure, giving a light tan solid in quantitative yield which was used without further purification.

$^{1}$H NMR (300 MHz, chloroform-*d*) δ ppm 1.51 (s, 9 H), 5.50 (br. s., 1 H), 6.36 (br. s., 1 H), 6.75 (d, 2 H), 7.18 (d, 2 H).

$^{13}$C NMR (75 MHz, chloroform-*d*) δ ppm 28.4, 80.4, 115.7, 121.3, 131.0, 151.9, 153.5.

HR-MS (ESI, 4.5 kV): *m/z* Calculated for $C_{11}H_{14}NO_3^-$ [**M** – H]$^-$: 208.0979; found: 208.0974.

**Synthesis of 4-((*tert*-butoxycarbonyl)amino)phenyl acrylate (Compound 2)**

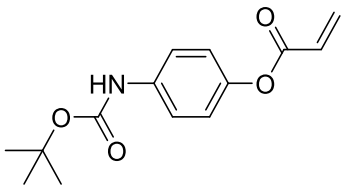


To a 100 mL flask containing the crude *tert*-butyl (4-hydroxyphenyl)carbamate (2.09 g, 10 mmol) was added 4.2 mL of triethylamine (30 mmol, Fisher) and 50 mL of dichloromethane, and the flask was stirred until the solid dissolved. A solution of 1.21 mL acryloyl chloride (45 mmol, Sigma Aldrich) dissolved in 10 mL DCM was added to the flask dropwise, with stirring. The reaction was monitored by TLC (40% EtOAc/60% hexanes), and judged complete after 2 hours. The solvent was removed from the crude mixture under reduced pressure, and the resulting tan solid was purified by column chromatography on an 80 g silica gel column (0 – 30% EtOAc/hexanes). The product was isolated as a crystalline white solid in quantitative yield.

$^{1}$H NMR (500 MHz, chloroform-*d*) δ ppm 1.47 (s, 9 H), 5.96 (d, 1 H), 6.26 (dd, 1 H), 6.55 (d, 1 H), 6.77 (br. s., 1 H), 7.01 (d, 2 H), 7.37 (d, 2 H).

$^{13}$C NMR (125 MHz, chloroform-*d*) δ ppm 28.3, 80.5, 119.3, 121.8, 127.9, 132.5, 136.1, 145.8, 152.7, 164.7.

HR-MS (ESI, 4.5 kV): *m/z* Calculated for $C_{14}H_{17}NNaO_4^+$ [**M** + Na]$^+$: 286.1050; found: 286.1052.

**Synthesis of 4-aminophenyl acrylate (Compound 3)**

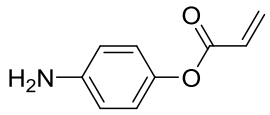

All of Compound 2 (~10 mmol) was dissolved in 150 mL of dichloromethane in a 250 mL round bottom flask. The flask was cooled on ice, and 14.5 mL of trifluoroacetic acid (50 mmol, Sigma Aldrich) was added dropwise. The flask was allowed to warm to room temperature, and was stirred overnight. The reaction mixture was poured into a 500 mL separatory funnel, neutralized with dilute sodium hydroxide, and washed with water. The solvent was removed *in vacuo*, and the resulting yellow-brown oil was purified by column chromatography on an 80 gram silica column using a 0 – 40% gradient of ethyl acetate in hexanes. The product was isolated as a yellow oil (darkens on standing) in 23% yield.

$^{1}$H NMR (500 MHz, chloroform-*d*) δ ppm 3.66 (br. s., 2 H), 5.98 (dd, 1 H), 6.31 (dd, 1 H), 6.58 (dd, 1 H), 6.68 (d, 2 H), 6.92 (d, 2 H).

$^{13}$C NMR (125 MHz, chloroform-*d*) δ ppm 115.6, 122.1, 128.1, 132.1, 142.7, 144.2, 165.1.

HR-MS (ESI, 4.5 kV): *m/z* Calculated for $C_9H_{10}NO_2^+$ [**M** + H]$^+$: 164.0706; found: 164.0706.

**Synthesis of poly(acrylic acid-*co*-4-aminophenyl acrylate) (Polymer 1)**

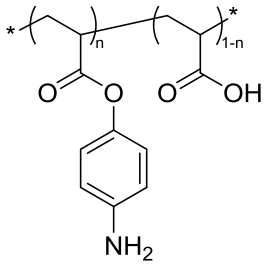


To a 25 mL polymerization ampoule equipped with a rotaflow stopcock was added 0.19 g 4-aminophenyl acrylate (Compound 3; 1.2 mmol), 0.45 mL acrylic acid (redistilled; 6.6 mmol), 0.0575 g AIBN (recrystallized from methanol, 4.5 mol %, Sigma Aldrich), and 16 mL THF (inhibitor free, HPLC grade). The solution was degassed with three cycles of freeze-pump-thaw, and was then purged with argon and sealed. The ampoule was stirred in a 60 °C oil bath for 48 hours, then cooled to room temperature. The solution was decanted from the ampoule, and the solvent removed *in vacuo*. The crude polymer was then redissolved in 5 mL THF, and slowly dropped into 200 mL dichloromethane with vigorous stirring. The solid was then filtered and dried *in vacuo*, yielding 0.51 g pale yellow solid in a 70.3% yield. $^1$H NMR shows a ratio of ~12:1 acrylic acid/aniline mers.

$^1$H NMR (500 MHz, DMSO-$d_6$) δ ppm 1.2 – 2.1 (-*CH*$_2$-CH-), 2.1 – 2.4 (-CH$_2$-*CH*-), 6.5 – 7.7 (arom. *CH*), 12.2 (-*COOH*).

GPC trace (THF): 18.4 minutes, corresponding to a MW = 2258 g·mol$^{-1}$ with a PDI = 1.29.

**Synthesis of poly(acrylic acid-*co*-(*E*)-(2-((4-(acryloyloxy)phenyl)diazenyl)-5-aminophenyl)boronic acid) (Polymer 1A)**

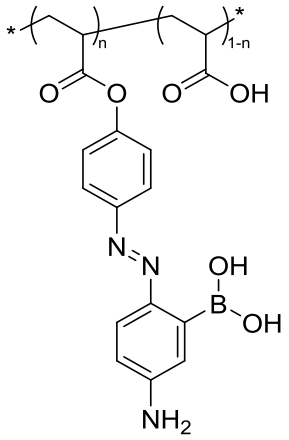

To a 25 mL round bottom flask was added 0.10 g Polymer 1 (0.1 mmol amine mer), 5 mL DMF, 5 mL water, and 0.13 mL c. HCl (1.5 mmol). The solution was stirred on ice until the temperature was <5 °C, then 0.50 mL of cold 0.2 M sodium nitrite was added dropwise. The solution was stirred on ice for 15 minutes to facilitate the formation of the diazonium salt, then a cold solution of 0.0138 g of 3-aminophenylboronic acid (0.1 mmol, Boron Molecular) in 1 mL water and 1 mL DMF was added dropwise. The solution was neutralized with 1 M $NH_4OH$, then allowed to stir on ice for 2 hours before being brought to room temperature. The solvent was removed under reduced pressure, yielding a reddish solid. The crude product was redissolved in 6 mL DMF, then added dropwise to a stirring flask of 250 mL ethyl acetate. The polymer suspension was covered and allowed to stir overnight, then filtered and washed with ethyl acetate, leaving a dark purple solid.

$^1$H NMR (500 MHz, DMSO-$d_6$) δ ppm 1.3 – 1.8 (-*CH*$_2$-CH-), 2.2 (-CH$_2$-*CH*-), 6.9 – 7.8 (arom. *CH*). The shift corresponding to the acrylate *COOH* is absent, likely due to the ammonium hydroxide used to neutralise the mixture.

**Synthesis of (2-((*m*-tolylamino)methyl)phenyl)boronic acid (Compound 4)**

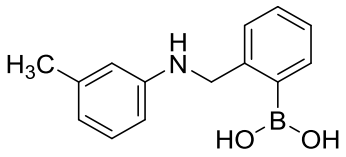


Adapted from Reference 17. To a solution of 0.90 g 2-formylbenzeneboronic acid (6 mmol) in 30 mL of dry methanol in a 100 mL round bottom flask was added a solution of 0.66 mL *m*-toluidine in 30 mL dry methanol. To this stirring solution was added, in small portions, 0.75 g sodium cyanoborohydride (12 mmol). The mixture was allowed to stir overnight, then the solvent was removed *in vacuo*, and the compound was dissolved in ethyl acetate and washed with brine. The ethyl acetate was removed *in vacuo*, and the crude solid was dissolved in 60 mL of methanol, then added dropwise to a slowly stirring beaker of 120 mL water. The suspension was filtered and rinsed with water, yielding slightly off-white platelike crystals in a 56% yield.

$^{1}$H NMR (500 MHz, methanol-$d_4$) δ ppm 2.19 (s, 3 H), 4.29 (s, 2 H), 6.55 (d, 1 H), 6.62 (d, 1 H), 6.60 (s, 2 H), 6.98 (t, 1 H), 7.16 – 7.20 (m, 1 H), 7.23 – 7.29 (m, 3 H).

$^{13}$C NMR (100 MHz, methanol-$d_4$) δ ppm 21.7, 49.4, 51.6, 114.6, 118.1, 122.4, 126.6, 127.6, 129.5, 129.8, 132.4, 139.8, 145.7, 148.6.

HR-MS (ESI, 4.5 kV): *m/z* Calculated for $C_{16}H_{20}BNNaO_2$ [**M** + $2CH_3OH$ – $2H_2O$ + Na]$^+$: 292.1479; found: 292.1482.

**Synthesis of poly(acrylic acid-*co*-(*E*)-(2-(((4-((4-(acryloyloxy)phenyl)diazenyl)-3-methylphenyl)amino)methyl)phenyl)boronic acid) (Polymer 1B)**

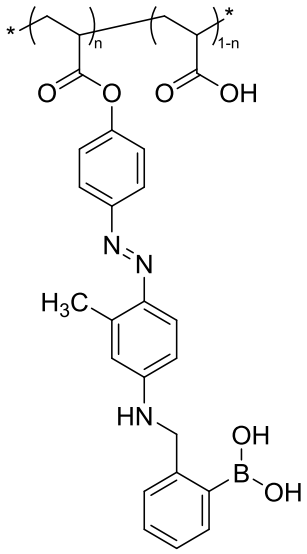

To a 25 mL round bottom flask was added 0.10 g Polymer 1 (0.1 mmol amine mer), 5 mL DMF, 5 mL water, and 0.13 mL c. HCl (1.5 mmol). The solution was stirred on ice until the temperature was <5 °C, then 0.50 mL of cold 0.2 M sodium nitrite (0.1 mmol, Sigma Aldrich) was added dropwise. The solution was stirred on ice for 15 minutes to facilitate the formation of the diazonium salt, then a cold solution of 0.0241 g of (2-((*m*-tolylamino)methyl)phenyl)boronic acid (0.1 mmol) in 1 mL water and 1 mL DMF was added dropwise. The solution was neutralized with 1 M $NH_4OH$, then allowed to stir on ice for 2 hours before being brought to room temperature. The solvent was removed under reduced pressure, yielding a reddish solid. The crude product was redissolved in 6 mL DMF, then added dropwise to a stirring flask of 250 mL ethyl acetate. The polymer suspension was covered and allowed to stir overnight, then filtered and washed with ethyl acetate, leaving behind a dark purple solid.

$^1$H NMR (500 MHz, DMSO-$d_6$) δ ppm 1.27 – 1.94 (-*CH*$_2$-CH-), 2.21 (-CH$_2$-*CH*-), 6.5 – 7.7 (arom. *CH*), 12.3 (-*COOH*).

### 6.3.3 Titration of Solution-Phase Indicators

The optical response of the covalently-functionalized polymers was assessed prior to testing them as part of a polyelectrolyte multilayer. Polymers were dissolved in 0.1 M phosphate buffer adjusted to pH = 7.4, at approximately 1 $mg \cdot mL^{-1}$. This concentration was found to give useful absorbance values (ca. 0.1 – 0.5). Samples were then titrated with dopamine from 0 – 100 mM, with a visible absorbance spectrum acquired at each step. UV-vis spectra were acquired with a Cary 100 dual-beam spectrophotometer equipped with a temperature controller set to 21.0 °C.

### 6.3.4 Polyelectrolyte Multilayers

The fabrication of polyelectrolyte multilayers has been described in detail in References 8 and 12. Briefly, glass slides and silicon wafers (used for ellipsometric thickness determination) were cleaned via immersion in acid piranha (3:1 conc. sulfuric acid/30% hydrogen peroxide solution), then immersed in alternating 10 mM solutions of pH-adjusted cationic and anionic polyelectrolytes with 10 mM sodium chloride. Glass fibres were cleaned with methanol to preserve the polymer cladding on the unexposed sections of fibre. PAH/HA multilayers were assembled at pH = 5.0 with 10 mM sodium chloride for all solutions. PDADMAC/Polymers 1A and 1B multilayers were assembled at pH = 7.0 with 10 mM sodium chloride for all solutions. The thickness of the resulting multilayers was measured on silicon using a single-wavelength null ellipsometer (633 nm, Gaertner Scientific). The dry $(PAH/HA)_{10}$ multilayers (where the subscript indicates the number of polyelectrolyte bilayers in the film) used for the small molecule uptake and dopamine response experiments were determined to be on the order of 50±5 nm thick (dry $n_D$ = 1.51±0.03).

### 6.3.5 Indicator Uptake

Substrates, including 200 μm glass core fibre (Thorlabs), single-crystal silicon wafers (100) (University Wafer, for ellipsometric thickness determination), or standard glass microscope slides (Fisher Scientific) coated with $(PAH/HA)_{10}$ multilayers, were immersed in a solution of 0.1 $mg \cdot mL^{-1}$ indicator, adjusted to pH = 3.0 with 10 mM NaCl to maintain a consistent ionic strength. After 24 hours of immersion (~1 hour for the fibres, where the uptake could be followed spectroscopically), the indicator-loaded films were rinsed with neutral water, then immersed in pH = 7.4 phosphate buffer (10 mM) for 12 hours to remove any excess indicator.

### 6.3.6 Optical Response to Analytes on Flat Substrates

Absorbance measurements on flat substrates were acquired by sandwiching the coated slides in between two fresh, uncoated microscope slides. This process ensured the films remained wetted, which helped to minimise the scattering inherent to PAH/HA PEMs. All absorbance measurements were referenced to an undoped, PEM-coated slide, prepared in the same manner.

To determine the time required to induce an optical response, coated slides were immersed in 5 mM dopamine dissolved in 10 mM pH = 7.4 buffer. The slide was removed and the absorbance measured every two minutes. The concentration response was analysed in a similar manner, by immersing a coated slides in various concentrations (1, 5, 10, 25, and 50 mM) of dopamine for five minutes, followed by acquisition of a visible absorbance spectrum.

### 6.3.7 Fibre Preparation

Glass-core, 300 – 1200 nm high-OH optical fibres with a core diameter of 200 μm were furnished by Thorlabs. The plastic exterior and cladding layers were removed mechanically with a razor blade, and the ends were cleaved by scoring with a diamond scribe, then pulled to complete the cleave. The ends were inspected with a dissection microscope to ensure a clean cleave. Typically, a 4 cm section of cladding was removed from the centre of the fibre section to act as the active sensing area. The fibres were then bent by approximately 45° while being heated over a Bunsen burner, allowing the sensing region to be completely immersed in a solution of analyte.

### 6.3.8 Optical Fibre Evanescent Wave Measurements

The evanescent-field absorbance through the fibre was monitored using the apparatus pictured in Figure 6.4. The fibre is held on one end by a bare fibre clamp and the other an SMA adapter, which is coupled to an SMA patch cable linked to an Ocean Optics USB2000 spectrometer. Light is coupled into the front end of the fibre probe from an Ocean Optics LS-1 tungsten halogen light source via fibre patch cable, and focussed into the fibre end using a short focal length lens. The central portion of the fibre, coated with indicator-doped PEM, was immersed in a solution of pH = 7.4 buffer held in a petri dish (equipped with magnetic stir bar, not pictured), where the concentration of dopamine was varied while the visible absorbance spectrum was monitored.

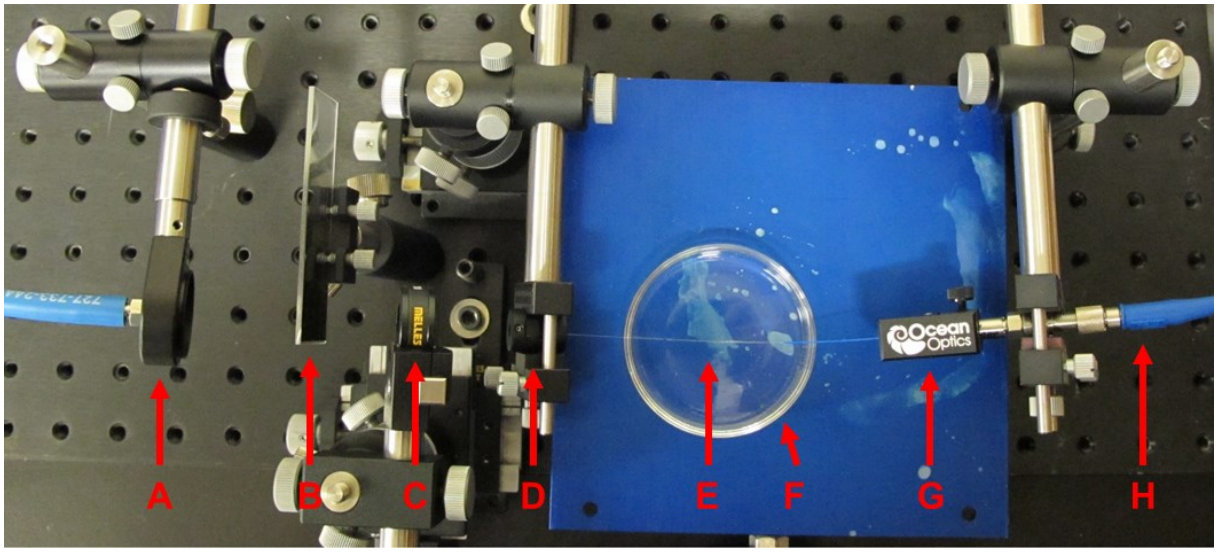


Figure 6.4 Overhead view of the fibre testing setup. A) Light from the tungsten-halogen source is carried via fibre optic through B) a variable neutral density filter to C) a lens to focus the light on D) the cleaved fibre end. E) The section of fibre coated with indicator-doped polyelectrolyte multilayer immersed in F) a solution of buffer with variable amounts of analyte held in a petri dish. The other end of the fibre is held by a clamped SMA adapter, which couples with H) a fibre connected to an Ocean Optics spectrophotometer.

## 6.4 Results and Discussion

### 6.4.1 Covalently Functionalized Polymer Solution Response to Dopamine

#### 6.4.1.1 Polymer 1A

Titration of a solution of Polymer 1A in pH = 7.4 buffer with dopamine shows a similar response to the small molecules investigated in Chapter 5, though the absorbance increases with increasing dopamine concentration in this case.

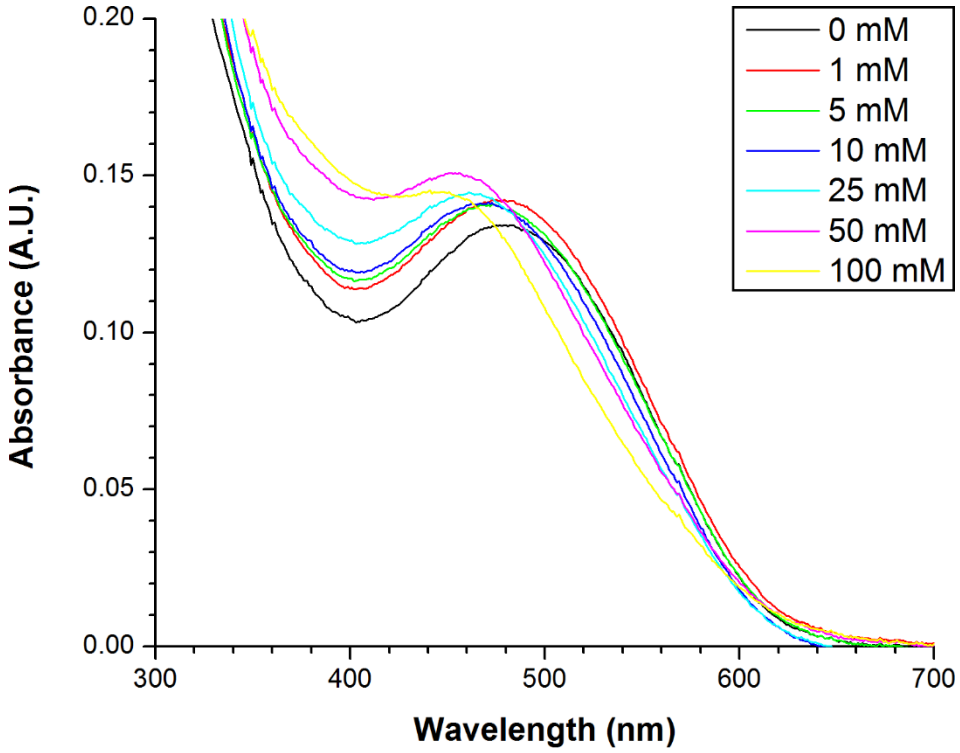


Figure 6.5 Spectral changes in Polymer 1A upon titration with dopamine (0 – 100 mM).

Although the solution-phase dopamine response for this polymer were encouraging, a stable multilayer could not be formed, suggesting decomposition of the polymer under azo coupling conditions. The GPC results for the polymer after azo functionalization were inconclusive due to low polymer solubility in THF (necessary for GPC), but did not appear to show the same high molecular weight peak as the parent Polymer 1.

#### 6.4.1.2 Polymer 1B

The second covalently-linked polymer indicator, 1B, exhibited no detectable optical response to dopamine in solution at pH = 7.4. This is consistent with the binding behaviour observed in Reference 17, where the small-molecule chromophore required significantly higher pH conditions to bind glucose and fructose.

### 6.4.2 Doped PEMs on Flat Substrates

#### 6.4.2.1 Uptake on Flat Substrates

Uptake of the candidate disulfonate indicator compounds (Compounds 7 – 9) generated stable PEM-indicator complexes, with the distinctive colouration of the small molecules preserved in the multilayer complex (Figure 6.6). Unlike in the solution phase, Compounds 7 and 8 appear stable to decomposition indefinitely in the dry multilayer (see Chapter 5).

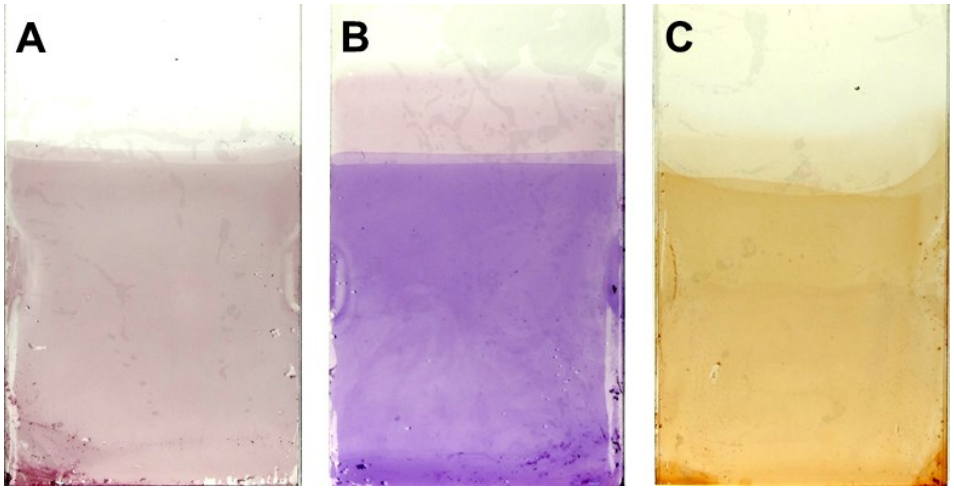


Figure 6.6 $(PAH/HA)_{10}$-coated slides after 24 hours immersed in 0.1 $mg \cdot mL^{-1}$ pH = 3.0 solutions of A) Compound 7, B) Compound 8, and C) Compound 9, followed by 12 hours of immersion in 10 mM pH = 7.4 buffer. The indicator compounds are stable in the film in neutral solution.

The absorbance spectra of all three indicators exhibit slight spectral shifts when absorbed by the PEM matrix, as shown in Figures 7 – 9 below. The $\lambda_{max}$ of Compound 7 blueshifts slightly, while Compounds 8 and 9 redshift slightly upon adsorption: this is consistent with the behaviour noted in Chromotrope 2R and Indoine Blue in the uptake study by Burke *et al.*[12]

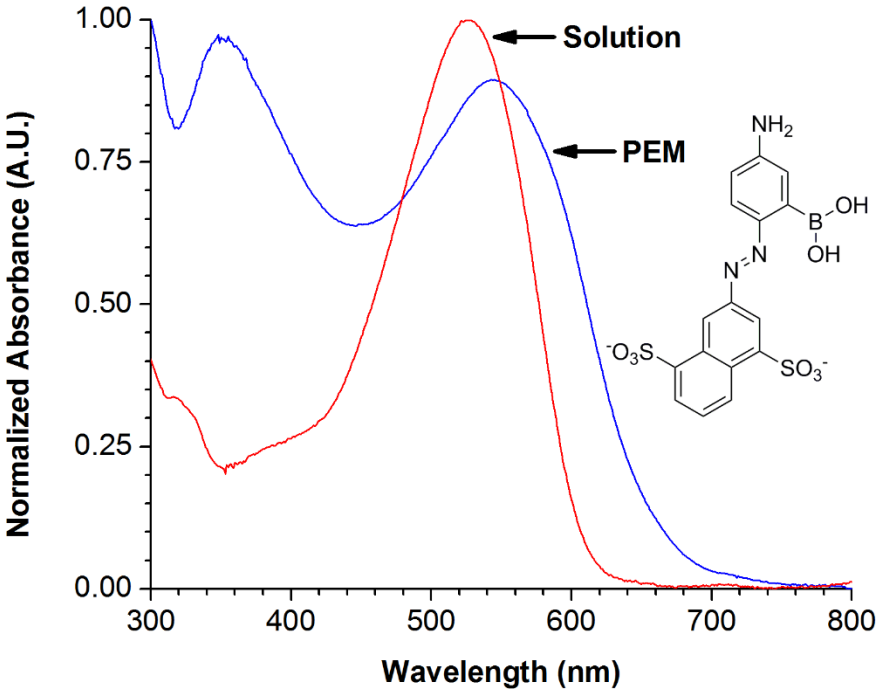


Figure 6.7 Absorbance spectrum of Compound 7 in pH = 7.4 buffer (red curve) and embedded in a $(PAH/HA)_{10}$-coated glass slide (blue curve).

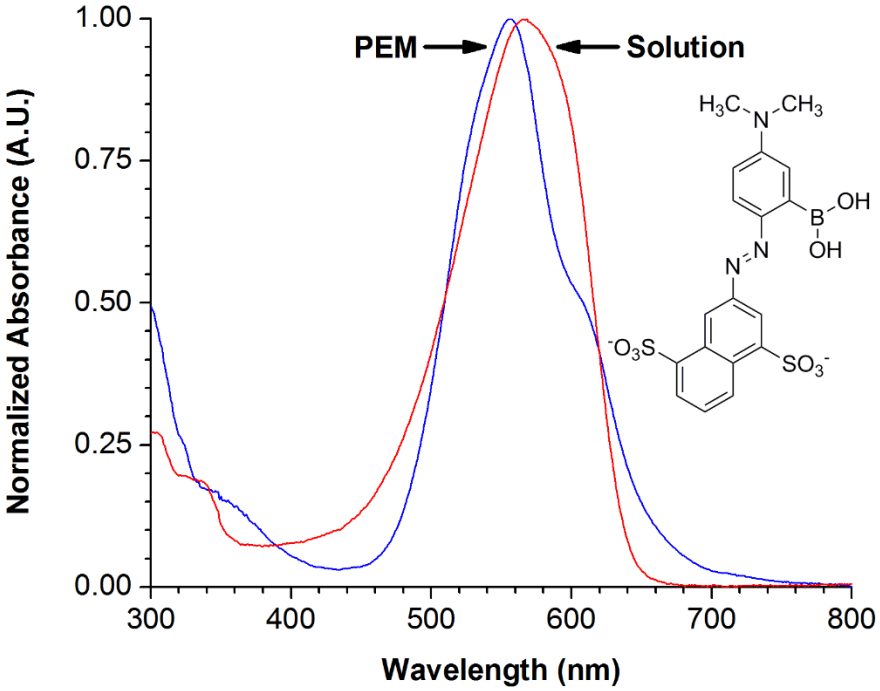


Figure 6.8 Absorbance spectrum of Compound 8 in pH = 7.4 buffer (red curve) and embedded in a $(PAH/HA)_{10}$-coated glass slide (blue curve).

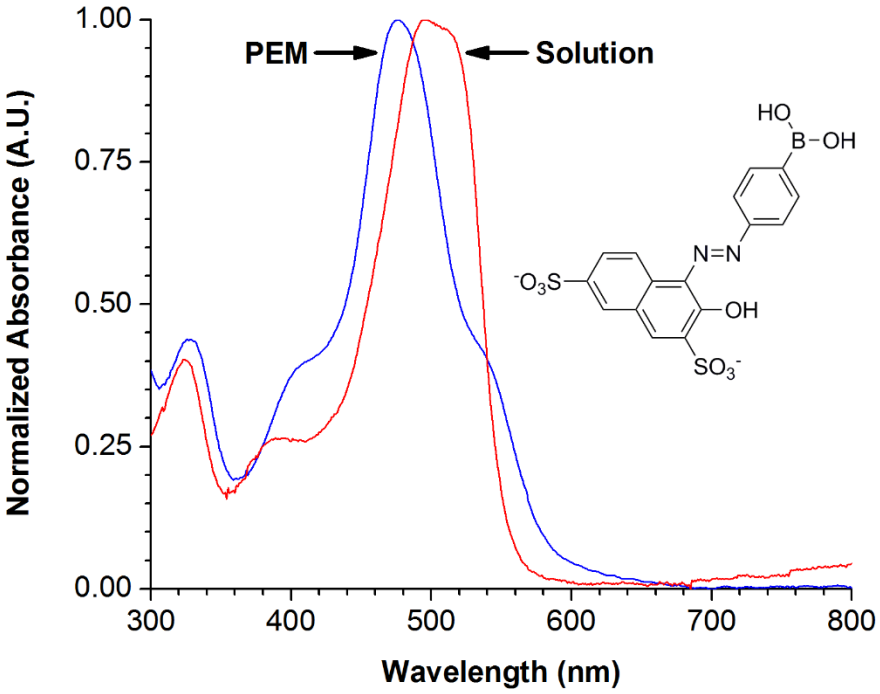


Figure 6.9 Absorbance spectrum of Compound 9 in pH = 7.4 buffer (red curve) and embedded in a $(PAH/HA)_{10}$-coated glass slide (blue curve).

#### 6.4.2.2 Indicator Stability on Flat Substrates

Stability of the indicators to leaching from the PEM matrix was variable, depending strongly on the pH and ionic strength of the rinse solution. No leaching was observed in pure, neutral water; however, higher ionic strength buffer solutions (ca. 100 mM) induced significant leaching. Reducing the buffer concentration to 10 mM was found to provide a good compromise between buffering capacity and indicator stability, and was used for all dopamine-response experiments.

### 6.4.3 Dopamine Optical Response on Flat Substrates

Glass slides coated with PEMs and doped with the three indicators exhibited somewhat different optical responses from their solution-phase analogues. Some leaching upon exposure to dopamine in solution was observed in all cases, most prominently in Compound 9. However, the reduction in absorption intensity in all cases was accompanied by a shift in the $\lambda_{max}$, indicating diffusion of analyte into the PEM matrix and binding with the indicator. The plots below (Figures

10 – 12, corresponding to immersion in 100 mM dopamine at pH = 7.4) are normalized to accentuate this difference.

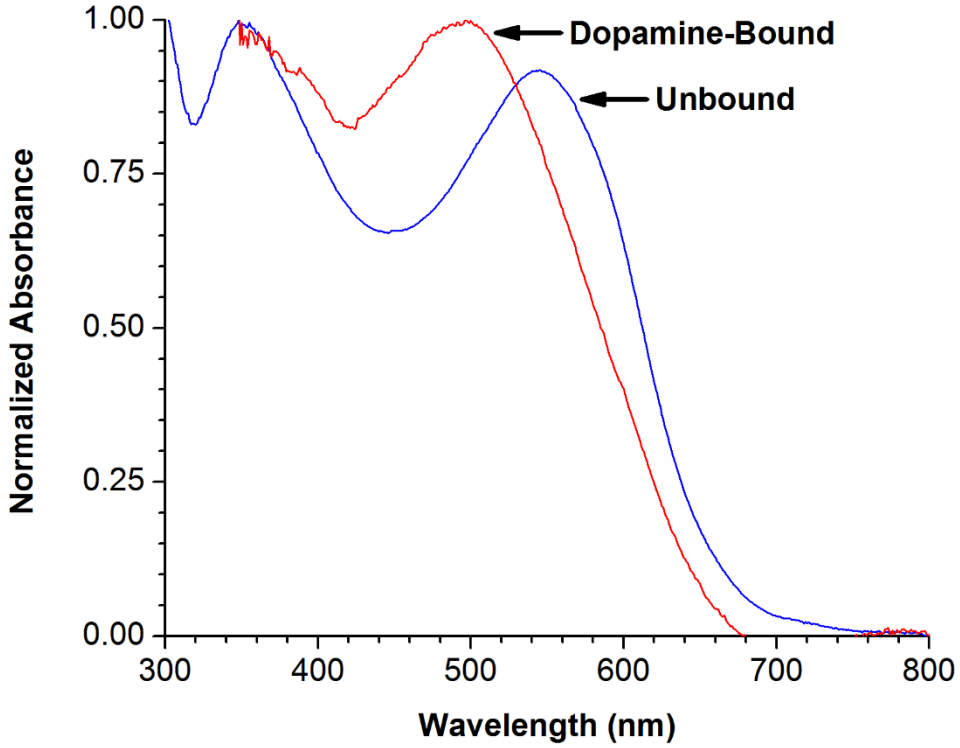


Figure 6.10 Optical response of Compound 7 in 100 mM dopamine and 50 mM pH = 7.4 buffer.

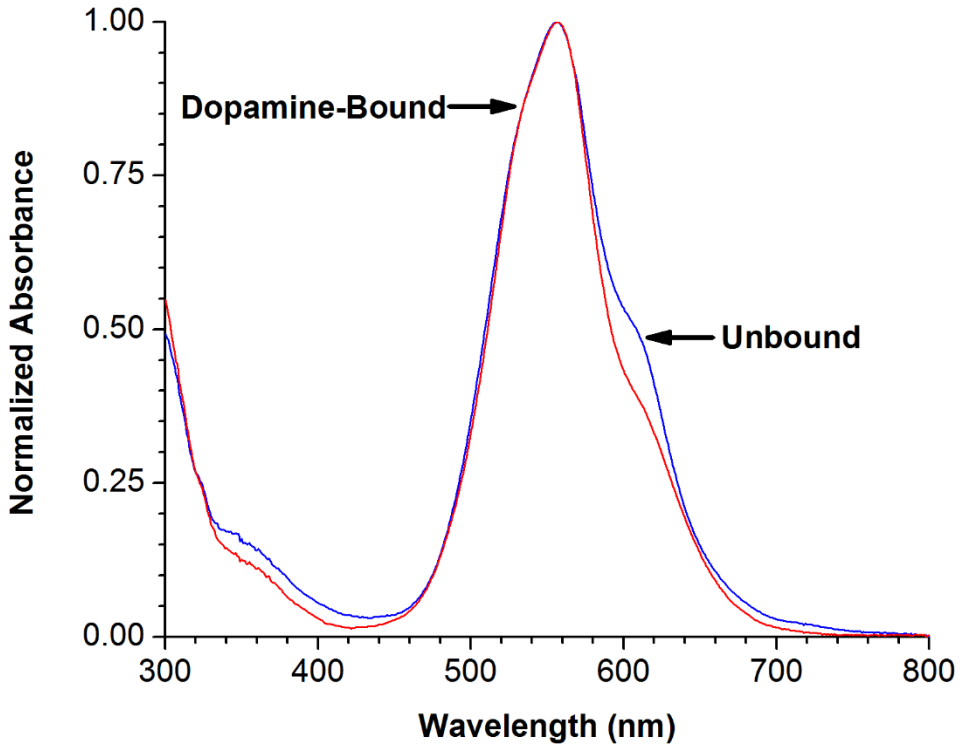


Figure 6.11 Optical response of Compound 8 in 100 mM dopamine and 50 mM pH = 7.4 buffer.

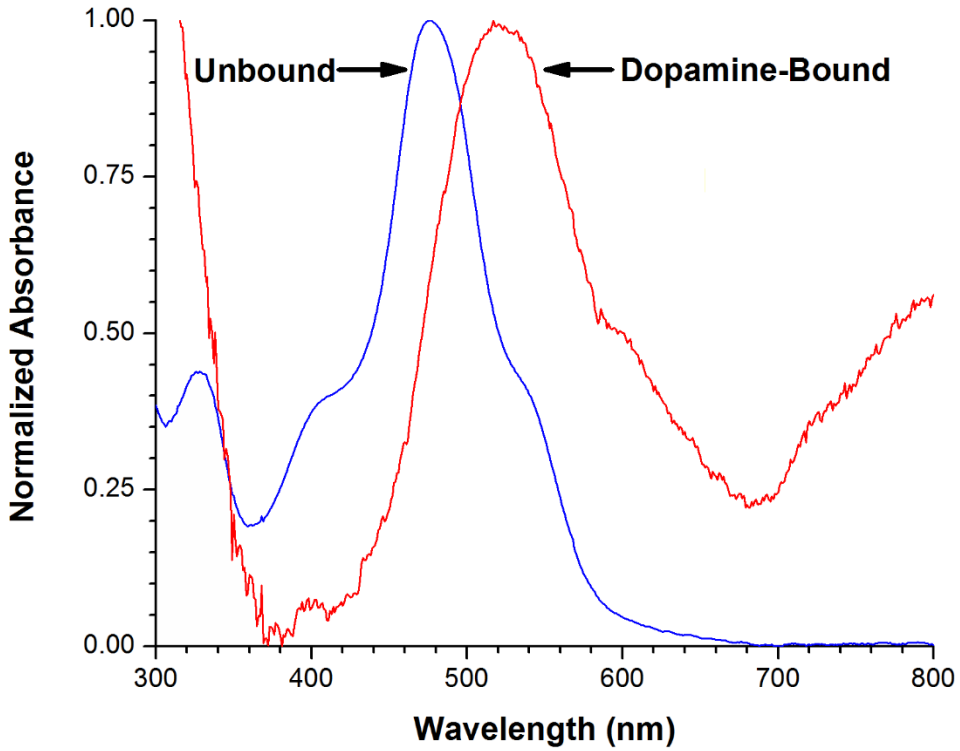


Figure 6.12 Optical response of Compound 9 in 100 mM dopamine and 50 mM pH = 7.4 buffer.

In addition to the spectral data, the change in visible appearance upon exposure to dopamine is quite pronounced, as shown in Figure 6.13 for a PEM doped with Compound 9. This colour change occurs at 5 mM and pH = 7.4, with a minimal amount of indicator leaching from the PEM matrix.

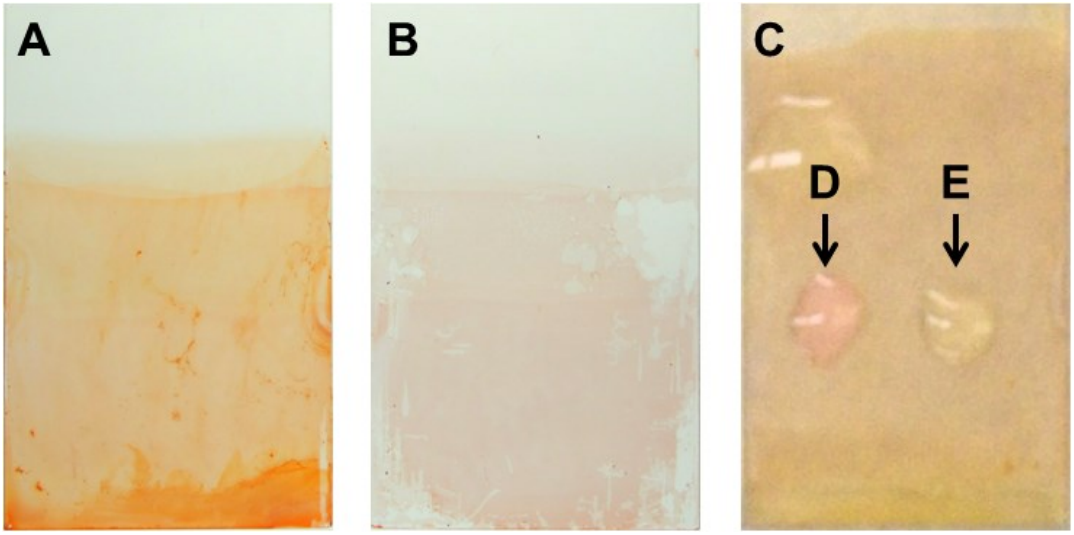


Figure 6.13 Glass slides coated with $(PAH/HA)_{10}$, doped with Compound 9. A) Fresh indicator-doped PEM, no dopamine exposure: note the strong orange colouration. B) Indicator-doped PEM after 15 minutes in 5 mM dopamine at pH = 7.4, which has changed to the red-pink colouration characteristic of dopamine-bound indicator observed in solution. C) A similar slide with a drop of D) 50 mM dopamine at pH = 7.4 and E) a drop of pH = 7.4 buffer. Note the pink colouration visible in the area exposed to dopamine, while no colour change occurs under the buffer, which were also confirmed reversible on rinsing.

#### 6.4.3.1 Temporal Dopamine Response

The optical response time to dopamine was investigated for Compound 9 immobilized in a $(PAH/HA)_{10}$ multilayer, at 5 mM dopamine concentration. The results are presented in Figure 6.14, and similar behaviour is observed to that exhibited by the small molecule in solution. The shoulder that develops at 523 nm grows by about 10% in the first two minutes (taken as a ratio to the main feature at 479 nm) and ultimately increases by about 40% after 30 minutes. The indicator exhibits slow leaching over time, though this process (at 5 mM dopamine) is much slower than the previous experiments conducted in 100 mM dopamine.

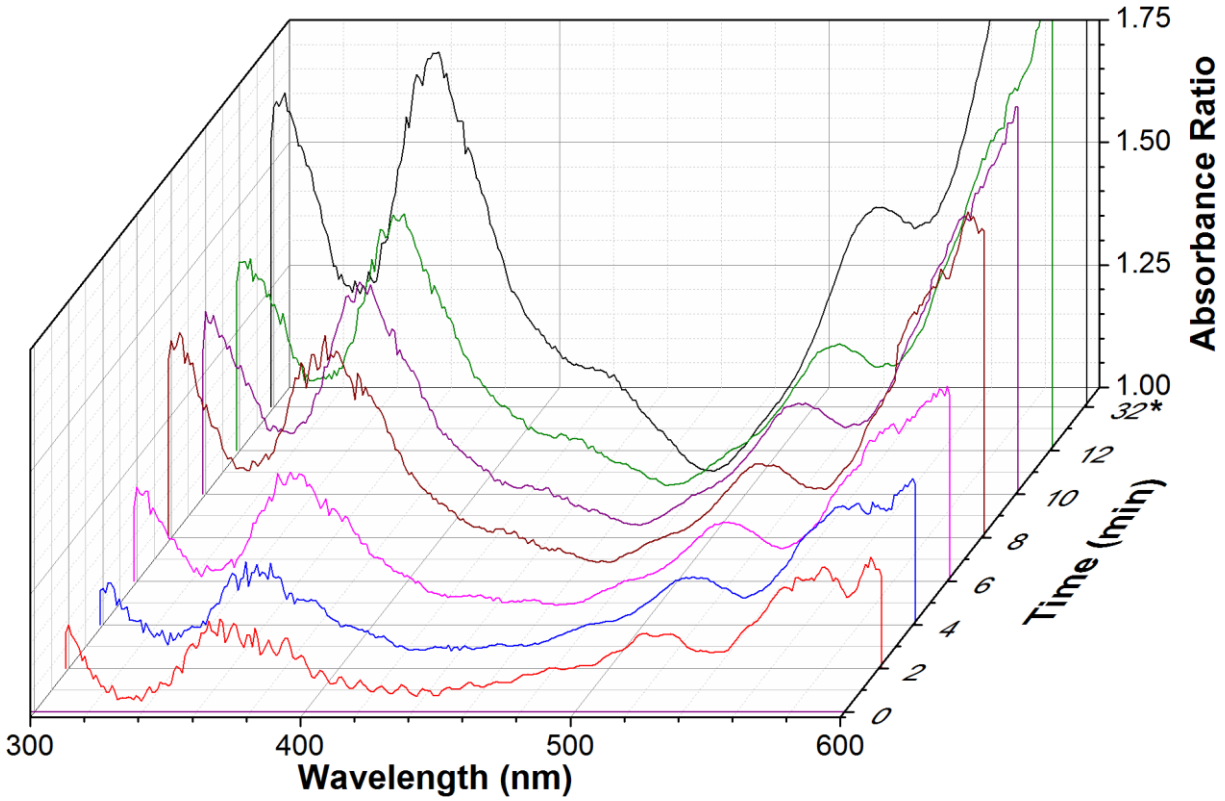


Figure 6.14 Glass slide coated with $(PAH/HA)_{10}$ loaded with Compound 9, immersed in 5 mM dopamine at pH = 7.4. *Note that the final time point is at 32 minutes.

The response to dopamine starts to become measurable over a matter of seconds, but the number of bilayers applied and pH/ionic strength of the PEM assembly conditions can be optimized to create a more permeable film, allowing dopamine to penetrate the matrix more easily and resulting in a faster optical response time. Improving the stability of the indicator to leaching by dopamine (either by altering the PEM assembly conditions, or by covalent linkage of the indicator) will also significantly improve the signal to noise ratio, allowing for more information to be extracted from the data.

It is important to note that the significant changes in absorption spectrum and external appearance in the above experiment occurred as a result of exposure to 5 mM dopamine, under biological pH conditions (pH = 7.4). This dopamine concentration is on the order (5 mM) of *in vivo* dopamine concentrations during a neuronal impulse,[5] indicating that this system has the potential to function as a dopamine detector in a biological setting. The indicator molecule is not prone to degradation under biological conditions (see Section 5.4.4 for stability of Compound 9),

and PEMs have been widely demonstrated by our group and others as excellent substrates for cell growth and adhesion.[9,10,18] As well, the binding between boronic acids and catecholates is reversible, so the indicator does not get consumed as repeated spikes in dopamine concentration are detected.

The PEM films used in this study have a dry thickness of 50±5 nm, allowing them to easily be scaled down to the size required for detection on a cellular level. Additionally, this thickness is of the appropriate length scale to couple well with the evanescent wave from an optical fibre, allowing its incorporation into an optical fibre-based probe of tens of nanometres. The thickness can also easily be tuned by altering the number of bilayers deposited, and by carefully selecting the refractive index of the fibre used for the probe to maximize the coupling between the indicator-doped PEM and the evanescent field.

#### 6.4.3.2 Concentration Dopamine Response

In addition to the temporal response, the optical response as a function of dopamine concentration was measured in a $(PAH/HA)_{10}$ film doped with Compound 9. Figure 6.15 shows a plot of the ratio of the $\lambda_{max}$ of the unbound indicator at 479 nm to the shoulder that develops at approximately 525 nm as a function of dopamine concentration. Analyzing this ratio eliminates any variation due to indicator leaching, which becomes significant at high dopamine concentrations (> 25 mM, much higher than biological conditions).

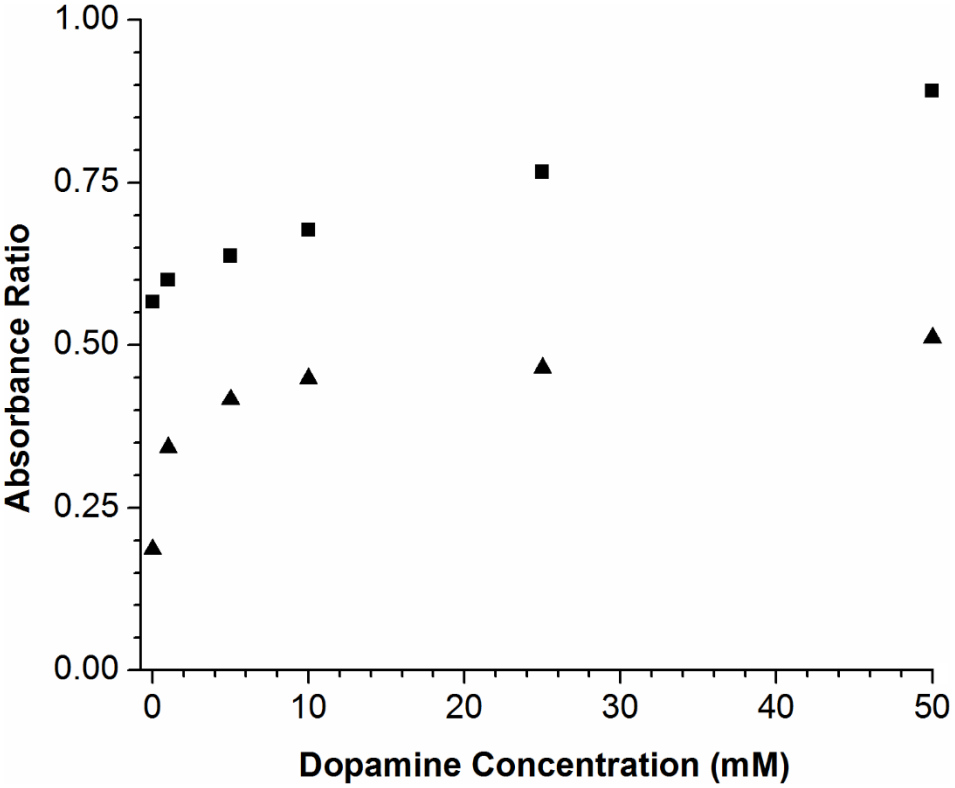


Figure 6.15 Optical response of Compound 9 in solution (triangles) and doped in a $(PAH/HA)_{10}$ multilayer film coated on a glass slide coated. The $\lambda_{max}$ (552 nm solution; 479 nm PEM) is taken as a ratio with the shoulder that develops due to dopamine binding (502 nm solution; 525 nm PEM).

The plot shows a clear optical response to dopamine, which is higher in all cases for the indicator immobilized in a PEM compared with the same molecule in solution. This is due to the very different chemical environment experienced by the indicator in the PEM matrix, which has a very different ionic strength and water content,[19,20] as well as very different pH conditions[21] to those found in the surrounding solution. This is consistent with the changes in indicator $\lambda_{max}$ observed upon uptake into the PEM film, as described in Section 6.4.2.1.

### 6.4.4 Doped PEMs on Fibre Optics

To demonstrate that the dopamine-responsive polymer films developed in this chapter can, in principle, be applied to a fibre optic probe, some preliminary results are presented as proof of principle. The following section demonstrates our ability to effectively coat fibres with a biocompatible PEM matrix, dope the assembled PEM with NT-indicator molecules while

following the uptake with evanescent wave spectroscopy, and record some preliminary results when the fibre is exposed to dopamine. In addition, we present some ideas for the future direction of this work, including the geometry of potential probes to be used for *in vitro* and eventually *in vivo* dopamine detection.

#### 6.4.4.1 Evanescent Field Absorption of Azobenzene-Functionalized Polyelectrolytes

To ensure the azo-doped polyelectrolyte multilayers were on the correct order of magnitude of thickness to couple effectively with the evanescent wave on a fibre surface, a test fibre was coated with poly(Disperse Red 1 acrylate-*co*-acrylic acid)/poly(allylamine hydrochloride) (p(DR1A-*co*-AA)/PAH; structure shown in Chapter 4). This well-characterized multilayer system has a strong absorbance centred at 470 nm, which matches well with the 488 nm laser line from an $Ar^+$-ion laser as shown in Figure 6.16 below.

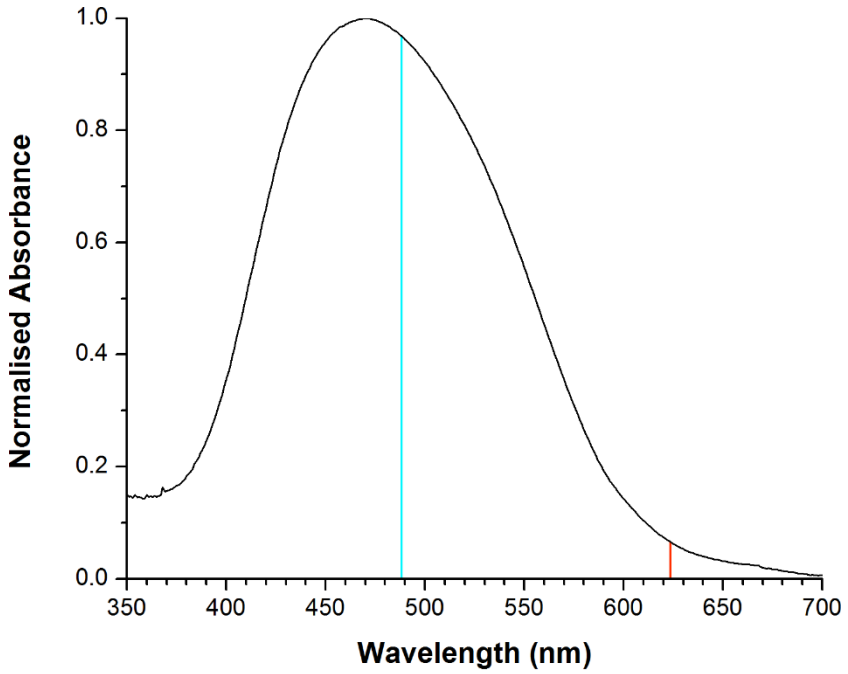


Figure 6.16 Absorbance spectrum of $(p(DR1A\text{-}co\text{-}AA)/PAH)_5$ on a glass slide. The position of 488 and 633 nm laser sources are indicated on the spectrum: note the difference in relative absorbance.

A 5 cm section of cladding was removed from the centre of a 20 cm length of optical fibre, which was then heated with a Bunsen burner and bent into a U shape (Figure 6.17A and C). An

identical fibre with a similar unclad section was coated with five bilayers of p(DR1A-*co*-AA)/PAH), and the two were tested for their ability to pass 488 and 633 nm light by coupling laser light into one end and monitoring the amount of light passed through the opposite end. The unclad fibre passes both wavelengths of light effectively, as shown in Figure 6.17 A and B. The fibre coated with p(DR1A-*co*-AA)/PAH) absorbs some light at 633 nm, as can be seen in Figure 6.17E; however, the 488 nm light is almost entirely absorbed (Figure 6.17F), indicating the azo chromophores are able to strongly couple with the evanescent field.

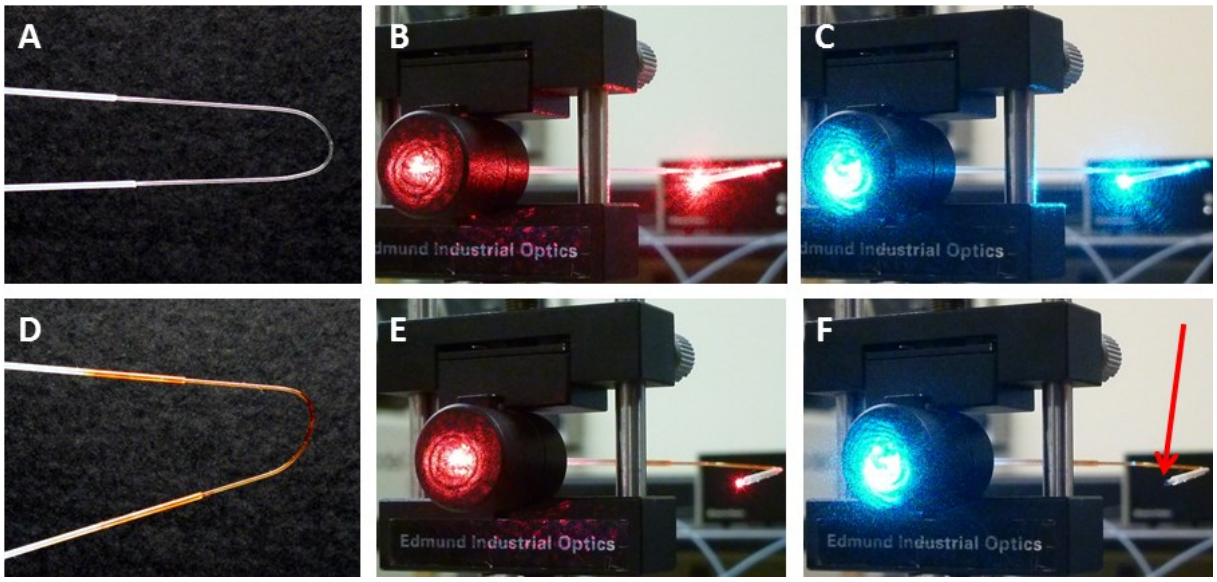


Figure 6.17 Demonstration of evanescent wave absorption by azo-functionalized polyelectrolyte multilayers coated on the surface of glass fibre optics. A) Glass fibre with a 5 cm unclad region, with B) 633 nm light and C) 488 nm light shining through it. Note the light is clearly visible in both cases at the opposite end of the fibre. D) Glass fibre coated with poly(Disperse Red 1 acrylate-*co*-acrylic acid)/poly(allylamine hydrochloride with E) 633 nm propagates through the fibre with little attenuation and F) the 488 nm light is completely attenuated (red arrow points to the fibre tip).

#### 6.4.4.2 Uptake on Fibre Optics

Similar dye uptake behaviour to the coated glass slides was observed in multilayers assembled on glass-core fibre optics, as seen in Figure 6.18 below, where photographs of a $(PAH/HA)_{10}$-coated fibre before and after immersion in pH = 3.0 azo dye indicator solution are presented, and the strong colouration evident.

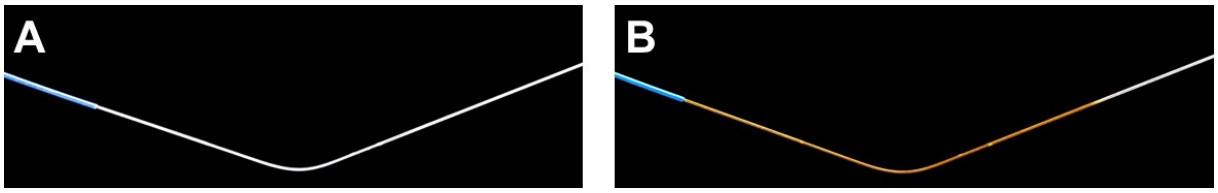


Figure 6.18 Glass 200 µm-core fibre optics with the outer blue coating visible. The outer coating and clear polymer cladding has been removed in the centre (~4 cm), and the glass core has been coated with A) a $(PAH/HA)_{10}$ multilayer film and B) a $(PAH/HA)_{10}$ multilayer film doped with Compound 9. Note the dark orange colouration of the indicator-doped layer.

The uptake was followed dynamically on the surface of the fibre by immersing a PEM-coated fibre into the solution of pH-adjusted indicator, and monitoring the evanescent wave absorbance spectrum. A plot of absorbance as a function of time for the uptake of Compound 9 into a 4 cm section of fibre is shown in Figure 6.21 below, with indicator saturation occurring after approximately 15 minutes.

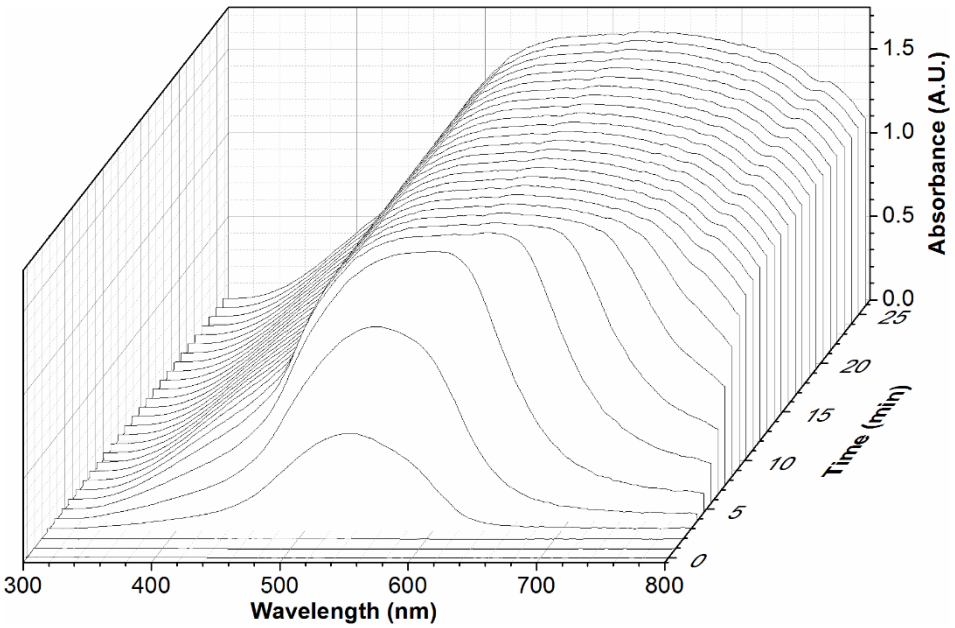


Figure 6.19 Uptake of Compound 7 into a section of $(PAH/HA)_{10}$-coated fibre. The multilayer coating becomes saturated after around 10 minutes (note the first three points are prior to immersion in the indicator solution).

Compounds 8 and 9 exhibit similar uptake curves, with saturation again occurring at about 10 minutes, as shown in Figures 20 and 21.

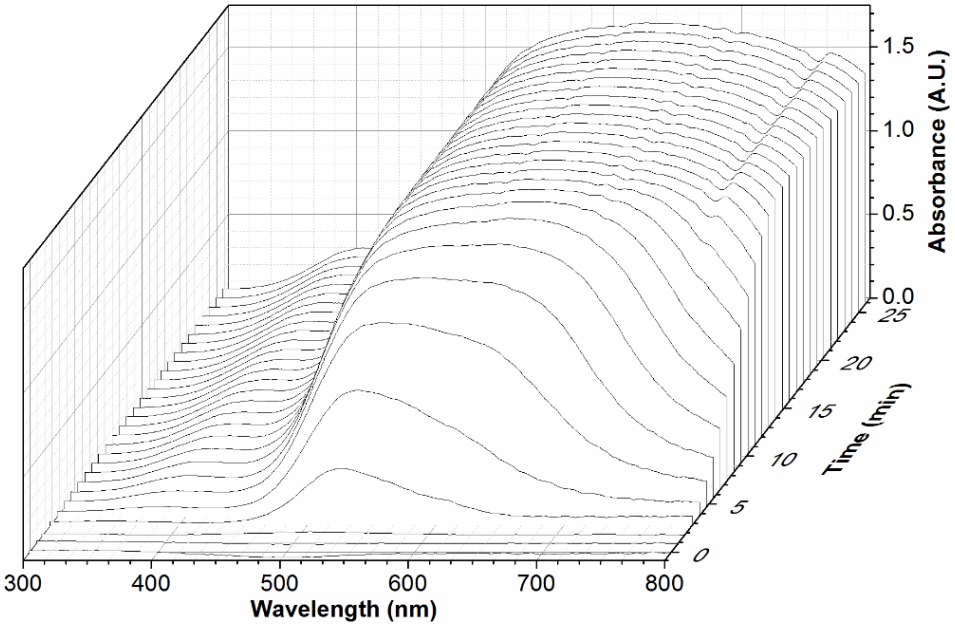


Figure 6.20 Uptake of Compound 8 into a section of $(PAH/HA)_{10}$-coated fibre. The multilayer coating becomes saturated after around 10 minutes (note the first three points are prior to immersion in the indicator solution).

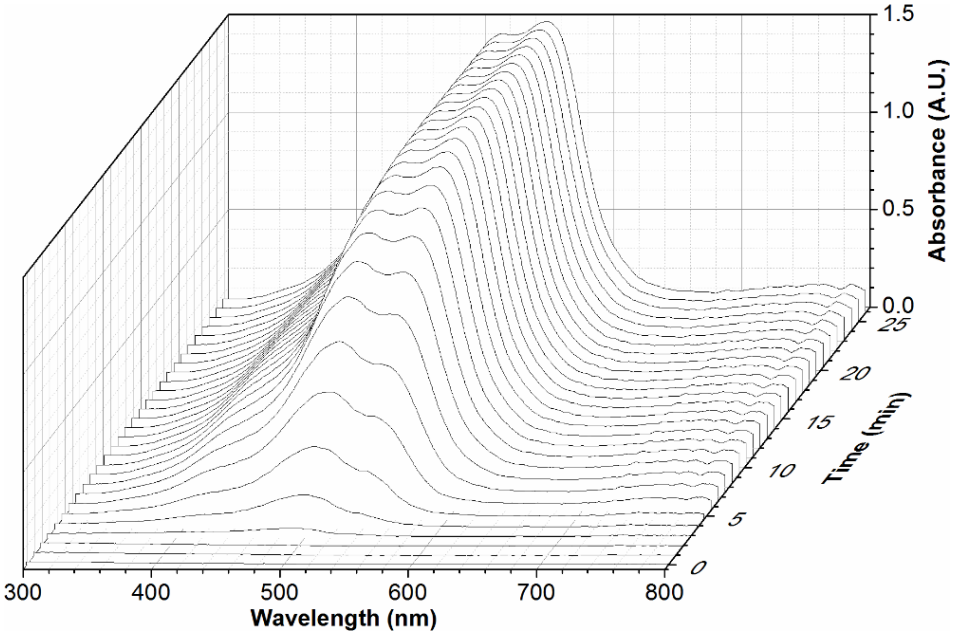


Figure 6.21 Uptake of Compound 9 into a section of $(PAH/HA)_{10}$-coated fibre. The multilayer coating becomes saturated after less than 15 minutes (note the first two points are prior to immersion in the indicator solution).

### 6.4.4.3 Indicator Stability on Fibre Surface

Although the external appearance of the indicator-doped multilayers stabilized quickly after immersion in neutral water or low ionic strength buffer solution, the evanescent-wave spectrum exhibited a different response. The evanescent-wave spectrum produced a striking difference depending on the pH of the rinse solution. Figure 6.22 shows two fibres doped with Compound 9 at pH = 3.0, followed by immersion in solutions of different pH. Upon immersion in pH = 7.4 buffer, the peak corresponding to the indicator drops from a peak absorbance value of ~1.4 to 0.2 almost immediately, before stabilizing at around 0.1 A.U. However, when the second fibre is immersed in a rinse solution of pH = 3.0, only a slight reduction in the indicator absorbance feature occurs before the peak stabilizes at ~99% the peak absorbance. Similar behaviour was noted for Compounds 7 and 8.

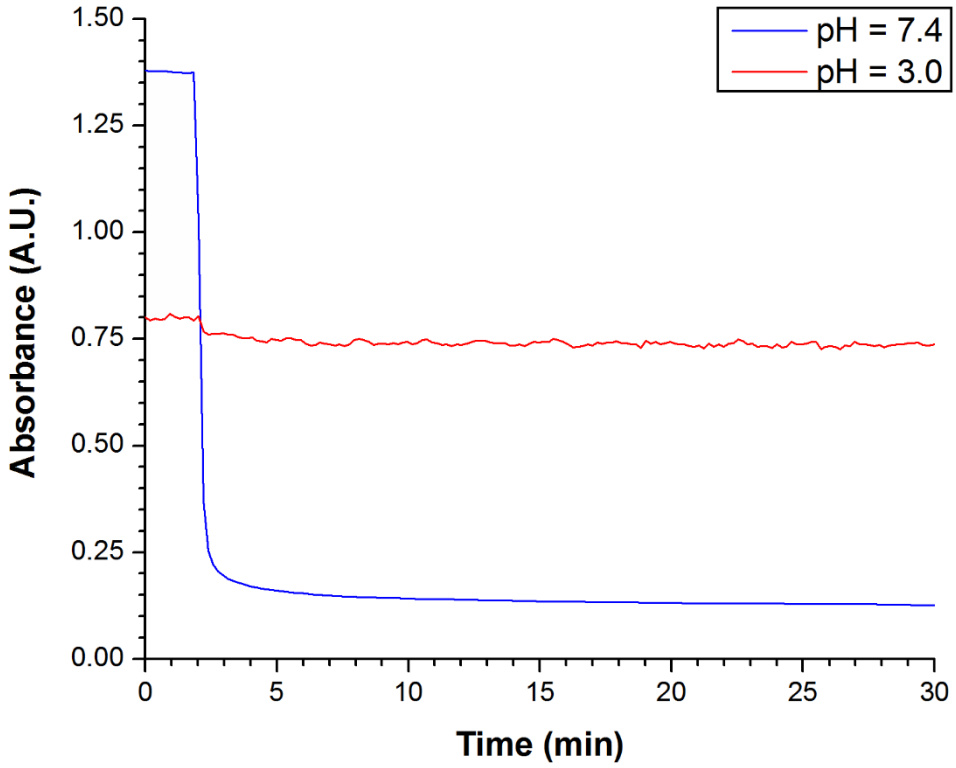


Figure 6.22 Plot of the evanescent absorbance at the $\lambda_{max}$ (546 nm) of two fibres coated with $(PAH/HA)_{10}$, doped with Compound 9. At 2 minutes, the fibres are moved from the pH = 3.0 solution of indicator to a rinse of either pH = 7.4 buffer (blue curve) or pH = 3.0 solution (red curve). Note the large drop in intensity upon immersion in pH = 7.4 buffer compared with the relatively small drop in intensity for the pH = 3.0 solution.

Although Figure 6.22 appears to suggest significant leaching of the indicator from the PEM matrix at pH = 7.4, effectively no change in the external appearance is observed. The report by Burke *et al.* on the uptake of azo compounds into PAH/HA multilayers also described the change in film thickness on exposure to different pH conditions.[12,22] The change in film thickness (approximately 2× from pH = 3.0 – 7.4)[22] is accompanied by a change in refractive index ($n_D$), due to the large change in ion concentration and water content in the film.[12,23] This change in $n_D$ alters the penetration depth of the evanescent wave to couple with the indicator, and reduces the effective absorbance.

In all cases, immersion of the doped fibres in dissolved dopamine resulted in some leaching of the indicator from the PEM, though the degree of leaching was found to be strongly dependent on the concentration of dopamine. The external appearance of the coated fibre was consistent with that of the coated slides after dopamine exposure, suggesting that effective coupling of the evanescent field with the PEM will result in a clear signal upon dopamine exposure.

#### 6.4.4.4 Dopamine Response on Fibre Optics

An example of a dopamine titration curve is shown in Figure 6.23. A fibre coated with a $(PAH/HA)_{10}$ PEM and doped with Compound 9 and rinsed in 10 mM pH = 7.4 buffer was immersed in a stirring solution of pH = 7.4 buffer. The concentration of dopamine was gradually increased from 0 to 20 mM dopamine at 2 minute intervals. The response was recorded as a difference with the baseline curve, corresponding to 100% unbound indicator: the feature that can be seen developing corresponds to a combination of indicator leaching from the PEM coating and the dopamine-bound indicator complex. The sudden, discontinuous jumps in the curve correspond addition of a new aliquot of dopamine (approx. 4 mM per addition).

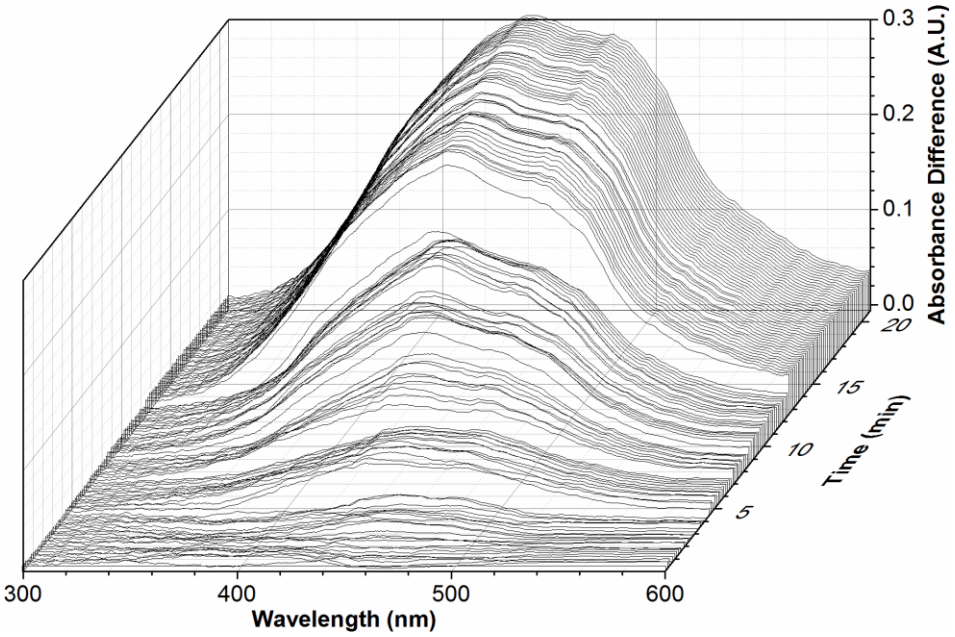


Figure 6.23 Optical response of a fibre optic coated with $(PAH/HA)_{10}$ and doped with Compound 9 upon exposure to a solution containing increasing concentrations of dopamine. The change in absorbance is a convolution of indicator leaching and dopamine binding, and would need further independent proof of spectral dopamine response. Note the y-axis is inverted for clarity.

The signal is dominated by the leaching curve, which represents one of the challenges future work in this area will have to address, but this represents the first preliminary response to dopamine on the surface of a fibre optic. Experimental design constraints with single-fibre data detection precluded replication of the same reference recording as for the coated slides in a UV-visible spectrophotometer, which would have permitted similar independent de-convolution of the 2 contributions. Future work to re-design the fibre spectrometer could address this issue, or using only covalently-bound azo dyes. Further work on reducing the size of the fibre probe to that of neural cells, as well as determining the optimal tip geometry (reflection from the tip, potentially with a mirror finish to enhance signal intensity; or the incorporation of a microsphere for whispering gallery-type measurements, as discussed in Chapter 1) can build on the preliminary results presented here, with the ultimate aim of developing a sensitive fibre probe able to measure changes in dopamine concentration on a cellular level.

## 6.5 Conclusions

Three of the indicator molecules described in Chapter 5 were successfully immobilized in a PAH/HA PEM matrix on various surface geometries, including the core of a fibre optic. An optical response to solution-phase dopamine was recorded for all three indicators, with a significant change in absorption spectrum even at the biological concentration of 5 mM dopamine for Compound 9. These results suggest these materials have the capability to measure dopamine in biological conditions, at the concentrations found *in vivo*.

The uptake of the indicator molecules was also observed via evanescent wave spectroscopy on the surface of a PEM-coated optical fibre, for which a strong signal was observed. The evanescent wave signal was greatly reduced upon exposure of the fibre to biological pH conditions due to the changing morphology of the film. This problem may be solved by optimizing the PEM assembly pH and ionic strength conditions to yield a film with a more favourable morphology at pH = 7.4, however it may ultimately necessitate covalent linkage of the indicator molecule to the polyelectrolyte backbone, where the assembly conditions can be optimized for the final $n_D$ without regard to uptake/immobilization concerns.

This work represents a first step towards the realization of an all-optical probe for neurotransmitter detection *in vivo*. Perhaps the most important problem in future research in this area is that of scale, to eventually build a device small and sensitive enough to operate on the micron sizescale of neurons. By pulling the tip of an already small-diameter optical fibre, using the same equipment and protocols for pulling patch clamps for electrophysiology, tips on the order of 1 μm can easily be attained (see Chapter 1). All fibre testing in the current work has been done in a transmission-type geometry for experimental simplicity, but probe tip optimization represents one of the most important aspects of future research in this area. As well, the geometry of the active sensing area is an important consideration for the eventual adaptation of this research into a working device. Reflection from the fibre tip[16] is the most convenient for implantation and to obtain the necessary size to interface with small numbers of neural cells, and most closely resembles the geometry of current neural implants. However, the curved geometry of microspheres attached to the fibre surface for whispering gallery-type features may prove interesting both for the enhanced signal to noise and their potential for encouraging cell growth.[24]

## 6.6 References


1. T. Stieglitz, in *Handbook of Neural Activity Measurement*, eds. R. Brette and A. Destexhe, Cambridge University Press, Cambridge, U.K., 2002, pp. 8–43.

2. V. S. Polikov, P. A. Tresco, and W. M. Reichert, *J. Neurosci. Methods*, 2005, **148**, 1–18.

3. P. Fattahi, G. Yang, G. Kim, and M. R. Abidian, *Adv. Mater.*, 2014, **26**, 1846–1885.

4. T. Pradhan, H. S. Jung, J. H. Jang, T. W. Kim, C. Kang, and J. S. Kim, *Chem. Soc. Rev.*, 2014, **43**, 4684–4713.

5. A. Scimemi and M. Beato, *Mol. Neurobiol.*, 2009, **40**, 289–306.

6. M. Chesler, *Physiol. Rev.*, 2003, **83**, 1183–1221.

7. G. Decher, *Science*, 1997, **277**, 1232–1237.

8. M. Sailer and C. J. Barrett, *Macromolecules*, 2012, **45**, 5704–5711.

9. M. Sailer, K. Lai Wing Sun, O. Mermut, T. E. Kennedy, and C. J. Barrett, *Biomaterials*, 2012, **33**, 5841–5847.

10. A. Goulet-Hanssens, K. Lai Wing Sun, T. E. Kennedy, and C. J. Barrett, *Biomacromolecules*, 2012, **13**, 2958–2963.

11. S. Y. Park, C. J. Barrett, M. F. Rubner, and A. M. Mayes, *Macromolecules*, 2001, **34**, 3384–3388.

12. S. E. Burke and C. J. Barrett, *Macromolecules*, 2004, **37**, 5375–5384.

13. A. Schneider, G. Francius, R. Obeid, P. Schwinté, J. Hemmerlé, B. Frisch, P. Schaaf, J. Voegel, B. Senger, and C. Picart, *Langmuir*, 2006, **22**, 1193–1200.

14. L. Richert, F. Boulmedais, P. Lavalle, J. Mutterer, E. Ferreux, G. Decher, P. Schaaf, J.-C. Voegel, and C. Picart, *Biomacromolecules*, 2004, **5**, 284–294.

15. J. R. E. Fraser, T. C. Laurent, and U. B. G. Laurent, *J. Intern. Med.*, 1997, **242**, 27–33.

16. B. Sciacca and T. M. Monro, *Langmuir*, 2014, **30**, 946–954.

17. D. Luvino, M. Smietana, and J.-J. Vasseur, *Tetrahedron Lett.*, 2006, **47**, 9253–9256.

18. A. Goulet-Hanssens and C. J. Barrett, *J. Polym. Sci. Part A Polym. Chem.*, 2013, **51**, 3058–3070.

19. O. M. Tanchak, K. G. Yager, H. Fritzsche, T. Harroun, J. Katsaras, and C. J. Barrett, *Langmuir*, 2006, **22**, 5137–5143.

20. O. M. Tanchak, K. G. Yager, H. Fritzsche, T. Harroun, J. Katsaras, and C. J. Barrett, *J. Chem. Phys.*, 2008, **129**, 084901.

21. S. E. Burke and C. J. Barrett, *Langmuir*, 2003, **19**, 3297–3303.

22. S. E. Burke and C. J. Barrett, *Biomacromolecules*, 2005, **6**, 1419–1428.

23. O. M. Tanchak and C. J. Barrett, *Chem. Mater.*, 2004, **16**, 2734–2739.

24. G. Gopalakrishnan, P. Thostrup, I. Rouiller, A. L. Lucido, W. Belkaïd, D. R. Colman, and R. B. Lennox, *ACS Chem. Neurosci.*, 2010, **1**, 86–94.

# Chapter 7: Conclusions and Outlook

This thesis described the development and characterization of new azo materials for a wide variety of applications, three of which were investigated and developed in detail.

Chapter 3 describes the behaviour of azobenzene derivatives under extremely high pressures. It was found that the fraction of chromophores in a polymer film that could be photoisomerized to the metastable *cis* form decreased from over 25% at ambient pressure to as pressure was increased to above 1 GPa. This indicates that the decrease in free volume in the film reduces the number of chromophores able to undergo photoisomerization from the *trans* to the *cis* isomer, but that there is still significant isomerization occurring even at GPa pressure levels. This has important implications in the use of the azobenzene chromophore as a muscle to power molecular machines and devices, as it demonstrates the tremendous ability of the chromophore to move even under extreme conditions. This is also a clear demonstration of the ability of azobenzene chromophores to harvest photons equivalent to sunlight to perform a considerable amount of mechanical work: thus these azo materials hold promise for solar light-transducing materials.

The work in this chapter also has implications in the bending of crystalline azobenzene compounds, another highly constrained system. We have shown that light is able to reversibly deform small crystals of many different azo compounds with visible light, even under the tight geometric constraints of the crystal lattice. Free volume (in this case, volume per non-hydrogen atom from the crystal structure) was also shown to correlate strongly with the degree of crystal deformation possible. Future work in this field should focus on the ability of the isomerization process to proceed when additional constraints are placed on the chromophore. For azobenzene to be an effective actuator, it should be able to move progressively larger loads against external resistance. A series of pressure-isomerization experiments, like those described in Chapter 3, attaching larger substituents to an azo chromophore and observing its ability to undergo isomerization could prove a valuable measure of the effective 'strength' of the process.

In Chapter 4, an inverse opal photonic crystal coated with an azobenzene-functionalized polymer was shown to undergo an irreversible change in wettability when irradiated with visible light. The sharply defined wetting threshold in the inverse opal film was continuously tuned with

both UV and visible light exposure, which photobleached the azobenzene chromophore and increased the surface energy of the structure, allowing water to infiltrate. The change in wetting was easy to identify due to the loss of the structural colour characteristic to inverse opals: these qualities make this type of material potentially useful as a tamper-indicating seal, where a simple test (immersing the structure in water) indicates exposure to light, possible only through tampering.

This work can be expanded in two ways: the first is to increase the sensitivity of the chromophoric polymer to light, allowing smaller doses to generate a higher response, while the second is to develop reversible switching. The photosensitivity can be increased by experimenting with different types of chromophores (*e.g.* spiropyrans or nitrobenzyl ethers), which provide a large optical response at the expense of the durability of the azo chromophore. The reversibility concern may be addressed by further experimentation with the polarization and irradiation angle of the incident light, as reported in other work by our group. The reversible surface energy effect is highly dependent on the irradiation parameters, and the complex internal geometry of the IOFs will require extensive experimentation to optimize these parameters inside the film.

The final two research chapters, 5 and 6, detail efforts to create an all-optical probe for neurotransmitters, based on boronic acid-functionalized azobenzene derivatives. These molecules undergo reversible binding with catechol derivatives, which form the core of several important neurotransmitter molecules (dopamine, adrenaline, and noradrenaline). Chapter 5 describes the synthesis of several novel azobenzene derivatives with a boronic acid moiety, and their optical response to dopamine, as well as the potentially interfering biogenic saccharides fructose and glucose.

Based on the results from Chapter 5, it seems that the most successful indicators incorporate larger, more highly-conjugated systems (*i.e.* those with a naphthyl moiety), and have boronic acid functionality *para* to the azo bond, as opposed to the *ortho* configuration determined to be most effective in sensors for saccharides. Synthesizing a broader library of compounds based on this substitution pattern may yield a more sensitive indicator, with a larger shift in absorbance spectrum.

Chapter 6 describes the transfer of the new azo indicator molecules described in Chapter 5 to a material that can be applied realistically to the development of fibre-optic probes, capable of optically indicating the presence of dopamine in the media surrounding the fibre via evanescent

wave spectroscopy. Three of the best candidate indicators from Chapter 5 were doped into biocompatible polyelectrolyte multilayers, and their response to dissolved dopamine was measured. The optical indicator effect was demonstrated on flat substrates at biological dopamine concentrations via transmission spectroscopy as a proof of concept, and the uptake of the indicators into polyelectrolyte multilayers coated on the surface of an optical fibre was successfully demonstrated via evanescent wave spectroscopy.

Future work in this field can focus on several main themes: the first is enhancing the stability of the indicator in the PEM matrix by careful optimization of the uptake pH and ionic strength conditions. It may prove advantageous to covalently link the indicator to the polymer chain itself, ensuring indefinite stability: however, the current method of pH-based immobilization allows a large number of candidate indicators to be screened without time-consuming polymer synthesis for each candidate. A combination of the two approaches may be the most efficient, with indicator response screened in the ionically-bound film, followed by covalent linkage of the most successful indicators onto a polyelectrolyte chain.

The second theme is enhancing the response time, which may be accomplished by reducing the thickness of the PEM layer and therefore the diffusion time for the analyte. Third, the optical sensitivity of the system may be enhanced by the addition of a reference channel to smooth out variations in the light source. This would improve the signal to noise ratio and allow more information to be extracted from the data, improving the reliability of the probe response.

One of the largest challenges for this project is the substantial reduction in the size of the fibre and sensing region required to be useful on the sizescale of small numbers of neurons. This can be addressed by pulling the working end of the fibre into a sharp point, which can reduce the effective size of the sensing region. Finally, optimization of the chemical and physical properties of the PEM coating (primarily charge and modulus, via pH and ionic strength at assembly) to make the optical probes compatible with neural tissue is a fundamental part of this project, which will benefit greatly from the work done by other current and future members of our group and our collaboration with the Montreal Neurological Institute.